



HAL
open science

Development of in-situ photoluminescence characterization tools for the study of semiconductors for photovoltaics application

Mengkoing Sreng

► **To cite this version:**

Mengkoing Sreng. Development of in-situ photoluminescence characterization tools for the study of semiconductors for photovoltaics application. Materials Science [cond-mat.mtrl-sci]. Institut Polytechnique de Paris, 2019. English. NNT : 2019IPPAX003 . tel-02496035

HAL Id: tel-02496035

<https://theses.hal.science/tel-02496035>

Submitted on 2 Mar 2020

HAL is a multi-disciplinary open access archive for the deposit and dissemination of scientific research documents, whether they are published or not. The documents may come from teaching and research institutions in France or abroad, or from public or private research centers.

L'archive ouverte pluridisciplinaire **HAL**, est destinée au dépôt et à la diffusion de documents scientifiques de niveau recherche, publiés ou non, émanant des établissements d'enseignement et de recherche français ou étrangers, des laboratoires publics ou privés.



Development of in-situ photoluminescence characterization tools for the real-time study of semiconductor materials for photovoltaic application

Thèse de doctorat de l'Institut Polytechnique de Paris
préparée à Ecole Polytechnique

École doctorale n°(626) Institut Polytechnique de Paris (IP Paris)
Spécialité de doctorat : Sciences et Technologies Industrielles

Thèse présentée et soutenue à Palaiseau, le 21/10/2019, par

Mengkoing SRENG

Composition du Jury :

| | |
|---|--------------------|
| M. Jean-Paul KLEIDER Directeur de Recherche, Université Paris-Saclay (GEEPs) | Président |
| Mme Anne KAMINSKI-CACHOPO Professeur, Grenoble INP (IMEP-LAHC/PHELMA) | Rapporteur |
| M. Stefan GLUNZ Professeur, Albert-Ludwigs-University Freiburg (Fraunhofer ISE) | Rapporteur |
| Mme Danièle BLANC-PELISSIER Chargé de Recherche, Institut des Nanotechnologies de Lyon (INL) | Examineur |
| Mme Isabelle BETREMIEUX Conseiller Scientifique, TOTAL | Examineur |
| M. Benjamin STRAHM Ingénieur de Recherche, Meyer Burger | Examineur |
| M. Jimmy MELSKENS Ingénieur de Recherche, Eindhoven University of Technology | Examineur |
| M. François SILVA Ingénieur de Recherche, Ecole Polytechnique (LPICM) | Directeur de thèse |

“There is nothing impossible for him who will try.”

Alexander the Great

To my dear parents and my beloved sisters.

ACKNOWLEDGMENT

During these three years, it has been a privilege and an adventure to work alongside many talented and inspiring individuals in both Institut Photovoltaïque d'Île-de-France (IPVF) and Laboratoire de Physique des Interfaces et des Couches Minces (LPICM, Ecole Polytechnique). As the journey has now come to an end, I would like to take this opportunity to thank everyone who has accompanied and contributed in this doctoral study.

First and foremost, I would like to thank my thesis director, François Silva, for his advices and support. I am so grateful to have worked with you to build these amazing in-situ photoluminescence characterization tools. It was not an easy task, but we finally made it. Thank you so much for giving me lots of freedom to work on the project from different angles. Also, thank you for always making yourself available when I need help for either scientific researches or administrative processes.

Next, I would like to express my deep gratitude to professor Pere Roca i Cabarrocas, the director of LPICM, for his guidance. It is through our many discussions that I have developed my research and analytical skills. Thank you so much for always giving me many valuable comments and encouraging me to interact with other researchers both inside and outside the laboratory. My gratitude also extends to professor Bernard Drévilion, who believes in me before I even have confidence in myself. I also want to thank Laurence Gérot, Gabriela Medina, and Fabienne Pandof, who always help me go through many complex administrative processes. Equally, I want to thank Eric Paillassa and Frédéric Liège, who always have solutions to every of my technical questions/problems.

Furthermore, I would like to thank Jean-Charles Vanel for many helps, in particular the development of a LabView-based graphic user interface to control the in-situ MPL system. My deep appreciation also goes to the BEER team: Cyril Jadaud, Jean-Luc Moncel, Jérôme Charliac, Frédéric Farci, Jonathan Meot, who have spent a lot of their time to help us build the new substrate holder. But more importantly, thank you all so much for always by my side when the plasmat reactor had problems. *Do you remember the day we had the black-out at the building 406? How about the day we tried to take a fragment of ceramic out of the turbo pump?* Also, I want to thank Pavel Bulkin for making Al₂O₃-passivated samples for all my experiments and helping me to characterize samples with exo-diffusion and FTIR. I also wish to acknowledge the help from Jacqueline Tran, Jean-Luc Maurice, Lenuta-Ileana Florea, and Sandrine Tusseau-Nenez, for AFM, TEM and XRR measurements. I also want to express my appreciation to Erik Johnson, Martin Foldyna, Nicolas Vaissière, Wanghua Chen, Dmitri Daineka, Denis Tondelier, and all other researchers at LPICM. I have learned a lot of things from our small talks.

I also owe my deep gratitude to Christophe Bonelli, Denis Jahan, and Bruno Carlotti, who give me opportunity to be part of IPVF. Furthermore, I want to thank Sonia Haouka, Bérengère

Larue, Ariana Salemi, and Liying Zhou-Ducret for many helps on the administrative processes. It is true that I can find the answer to every of my questions concerning the administrative processes by going to your office, not to mention the chocolate. Also, I would like to thank Olivier Roussel, Alexis Denis, and Côme Cabriel, who always work to ensure security and facilitate the research processes in the laboratory at IPVF. My appreciation also extends to Ines Bouzidi, who helped me through the patent application process.

Moreover, I would like to dedicate a special thank to Daniel Suchet, Laurent Lombez, Daniel Ory, and Baptiste Bérenguier, who frequently shares many fascinating discussions regarding photoluminescence. Also, I would like to thank Jean-Paul Kleider, José Alvarez, and Alexandre Jaffre from GEEPs for giving us many interesting comments on the MPL system. In addition, I wish to thank Sylvain Pouliquen and Andy Zauner from Air Liquid, with whom I occasionally have interesting discussions concerning surface passivation provided by aluminum oxide. I would also like to thank researchers from Fraunhofer ISE (Frank Feldmann and Martin Bivour) and INES (Romain Cariou and Karim Medjoubi) for providing oxide-passivated c-Si wafer and tandem cells respectively.

I also wish to extend my gratitude to the TOTAL research team: Etienne Drahi, Sergej Filonovich, Perine Jaffrennou, Ludovic Hudanski, Martin Sander, Jara Fernandez Martin, Vincent Maillard, Patricia Prod'homme, Amjad Deyine, Julien Penaud, and Nacib Benmammar, for a very warm welcome during almost two years of my PhD in the building 404A. Thank you so much for allowing me to benefit many characterization tools in the building. Also, thank you for many small yet interesting chats during the coffee break. That really helped improve my French languages.

My grateful thank also goes to all colleagues (Ph.D. students and Post-Doc) at both LPICM and IPVF, who share happiness and sometimes misery during these three years. First, I want to thank Fabien Lebreton, who introduced me to the surface passivation of crystalline silicon wafer and made me fall in love with it. Then, I would like to sincerely thank Guillaume Fischer, Marta Chrostowski, and Chloé Dindault, who always motivate and help me to go through many problems in the research as well as in life. Also, I want to thank Rasha Khoury, Karim Ouaras, Jean-Maxime Orlac'h, who were wonderful office mates. It was great to share some small talks with all of you. Furthermore, I would like to thank all other colleagues: Paul Narchi, Ronan Léa, Gwénaëlle Hamon, Rafaël Peyronnet, Mutaz Al-Ghzaiwat, Letian Dai, Arvid Lindberg, Hindia Nahdi, Eric Ngo, Tanguy Levent, Hee Ryung Lee, Minjin Kim, Anatole Desthieux, Ghewa Akiki, Romain Bude, Junkang Wang, Thomas Yoo, Arthur Marronnier, Harold Le Tulzo, Romaric de Lépinau, Adrien Bercegol, Amadéo Michaud, Julie Goffard, Simone Bernardini, Matteo Balestrieri, Wei Zhao, Yong Huang, Ahmed Ben Slimane, Baljeet Goraya, Amelle Rebai, Cécile Molto, ... Doctoral life may not be fun without all of you.

I would also like to extend my appreciation to the Student Chapter of Optics Paris (SCOP): Samuel F. Serna, Benjamin Madon, Jeséphine Morizet, Lipsa Nag, Seonyong Park, Olivier Lefebvre, Alexandra Petreto, and many other new members. Thank you for letting me to learn from you and to take a small part in organizing the IONS conference. A very special thank to AXX team: professor Buntha Ea-Kim, Chetra Mang, Muy Sokseiha, Angkeara Sway, Dara Se (*chef*), Seav Er Huy, Seiha Im, Bunnarith Uch, Sopheasith Hem, Mohethrith Eang, Sodarith Seng, Ladya Khun, Force Fidele Kien, Sothea Has, Kimsy Thor, Pichata Kim (*sous-chef*), Ratanak Din (*musician*), Bunthan Iea, Kimang Khun, Poseng Than, Sithea Nou (*Peanut*), Kimhong Chao (*magician*), Vibolroth Sambath, Vathana Thy, Bunthet Say (*poet*), and Hengrina Ly, who always make me feel like home.

Also I would like to thank all the jury members of my thesis defense: professor Anne Kaminski-Cachopo, professor Stefan Glunz, professor Jean-Paul Kleider, Mme Danièle Blanc-Pélessier, Mme Isabelle Betremieux, Mr. Benjamin Strahm, and Mr. Jimmy Melskens, for spending their time evaluating my doctoral thesis.

Last but not least, I would like to thank my dear parents, Nhor Sreng and Mouylin Ly, who always by my side no matter what. Thank you so much for your sacrifices and unconditional love. A very special thank to my two little sisters for always supporting and challenging me to go forward. I would also like to thank Laurence Villeneuve, Philippe Delande, and François Amzulesco for their generous support and many valuable advices.

Once again, thank you so much everyone for taking part in this amazing journey. I never expected that I would make it this far. I am glad that we have successfully built the in-situ photoluminescence characterization tools. But most importantly, I have built with you during these three years many great memories that will always be with me.

Contents

| | |
|--|-------------|
| ACKNOWLEDGMENT | iii |
| LIST OF FIGURES | xi |
| LIST OF TABLES | xvii |
| LIST OF ACRONYMS | xix |
| LIST OF SYMBOLS | xxi |
| INTRODUCTION | 1 |
| 0.1 Overview of global energy consumption | 1 |
| 0.2 Toward renewable energy production | 2 |
| 0.3 Thesis aim and outline | 4 |
| 1 PHYSICS OF SOLAR CELL | 7 |
| 1.1 Basics of semiconductor physics | 8 |
| 1.1.1 Thermal equilibrium | 9 |
| 1.1.2 Steady-state condition | 9 |
| 1.2 Generation of electron-hole pairs | 10 |
| 1.3 Recombination & Carrier lifetime | 11 |
| 1.3.1 Radiative recombination | 11 |
| 1.3.2 Auger recombination | 12 |
| 1.3.3 Defect-assisted recombination | 13 |
| 1.3.4 Effective carrier lifetime | 15 |
| 1.4 Transport of charge carriers | 16 |
| 1.4.1 Diffusion | 16 |
| 1.4.2 Drift | 17 |
| 1.5 P-N junctions | 17 |
| 1.6 Crystalline silicon solar cells | 18 |
| 1.6.1 Cell structure | 18 |
| 1.6.2 Working principle and cell characteristics | 19 |
| 1.6.3 Technological developments | 21 |
| 2 SILICON DEFECTS AND SURFACE PASSIVATION | 29 |
| 2.1 Defects in bulk silicon | 30 |
| 2.1.1 Intrinsic defects | 30 |
| 2.1.2 Extrinsic defects | 31 |
| 2.2 Silicon dangling bonds | 31 |

| | | |
|----------|--|-----------|
| 2.2.1 | Trap density | 31 |
| 2.2.2 | Charge states | 32 |
| 2.3 | Passivation mechanism | 33 |
| 2.3.1 | Chemical passivation | 33 |
| 2.3.2 | Field-effect passivation | 33 |
| 2.4 | Passivating materials | 34 |
| 2.4.1 | Hydrogenated amorphous silicon | 34 |
| 2.4.2 | Aluminum oxide | 35 |
| 3 | PHOTOLUMINESCENCE | 41 |
| 3.1 | Emission of light | 42 |
| 3.1.1 | Thermal radiation | 42 |
| 3.1.2 | Non-thermal radiation | 43 |
| 3.2 | Photoluminescence | 44 |
| 3.2.1 | Excitation energy | 45 |
| 3.2.2 | Excitation intensity | 46 |
| 3.3 | Steady-state photoluminescence | 46 |
| 3.3.1 | Spectral analysis | 46 |
| 3.3.2 | PL intensity | 47 |
| 3.4 | Modulated photoluminescence | 48 |
| 3.4.1 | Carrier lifetime measurement | 48 |
| 3.4.2 | Differential vs Steady-state lifetime | 49 |
| 4 | IN-SITU SSPL: A UNIQUE CHARACTERIZATION TOOL | 53 |
| 4.1 | Introduction to in-situ SSPL | 54 |
| 4.1.1 | Tool configuration | 54 |
| 4.1.2 | Operation mode | 56 |
| 4.2 | In-situ study of plasma effects on surface passivation | 57 |
| 4.2.1 | Experiments | 58 |
| 4.2.2 | Results | 59 |
| 4.2.3 | Root cause of plasma effects | 61 |
| 4.2.4 | Mechanisms behind the plasma-induced modifications of surface pas- sivation | 65 |
| 4.2.5 | Effect of passivation layer thickness | 68 |
| 4.2.6 | Effect of RF power & pressure | 69 |
| 4.2.7 | Effect of substrate temperature | 70 |
| 4.2.8 | Recovery of surface passivation | 73 |
| | Summary | 75 |
| 5 | IN-SITU MPL: FROM A QUALITATIVE TO A QUANTITATIVE TECHNIQUE | 79 |
| 5.1 | System design | 81 |
| 5.1.1 | Excitation system | 81 |
| 5.1.2 | Detection system | 82 |
| 5.1.3 | Optical acquisition system | 82 |
| 5.1.4 | Flexibility of system | 84 |
| 5.2 | Calibration of the system | 86 |
| 5.2.1 | Phase shift calibration | 86 |
| 5.2.2 | Study and optimization of system parameters | 88 |
| 5.3 | Determination of minority carrier lifetime at a specific carrier density | 91 |

| | | |
|-------|--|------------|
| 5.4 | Development of graphic user interface | 93 |
| 5.5 | Carrier lifetime correction | 95 |
| 5.6 | Carrier lifetime vs Temperature | 97 |
| 5.7 | In-situ study of surface passivation during deposition of passivation layers . . . | 100 |
| 5.7.1 | Sample & experimental set-up | 100 |
| 5.7.2 | Results & Discussion | 101 |
| 5.8 | In-situ study of surface passivation during annealing | 103 |
| 5.8.1 | Sample & experimental set-up | 103 |
| 5.8.2 | Results | 104 |
| 5.8.3 | Discussion | 106 |
| 5.9 | In-situ study of surface passivation during deposition of ARC layer | 107 |
| 5.9.1 | Experimental set-up | 107 |
| 5.9.2 | Results | 108 |
| 5.9.3 | Discussion | 110 |
| | Summary | 112 |
| | CONCLUSION & PERSPECTIVES | 117 |
| | A IN-SITU PLt: BEYOND THE MONOJUNCTION SOLAR CELL | 121 |
| | B IN-SITU MPL IN MVS CLUSTER | 129 |

LIST OF FIGURES

| | | |
|------|---|----|
| 1 | Evolution of the global total annual primary energy consumption (TAPEC) from 1900 to 2017 [1]. The pie chart represents the global TAPEC by fuel in 2017. | 1 |
| 2 | a) Shares of various renewable energy resources in the global electricity production in late 2017 [4]. b) The evolution of the annual installed capacity of solar PV and wind energy from 1997 to 2017 [1]. | 2 |
| 3 | Evolution of the market shares of different solar PV technologies (Note: the share of ribbon solar cell is included in the multi-Si share.) | 3 |
| 1.1 | Atomic structure of doped crystalline silicon: a) phosphorous doped (n-type), b) boron doped (p-type). | 8 |
| 1.2 | Schematic of radiative recombination process. Electron and hole recombine by emitting a photon with energy equal to the energy gap of material. | 12 |
| 1.3 | Schematic of Auger recombination process. Electron and hole recombine by transferring its energy to another electron. | 12 |
| 1.4 | Schematic of defect-assisted recombination. The electrons and holes can be trapped to defect with respective capture coefficient C_n and C_p and detrapped with respective emission coefficient E_n and E_p | 13 |
| 1.5 | Carrier lifetime profiles (τ_{Rad} , τ_{Aug} , τ_{SRH} , and τ_{Bulk}) as a function of excess carrier density. | 15 |
| 1.6 | Schematic of a conventional crystalline silicon solar cell structure. | 19 |
| 1.7 | Energy band diagram of a p-n junction under illumination. | 20 |
| 1.8 | The J-V curve of an operating solar cell: (Black curve) the current density and (Red curve) the power density. A blue point on the black curve corresponds to the maximum power point (MPP) of the solar cell. | 21 |
| 1.9 | a) Fine geometry contact pattern on the front surface of Violet cell, b) Schematic of solar cell structure resulted from a combination of Violet cell, Black cell and BSF technologies. | 22 |
| 1.10 | a) Passivated Emitter Solar Cell (PESC), b) Passivated Emitter and Rear Cell (PERC) developed by researchers at UNSW. | 23 |
| 1.11 | Schematic of the a) passivated emitter and rear locally diffused (PERL), b) interdigitated back contact (IBC) solar cell from SunPower | 23 |
| 1.12 | Schematic of a) solar cell features TOPCon structure at rear surface, b) IBC solar cell with n ⁺ - and p ⁺ -type poly-Si contact fingers separated by an intrinsic poly-Si. | 24 |
| 1.13 | a) Schematic of both-sides contact silicon heterojunction with intrinsic thin layer (HIT) cell, b) Schematic of HIT solar cell with an interdigitated pattern at rear surface. | 25 |

| | | |
|------|--|----|
| 2.1 | Schematics of intrinsic and extrinsic point defects in crystalline silicon: a) vacancy and self-interstitial, b) oxygen-vacancy center. | 31 |
| 2.2 | Schematic models of a) dangling bond on Si(100) surface, b) symmetric Si-Si dimer bond [6]. | 32 |
| 2.3 | Schematic model represents the chemical passivation mechanism. | 33 |
| 2.4 | Schematic model represents the field-effect passivation mechanism. | 34 |
| 2.5 | Schematic represents the atomic layer deposition(ALD) process. | 36 |
| 3.1 | Planckian locus in the CIE 1931 color space. The diagram shows the color locus (path) of incandescence black body radiation as a function of the black body temperature. Note, X and Y are the two chromaticity coordinates. | 43 |
| 3.2 | PL spectra emitted from a) AlGaAs ($E_{g,AlGaAs} = 1.75 \text{ eV}$) and b) c-Si ($E_{g,c-Si} = 1.12 \text{ eV}$) | 45 |
| 3.3 | Radiative recombination paths: a) band-to-band; b) donor state to valence band; c) conduction band to acceptor state. | 47 |
| 3.4 | Schematic represents the modulation of excitation intensity and emitted photoluminescence as a function of time during the MPL measurement. | 49 |
| 4.1 | Detail configuration of the in-situ SSPL characterization tool. | 54 |
| 4.2 | a) Schematic of the optical cube (top view, not to scale); b) the transmission and reflection properties of the dichroic mirror with a cut-off wavelength at 950 nm | 55 |
| 4.3 | A series of full PL spectra detected by in-situ SSPL in the 1 st operation modes. These full PL spectra were measured during a thermal treatment of an AlGaAs solar cell at 80°C in the hydrogen environment. | 56 |
| 4.4 | PL intensity detected by in-situ SSPL in the 2 nd operation modes. The evolution of the PL intensity (@ 1130 nm) detected during the deposition of an a-Si:H passivation layer on a single-side passivated c-Si wafer. | 57 |
| 4.5 | Schematic of the simplified configuration of in-situ SSPL in the PLASMAT reactor during the plasma exposure experiments. | 59 |
| 4.6 | Evolution of the PL signals (normalized) emitted from samples passivated by 9 nm of Al_2O_3 and a-Si:H observed during the Ar/ H_2 plasma exposure at room temperature. | 59 |
| 4.7 | Evolution of the PL signals (normalized) emitted from samples passivated by Al_2O_3 observed during a short ($\approx 1 \text{ s}$) Ar/ H_2 plasma exposure at room temperature. | 60 |
| 4.8 | Strong emission line of Argon and Hydrogen glow discharges. Data is obtained from the online publication of the Physical Measurement Laboratory at NIST [28] and Observatoire de Paris [29] | 61 |
| 4.9 | Evolution of the PL signals emitted from sample passivated by Al_2O_3 observed during the pure-Ar plasma exposure at room temperature. It is compared to the PL signal emitted from identical sample observed during the Ar/ H_2 plasma exposure. | 62 |
| 4.10 | Evolution of the PL signal emitted from an Al_2O_3 -passivated sample observed during the plasma exposure through an MgF_2 optical window at room temperature compared to the PL signal obtained during the experiment without an optical window. | 63 |

| | | |
|------|--|----|
| 4.11 | Evolution of the PL signals (normalized) emitted from the Al ₂ O ₃ -passivated sample observed during the plasma exposure through a Corning glass window at room temperature compared to the signal obtained during the experiment without an optical window. | 64 |
| 4.12 | Evolution of the PL signals (normalized) emitted from a c-Si wafer passivated by a 9 nm of a-Si:H observed during the plasma exposure through a Corning glass window at room temperature compared to the signal obtained during the experiment without an optical window. | 65 |
| 4.13 | Evolution of the PL signals (normalized) emitted from as-deposited and annealed samples passivated by Al ₂ O ₃ observed during the plasma exposure at room temperature. It is important to mention that the initial PL intensity of the annealed sample is higher than the initial intensity of the as-deposited sample, due to the fact that the surface passivation of annealed sample had been improved by annealing. | 67 |
| 4.14 | The evolution of the PL signals (normalized) emitted from samples passivated by a-Si:H at different thickness, observed during the plasma exposure at room temperature. | 68 |
| 4.15 | Evolution of the PL signals (normalized) emitted from Al ₂ O ₃ -passivated sample observed during the plasma exposure at a) different chamber pressure; c) different applied RF power. The emission of room-temperature Ar/H ₂ at b) different chamber pressure (constant RF power 15 W); d) different applied RF power (constant pressure 0.3 Torr). | 70 |
| 4.16 | Evolution of the PL signals (normalized) emitted from samples symmetrically passivated by 9 nm Al ₂ O ₃ layers, observed during the Ar/H ₂ plasma exposure at room temperature and at 200°C. | 71 |
| 4.17 | Evolution of the PL signals (normalized) emitted from samples symmetrically passivated by 20 nm a-Si:H layers, observed during the plasma exposure at room temperature and at 200°C. | 72 |
| 4.18 | Evolution of the PL signals (normalized) emitted from samples passivated by 9 nm of Al ₂ O ₃ and a-Si:H layers after the plasma exposure at room temperature. | 73 |
| 4.19 | Evolution of the PL signals (normalized) emitted from the plasma-exposed sample passivated by Al ₂ O ₃ during the annealing at 200°C. | 74 |
| 5.1 | Schematic diagram of in-situ MPL characterization tool. The tool was designed in such a way that can be attached to a PECVD reactor (PLASMAT). | 80 |
| 5.2 | Main components of the excitation system of in-situ MPL: a) the fiber-pigtailed laser diode; b) the programmable current/temperature controller. | 81 |
| 5.3 | a) High-sensitivity InGaAs photodiode; b) High-speed pre-amplifier. | 82 |
| 5.4 | Lock-in amplifier model SR830 (phase shift detection) | 82 |

| | | |
|------|--|----|
| 5.5 | Comparison of phase shift data measured by the in-situ MPL with different optical system: old system (optical cube with a dichroic mirror) and newly-designed system (cube with a parabolic mirror). With the old optical system, a high laser intensity is required, so the collected modulated PL signal was strong enough for the phase shift measurement. In this case, the minority carrier density in the sample is approximately $4.9 \times 10^{16} \text{ cm}^{-3}$. With the newly-designed system, the modulated PL signal could be strongly increased, while keeping the minority carrier density at low injection level ($\approx 3.5 \times 10^{14} \text{ cm}^{-3}$). Note: a c-Si wafer symmetrically passivated by a stack of $\text{Al}_2\text{O}_3/\text{a-SiN}_x\text{:H}$ was used as the sample in this measurements. | 83 |
| 5.6 | New optical system for in-situ MPL (substrate holder + optical system). The system is particularly designed to increased the amount of modulated PL signal collected, while maintaining the carrier concentration at low injection level. . . | 84 |
| 5.7 | a) Variation of size of detection zone by modifying the distance between the sample and the parabolic mirror (not to scale); b) Intensities of modulation MPL signal detected at different position when the parabolic mirror is move toward the sample. | 85 |
| 5.8 | a) Schematic of the sample arrangement (backside view of the substrate holder, not to scale) during the surface scanning test; b) Phase shift data obtained from both surfaces (replicate an inhomogeneous surface) during the test. | 86 |
| 5.9 | Variation of system-induced phase delay as a function of modulation frequencies. The dots in the figure represent the phase delay measured at different laser intensities. The red line represents the fitting data, using equation ($\phi_{system} = A + B \text{ Freq} + B \text{ Freq}^2$). | 87 |
| 5.10 | Calibrated phase shifts of modulated PL signals emitted from sample under excitation at different modulation frequencies (constant average laser intensity $I_{laser} = 8.8 \text{ mW}$). | 88 |
| 5.11 | Calibrated phase shifts of modulated PL signals emitted from sample under excitation at different average laser intensities and a constant modulation depth (6%). | 89 |
| 5.12 | Calibrated phase shifts of modulated PL signals emitted from sample detected with different parameters (TC, ITF) of the lock-in amplifier. The parameters of the excitation system are 1.7 mW and 6% (the experiments were also conducted at other laser excitation intensities). | 90 |
| 5.13 | Work flow during the in-situ MPL measurement of minority carrier lifetime of the sample at a specific minority carrier density. | 92 |
| 5.14 | LabView-based graphic user interface, developed for automatic control of the in-situ MPL system. The interface controls all the parameters of the excitation system (blue box), the detection system (yellow box), the in-situ measurement process (red box), and the temperature of substrate holder of PLASMAT reactor. | 94 |
| 5.15 | Minority carrier lifetime as a function of minority carrier density (MCD). The black squares (filled) is the carrier lifetime profile provided by Sinton WCT-120. The black squares (unfilled) and the red circles (unfilled) are the carrier lifetime profile obtained from MPL measurement before and after applying the lifetime correction respectively. | 96 |

| | | |
|------|--|-----|
| 5.16 | Evolution of minority carrier lifetime, as a function of temperature, of a c-Si wafer passivated by a stack of SiO _x /pc-Si. Prior to the experiment, the surface passivation properties of the stack had already been activated by annealing (600°C < T _{anneal} < 1000°C). It is worth mentioning that these minority carrier lifetimes were corrected and determined at a minority carrier density of 10 ¹⁵ cm ⁻³ | 98 |
| 5.17 | Comparison of minority carrier lifetime profiles before and after applying the temperature correction. The data is obtained during annealing of a c-Si wafer, passivated by Al ₂ O ₃ , at 350°C for 30 minutes. | 99 |
| 5.18 | Evolution of minority carrier lifetime of the sample (one surface passivated) during the deposition of an a-Si:H passivation layer (on the second surface) by a PECVD process. Each blue dash line marks the transition from one process step to another: ① the substrate temperature started to increase, ② the PECVD plasma for a-Si:H deposition was ignited, ③ the plasma was turned off. It should be mentioned that the thickness of the newly-deposited a-Si:H passivation layer after is about 85 nm. | 101 |
| 5.19 | Schematic of the <100> c-Si surface after wet-chemical cleaning in a HF solution. | 102 |
| 5.20 | Evolution of minority carrier lifetime of an Al ₂ O ₃ -passivated c-Si wafer during annealing at 350°C for 30 minutes plateau in hydrogen environment. Note: ① the substrate temperature started to increase, ② the heating element was turned off and substrate temperature started to cool down. | 104 |
| 5.21 | Evolution of minority carrier lifetime of an Al ₂ O ₃ -passivated c-Si wafer during annealing at 350°C for less than 1 minutes plateau in hydrogen environment. Note: ① the substrate temperature started to increase, ② the heating element was turned off and substrate temperature started to cool down. | 105 |
| 5.22 | Evolution of minority carrier lifetime of an Al ₂ O ₃ -passivated c-Si wafer during annealing at 250°C for less than 1 minutes plateau in hydrogen environment. Note: ① the substrate temperature started to increase, ② the heating element was turned off and substrate temperature started to cool down. | 106 |
| 5.23 | Evolution of minority carrier lifetime of an Al ₂ O ₃ -passivated c-Si wafer during deposition of a-SiN _x :H anti-reflection layer at 350°C. In the same experiment, prior to the deposition, the sample was pre-annealed at 350°C for 30 minutes. Note: ① the substrate temperature started to increase, ② the plasma for a-SiN _x :H deposition was ignited, ③ the plasma was turned off and the substrate temperature started to cool down. | 109 |
| 5.24 | Evolution of minority carrier lifetime of an Al ₂ O ₃ -passivated c-Si wafer during deposition of a-SiN _x :H anti-reflection layer at 250°C. Here, the PECVD plasma for a-SiN _x :H deposition was started as soon as the substrate temperature reached the setpoint. Note: ① the substrate temperature started to increase, ② the PECVD plasma for a-SiN _x :H deposition was ignited, ③ the plasma was turned off and the substrate temperature started to cool down. | 110 |
| A.1 | Schematic of the structure of tandem solar cells: a) tandem solar cells in 4-terminal configuration; b) tandem solar cell in 2-terminal configuration. | 122 |
| A.2 | Schematic diagram of the in-situ PLt characterization tool. The line colors represent the laser light and the photoluminescence signals in each system, steady-state PL system (blue) and modulated PL system (red). | 124 |

| | | |
|-----|---|-----|
| A.3 | Schematic diagram of the optical lens system of the in-situ PLt characterization tool. a) the complete optical system; b) the optical part used for collection of steady-state PL signal (before the modification); c) the optical part used for collection of steady-state PL signal (after the modification). | 125 |
| A.4 | Comparison of PL spectra of a perovskite cell measured by the in-situ PLt with the old and new optical systems. | 126 |
| A.5 | Results obtained from the in-situ PLt measurement of an AlGaAs/c-Si tandem solar cell. a) steady-state PL spectra of the top sub-cell (AlGaAs); b) minority carrier lifetime of the c-Si bottom sub-cell. It is important to mention that, in this test, the PL spectral measurements were configured to re-start the cycle at the same time the MPL cycle started. | 127 |
| B.1 | a) MVS cluster view from the top. The large cylinder in the middle is the ITZ zone, surrounded by deposition chambers and characterization units. b) Schematic of a PECVD chamber of the MVS cluster. | 130 |
| B.2 | Schematic of in-situ MPL on MVS cluster. | 131 |
| B.3 | Optical system designed for integration of in-situ MPL into MVS cluster. . . . | 132 |
| B.4 | TO-package laser diode setup used in the new in-situ MPL. | 133 |
| B.5 | Phase shifts introduced by the in-situ MPL system (on MVS cluster). | 133 |
| B.6 | Evolution of minority carrier lifetime of a c-Si wafer during the deposition of a-Si:H in the MVS cluster. | 135 |

LIST OF TABLES

| | | |
|-----|---|-----|
| 4.1 | Baseline plasma conditions during the plasma exposure experiments. | 58 |
| 4.2 | Plasma conditions during the study of the influence of chamber pressure and applied RF power on the plasma-induced surface passivation modification. . . . | 69 |
| 5.1 | Summary of experimental results on the optimization of parameters of detection system. YES means that the phase value measured at this combination is the same as the reference signal. NO means otherwise. | 91 |
| 5.2 | Plasma conditions used for deposition of a-Si:H film (second passivation layer) in the PLASMAT reactor. | 100 |
| 5.3 | Plasma conditions used for deposition of the a-SiN _x :H anti-reflection layer. . . | 108 |
| 5.4 | Optical properties of the a-SiN _x :H films, deposited during the experiments. . . | 111 |
| B.1 | Plasma conditions used for deposition of the a-Si:H passivation layer in the MVS cluster tool. | 134 |

LIST OF ACRONYMS

| | |
|----------------|--|
| ALD | Atomic Layer Deposition |
| ARC | Anti-reflection coating |
| BSF | Back Surface Field |
| BSR | Back Surface Reflection |
| CCP | Capacitively Coupled Plasma |
| FCC | Face-Center Cube |
| FhG-ISE | Fraunhofer Institute of Solar Energy System |
| FZ | Float Zone |
| HIT | Heterojunction with Intrinsic Thin-layer |
| HWCVD | Hot-Wire Chemical Vapor Deposition |
| IBC | Interdigitated Back Contacts (<i>cell structure</i>) |
| IPCC | Intergovernmental Panel on Climate Change |
| IPVF | Institut Photovoltaïque d'Île-de-France |
| ISFH | Institute for Solar Energy Research Hamelin |
| ITZ | Isolation and Transfer Zone |
| MCD | Minority Carrier Density |
| MIS | Metal Insulator Semiconductor |
| MPL | Modulated Photoluminescence |
| PECVD | Plasma-Enhanced Chemical Vapor Deposition |
| PERC | Passivated Emitter and Rear Cell (<i>cell structure</i>) |
| PERL | Passivated Emitter and Rear Locally diffused (<i>cell structure</i>) |
| PERT | Passivated Emitter and Rear Totally diffused (<i>cell structure</i>) |
| PL | Photoluminescence |
| POLO | Polycrystalline Silicon on Oxide |

| | |
|---------------|---|
| PV | Photovoltaic |
| RF | Radio-Frequency |
| RT | Room Temperature |
| SRH | Shockley-Read-Hall recombination |
| SRV | Surface Recombination Velocity |
| SSPL | Steady-State Photoluminescence |
| TAPEC | Total Annual Primary Energy Consumption |
| TMA | Trimethylaluminum |
| TOPCon | Tunnel Oxide Passivated Contact (<i>cell structure</i>) |
| UNSW | University of New South Wales |
| VUV | Vacuum Ultra-Violet |

LIST OF SYMBOLS

| | |
|--------------------|--|
| B_{rad} | Radiative recombination coefficient |
| C_n, C_p | Electron/Hole capture coefficient |
| $C_{a,n}, C_{a,p}$ | Auger recombination coefficient |
| D_n, D_p | Diffusion coefficient for electrons/holes |
| E_d, E_a | Donor/Acceptor level |
| E_f | Fermi level |
| E_g | Band gap or Band energy |
| E_i | Intrinsic Fermi level |
| E_n, E_p | Electron/Hole emission coefficient |
| E_t | Trap energy level |
| E_{fn}, E_{fp} | Quasi-Fermi level for electrons/holes |
| E_{ph} | Photon energy |
| FF | Fill Factor |
| G | Carrier generation rate |
| J_{sc} | Short-circuit current |
| L_n, L_p | Electron/Hole diffusion length |
| N_D, N_A | Concentration of donor/acceptor atoms |
| N_c, N_v | Effective density of states within the conduction/valance band |
| N_t | Total number of traps |
| N_{in} | Incident photon flux |
| R_{Aug} | Auger recombination rate |
| R_{Rad} | Radiative recombination rate |
| R_{SRH} | Shockley-Read-Hall recombination rate |
| R_{cn}, R_{cp} | Trap capture rate for electrons/holes |

| | |
|----------------------|--|
| R_{en}, R_{ep} | Trap emission rate for electrons/holes |
| T | Temperature |
| V_{bi} | Built-in voltage |
| V_{oc} | Open circuit voltage |
| Δ_n | Excess electron density |
| α | Absorption coefficient |
| η | Conversion efficiency |
| \hbar | Reduced Planck constant |
| λ | wavelength |
| μ_n, μ_p | Mobilities of electrons/holes |
| ω | Modulation frequency |
| ϕ | Phase shift |
| τ_{Aug} | Auger carrier lifetime |
| τ_{Rad} | Radiative carrier lifetime |
| τ_{SRH} | SRH carrier lifetime |
| τ_{dif}, τ_m | Differential carrier lifetime |
| τ_{eff} | Effective minority carrier lifetime |
| τ_{ss} | Steady-state or Actual carrier lifetime |
| \vec{E} | Electric field |
| \vec{J}_{dif} | Diffusion current densities |
| $f(E_t)$ | Probability a trap is occupied |
| k_B | Boltzmann constant |
| n, p | Electron/Hole concentration in conduction/valance band at steady-state condition |
| n_0, p_0 | Electron/Hole concentration in conduction/valance band at thermal equilibrium |
| n_i | Intrinsic carrier concentration |
| q | Elementary charge |

INTRODUCTION

0.1 Overview of global energy consumption

Energy is the lifeblood of the global economy – a crucial input to almost every good and service of the modern world. The growth of energy consumption is directly linked to the well-being and prosperity of every nation around the globe. The Growth of global population during the last few decades and the increase of standard of living for millions of people, particularly in developing countries, have pushed the world total annual primary energy consumption (TAPEC) in 2017 to nearly double the average annual consumption in the 1980s [1] (see **Figure 1**). To fulfill this demand, the consumption of fossil fuels (coal, oil and natural gas) has been considerably increased from approximately 6100 Mtoe (1980s) to 11500 Mtoe (2017), accounting for more than 85% of the global TAPEC in 2017 (see pie chart in **Figure 1**). The remaining 15% of world energy mix is generated by nuclear energy (4.41%) and various renewable energy resources (10.4%), such as solar, wind, hydropower, biomass, geothermal, etc.

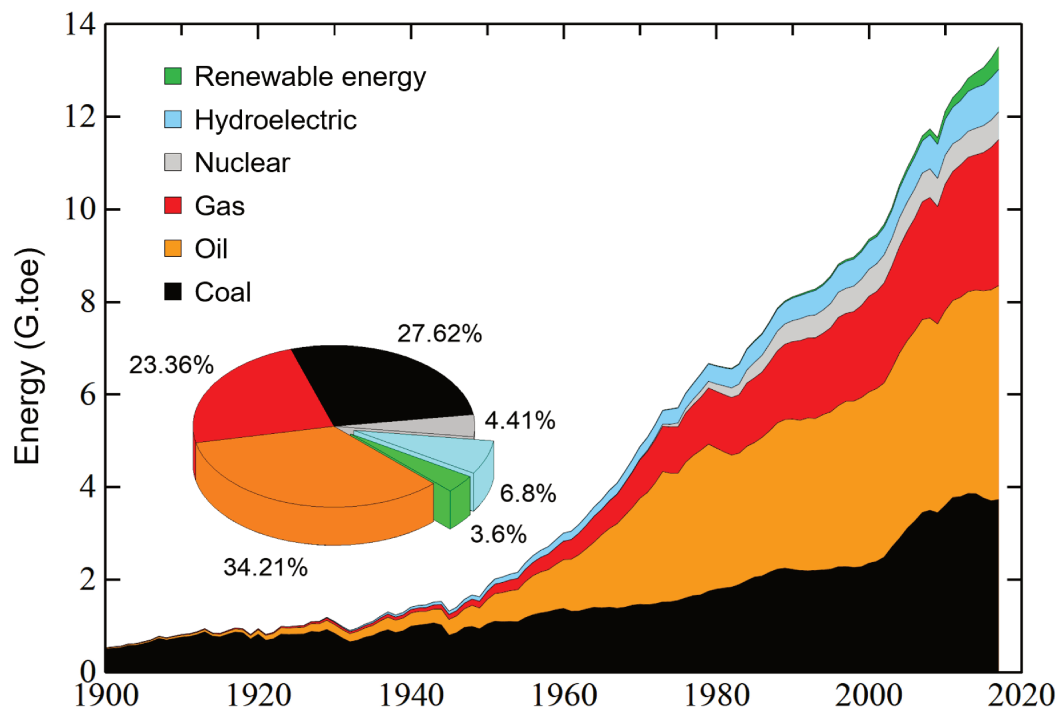


Figure 1 – Evolution of the global total annual primary energy consumption (TAPEC) from 1900 to 2017 [1]. The pie chart represents the global TAPEC by fuel in 2017.

However, consuming such a large amount of fossil fuels has led to various chronic problems, including air pollution due to emission of toxic gases (e.g. sulfur dioxide, nitrogen oxide, particulate matter, etc.) and global warming resulting from increasing atmospheric carbon dioxide concentration (up to 411 ppm in the early 2019, about 100 ppm higher than the average concentration in the 1950s [2]). In late 2018, the Intergovernmental Panel on Climate Change (IPCC) reported that the average global surface temperature has increased by 0.87°C compared to the average temperature over the period 1850-1900 [3]. The Arctic air temperature also continues to increase at double the increasing rate of global mean air temperature, leading to significantly shrinking of summertime sea ice (12.8% decline per decade [2]) as well as disruption in the Arctic ecosystem. Furthermore, changing in the polar regions has far-reaching effects on the global climate, as they play a major role in regulating the atmospheric and ocean circulation. The melting ice caps coupled with increasing global ocean temperature bring up another great challenge, the rise of global average sea level (3.3 mm increase per year [2]), threatening many low-lying areas along the coastlines.

0.2 Toward renewable energy production

To sustainably deal with these problems, renewable energy has been seen as the most promising option due to its inexhaustible resources (e.g. the total annual solar radiation falling on the earth is more than 7500 times the world TAPEC [5]) and its environment-friendly characteristic (i.e. zero emission of toxic or greenhouse gases during the operation). Over the last decade, the transition of primary energy consumption from fossil fuels to renewable energy resources (particularly solar and wind) has been observed, mainly in the electricity generation sector.

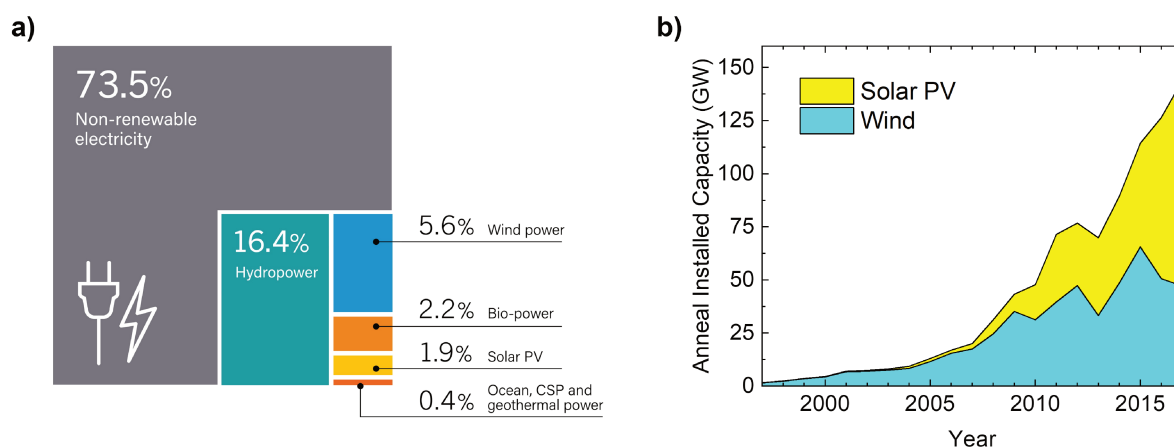


Figure 2 – a) Shares of various renewable energy resources in the global electricity production in late 2017 [4]. b) The evolution of the annual installed capacity of solar PV and wind energy from 1997 to 2017 [1].

In 2017, renewable energy accounted for 26.5% of global electricity production (see **Figure 2a**), with a 5.4% average growth rate [4]. It is important to notice that electricity is the second most consumed final energy after oil, and it is expected to further increase in the following years due to electrification of heating and transportation, growth of connected devices, and digitization of modern economics. Among various renewable energy technologies, solar

photovoltaic (PV) cell led the way in terms of newly installed renewable power capacity in the recent years (see **Figure 2b**). Solar PV makes up to nearly 55% of the installed capacity in 2017, while wind (29%) and hydropower (11%) accounted for most of the remaining renewable capacity [4].

Solar PV is divided into three main categories called generations up to recent years, depending on the semiconductor materials and technologies that are used to produce the cells. The first generation is the traditional crystalline silicon (c-Si) solar cell technology, the first commercial terrestrial solar cell as well as the most efficient single-junction solar cell available on the market today. As the name suggests, c-Si solar cells are made of c-Si materials, e.g. monocrystalline silicon (mono-Si), multicrystalline silicon (multi-Si) and ribbon silicon. Thanks to the well-developed knowledge and technology for silicon devices in microelectronic industry, the conversion efficiency of c-Si solar cells, particularly mono-Si cells, has been rapidly improved (please refer to section 1.6.3 for more information). The second generation is the thin-film solar cell technology, including hydrogenated amorphous silicon (a-Si:H), copper indium gallium selenide (CIGS), cadmium telluride (CdTe), etc. These cell technologies benefit from the possibility to considerably reduce material consumption in order to cut down the production cost; however, the problems of using toxic materials (e.g. cadmium, etc.) and low conversion efficiency remain the main factors limiting its market shares. Lastly, the third generation solar cells are all novel concept cells that have potential to overcome the Shockley-Queisser limit of the single-junction solar cell [6]. This includes multi-junction solar cell, hot carrier solar cell, intermediate and solar cell, photon up/down conversion solar cell, etc. Despite the fact that recent tandem c-Si/perovskite cell has made significant efficiency improvement, the third generation cells are not mature enough for commercialization.

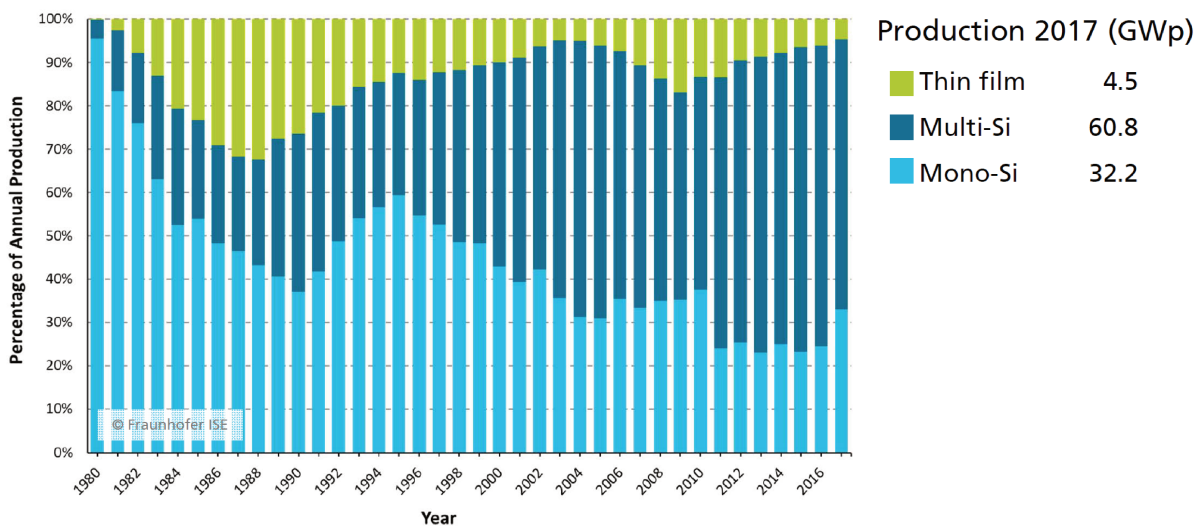


Figure 3 – Evolution of the market shares of different solar PV technologies (Note: the share of ribbon solar cell is included in the multi-Si share.)

Figure 3 shows the evolution of market shares of different solar PV technology. It can be seen that the first generation solar cell (mono-Si and multi-Si) has always been dominating the PV market, accounting for more than 95% of global annual production in 2017. The high market share of c-Si solar cells is attributed to the low cost, high conversion efficiency as well as the cell stability over a period of more than 25 years.

0.3 Thesis aim and outline

In the framework of project H “Advanced characterization and modeling” of the Institut Photovoltaïque d’Île-de-France (IPVF), my doctoral studies have been focused on the development of in-situ photoluminescence characterization tools that allow us to study, in real time during the processes, the properties of semiconductor materials, the main building blocks of photovoltaic solar cells. This thesis is structured as follows:

- Chapter 1 briefly reviews the physics of solar cell, allowing a better understanding of the relationship between the properties of semiconductor materials and the conversion efficiency of solar cells, in particular crystalline silicon solar cells. Also, the technological development of c-Si solar cell is summarized.
- Chapter 2 focuses on the characteristics of defects, mainly of the dangling bonds on the surface of c-Si wafer. Furthermore, it introduces the concept of surface passivation as well as the passivation materials that are commonly used in c-Si solar cell.
- Chapter 3 is dedicated to the physics behind the photoluminescence process. Here, the characteristics of two potential photoluminescence characterization techniques (steady-state photoluminescence and modulated photoluminescence) are also presented.
- Chapter 4 describes the first in-situ characterization tool (so-called in-situ PL) and its application in the study of surface passivation of crystalline silicon wafer under plasma exposure at various condition. Based on the experimental results, this chapter also discusses the mechanisms behind the evolution of surface passivation of c-Si wafers during the plasma exposure.
- Chapter 5 details the development of another in-situ tool (in-situ MPL), including the design, optimization of parameters, and calibration of both the system and the obtained data. Also, the chapter presents several interesting results regarding the evolution of minority carrier lifetime of passivated c-Si wafer, observed during the deposition of passivation layer, thermal annealing, and deposition of anti-reflection coating.
- Last but not least, the first appendix brings forward another in-situ characterization tool (in-situ PLt) that was built for the real-time study of tandem solar cells, while the second appendix shows the transfer of in-situ MPL from an in-house made PECVD reactor to a commercial reactor.

Summary and general conclusion are finally drawn from these doctoral works, and the possibilities for further research are outlined.

Bibliography

- [1] Centre for Energy Economics Research and Policy (BP plc). BP statistical review of world energy. <https://www.bp.com/en/global/corporate/energy-economics/statistical-review-of-world-energy.html>, June 2018.
- [2] The National Aeronautics and Space Administration (NASA). Global climate change, vital signal of the planet. <https://climate.nasa.gov/vital-signs/>. March 25th, 2019.
- [3] V. Masson-Delmotte, P. Zhai, H.-O. Pörtner, D. Roberts, J. Skea, P.R. Shukla, A. Pirani, W. Moufouma-Okia, C. Péan, R. Pidcock, S. Connors, J.B.R. Matthews, Y. Chen, X. Zhou, M.I. Gomis, E. Lonnoy, T. Maycock, M. Tignor, and T. Waterfield. Global warming of 1.5 degree celsius. <https://www.ipcc.ch/sr15/>, January 2019.
- [4] Renewable Energy Policy Network for 21st Century. Renewables 2018 global status report. <http://www.ren21.net/status-of-renewables/global-status-report/>, 2018.
- [5] World Energy Council. World energy resource: Solar. https://www.worldenergy.org/wp-content/uploads/2013/10/WER_2013_8_Solar_revised.pdf, 2013.
- [6] William Shockley and Hans J. Queisser. Detailed balance limit of efficiency of pn junction solar cells. *Journal of Applied Physics*, 32(3):510–519, 1961.

Chapter 1

PHYSICS OF SOLAR CELL

Contents

| | | |
|------------|---|-----------|
| 1.1 | Basics of semiconductor physics | 8 |
| 1.1.1 | Thermal equilibrium | 9 |
| 1.1.2 | Steady-state condition | 9 |
| 1.2 | Generation of electron-hole pairs | 10 |
| 1.3 | Recombination & Carrier lifetime | 11 |
| 1.3.1 | Radiative recombination | 11 |
| 1.3.2 | Auger recombination | 12 |
| 1.3.3 | Defect-assisted recombination | 13 |
| 1.3.4 | Effective carrier lifetime | 15 |
| 1.4 | Transport of charge carriers | 16 |
| 1.4.1 | Diffusion | 16 |
| 1.4.2 | Drift | 17 |
| 1.5 | P-N junctions | 17 |
| 1.6 | Crystalline silicon solar cells | 18 |
| 1.6.1 | Cell structure | 18 |
| 1.6.2 | Working principle and cell characteristics | 19 |
| 1.6.3 | Technological developments | 21 |

1.1 Basics of semiconductor physics

Semiconductors are the main building block of photovoltaic solar cells. They can be taken on a single element from group IV (e.g. silicon, germanium, etc.) or a compound element from group III-V or II-VI (e.g. gallium arsenide, aluminum gallium arsenide, gallium indium phosphor, etc.). Having enough electrons to fill their valence band but no free electrons, the electrical conductivity of these materials falls between that of metals and that of insulators. It means that unless external energy (e.g. raising temperature, applying an electric field, exposing to light, etc.) is provided to the system, the material will remain as an insulator.

A significant feature of semiconductors is their ability to be doped, by inserting specific atoms (dopants) into their crystalline structures. Doped semiconductors can be divided into two main groups: n-type semiconductors (intrinsic materials doped with electron excess atoms) and p-type semiconductors (intrinsic materials doped with electron deficiency atoms). **Figure 1.1** shows, as an example, the atomic structure of crystalline silicon wafers, doped with phosphorous atoms (n-type semiconductor) and with boron atoms (p-type semiconductor). By adding extra electrons or holes to the intrinsic semiconductor, the electrical conductivity of materials is greatly enhanced, but it also means that impurities in the form of foreign atoms are introduced into the crystal lattice. This leads to the formation of energy levels in the forbidden gap, a donor level (E_d) for n-type semiconductor and an acceptor level (E_a) for p-type. Note that these two types of doping are crucial to solar cells since they are actually often built with a combination of both types.

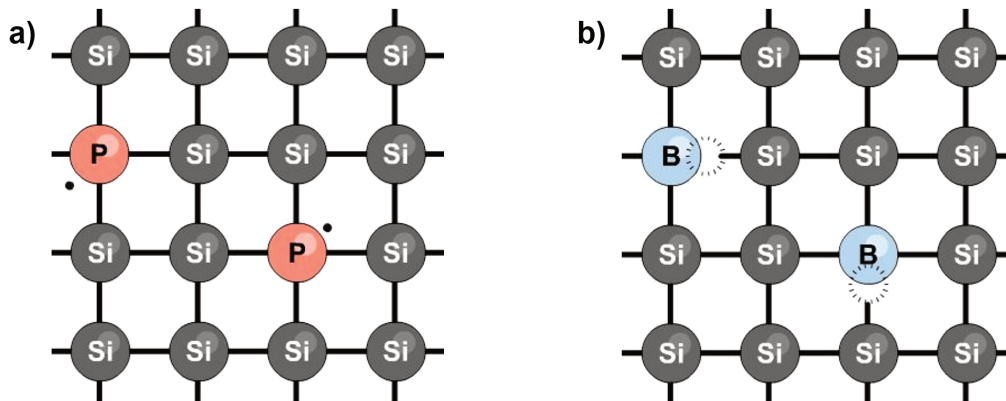


Figure 1.1 – Atomic structure of doped crystalline silicon: a) phosphorous doped (n-type), b) boron doped (p-type).

An electron moving in the semiconductor is analogous to a particle confined in a three-dimensional box, having a complex interior structure due to potential fields surrounding the compound atom's nucleus and the bound core electrons. By solving electron wavefunction, the band structure (allowed electron energy) is defined. The highest range of filled electron energies is called valence band (E_v), while the lowest range of vacant electronic state is called conduction band (E_c). The minimum energy between the conduction band and the valence band is known as the bandgap or energy gap (E_g) of semiconductor.

1.1.1 Thermal equilibrium

At thermal equilibrium (i.e. uniform temperature with no external injection or generation of carriers), the electron concentration in the conduction band can be obtained from the Fermi-Dirac statistics [1].

$$n_0 = N_c \exp\left(-\frac{E_c - E_f}{k_B T}\right) \quad (1.1)$$

Where N_c is the effective density of states within the conduction band, E_c and E_f are the bottom of conduction band energy and Fermi energy respectively, k_B is the Boltzmann constant.

Similarly, the hole density in the valence band is defined by:

$$p_0 = N_v \exp\left(-\frac{E_f - E_v}{k_B T}\right) \quad (1.2)$$

Where N_v is the effective density of states within the valence band.

In non-degenerate semiconductors (no significant interaction between dopant atoms), the product of the equilibrium electron and hole concentrations is independent of the location of Fermi energy.

$$n_0 p_0 = N_c N_v \exp\left(-\frac{E_c - E_v}{k_B T}\right) = N_c N_v \exp\left(-\frac{E_g}{k_B T}\right) = n_i^2 \quad (1.3)$$

where $E_g = E_c - E_v$ is the band gap energy, and n_i is the intrinsic carrier concentration.

1.1.2 Steady-state condition

Note that the above mentioned relations are true only in thermal equilibrium condition. However, when the semiconductor is exposed to light (operation condition of solar cell), excess electrons and holes are generated. These carriers stabilized momentarily in a quasi-thermal equilibrium within their respective band. In this case, the so-called quasi-Fermi level for electrons (E_{fn}) and for holes (E_{fp}) are used instead of Fermi level to define the carrier concentration.

Under illumination, the electron concentration in the conduction band is given by:

$$n = N_c \exp\left(-\frac{E_c - E_{fn}}{k_B T}\right) \quad (1.4)$$

Whereas the density of hole is given by:

$$p = N_v \exp\left(-\frac{E_{fp} - E_v}{k_B T}\right) \quad (1.5)$$

With a product of both concentrations:

$$np = n_i^2 \exp\left(\frac{E_{fn} - E_{fp}}{k_B T}\right) \quad (1.6)$$

Where $E_{fn} - E_{fp}$ is known as the quasi-Fermi level splitting.

1.2 Generation of electron-hole pairs

Sunlight, as well as other electromagnetic radiation, can be viewed as a stream of particles called photons that carry specific amounts of energy ($E_{ph} = \hbar\omega$). Under illumination, photons incident upon the surface of a solar cell can be reflected from the top surface, absorbed in the semiconductor material or transmitted through. The absorption or transmission of photons is determined by two main parameters: the photon energy ($\hbar\omega$) and the energy gap of semiconductor (E_g). Only if the photon has greater or equal energy to the energy gap ($\hbar\omega \geq E_g$) will the electron be excited from the valence band to the conduction band (also known as the generation of electron-hole pair). The photon with lower energy ($\hbar\omega < E_g$) will be transmitted through the material and considered as lost, as no charge carrier is generated. The probability for absorption of a photon is determined by the absorption coefficient $\alpha(\hbar\omega)$, which varies depending on the nature of materials. It is worth mentioning that the conservation of momentum and energy must be attained in the generation of charge carriers.

The generation of electron-hole pairs can occur via two different mechanism: the direct transition and the indirect transition. In the direct transition, electrons jump directly from the valence band to the conduction band by absorbing high energy photons ($\gamma \rightarrow e + h$) [2]. The momentum of the electron-hole system does not change in this case, and so does the energy of the system.

$$p_\gamma = p_e + p_h \quad (1.7)$$

$$\hbar\omega = \varepsilon_e + \varepsilon_h \quad (1.8)$$

Owing to a large absorption coefficient which leads a small penetration depth of photons in semiconductors with direct transition (direct band gap), a solar cell made of these materials does not require to be thicker than a few micrometers in order to absorb all the corresponding solar spectrum.

In the indirect transition, however, electrons cannot jump directly from the maximum of valence band to the minimum of conduction band by only absorbing the photons. They require the absorption or emission of phonons with energy $\hbar\Omega$, the lattice vibration, to fulfill the transition ($\gamma \rightarrow e + h \pm \Gamma$). The participation of phonons allows photo-induced transition from every state of the valence band to every state of the conduction band as long as the energy and momentum balance are satisfied.

$$p_\gamma = p_e + p_h \pm p_\Gamma \quad (1.9)$$

$$\hbar\omega = \varepsilon_e + \varepsilon_h \pm \hbar\Omega \quad (1.10)$$

Due to the requirement of phonon participation to satisfy energy and momentum conservation, the absorption coefficient of an indirect bandgap semiconductor is small compared to that of a direct bandgap semiconductor. Therefore, the penetration depth of photons is large, and thicker wafers (generally more than 100 μm) is required to absorb all photons of the solar spectrum.

By solving the continuity equation for photon penetration in a semiconductor, the photon current density at any depth, (x) from the surface, in the device can be calculated by:

$$j_\gamma(x) = (1 - r)j_{\gamma,in}exp(-\alpha x) \quad (1.11)$$

Where $j_{\gamma,in}$ is the incident photon current density upon the surface and r is the reflection at front surface.

Supposing that one absorbed photon generates one electron-hole pair, the charge carrier generation rate in a thin slide of semiconductor (x and $x + dx$) can be determined by the change in photon current density across the slide, becoming the differentiation of the equation 1.11 as the slide becomes very thin.

$$G = (1 - r)\alpha N_{in} \exp(-\alpha x) \quad (1.12)$$

Where N_{in} is the incident photon flux upon the surface of semiconductor.

1.3 Recombination & Carrier lifetime

Excited from the valence band to the conduction band, the free electrons are in a meta-stable state. Eventually, they will stabilize back to a lower energy position in the valence band by recombining with holes. The average time a charge carrier remains in an excited state (conduction band) after electron-hole generation before it recombines is referred to as minority carrier lifetime, denoted by τ . The carrier lifetime has nothing to do with the stability of materials but everything to do with the conversion efficiency of solar cell. Depending on the structure, solar cells made from wafers with high carrier lifetime will usually be more efficient than those made from wafers with low carrier lifetime. The minority carrier lifetime in steady-state condition can be determined by [3]:

$$\tau = \frac{\Delta n}{G} \quad (1.13)$$

Where τ is the minority carrier lifetime, Δn is the excess minority carrier concentration, and G is the carrier generation rate. It is important to mention that in the steady-state condition, the generation rate (G) is equal to the recombination rate (R).

Depending on how the excited electrons relax back to the valence band, the recombination of electrons and holes can be divided into three different mechanisms: radiative, Auger, and Shockley-Read-Hall recombination.

1.3.1 Radiative recombination

Radiative recombination is a band-to-band recombination process, which is exactly the reverse of the absorption of a photon. In this recombination process, an electron from the conduction band directly recombines with a hole in the valence band, resulting in the emission of a photon with an energy approximately equal to the band gap of the semiconductor (see **Figure 1.2**). It is worth mentioning that radiative recombination mainly occurs in direct bandgap semiconductors, yet quite limited in the indirect semiconductor as the transfer of both energy and momentum must occur simultaneously for an electron to directly recombine with a hole.

Since a free electron and a free hole must find each other to radiatively recombine, the recombination rate via this process increases with the carrier concentration [4].

$$R_{Rad} = B_{rad}np \quad (1.14)$$

Where n is the electron concentration, p is the hole concentration and B_{rad} is the radiative recombination coefficient, calculated from the absorption coefficient of materials.

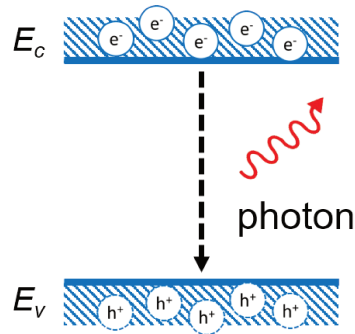


Figure 1.2 – Schematic of radiative recombination process. Electron and hole recombine by emitting a photon with energy equal to the energy gap of material.

From the definition of minority carrier lifetime, the radiative lifetime of a semiconductor can be determined by:

$$\tau_{Rad} = \frac{\Delta n}{B_{rad}np} \quad (1.15)$$

1.3.2 Auger recombination

Auger recombination is a three-particle recombination process, which involves the transfer of energy and momentum from a recombining electron-hole pair to a third particle (an electron or a hole). Receiving excess energy, the third particle is excited deep into the band (conduction or valance band) and subsequently relaxes back to the band edge through thermalization process, i.e. a series of collisions with the lattice (see **Figure 1.3**).

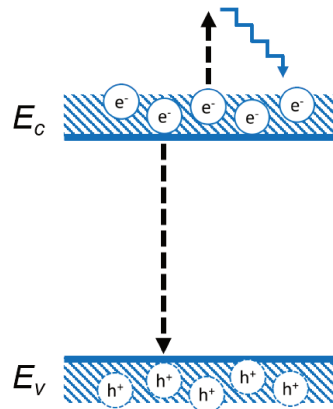


Figure 1.3 – Schematic of Auger recombination process. Electron and hole recombine by transferring its energy to another electron.

As the Auger recombination process is a result of the interaction between multiple particles, the recombination rate (R_{Aug}) is strongly determined by the carrier concentrations [4] and is defined by:

$$R_{Aug} = C_{a,n}n^2p + C_{a,p}np^2 \quad (1.16)$$

Where $C_{a,n}$ and $C_{a,p}$ are the Auger coefficients (proportionality constant), which are strongly dependent on temperature.

By definition of carrier lifetime, the Auger lifetime of a semiconductor is given by:

$$\tau_{Aug} = \frac{\Delta n}{C_{a,n}n^2p + C_{a,p}np^2} \quad (1.17)$$

1.3.3 Defect-assisted recombination

Defect-assisted recombination, also known as the Shockley-Read-Hall (SRH) recombination, is a multiple-step recombination process that involves trapping and detrapping of electrons or holes by energy states in the bandgap (see **Figure 1.4**). In this recombination process, an electron in the conduction band can relax to various energy levels and eventually to the valence band, annihilating a hole in the process.

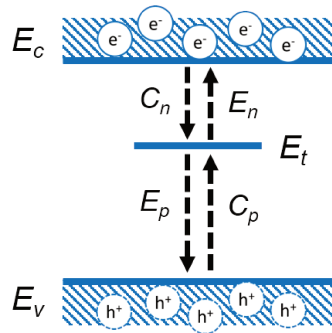


Figure 1.4 – Schematic of defect-assisted recombination. The electrons and holes can be trapped to defect with respective capture coefficient C_n and C_p and detrapped with respective emission coefficient E_n and E_p .

The rate at which a charge carrier moves into the energy level in the forbidden gap depends on the distance between the introduced energy level from either band edge. If an energy level is introduced close to one band edge, the recombination is less likely to occur as the trapped carriers will move back to their previous band energy before another carrier type jumps to the same level. However, if the energy level is introduced in the middle of the gap energy, the recombination becomes more important as the chance that an electron and a hole move to the same level is increased.

For electrons, the trap capture rate (R_{cn}) is directly proportional to the number of empty traps and the concentration of electrons in the conduction band (n) [5].

$$R_{cn} = C_n n N_t [1 - f(E_t)] \quad (1.18)$$

Where $C_n = v_{th} \sigma_n$ is the capture coefficient, N_t is the total number of traps, and $[1 - f(E_t)]$ is the probability that a trap is unoccupied. Similarly, the emission rate (E_{en}) of an electron from the trap is proportional to the number of filled traps, and it is written as:

$$R_{en} = E_n N_t f(E_t) \quad (1.19)$$

In equilibrium, the trap capture rate is equal to the trap emission rate ($R_{cn} = R_{en}$). From this, we get:

$$E_n = C_n n_0 \frac{[1 - f_0(E_t)]}{f_0(E_t)} \quad (1.20)$$

Where n_0 is the equilibrium electron concentration, and $f_0(E_t)$ is the equilibrium distribution function (Fermi-Dirac function). This distribution function is given by:

$$f_0(E_t) = \frac{1}{1 + \exp\left(\frac{E_t - E_f}{k_B T}\right)} \quad (1.21)$$

By substituting $f_0(E_t)$ into equation 1.20, the emission cross section becomes:

$$\begin{aligned} E_n &= C_n n_0 \exp\left(\frac{E_t - E_f}{k_B T}\right) \\ &= C_n n_i \exp\left(\frac{E_f - E_i}{k_B T}\right) \exp\left(\frac{E_t - E_f}{k_B T}\right) \\ &= C_n n_1 \quad \text{where, } n_1 = n_i \exp\left(\frac{E_t - E_i}{k_B T}\right) \end{aligned}$$

Under illumination, the trap capture rate is different from the trap emission rate. The net capture rate for electrons is given by:

$$R_n = C_n N_t \{n[1 - f(E_t)] - n_1 f(E_t)\} \quad (1.22)$$

For holes, similar capture and emission rates can be obtained. The hole capture rate depends on the number of holes in valence band and the number of filled traps, while the hole emission rate depend on the number of empty traps.

$$R_{cp} = C_p p N_t f(E_t) \quad (1.23)$$

$$R_{ep} = E_p N_t [1 - f(E_t)] \quad (1.24)$$

Where C_p and E_p are respectively the capture and emission cross section. In a way similar to electrons, the hole emission cross section can be determined in equilibrium condition.

$$\begin{aligned} E_p &= C_p p_0 \frac{f_0(E_t)}{1 - f_0(E_t)} \\ &= C_p p_0 \exp\left(-\frac{E_t - E_f}{k_B T}\right) \\ &= C_p p_i \exp\left(-\frac{E_f - E_i}{k_B T}\right) \exp\left(-\frac{E_t - E_f}{k_B T}\right) \\ &= C_p p_1 \quad \text{where, } p_1 = n_i \exp\left(-\frac{E_t - E_i}{k_B T}\right) \end{aligned}$$

Under illumination, the net capture rate for holes is given by:

$$R_p = C_p N_t \{p f(E_t) - p_1 [1 - f(E_t)]\} \quad (1.25)$$

In the steady-state condition, the net capture rate for electrons and for holes are equal. Therefore, the distribution function can be obtained:

$$f(E_t) = \frac{C_n n + C_p n_1}{C_n (n + n_1) + C_p (p + p_1)} \quad (1.26)$$

By substituting $f(E_t)$ in equation 1.26 into equation 1.22, the SRH recombination rate ($R_{SRH} = R_n = R_p$) can be obtained:

$$R_{SRH} = \frac{C_n C_p N_t (np - n_i^2)}{C_n (n + n_1) + C_p (p + p_1)} \quad (1.27)$$

The SRH lifetime is given by:

$$\tau_{SRH} = \frac{\Delta n}{np - n_i^2} \left[\frac{1}{C_p N_t} (n + n_1) + \frac{1}{C_n N_t} (p + p_1) \right] \quad (1.28)$$

By taking $\tau_{p0} = 1/(C_p N_t)$ and $\tau_{n0} = 1/(C_n N_t)$, the SRH lifetime can be expressed as:

$$\tau_{SRH} = \frac{\Delta n}{np - n_i^2} [\tau_{p0}(n + n_1) + \tau_{n0}(p + p_1)] \quad (1.29)$$

1.3.4 Effective carrier lifetime

As the free charge carriers in a semiconductor recombine via either radiative, Auger, or defect-assisted (SRH) recombination process, the effective minority carrier lifetime of the bulk (τ_{bulk}) can be determined by:

$$\frac{1}{\tau_{Bulk}} = \frac{1}{\tau_{Rad}} + \frac{1}{\tau_{Aug}} + \frac{1}{\tau_{SRH}} \quad (1.30)$$

Where τ_{rad} , τ_{aug} and τ_{SRH} are the radiative, Auger, and Shockley-Read-Hall lifetime respectively. **Figure 1.5** shows carrier lifetime profiles (τ_{Rad} , τ_{Aug} , τ_{SRH} , and τ_{Bulk}) as a function of excess carrier density of a passivated c-Si wafer obtained from an online simulation (pv-lighthouse.com.au). In this simulation, the wafer were set to an n-type c-Si with a doping concentration of about $2 \times 10^{15} \text{ cm}^{-3}$. The τ_{n0} and τ_{p0} were set to $200 \mu\text{s}$ and $100 \mu\text{s}$ respectively, while the energy level induced by traps E_t was set to 0.43 eV from the intrinsic energy level.

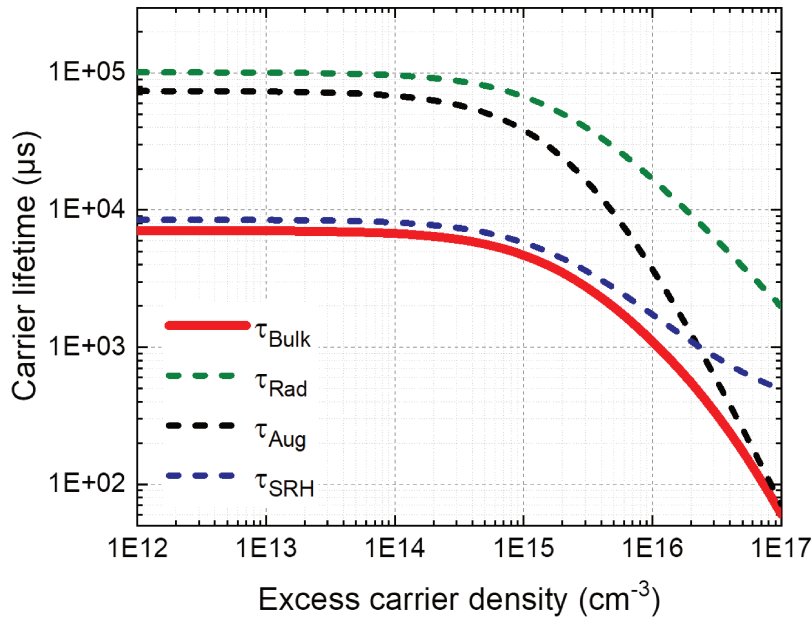


Figure 1.5 – Carrier lifetime profiles (τ_{Rad} , τ_{Aug} , τ_{SRH} , and τ_{Bulk}) as a function of excess carrier density.

At the surface, due to the high density of dangling bonds, the recombination of charge carrier mainly occurs via defect-assisted process. For that reason, the surface recombination is

commonly modeled in the same way as SRH recombination in the bulk, given by:

$$\tau_{\text{surf}} = \frac{\Delta n_s}{n_s p_s - n_i^2} \left[\frac{1}{C_p N_{t,s}} (n_s + n_1) + \frac{1}{C_n N_{t,s}} (p_s + p_1) \right] \quad (1.31)$$

where C_n and C_p are the capture cross section for electron and hole respectively, $N_{t,s}$ is total number of traps at the surface, n_s and p_s are the electron and hole density close to the surface, n_i intrinsic carrier density, $n_1 = n_i \exp((E_t - E_i)/(k_B T))$ and $p_1 = p_i \exp(-(E_t - E_i)/(k_B T))$.

Because no crystal is infinite. Therefore, the effective minority carrier lifetime has to take into account the bulk and the surface lifetime. The final effective carrier lifetime (τ_{eff}) can be expressed as:

$$\frac{1}{\tau_{\text{eff}}} = \frac{1}{\tau_{\text{bulk}}} + \frac{1}{\tau_{\text{surf}}} \quad (1.32)$$

1.4 Transport of charge carriers

Electrons in the conduction band and holes in the valence band are considered as free carriers in a sense that they can move throughout the semiconductor lattice. The movement of these carriers is directionally random, and their trajectory is changed by colliding with lattice atoms. Except in the case of a concentration gradient or an electric field, the net displacement of the charge carriers is zero in any directions. The probability a carrier moves in each direction is exactly the same, therefore the motion of a carrier in one direction will eventually be balanced by the movement in the opposite direction.

1.4.1 Diffusion

The constant random motion can lead to a net displacement of charge carriers, if one particular region has a higher carrier concentration than another region. For instance, in an illuminated solar cell, a huge amount of charge carriers are generated near the front surface, but less in the bulk. This leads to what is known as a carrier concentration gradient within the semiconductor. The generated carriers then randomly diffuse from the region of high carrier concentration to the region of low carrier concentration, until they are uniformly distributed.

The diffusivity of charge carriers depends on two main factors, the carrier thermal velocity and the mean free path (average distance between two subsequent collisions). Rising the temperature will increase the carrier velocity and thus lead to a faster carrier diffusion. From the molecular physics, the flux of diffusing particles is proportional to the concentration gradient, and the one-dimensional diffusion equations for electrons and holes are given by:

$$\vec{J}_{n,\text{diff}} = q D_n \vec{\nabla} n \quad (1.33)$$

$$\vec{J}_{p,\text{diff}} = -q D_p \vec{\nabla} p \quad (1.34)$$

Where $\vec{J}_{n,\text{diff}}$ and $\vec{J}_{p,\text{diff}}$ are the diffusion current densities for electrons and holes respectively, D_n and D_p are diffusion coefficient, n and p are electron and hole concentrations, and q is the elementary charge.

1.4.2 Drift

In the presence of electric field, superimposed on the random motion, each type of charge carriers tend to move in a net direction. While holes are accelerated in the direction of the field, electrons (holding negative charge) are accelerated in the opposite direction. The trajectory of carriers is obtained as a vector addition between its direction and the electric field, and the net carrier movement is characterized by the carrier mobility, which varies between different semiconductor materials. This movement of carriers due to the presence of electric field is called drift transport, and the one-dimensional drift equation is given by:

$$\vec{J}_{n,\text{drif}} = qn\mu_n\vec{E} \quad (1.35)$$

$$\vec{J}_{p,\text{drif}} = qp\mu_p\vec{E} \quad (1.36)$$

Where $\vec{J}_{n,\text{drif}}$ and $\vec{J}_{p,\text{drif}}$ are the drift current density for electrons and for holes, μ_n and μ_p are the electron and hole mobilities, n and p are carrier concentrations, and q is the elementary charge.

In case where a gradient of electrical energy and a gradient of the chemical potential are present simultaneously, the total current density of electrons and holes is given by the sum of the diffusion current density \vec{J}_{diff} and the drift current density \vec{J}_{drif} . It is worth mentioning that the carrier transport equations describe how charge carriers move, e.g. the flow of current, etc.

$$\vec{J}_n = qn\mu_n\vec{E} + qD_n\vec{\nabla}n \quad (1.37)$$

$$\vec{J}_p = qp\mu_p\vec{E} - qD_p\vec{\nabla}p \quad (1.38)$$

1.5 P-N junctions

A p-n junction is formed when the n-type and p-type semiconductor are joined together, either by diffusing dopants into or by depositing an additional doped layer on a pre-doped substrate with opposite dopant. In this case, the resulting semiconductor is inhomogeneous in terms of free carrier concentration (high electron concentration in n-type region and high hole concentration in p-type region). This leads to diffusion of electrons from n-type side to p-type side and diffusion of hole from p-type side to n-type side. However, when the electrons and holes move to another side of the junction, they leave behind charge on the dopant atom sites that are fixed in the crystal lattice. The positive ion cores appear in n-type material, while negative ion cores appear in the p-type. Therefore, an electric field (\vec{E}), with a direction from n-type to p-type region, is formed and counteracts the diffusion of electrons and holes. This region is called space-charge region or commonly known as depletion region, since it is effectively depleted of free carriers. In thermal equilibrium, the diffusion and drift currents for each carrier type exactly balance, so there is no net current flow.

$$\vec{J}_n = qn_0\mu_n\vec{E} + qD_n\vec{\nabla}n = 0$$

$$\vec{J}_p = qp_0\mu_p\vec{E} - qD_p\vec{\nabla}p = 0$$

Using Einstein relationship, the electric field can be written as:

$$\vec{E} = \frac{k_B T}{q} \frac{1}{p_0} \frac{dp_0}{dx} \quad (1.39)$$

The built-in voltage, which arises from the exposure of the positive and negative space charge at the depletion region, can be obtained by integration of the electric field across the region

$$V_{bi} = \int_{-x_N}^{x_P} E dx = \int_{-x_N}^{x_P} \frac{k_B T}{q} \frac{1}{p_0} \frac{dp_0}{dx} dx = \frac{k_B T}{q} \int_{p_0(-x_N)}^{p_0(x_P)} \frac{dp_0}{p_0} = \frac{k_B T}{q} \ln \left[\frac{p_0(x_P)}{p_0(-x_N)} \right]$$

For non-degenerate semiconductor, $p_0(x_P) = N_A$ and $p_0(-x_N) = n_i^2/N_D$. Therefore, the built-in voltage is

$$V_{bi} = \frac{k_B T}{q} \ln \left[\frac{N_D N_A}{n_i^2} \right] \quad (1.40)$$

The current flowing through the p-n junction at thermal equilibrium (in the dark) is given by the Shockley diode equation,

$$J(V) = J_0 \left[\exp\left(\frac{qV}{nk_B T}\right) - 1 \right] \quad (1.41)$$

Where J_0 is the diode dark saturation current, V is the applied voltage, and n is the ideality factor ($n = 1$ for ideal diode). J_0 is an important parameter, which describes the recombination rate in the device (The bigger the recombination is the larger the J_0).

Under light exposure, excess free carriers are generated through out the semiconductor, leading to an opposing current (J_L). So the current flow through the junction in this case is,

$$J(V) = J_0 \left[\exp\left(\frac{qV}{nk_B T}\right) - 1 \right] - J_L \quad (1.42)$$

1.6 Crystalline silicon solar cells

Among many, crystalline silicon is the mostly used semiconductor for photovoltaic application for many reasons. First and foremost, the absorption characteristic of crystalline silicon (energy gap) matches fairly well to the solar spectrum, allowing almost an optimal conversion of solar energy to electrical energy. In addition, the properties of crystalline silicon material have been thoroughly studied and understood thanks to the electronic industry, not to mention the well-developed crystalline silicon fabrication technologies. Last but not least, silicon is an abundant materials, allowing the low production cost.

1.6.1 Cell structure

For a working solar cell, at least three structure elements are required: an absorber layer, a carrier-selective/carrier-separation layer, and the electrical contacts. For most of the commercially available silicon solar cells, the absorber layer is made of the lightly doped ($N_{Dope} \approx 10^{16} \text{ cm}^{-3}$) crystalline silicon wafer, with a thickness around $100 \mu\text{m}$ to absorb the incoming photons.

On top of the absorber, a thin highly opposite doped ($N_{Dope} > 10^{20} \text{ cm}^{-3}$) layer is introduced by either implantation, diffusion process, or deposition of epitaxy layer. This leads to

the formation of a p-n junction and further induces the internal electric field that prevents the diffusion of majority carrier across the junction.

The electrical contacts are made on both surfaces (front and back) of the wafer in order to collect free carriers and connect to the external circuit. The front metal contacts are made of tiny finger grids for the purpose of allowing the photons to reach the absorber layer while keeping the front contact series resistance low. All finger grids are also connected to busbars to further improve the conductivity. On the other hand, the back contact is generally made of full area metal contact in order to have minimal back contact series resistance.

To improve the conversion efficiency, different layers and architectures have been introduced to this basic structure. For instance, passivation layers are introduced to the front and back surface of solar cell so as to neutralize the dangling bonds and thus reduce the surface carrier recombination (for more detail, please refer to chapter 2). Furthermore, one or two layers are added on top of the front passivation layer (see **Figure 1.6**) in order to reduce the optical reflection by using the interference effect.

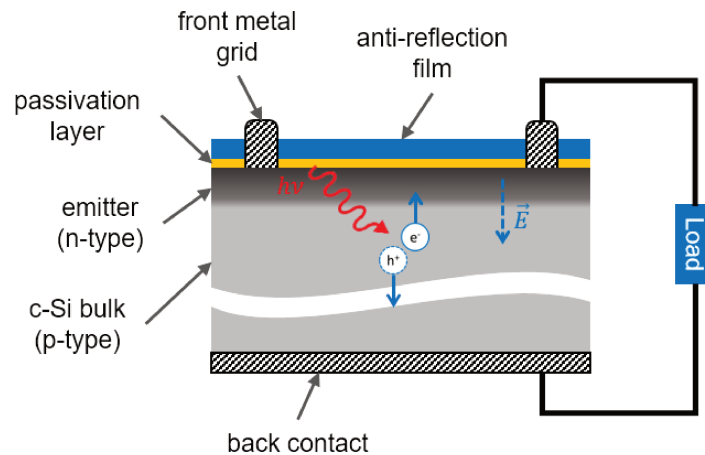


Figure 1.6 – Schematic of a conventional crystalline silicon solar cell structure.

1.6.2 Working principle and cell characteristics

Despite being fabricated from different semiconductor materials with different technologies, every photovoltaic cell works on similar principles. Under illumination, the absorber layer absorbs the incoming photons ($\hbar\omega \geq E_g$), and thus free charge carriers are generated. These carriers will eventually recombine (as described in section 1.3), and their lifetime depends strongly on the quality of absorber layer (bulk silicon) and the surface quality.

The generated charge carriers move around in random directions. The majority carriers that move close to the p-n junction will be pulled back into their previous parts, while the minority carriers will be accelerated by the electric field to other side of the junction (drift motion). This mechanism separates the charge carriers by keeping electrons in the n-type region and holes in the p-type region. Therefore, the homogeneous distribution of charge carriers throughout the solar cell is prevented.

It is worth mentioning that as the excess carriers are generated, the Fermi level inside the semiconductor is split into two: the quasi-Fermi level for electrons and the quasi-Fermi level for

holes (see **Figure 1.7**). These quasi-Fermi levels bend toward each other and eventually merge into a single energy level at the surface of the solar cell [2]. This is due to a strong carrier recombination at the surface, leading to low carrier concentrations and thus inducing carrier concentration gradient that drives electrons and holes toward the surface (diffusion motion). In the n-type region, the gradient of quasi-Fermi level for electron (majority carrier) is much smaller than the quasi-Fermi level for hole (minority carrier), and vice versa in the p-type region. Therefore, a difference in the Fermi levels between the two surfaces (front and back) appears, fixing the carrier concentrations at the surfaces at different values.

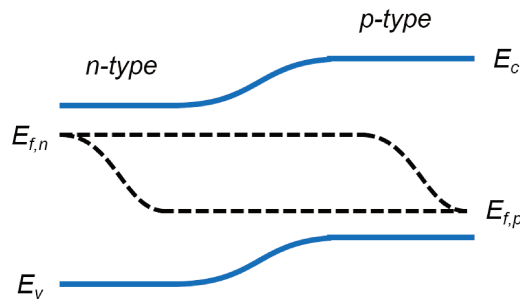


Figure 1.7 – Energy band diagram of a p-n junction under illumination.

As the solar cell is connected to the external electrical circuit, the charge carriers will start to flow through the circuit from the region with high carrier concentration to the region with low carrier concentration. It means that free electrons will flow from the n-type material to the p-type material, while free holes will flow in the opposite direction. The flow of charge particles produced the electrical energy, powering the load. This carrier flow continues endlessly, as long as the charge carriers are generated in the solar cell, due to the carrier concentration gradient. However, the strong gradient of the quasi-Fermi level for majority carriers is not an ideal condition for the conversion of chemical energy to electrical energy, because the Fermi level difference between both surfaces is less than the separation within the semiconductor. The chemical energy per electron-hole pair ($E_c - E_v$) resulting from light exposure cannot be fully utilized by the external circuit.

The current voltage characteristic of a solar cell is governed by the Shockley diode equation under light excitation. But instead of considering the device as a diode, here it is a current source.

$$J(V) = J_L - J_0 \left[\exp\left(\frac{qV}{nk_B T}\right) - 1 \right] \quad (1.43)$$

Figure 1.8 shows the J-V characteristic of a working solar cell. It is one of the most important parameters for accessing the cell performance.

The maximum voltage available from a solar cell, also known as open-circuit voltage (V_{oc}), occurs at zero current. Therefore,

$$V_{oc} = \frac{nk_B T}{q} \ln \left(\frac{J_L}{J_0} + 1 \right) \quad (1.44)$$

It is worth mentioning that a causal inspection of the above equation might indicate that V_{oc} goes up linearly with temperature. However, it is not the case as J_0 increases rapidly with temperature primarily due to changes in the intrinsic carrier concentration (n_i). The effect of temperature is complicated and varies with cell technologies.

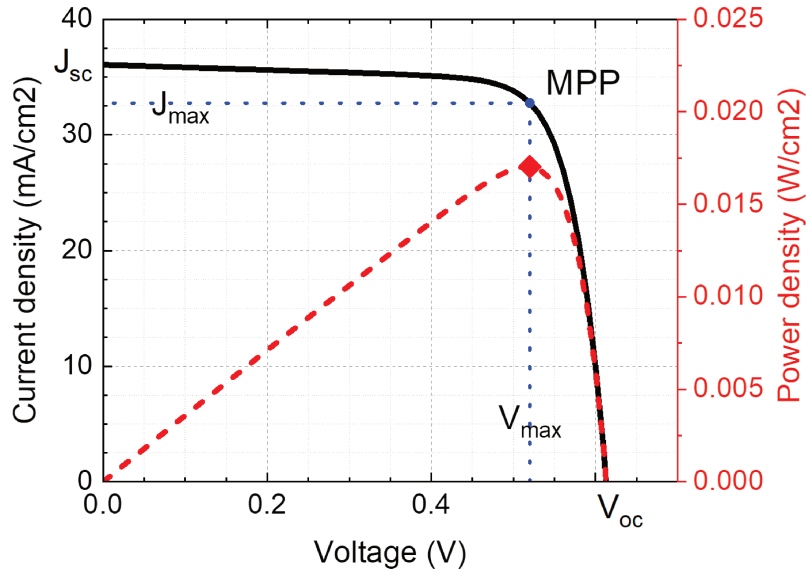


Figure 1.8 – The J-V curve of an operating solar cell: (Black curve) the current density and (Red curve) the power density. A blue point on the black curve corresponds to the maximum power point (MPP) of the solar cell.

For a perfectly passivated solar cell with uniform carrier generation, the maximum current also called short circuit current J_{sc} , can be approximated as

$$J_{sc} = qG(L_n + L_p) \quad (1.45)$$

Where G is the generation rate, while $L_n = \sqrt{D_n \tau_n}$ and $L_p = \sqrt{D_p \tau_p}$ are electron and hole diffusion length respectively.

Affected by the series and shunt resistance, the operating voltage and current of solar cell are smaller than the V_{oc} and I_{sc} . A term, which characterizes this behavior of solar cell, is known as Fill Factor (FF), and it is given by:

$$FF = \frac{V_{max} J_{max}}{V_{oc} J_{sc}} \quad (1.46)$$

The conversion efficiency (η) of a solar cell is defined as the ratio of electrical output power (P_{out}) to incident input power (P_{in}). It can be expressed as:

$$\eta = \frac{P_{out}}{P_{in}} = \frac{V_{max} J_{max}}{P_{in}} \quad (1.47)$$

1.6.3 Technological developments

The physical phenomenon responsible for converting light to electricity – photovoltaic effect – was first discovered in 1839 by a 19-year-old French physicist, Alexandre Edmond Becquerel, while he was doing the experiment in his father laboratory in Paris. However, a major key technology for silicon solar cell came about a century later (in 1940s and early 1950s) when

the Czochraski method was developed for producing highly pure crystalline silicon. In 1954, three scientists (Daryl M. Chapin, Calvin S. Fuller and Gerald L. Pearson) from Bell Telephone Laboratories announced the invention of the first silicon solar cell with an efficiency of approximately 6% [6]. Then Hoffman Electronics further pushed the cell conversion efficiency to about 10% in 1959, by introducing the front grid contacts and thus considerably reduced the series resistance of the solar cell.

Later in 1972, Lindmayer and Allison from COMSAT Laboratories developed the so-called "Violet cell" with an efficiency up to 13.5%, marking a significant advance in crystalline silicon solar cell technology. In this solar cell, the junction depth was reduced compared to the conventional structure in order to eliminate the dead layer, a region of almost constant impurity concentration at the front surface, which inhibited the acceleration of minority carriers toward the junction. In addition, a fine 60-line front contact grid (see **Figure 1.9.a**) offset the higher sheet resistance caused by the shallower junction and reduced the shading loss from 10% to 6%. Finally, a TaO_5 anti-reflective coating reduced the reflection and increased transmission of light into the solar cell. That same year, Mandelkorn and Lamneck from NASA Lewis Research

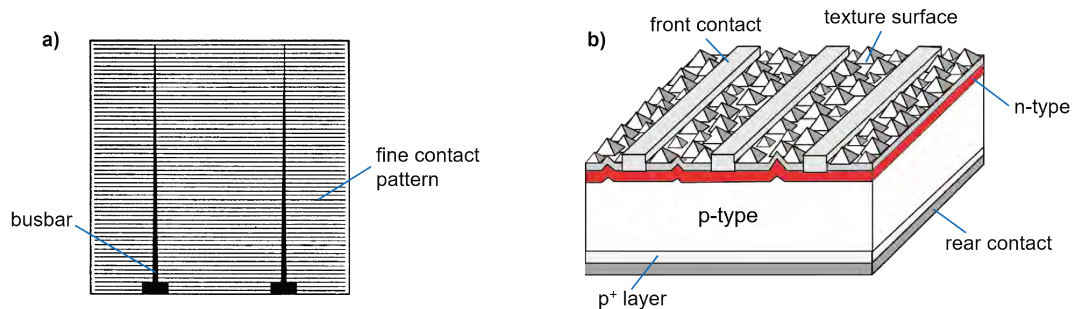


Figure 1.9 – a) Fine geometry contact pattern on the front surface of Violet cell, b) Schematic of solar cell structure resulted from a combination of Violet cell, Black cell and BSF technologies.

Center introduced another configuration of crystalline solar cell, known as back surface field (**BSF**). This structure is formed by driving in a p^+ impurity into the back of silicon wafer, which therefore accelerate minority carriers generated in the base of the cell towards the junction. Two years later (1974), COMSAT laboratories announced another breakthrough in crystalline silicon solar cell, known as "Black cell". This cell was produced by selectively etching the front surface of c-Si wafer to form light-trapping pyramids which effectively decreased the reflection loss. By incorporating the Violet cell and BSF technologies into Black cell, COMSAT laboratories attained a new crystalline silicon solar cell with an efficiency of approximately 15%. The schematic of this solar cell structure is shown in **Figure 1.9.b**. In 1977, J. Scoot-Monck introduced a thin layer of copper, silver, gold or aluminum on the back surface of solar cell, known as back surface reflection (**BSR**), in order to increase internal reflection of photons in the light-absorbing material. This effect gives photons chance to either generate more current or pass out through the front surface of the solar cell and thus reduce cell temperature.

In 1982, professor Martin Green from the University of New South Wales (UNSW) presented a new structure of crystalline silicon solar cell, known as **MINP** [7], which is a combination of the earlier developed MIS (Metal-Insulator-Semiconductor) structure and the n/p homojunction. A remarkable advancement in this new structure is the use of a thin insulating layer (e.g. 20-30 nm of SiO_2) at the front surface which considerably reduced the electronic activity of defects (recombination of carriers) and thereby increased the open-circuit voltage.

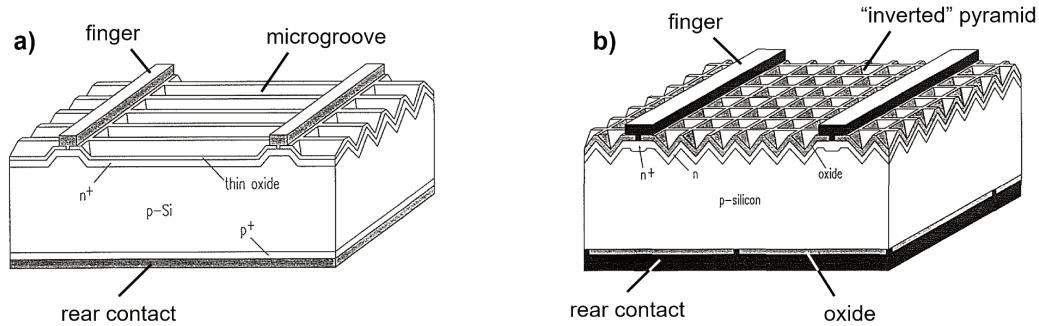


Figure 1.10 – a) Passivated Emitter Solar Cell (**PESC**), b) Passivated Emitter and Rear Cell (**PERC**) developed by researchers at UNSW.

In early 1984, the MINP cell was further developed to the so-called passivated emitter solar cell (**PESC**). The front contact of this solar cell was made through pre-patterned holes in the insulating layer to reduce the metallisation contact area. This small-area contact was to attenuate the impact of poor electronic properties at the metal/silicon interface and therefore further reduce the surface recombination. The initial efficiency of PESC cell was 19.1% [8], which was then increased to 19.8% by process refinement and later to 20.9% by incorporating microgrooved surface [9] (see **Figure 1.10.a**). In 1988, UNSW made another advancement in single-junction monocrystalline silicon solar cell by applying the passivation to rear side of the wafer, presenting a new solar cell structure known as passivated emitter and rear cell (**PERC**) with 22.8% efficiency [10] (see **Figure 1.10.b**). In addition, the inverted pyramid structure along the front surface was incorporated in order to reduce the surface reflection and to combine with the rear reflector to form an efficient light trapping scheme. Progressively refining the PERC cell, UNSW developed another new structure known as passivated emitter and rear locally diffused (**PERL**) as shown in **Figure 1.11.a**. Instead of depositing full-area metal contact on the rear passivation layer as in PERC structure, the localized point contact are made directly on the absorber material through small holes in the passivation layer. Furthermore, the heavily doped areas are introduced to each point contact in order to reduce the recombination as well as contact resistance. The initial efficiency of PERL cell is 23.3% in 1991 [11] and later increases to 24.7% in 1999 [12]. Between 1983 and 2014, UNSW was successively attaining 18 out of 20 world records for single-junction monocrystalline silicon solar cell and establishes an international reputation as the "Four-minute mile" in the field.

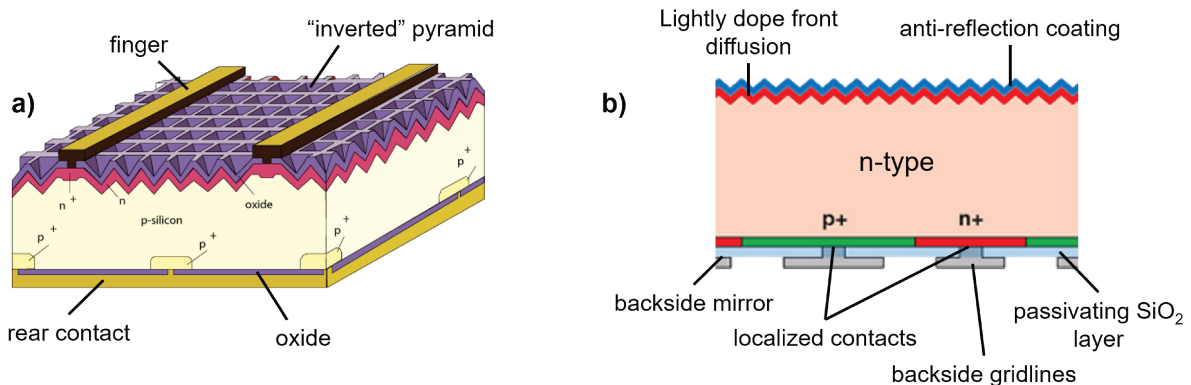


Figure 1.11 – Schematic of the a) passivated emitter and rear locally diffused (**PERL**), b) interdigitated back contact (**IBC**) solar cell from SunPower

After a 15-year pause, the record efficiency of single-junction monocrystalline silicon solar cell has been seen to increase again in the last 5 years. In late 2014, Sunpower announced a new record cell with 25% of efficiency using the interdigitated back contact (IBC) technology [13] (see **Figure 1.11.b**). First developed by Stanford University in the mid- to late-1980s, this solar cell structure has both polarity contacts located at rear surface and thus eliminates the shading loss on the front surface. It is worth mentioning that the V_{oc} of this solar cell is noticeably high due to the use of 145- μm -thick silicon wafer and the improvement in surface passivation quality resulting from new technologies, e.g. passivated contact. In September

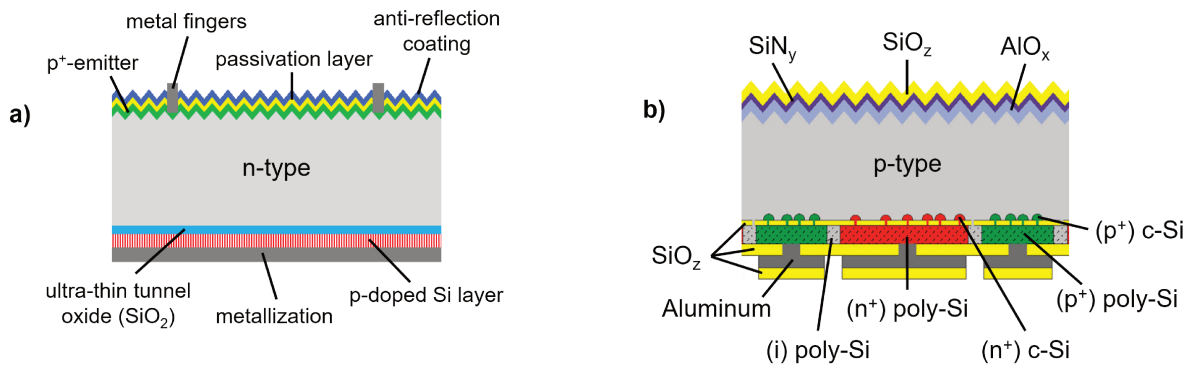


Figure 1.12 – Schematic of a) solar cell features TOPCon structure at rear surface, b) IBC solar cell with n^+ - and p^+ -type poly-Si contact fingers separated by an intrinsic poly-Si.

2015, Fraunhofer Institute of Solar Energy System (FhG-ISE) succeeded in fabricating another world record single-junction monocrystalline silicon solar cell with an efficiency of 25.1% [14], which was quickly increased to 25.7% in 2017 by process refinement [15]. These record cells feature the so-called TOPCon (Tunnel Oxide Passivated Contact) structure at rear surface (see **Figure 1.12.a**), providing a low series resistance yet high surface passivation properties. This can be achieved by introducing a carrier-selective passivated contact, made of a thin layer of tunnel oxide (one to two nanometers) to ensure good tunneling effect with low carrier recombination and a layer of highly doped semi-crystalline silicon to obtain high lateral conductivity. It should be pointed out that due to good electrical conductivity of TOPCon structure, the metal contacts are applied directly to the entire rear surface without patterning. In early 2018, the Institute for Solar Energy Research Hamelin (ISFH) has brought the cell record efficiency up to 26.1%, by combining POLO (polycrystalline silicon on oxide) junction and IBC technology [16]. The key features in this solar cell is the high selectivity of POLO junctions, which are being applied in an interdigitated pattern at the rear side in order to minimize the parasitic absorption in poly-Si and avoids the shading by front metallisation (see **Figure 1.12.b**).

Another interesting structure of monocrystalline silicon solar cell is the silicon heterojunction with intrinsic thin-layer (HIT) cell, developed in 1992 by SANYO (currently Panasonic) [17]. This solar cell takes advantages of excellent surface passivation properties of the stacked intrinsic and doped hydrogenated amorphous silicon (a-Si:H) layers in order to improve open-circuit voltage (V_{oc}) as well as decrease series resistance of the cell. **Figure 1.13.a** shows the schematic of the cell structure. For about 20 years, the conversion efficiency of HIT cell had been continuously pushed up until reaching 24.7% in 2013 [18]. Despite the high V_{oc} and low series resistance, the HIT cell still suffers from low short-circuit current (J_{sc}) due to parasitic absorption induced by the a-Si:H layers. Panasonic overcame this problem by merging the HIT and IBC technology, applying the HIT structure in an interdigitated pattern at rear surface (see

Figure 1.13.b), leading to a new record efficiency of 25.6% in 2014 [19]. By early 2017, with process refinement, Kaneka brought the conversion efficiency of HIT cell up to 26.7% [20], setting the highest conversion efficiency of monocrystalline silicon solar cell up to date.

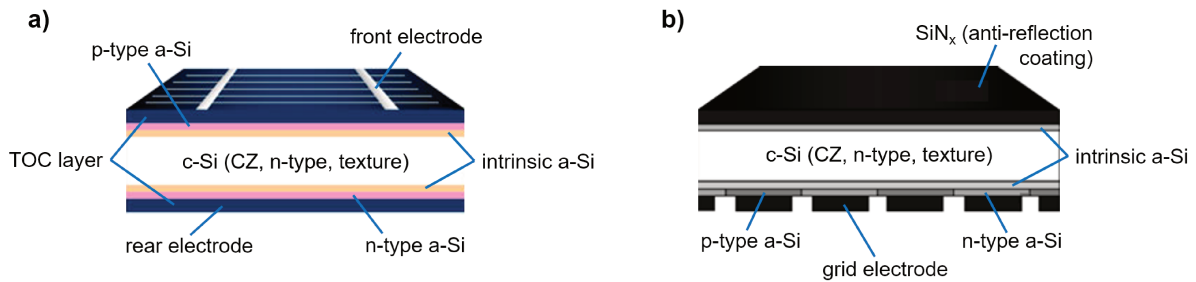


Figure 1.13 – a) Schematic of both-sides contact silicon heterojunction with intrinsic thin layer (HIT) cell, b) Schematic of HIT solar cell with an interdigitated pattern at rear surface.

Since the first invention in 1954, crystalline silicon solar cell has been through many technological developments, which have brought the conversion efficiency of solar cell from 6% to 26.7%, almost reaching the Shockley-Queisser theoretical limit. Among many technologies, the incorporation of surface passivation layer is a major advancement, holding an extremely crucial key for the high efficiency solar cells that have been developed and possibly other record-breaking solar cells that are to come.

Bibliography

- [1] Jeffery L. Gray. The physics of the solar cell. In Antonio Luque and Steven Hegedus, editors, *Handbook of photovoltaic science and engineering*, chapter 3, pages 82–129. John Wiley & Sons, Indiana, USA, 2011.
- [2] Peter Würfel and Uli Würfel. *Physic of solar cells: from basic principles to advanced concepts, third edition*. Wiley-VCH Verlag GmbH & Co. KGaA, Weinheim, Germany, 2016.
- [3] Henning Nagel, Christopher Berge, and Armin G. Aberle. Generalized analysis of quasi-steady-state and quasi-transient measurements of carrier lifetimes in semiconductors. *Journal of Applied Physics*, 86(11):6218–6221, 1999.
- [4] Arno H.M. Smets, Klaus Jäger, Olindo Isabella, René A.C.M.M. van Swaaij, and Miro Zeman. *Solar energy, the physics and engineering of photovoltaic conversion technologies and systems*. UIT Cambridge Ltd, England, 2016.
- [5] Kevin F. Brennan. *Generation and Recombination Processes In Semiconductors*, page 489543. Cambridge University Press, 1999.
- [6] D. M. Chapin, C. S. Fuller, and G. L. Pearson. A new silicon pn junction photocell for converting solar radiation into electrical power. *Journal of Applied Physics*, 25(5):676–677, 1954.
- [7] M. A. Green, A. W. Blakers, , E. M. Keller, and S. R. Wenham. High-efficiency silicon solar cells. *IEEE Transactions on Electron Devices*, 31(5):679–683, May 1984.
- [8] M. A. Green, A. W. Blakers, Jiqun Shi, E. M. Keller, and S. R. Wenham. 19.1% efficient silicon solar cell. *Applied Physics Letters*, 44(12):1163–1164, 1984.
- [9] A. W. Blakers and M. A. Green. 20% efficiency silicon solar cells. *Applied Physics Letters*, 48(3):215–217, 1986.
- [10] Andrew W. Blakers, Aihua Wang, Adele M. Milne, Jianhua Zhao, and Martin A. Green. 22.8% efficient silicon solar cell. *Applied Physics Letters*, 55(13):1363–1365, 1989.
- [11] Martin A. Green. Recent advances in silicon solar cell performance. In A. Luque, G. Sala, W. Palz, G. Dos Santos, and P. Helm, editors, *Tenth E.C. Photovoltaic Solar Energy Conference*, pages 250–253, Dordrecht, 1991. Springer Netherlands.
- [12] Jianhua Zhao, Aihua Wang, and Martin A. Green. 24.5% efficiency silicon pert cells on mcz substrates and 24.7% efficiency perl cells on fz substrates. *Progress in Photovoltaics: Research and Applications*, 7(6):471–474, 1999.
- [13] D. D. Smith, G. Reich, M. Baldrias, M. Reich, N. Boitnott, and G. Bunea. Silicon solar cells with total area efficiency above 25 In *2016 IEEE 43rd Photovoltaic Specialists Conference (PVSC)*, pages 3351–3355, June 2016.
- [14] S.W. Glunz, F. Feldmann, A. Richter, M. Bivour, C. Reichel, H. Steinkemper, J. Benick, and M. Hermle. The irresistible charm of a simple current flow pattern-25% with a solar cell featuring a full-area back contact. In *the 31st European Photovoltaic Specialists Conference and Exhibition*, pages 259–263, September 2015.
- [15] Armin Richter, Jan Benick, Frank Feldmann, Andreas Fell, Martin Hermle, and Stefan W. Glunz. n-type si solar cells with passivating electron contact: Identifying sources for efficiency limitations by wafer thickness and resistivity variation. *Solar Energy Materials and Solar Cells*, 173:96 – 105, 2017. Proceedings of the 7th international conference on Crystalline Silicon Photovoltaics.

- [16] Felix Haase, Christina Hollemann, Sören Schäfer, Agnes Merkle, Michael Rienäcker, Jan Krügener, Rolf Brendel, and Robby Peibst. Laser contact openings for local poly-si-metal contacts enabling 26.1 *Solar Energy Materials and Solar Cells*, 186:184 – 193, 2018.
- [17] Makoto Tanaka, Mikio Taguchi, Takao Matsuyama, Toru Sawada, Shinya Tsuda, Shoichi Nakano, Hiroshi Hanafusa, and Yukinori Kuwano. Development of new a-si/c-si heterojunction solar cells: ACJ-HIT (artificially constructed junction-heterojunction with intrinsic thin-layer). *Japanese Journal of Applied Physics*, 31(Part 1, No. 11):3518–3522, nov 1992.
- [18] M. Taguchi, A. Yano, S. Tohoda, K. Matsuyama, Y. Nakamura, T. Nishiwaki, K. Fujita, and E. Maruyama. 24.7 *IEEE Journal of Photovoltaics*, 4(1):96–99, Jan 2014.
- [19] K. Masuko, M. Shigematsu, T. Hashiguchi, D. Fujishima, M. Kai, N. Yoshimura, T. Yamaguchi, Y. Ichihashi, T. Mishima, N. Matsubara, T. Yamanishi, T. Takahama, M. Taguchi, E. Maruyama, and S. Okamoto. Achievement of more than 25% conversion efficiency with crystalline silicon heterojunction solar cell. *IEEE Journal of Photovoltaics*, 4(6):1433–1435, Nov 2014.
- [20] K. Yoshikawa, H. Kawasaki, W. Yoshida, T. Irie, K. Konishi, K. Nakano, T. Uto, D. Adachi, M. Kanematsu, H. Uzu, and K. Yamamoto. Silicon heterojunction solar cell with interdigitated back contacts for a photoconversion efficiency over 26%. *Nature Energy*, 2(17032), March 2017.

Chapter 2

SILICON DEFECTS AND SURFACE PASSIVATION

Contents

| | | |
|------------|--|-----------|
| 2.1 | Defects in bulk silicon | 30 |
| 2.1.1 | Intrinsic defects | 30 |
| 2.1.2 | Extrinsic defects | 31 |
| 2.2 | Silicon dangling bonds | 31 |
| 2.2.1 | Trap density | 31 |
| 2.2.2 | Charge states | 32 |
| 2.3 | Passivation mechanism | 33 |
| 2.3.1 | Chemical passivation | 33 |
| 2.3.2 | Field-effect passivation | 33 |
| 2.4 | Passivating materials | 34 |
| 2.4.1 | Hydrogenated amorphous silicon | 34 |
| 2.4.2 | Aluminum oxide | 35 |

In crystalline solids, the constituents (e.g. atoms, molecules, or ions) are arranged in a highly ordered microscopic structure, forming a crystal lattice that extends in all directions. The entire lattice can be considered as a large number of unit cells, stacking together periodically. It should be mentioned that the unit cell can have various shapes (i.e. cubic, tetragonal, monoclinic, orthohombic, rhombohedral, hexagonal, triclinic), depending on the lengths and angles between the cell edges. In crystalline silicon, the atoms are arranged in a diamond lattice structure, represented by two interpenetrating face-center cube (FCC) unit cells in which the second unit cell is shifted one-fourth along the diagonal of the first unit cell [1]. The sidelength of the cubic unit cell (the lattice constant) is 5.4307 Å, and the bond length between two silicon atoms (Si-Si) is approximately 2.3515 Å. Possessing four valence electrons, each silicon atom establishes four covalent bonds with its nearest neighbors, and therefore no unsaturated bond is left behind (except in the vicinity of defects and the surface).

2.1 Defects in bulk silicon

The atomic arrangement in the crystalline silicon bulk is not always perfect. Somewhere in the silicon lattice, defects exist and their effects cannot be neglected. The lattice defects can be classified into three main categories depending on their dimension [2]. The 0-dimensional defects consist of isolated sites in the crystal structure, and are hence called point defects. An example is a solute or impurity atom, which alters the crystal pattern at a single point. The 1-dimensional defects are called dislocations. They are lines along which the crystal pattern is broken, e.g. the grain boundaries along which distinct crystallites are joint together. The 3-dimensional defects change the crystal pattern over a finite volume, e.g. voids, precipitates, etc. Thanks to the development of crystal growth technology, the large-defect issues such as dislocation and sizable precipitate can be avoided. However, point defects remain the main problem, affecting the performance of silicon devices. Disturbing the crystal pattern at isolated sites, the point defects can be further divided into two sub-categories: the intrinsic defects and the extrinsic defects.

2.1.1 Intrinsic defects

In a pure silicon material, the intrinsic defect is formed when an atom is missing from a position that ought to be filled in the crystal, creating vacancy, or when an atom occupies an interstitial site where no atom would ordinary appear, causing an interstitialcy (see **Figure 2.1.a**). Because the interstitial sites in most crystalline solids are small or have an unfavorable bonding configuration, the interstitialcies are high-energy defects that are relatively uncommon. Vacancies, on the other hand, are present in a significant concentration in all crystalline materials. Both vacancies and self-interstitials are not stable, and they can migrate around inside the crystal under certain conditions. While interstitial atoms are considered to be mobile at all temperatures, annealing has been pointed to be the main reason behind the long range migration of vacancy [3, 4]. These intrinsic point defects can aggregate leading to the formation of micro-voids or silicon interstitial clusters, which induce detrimental effects on the crystal electrical properties. It is worth mentioning that the intrinsic point defects are not easy to detect because their signal is often below the detection limit of most characterization tools.

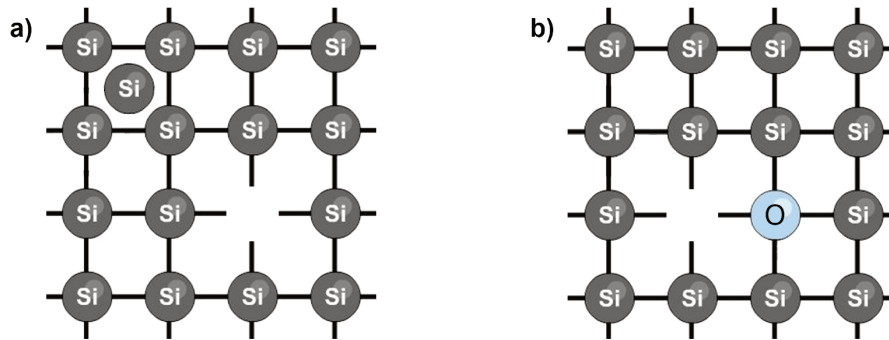


Figure 2.1 – Schematics of intrinsic and extrinsic point defects in crystalline silicon: a) vacancy and self-interstitial, b) oxygen-vacancy center.

2.1.2 Extrinsic defects

The extrinsic point defects are foreign atoms, which are called solutes if they are intentionally added to the material and called impurities if they are not. In this section, we focus more on impurities that are unintentionally added to the crystal lattice. The foreign atom may occupy a lattice site, in which case it is called a substitutional impurity or it may fill an interstitial site, in which case it is called an interstitial impurity. Since the interstitial site is relatively small, the interstitial impurity is commonly limited to small atoms such as oxygen, carbon, nitrogen, etc. Among these, interstitial oxygen is one of the main impurity in crystalline silicon. When heated to 430-450°C, it forms defects which act as donors [5]. Oxygen impurities can diffuse around and aggregate with other defects (see **Figure 2.1.b**), e.g. other oxygen impurities to form clusters, intrinsic interstitial to form the oxygen-vacancy center (V_iO_j), etc. Another interesting impurity is carbon. Coming from group IV, carbon is electrically neutral and has no static dipole moment because of the tetrahedral symmetry. Carbon can move around at room temperature. It can be captured by carbon substitutional (C_s) to form the carbon interstitial-carbon substitutional (C_iC_s) complex, or by interstitial oxygen (O_i) to form the oxygen interstitial-carbon interstitial (C_iO_i) complex [5].

2.2 Silicon dangling bonds

At the surface of a crystalline silicon wafer, the periodic arrangement of the silicon atoms is interrupted. Consequently, the surface atoms cannot be fully saturated due to the fact that some of their valence electrons are left unbonded (half-filled orbitals), forming the so-called surface dangling bonds (DBs).

2.2.1 Trap density

The number of the unbonded electrons per surface atom varies depending on the surface orientation, e.g. the $\langle 100 \rangle$ surface has two half-filled sp^3 orbitals per atom, while the $\langle 111 \rangle$ surface has only one. These surface dangling bonds are chemically active and eager to lower their energy by forming chemical bonds. As there is no other atoms available, the adjacent unsaturated atoms tend to pair with each other. However, due to the distance between each dangling bond, the crystal lattice has to be strained in order to bring pairs of surface atoms closer together to

form new chemical bonds, known as Si-Si dimer bonds (see **Figure 2.2**). Despite the formation of these dimer bonds, each silicon atom on the $\langle 100 \rangle$ oriented surface has at least one dangling bond remaining active.

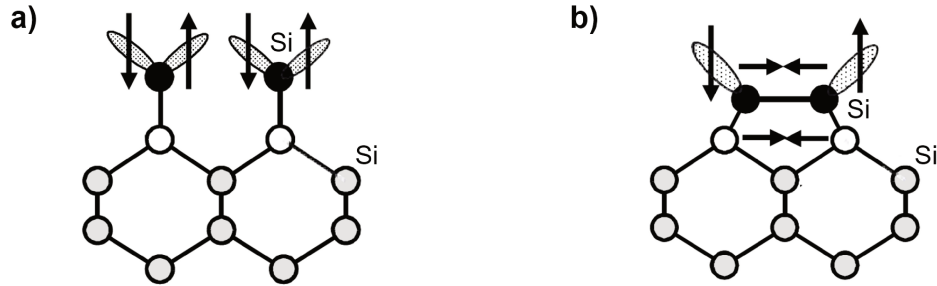


Figure 2.2 – Schematic models of a) dangling bond on Si(100) surface, b) symmetric Si-Si dimer bond [6].

The presence of dangling bonds introduce localized states with associated energy levels in the silicon bandgap. On a bare crystalline silicon surface, the density of trap levels (D_{it}) is approximately $10^{14} \text{cm}^{-2} \text{eV}^{-1}$. This trap density is reduced to approximately $10^{12} \text{cm}^{-2} \text{eV}^{-1}$ on the naturally oxidized surface [7].

2.2.2 Charge states

Introducing a mid-gap energy level, dangling bonds have the possibility of being in one of the three occupation states: completely unoccupied, singly occupied (with either spin state) and doubly occupied (with one electron of each spin state). When the dangling bond is completely unoccupied, no electron can compensate the nucleus charge, so the silicon atom behaves as a point-like positive charge, denoted by (DB^+) . The singly occupied dangling bond has neutral charge (DB^0) , while doubly occupied dangling bond has negative charge (DB^-) [8]. Also, it is important to mention that the energy level introduced by a dangling bond is not fixed. Firstly, it can be shifted up or down by an electrostatic potential. Secondly, this energy level varies depending on its own occupation state: the energy level of an unoccupied dangling bond is lower than the energy level introduced by a singly occupied dangling bond. Sometimes, these trap levels are viewed as the energy required for the transition of the charge states of the dangling bonds, from positive to neutral $(+/0)$ and from neutral to negative $(0/-)$. So when the Fermi level is below both transition levels, it is highly probable that the dangling bond is positively charged (unoccupied). In case the Fermi level is between both the two levels, the possibility of $+/0$ transition increases and thus the dangling bond is neutral. The dangling bond can be negatively charged when the Fermi level is above both transition level.

Introducing energy levels in the bandgap of a material, bulk defects and dangling bonds act as active traps, capturing the free charge carriers. In high quality crystalline silicon wafers (e.g. float zone c-Si), the bulk defects are considerably reduced thanks to the development of crystal growth technology [9]. However, the surface dangling bonds remain high, leading to a very strong SRH recombination of charge carriers (see section 1.3). This strong carrier recombination at the surface affects the open-circuit voltage (V_{oc}), the short-circuit current (I_{sc}), and the fill factor (FF) of the solar cells, limiting its conversion efficiency.

2.3 Passivation mechanism

As mentioned previously, due to the continuous improvement of the crystalline silicon bulk material and the tendency to reduce wafer thickness, the recombination of charge carriers caused by surface dangling bonds has become the critical factor limiting the conversion efficiency of solar cells. To overcome this problem, a thin semiconductor or dielectric layer is commonly introduced on the wafer surface so as to neutralize the dangling bonds. This technique is known as the surface passivation, and it is able to effectively reduce the carrier recombination at the surface via two main mechanisms: the chemical passivation and the field-effect passivation.

2.3.1 Chemical passivation

It is worth mentioning that recombination of charge carriers at the surface is directly proportional to the density of the dangling bonds. So the first approach to tackle the surface recombination issue is to reduce the density of dangling bonds, commonly known as chemical passivation [10].

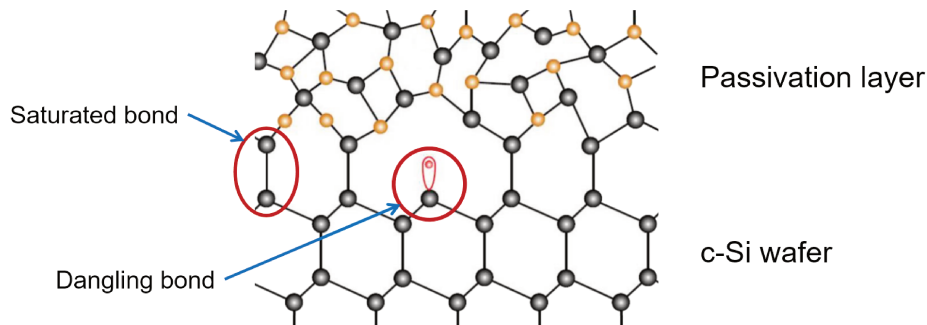


Figure 2.3 – Schematic model represents the chemical passivation mechanism.

This can be obtained by depositing an appropriate passivation layer (see section 2.4) on top of the crystalline silicon surface or by immersing the sample into polar liquids [11]. By doing so, the unsaturated silicon atoms at the wafer surface are able to form chemical bonds with various atoms of the deposited materials (particularly hydrogen), and therefore the dangling bonds are saturated chemically and electrically (see **Figure 2.3**).

2.3.2 Field-effect passivation

In addition to chemical passivation, the surface recombination can be further reduced by altering the carrier concentration, which is generally known as the charge-induced passivation or the field-effect passivation [10]. Knowing that the carrier recombination through SRH process involves one electron and one hole, the highest surface recombination will occur when the concentrations of both charge carriers (electrons and holes) are approximately equal. That is to say if the concentration of one charge carrier is reduced, the surface recombination will be drastically reduced as well. As electron and hole carry an electrical charge, such a reduction of the concentration of one carrier type (either electrons or holes) can be realized by the formation of electrostatic charges in the passivation layer (see **Figure 2.4**), mainly near the interface between the silicon wafer and the passivation layer.

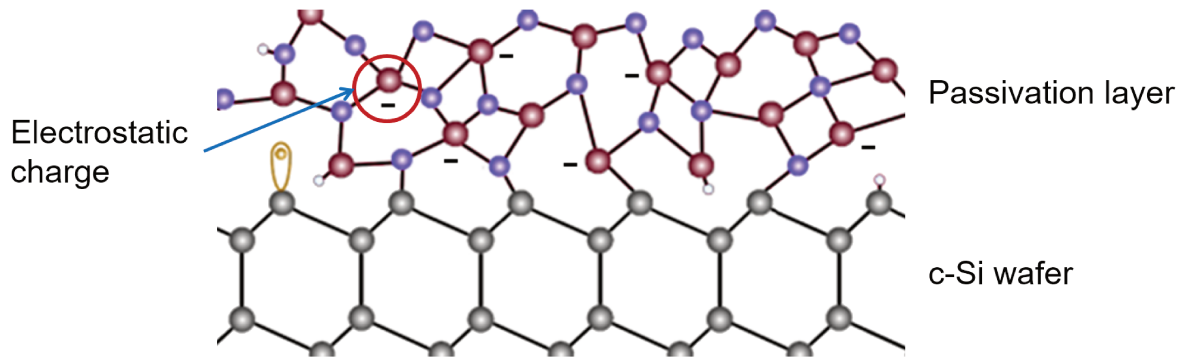


Figure 2.4 – Schematic model represents the field-effect passivation mechanism.

These fixed charges attract the carriers of opposite polarity to the surface and repel the carriers of the same polarity away. Therefore, depending on the polarity of the fixed charges in the passivation layer, the electronic band structure at silicon surface can be modified from an accumulation mode (attract majority carriers) to an inversion mode (repel majority carriers). One should notice that accumulation mode is more favorable than the inversion mode, which is the reason why the passivation layers with negative fixed charges are commonly used on the p-type crystalline silicon surface, while those with positive fixed charges are used on the n-type surface.

In practical crystalline silicon solar cells, the above-mentioned passivation approaches are often combined to achieve minimum surface recombination.

2.4 Passivating materials

Different materials can be used to provide surface passivation for crystalline silicon solar cells. It can be either a semiconductor (e.g. intrinsic and doped hydrogenated amorphous silicon, etc.), a dielectric material (e.g. silicon dioxide, hydrogenated amorphous silicon nitride, etc.), or metal oxide (e.g. aluminum oxide, zinc oxide, etc.). Silicon dioxide (SiO_2) grown by thermal oxidation at high temperature (1000°C) is one of the standard materials firstly used for passivation purposes in crystalline silicon technology. Thanks to the formation of strong chemical bonds between silicon and oxygen at the interface, SiO_2 provides excellent chemical passivation for crystalline silicon solar cell ($D_{it} = 10^9 \text{cm}^{-2} \text{eV}^{-1}$) [12]. However, the excellent passivation properties provided by SiO_2 cannot be maintained when samples are exposed to UV photons. Another issue arises from high temperature process, which can lead to a degradation of bulk materials, mainly p-type crystalline silicon. For these reasons, significant effort has been devoted to the development of low temperature ($<400^\circ\text{C}$) surface passivation schemes as an alternative to the high temperature SiO_2 . Today, hydrogenated amorphous silicon (a-Si:H), and aluminum oxide (Al_2O_3) are the two commonly used passivation materials for crystalline silicon solar cells.

2.4.1 Hydrogenated amorphous silicon

In the photovoltaic community, hydrogenated amorphous silicon (a-Si:H) was first fabricated and used as an absorbing material for thin film solar cell. Then, due to the presence of hydro-

gen atoms in a-Si:H structure, the film was incorporated into crystalline silicon solar cell as a surface passivation layer [13–16]. The chemical passivation properties provided by a-Si:H, particularly intrinsic a-Si:H, allow to reduce the defect state density (D_{it}) to values as low as $10^{10} \text{cm}^{-2} \text{eV}^{-1}$. In general, another doped (n-type or p-type) a-Si:H layer is added on top of the intrinsic layer in order to provide the field-effect passivation. According to the doping profile, the Fermi level can be shifted toward the conduction band or the valence band, which further causes the band bending in the electronic structure of solar cells. Thanks to this band bending, an internal electric field is induced and the carriers photo-generated in c-Si can be selectively collected to their corresponding terminals. In addition to its excellent passivation properties, a-Si:H films also have quite good conductivity properties. Therefore, the electrical contacts can be deposited (or printed) directly on top of the passivation layer without the need of laser scribing or other surface opening processes.

Different processes can be used to deposit the a-Si:H film, but the low temperature plasma-enhanced chemical vapor deposition (PECVD) is the most common one. The pure silane (SiH_4) or the mixture of silane (SiH_4) and hydrogen (H_2) are commonly used as the precursor gases for deposition of intrinsic a-Si:H. Phosphine (PH_3) or diborane (B_2H_6) gases can also be added to the mixture in order to obtain n-type or p-type a-Si:H respectively.

Despite of its many advantages, using a-Si:H as a passivation layer for crystalline silicon also has some drawbacks. Firstly, the parasitic absorption is one of the main issues to deal with when using a-Si:H to passivate the front surface. Having a quite small energy gap ($E_{a\text{-Si:H}} \approx 1.7 \text{ eV}$ [17]) with the direct band properties, the a-Si:H layer will absorb partly the photons ($E_{ph} \geq E_{a\text{-Si:H}}$) from sunlight and thus reduce the number of photons absorbed by the crystalline silicon wafer beneath. For this reason, the thickness of the front a-Si:H layer has to be carefully designed to minimize the absorption losses while maintaining excellent surface passivation. Secondly, the passivation provided by a-Si:H is vulnerable to intense light/UV light soaking. When the sample is exposed to light with high intensity, the weak chemical bonds in the a-Si:H layer, particularly at the c-Si/a-Si:H interface, are believed to break down and thus induce new silicon dangling bonds. This phenomena is known as the Staebler-Wronski effect [18, 19]. Last but not least, due to the stability problem of a-Si:H layer, the fabrication processes of solar cells with a-Si:H layer have to be specifically designed at temperature below 250°C .

2.4.2 Aluminum oxide

Aluminum oxide (Al_2O_3), also known as alumina, is an interesting passivation material for crystalline silicon solar cells due to the fact that it provides both chemical and field-effect passivation [20, 21]. Thanks to the formation of thin silicon oxide (SiO_x) layer at the c-Si/ Al_2O_3 interface during annealing, the surface defect density can be significantly reduced [22]. Furthermore, the Al_2O_3 film also contains high density of negative fixed charges ($> 10^{12} \text{cm}^{-2}$) and thus provides excellent field-effect passivation [23]. For these reasons, the thickness of the Al_2O_3 passivation layer can be reduced to a few nanometers [24–26]. The electric field induced by negative fixed charges in Al_2O_3 prevents electrons from approaching the surface, which is the reason why Al_2O_3 is commonly used as a passivation layer for p-type surface. In addition to its excellent passivation properties, Al_2O_3 has also large energy gap ($E_{g,\text{Al}_2\text{O}_3} \approx 7.5 \text{ eV}$) [27, 28]. Therefore, the film can be incorporated as a passivation layer on the front surface without worrying about parasitic absorption. Furthermore, the Al_2O_3 film is also known for its stability under light soaking at high temperature ($\approx 75^\circ\text{C}$). These correspond well to the

properties of crystalline silicon solar cell that should remain stable for at least three decades.

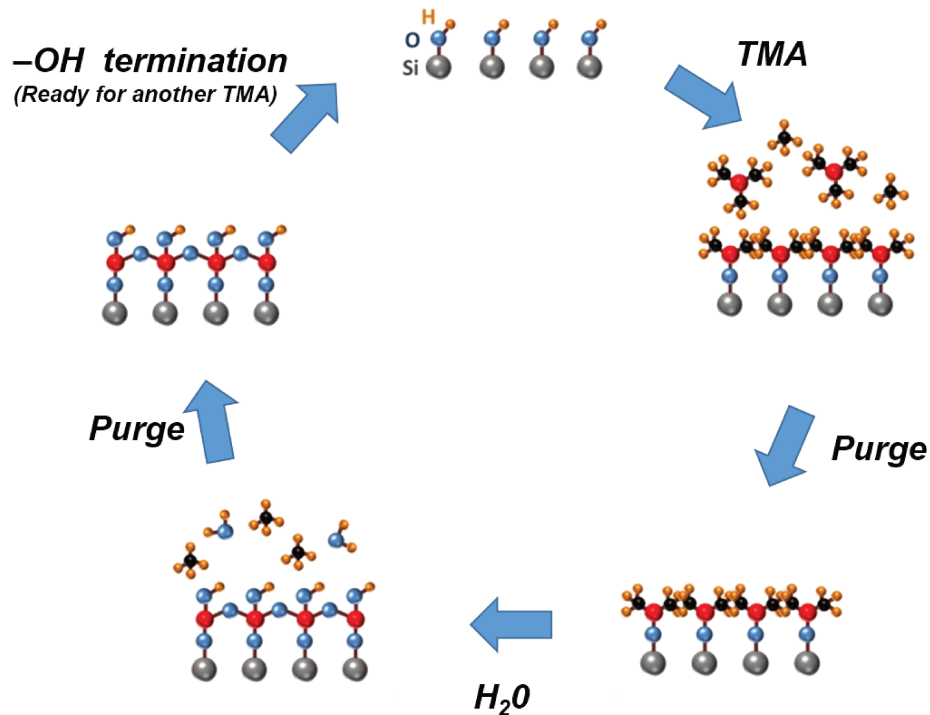
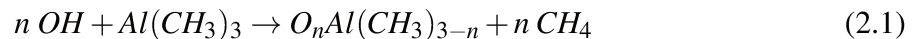
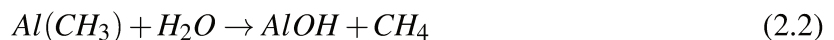


Figure 2.5 – Schematic represents the atomic layer deposition(ALD) process.

Different deposition methods can be used to grow Al₂O₃ layers, such as plasma-enhanced chemical vapor deposition (PECVD) [29], atomic layer deposition (ALD) [21], etc. Due to a very accurate thickness control coupled with the ability to provide an excellent conformal films even on a textured surface, the ALD process has attracted lots of attention in the photovoltaic community. This grow process is based on a self-limiting reaction, in which the precursors and inert gases are sequentially pulsed into the reactor. The purge of inert gases (Ar or N₂) is performed between each pulse so as to remove the by product and the remaining precursor from the reactor. Generally, trimethylaluminum (TMA) is used as an aluminum precursor, while water vapor (H₂O) or ozone (O₃) is used for oxidation. Assuming that the initial surface of the c-Si substrate is fully covered by the hydroxyl group (-OH) after the wet chemical cleaning process. As TMA is pulsed into the reactor, the ligand exchange reaction between TMA molecules and the -OH terminated surface will occur as shown in Equation 2.1:



When all the reactive sites (-OH) are saturated, the reaction will genuinely terminate. Then the purge of inert gases will start. After purging, water vapor is introduced to the chamber. Another ligand-exchange reaction will occur between Al(CH₃)_x terminated surface and water (Equation 2.2).



At the end of this reaction, the -OH terminated surface reappears. The presence of these -OH terminated sites indicates that the surface is ready for the next ALD cycle after the purging. This cycle (see **Figure 2.5**) is continuously repeated until the desired thickness of the Al₂O₃ layer is obtained. It is important to note that the layer thickness can be precisely defined by the number of ALD cycles.

Using Al_2O_3 as the passivation layer for c-Si solar cell provides many interesting advantages. However, the film has a high dielectric constant (approximately 9) that can lead to high series resistance, particularly on the front grid contacts. Thus, a laser scribing process is commonly required to ensure a proper electrical contact with low series resistance. Lastly, another challenge of using Al_2O_3 passivation layer is the deposition time. As the conventional ALD process requires pulsing and purging the chamber, it may take several seconds to complete one cycles.

Bibliography

- [1] Jeffery L. Gray. The physics of the solar cell. In Antonio Luque and Steven Hegedus, editors, *Handbook of photovoltaic science and engineering*, chapter 3, pages 82–129. Jonh Wiley & Sons, Indiana, USA, 2011.
- [2] J. W. Morris Jr. Defects in crystals. In *Materials science and engineering: An introduction*, pages 76 – 107. Wiley, 2013.
- [3] M. L. Ciurea, V. Iancu, S. Lazanu, A.-M. Lepadatu, E. Rusnac, and I. Stavarache. Defects in silicon: from bulk crystals to nanostructures. *Romanian Reports in Physics*, 60(3):735–748, March 2008.
- [4] F. M. Li and A. Nathan. *CCD image sensors in deep-ultraviolet: degradation behavior and damage mechanisms*. Springer-Verlag Berlin Heidelberg, the Netherlands, 2005.
- [5] R. C. Newman. Defects in silicon. *Reports on Progress in Physics*, 45(10):1163–1210, oct 1982.
- [6] S. Morita, N. Oyabu, T. Nishimoto, R. Nishi, O. Custance, I. Yi, and Y. Sugawara. Functions of NC-AFM on atomic scale. In *Scanning Probe Microscopy: Characterization, Nanofabrication and Device Application of Functional Materials*, pages 173 – 195. Springer Netherlands, 2005.
- [7] H. Shimizu, K. Kinameri, N. Honma, and C. Munakata. Determination of surface charge and interface trap densities in naturally oxidized n-type si wafers using ae surface photovoltages. *Japanese Journal of Applied Physics*, 26(Part 1, No. 2):226–230, feb 1987.
- [8] M. Taucer. *Silicon dangling bonds: non-equilibrium dynamics and applications*. PhD thesis, University of Alberta, 2015.
- [9] J. Vedde, T. Clausen, J. Borregaard, and P. Kringhoj. Float-zone crystal growth for pv - where is the future? In *Proc. 23rd European Photovoltaic Solar Energy Conference and Exhibition*, Valencia, Spain, 2008.
- [10] M. Z. Rahman and S. I. Khan. Advances in surface passivation of c-si solar cells. *Materials for Renewable and Sustainable Energy*, 1(1):1, Oct 2012.
- [11] Nicholas E. Grant and John D. Murphy. Temporary surface passivation for characterisation of bulk defects in silicon: A review. *physica status solidi (RRL) Rapid Research Letters*, 11(11):1700243, 2017.
- [12] Armin G Aberle. Surface passivation of crystalline silicon solar cells: a review. *Progress in Photovoltaics: Research and Applications*, 8(5):473–487, 2000.
- [13] Makoto Tanaka, Mikio Taguchi, Takao Matsuyama, Toru Sawada, Shinya Tsuda, Shoichi Nakano, Hiroshi Hanafusa, and Yukinori Kuwano. Development of new a-si/c-si heterojunction solar cells: ACJ-HIT (artificially constructed junction-heterojunction with intrinsic thin-layer). *Japanese Journal of Applied Physics*, 31(Part 1, No. 11):3518–3522, 1992.
- [14] M. Taguchi, A. Yano, S. Tohoda, K. Matsuyama, Y. Nakamura, T. Nishiwaki, K. Fujita, and E. Maruyama. 24.7 *IEEE Journal of Photovoltaics*, 4(1):96–99, Jan 2014.
- [15] K. Masuko, M. Shigematsu, T. Hashiguchi, D. Fujishima, M. Kai, N. Yoshimura, T. Yamaguchi, Y. Ichihashi, T. Mishima, N. Matsubara, T. Yamanishi, T. Takahama, M. Taguchi, E. Maruyama, and S. Okamoto. Achievement of more than 25% conversion efficiency with crystalline silicon heterojunction solar cell. *IEEE Journal of Photovoltaics*, 4(6):1433–1435, Nov 2014.
- [16] K. Yoshikawa, H. Kawasaki, W. Yoshida, T. Irie, K. Konishi, K. Nakano, T. Uto, D. Adachi,

- M. Kanematsu, H. Uzu, and K. Yamamoto. Silicon heterojunction solar cell with interdigitated back contacts for a photoconversion efficiency over 26%. *Nature Energy*, 2(17032), March 2017.
- [17] A. Fontcuberta i Morral, P. Roca i Cabarrocas, and C. Clerc. Structure and hydrogen content of polymorphous silicon thin films studied by spectroscopic ellipsometry and nuclear measurements. *Phys. Rev. B*, 69:125307, Mar 2004.
- [18] D. L. Staebler and C. R. Wronski. Reversible conductivity changes in dischargeproduced amorphous si. *Applied Physics Letters*, 31(4):292–294, 1977.
- [19] T. Shimizu. Staebler-wronski effect in hydrogenated amorphous silicon and related alloy films. *Japanese Journal of Applied Physics*, 43(6A):3257–3268, jun 2004.
- [20] J. Schmidt, A. Merkle, R. Brendel, B. Hoex, M. C. M. van de Sanden, and W. M. M. Kessels. Surface passivation of high-efficiency silicon solar cells by atomic-layer-deposited al₂o₃. *Progress in Photovoltaics: Research and Applications*, 16(6):461–466, 2008.
- [21] G. Dingemans and W. M. M. Kessels. Status and prospects of al₂o₃-based surface passivation schemes for silicon solar cells. *Journal of Vacuum Science & Technology A*, 30(4):040802, 2012.
- [22] Volker Naumann, Martin Otto, Ralf B. Wehrspohn, and Christian Hagendorf. Chemical and structural study of electrically passivating al₂o₃/si interfaces prepared by atomic layer deposition. *Journal of Vacuum Science & Technology A*, 30(4):04D106, 2012.
- [23] Florian Werner, Boris Veith, Dimitri Zielke, Lisa Kühnemund, Christoph Tegenkamp, Michael Seibt, Rolf Brendel, and Jan Schmidt. Electronic and chemical properties of the c-si/al₂o₃ interface. *Journal of Applied Physics*, 109(11):113701, 2011.
- [24] D. Schuldis, A. Richter, J. Benick, P. Saint-Cast, M. Hermle, and S. W. Glunz. Properties of the c-si/al₂o₃ interface of ultrathin atomic layer deposited al₂o₃ layers capped by sinx for c-si surface passivation. *Applied Physics Letters*, 105(23):231601, 2014.
- [25] Armin Richter, Jan Benick, Martin Hermle, and Stefan W. Glunz. Excellent silicon surface passivation with 5 Å thin ald al₂o₃ layers: Influence of different thermal post-deposition treatments. *physica status solidi (RRL) Rapid Research Letters*, 5(56):202–204, 2011.
- [26] G. Dingemans, R. Seguin, P. Engelhart, M. C. M. van de Sanden, and W. M. M. Kessels. Silicon surface passivation by ultrathin al₂o₃ films synthesized by thermal and plasma atomic layer deposition. *physica status solidi (RRL) Rapid Research Letters*, 4(12):10–12, 2010.
- [27] Elena O. Filatova and Aleksei S. Konashuk. Interpretation of the changing the band gap of al₂o₃ depending on its crystalline form: Connection with different local symmetries. *The Journal of Physical Chemistry C*, 119(35):20755–20761, 2015.
- [28] Perevalov, T. V., Gritsenko, V. A., and Kaichev, V. V. Electronic structure of aluminum oxide: ab initio simulations of ses and comparison with experiment for amorphous films. *European Physical Journal Applied Physics*, 52(3):30501, 2010.
- [29] Shinsuke Miyajima, Junpei Irikawa, Akira Yamada, and Makoto Konagai. High quality aluminum oxide passivation layer for crystalline silicon solar cells deposited by parallel-plate plasma-enhanced chemical vapor deposition. *Applied Physics Express*, 3(1):012301, dec 2009.

Chapter 3

PHOTOLUMINESCENCE

Contents

| | |
|---|-----------|
| 3.1 Emission of light | 42 |
| 3.1.1 Thermal radiation | 42 |
| 3.1.2 Non-thermal radiation | 43 |
| 3.2 Photoluminescence | 44 |
| 3.2.1 Excitation energy | 45 |
| 3.2.2 Excitation intensity | 46 |
| 3.3 Steady-state photoluminescence | 46 |
| 3.3.1 Spectral analysis | 46 |
| 3.3.2 PL intensity | 47 |
| 3.4 Modulated photoluminescence | 48 |
| 3.4.1 Carrier lifetime measurement | 48 |
| 3.4.2 Differential vs Steady-state lifetime | 49 |

3.1 Emission of light

Light refers to electromagnetic radiation of any wavelength, either it is visible or not. Based on its wavelength, the electromagnetic radiation can be categorized as radio, microwave, infrared, visible, ultraviolet, X-rays and gamma rays. The radio has longest wavelength (low frequency), while gamma rays have short wavelength (high frequency). It is worth mentioning that, through the work of Albert Einstein, Louis de Broglie, and many others, light has both wave and particle nature (commonly known as wave-particle duality). As a wave, light is characterized by velocity (speed of light), wavelength, and frequency. As particle, light is considered as a stream of photons with an energy (E_{photon}) related to the frequency of the wave given by Planck's relation:

$$E_{\text{photon}} = \frac{hc}{\lambda} \quad (3.1)$$

Where h is the Planck constant ($6.626 \times 10^{-34} \text{ m}^2 \cdot \text{kg} \cdot \text{s}^{-1}$), c is the speed of light in vacuum ($2.997 \times 10^8 \text{ m} \cdot \text{s}^{-1}$), and λ is the photon's wavelength.

From this relation, it is obvious that light with short wavelength has higher photon energy than that with long wavelength. Basically, the sources of light can be divided into two main categories: thermal radiation (incandescence) and non-thermal radiation (luminescence).

3.1.1 Thermal radiation

Thermal radiation (incandescence) is the continuous emission of photons from every physical body at thermal equilibrium above absolute zero. The thermal radiation involves the vibration of entire atoms inside the body, leading to emission of electromagnetic radiation. Depending on the temperature of materials, the emitted photons vary in their energies and colors. At low temperature, the materials commonly emit invisible light in the infrared region. However, as the temperature increases above a few hundreds degree Celsius, the emitted light can be visible, changing its color from red to yellowish and finally bluish-white (see **Figure 3.1**). With the increase of temperature, the peak of the emission spectrum also starts shifting to shorter wavelengths (high photon energy), commonly known as blueshift. This phenomenon can be observed, for example when the metal is heated. Both intensity and spectrum of thermal radiation are strongly dependent on the emitter's temperature and are governed by the Planck's law (Max Planck, 1901).

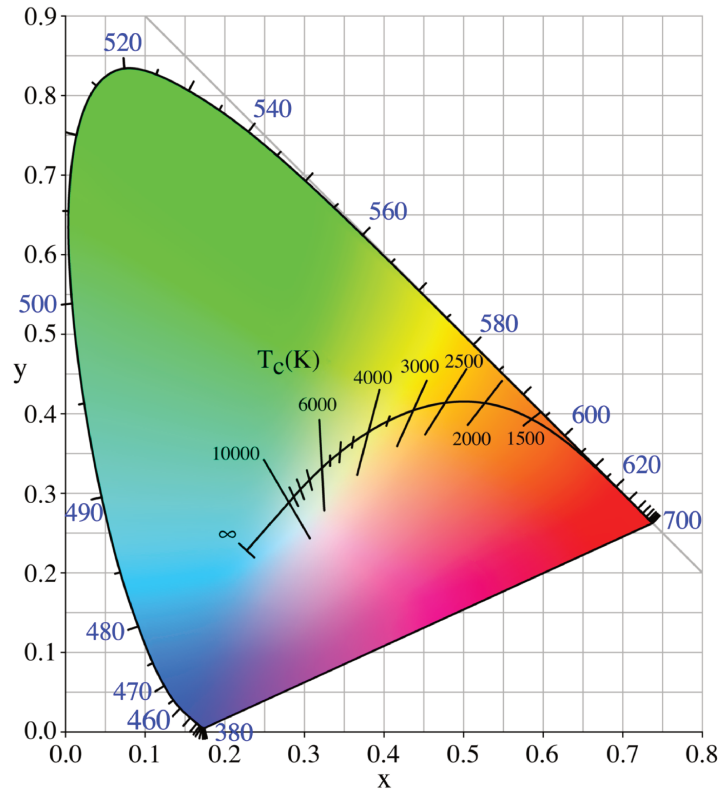
A black body is an ideal body, which emits the maximum possible thermal radiation. The spectral emission intensity $I_{bb}(\hbar\omega)$ of a black body is given by [1]:

$$I_{bb}(\hbar\omega) = \frac{(\hbar\omega)^3}{4\pi^2\hbar^3c^2} \left[\exp\left(\frac{\hbar\omega}{k_B T}\right) - 1 \right]^{-1} \quad (3.2)$$

where $\hbar = h/2\pi$ is the reduced Planck constant, ω is the angular frequency, c is the speed of light in the vacuum, k_B is the Boltzmann constant, and T is the temperature of the material.

As an ideal body, the thermal radiation of the black body has been used as the standard for the comparison with the radiation of real physical bodies. Coupled with the Kirchhoff's law, which claimed that the emissivity and absorptivity of materials are equal under thermodynamic equilibrium, the expression of energy distribution of the black body can be extended to the

Figure 3.1 – Planckian locus in the CIE 1931 color space. The diagram shows the color locus (path) of incandescence black body radiation as a function of the black body temperature. Note, X and Y are the two chromaticity coordinates.



emission of non-black body (commonly known as gray body). The spectral emission intensity $I(\hbar\omega) < 1$ of a gray body with an absorptivity $\alpha(\hbar\omega)$ is given by [2]:

$$I(\hbar\omega) = \alpha(\hbar\omega) I_{bb}(\hbar\omega) \quad (3.3)$$

This concept is so important that it is actively used in the study of not only the intrinsic thermal radiation, but also radiation caused by different physical nature.

3.1.2 Non-thermal radiation

Non-thermal radiation (luminescence) is generally recognized by its high emission intensity, which is far too large to be thermally radiated at the actual temperature of the emitting body. In contrast to thermal radiation that involves the vibration of entire atoms, luminescence concerns only the transition of electrons between energy levels. Luminescence light is produced when electrons release some of their energy during the jump from a high energy state to a lower one. Generally speaking to maintain continuous amounts of luminescence, the electrons require a continuous push to be lifted up to high energy states so that the cycle continues. This push can be provided by a range of sources, such as chemical reaction, electrical current, photon absorption, etc. For luminescence radiation, the actual temperature of the emitting body seems to be of little important.

Luminescence radiation was first treated thermodynamically like the black body radiation. But instead of using the real emitting-body temperature, an effective temperature was used. This effective temperature is the temperature of black body radiation having the same emission intensity in a given photon energy range, and it does not exist in any parts of the system emitting luminescence radiation. Later, the difference between thermal and non-thermal radiation

was accounted for by the chemical potential of the emitting materials. In contrast to effective temperature, this quantity is experimentally accessible. It is worth mentioning that thermal radiation can be emitted by any material, and its spectrum may contain photons with any energy $\hbar\omega > 0$. In contrast, the spectrum of luminescence radiation is characterized by some threshold photon energy ($\hbar\omega_0$), with photons of smaller energy ($\hbar\omega < \hbar\omega_0$) missing. This threshold photon energy ($\hbar\omega_0$) is a consequence of a gap (ΔE_g) in the distribution of states as a function of energy, a characteristic of luminescent materials.

A semiconductor is a typical luminescent material, for which ΔE_g is the gap between the valence band (E_v) and conduction band (E_c). The intensity of the luminescence radiation of a semiconductor at a given temperature is strongly related to the concentration of electrons in the conduction band and of holes in the valence band. In addition, the generalized Planck law can be used to predict the spectrum of the luminescence radiation of the direct-bandgap semiconductors. Different from the simple Planck's law for thermal radiation, the generalized Planck law takes into account the non-zero chemical potential ($\mu_\gamma = \varepsilon_{F,c} - \varepsilon_{F,v}$) of the semiconductor, the only parameter that distinguishes luminescence from thermal radiation. The luminescence spectral emission intensity $I_L(\hbar\omega)$ of a semiconductor material with a chemical potential (μ_γ) and absorption coefficient $\alpha(\hbar\omega)$ is given by [1]:

$$I_L(\hbar\omega) = \alpha(\hbar\omega) \frac{(\hbar\omega)^3}{4\pi^2\hbar^3c^2} \left[\exp\left(\frac{\hbar\omega - \mu_\gamma}{k_B T}\right) - 1 \right]^{-1} \quad (3.4)$$

For indirect-bandgap semiconductors (e.g. crystalline silicon, etc.), the absorption and emission of phonons is required during the direct transition of electrons between energy levels. For this reason, one may doubt the validity of the generalized Planck's law for such materials. By using the principle of detailed balance coupled with experimental data, it has been proved that the generalized Planck's law is valid for indirect bandgap semiconductors, both for the homogeneous body and for the inhomogeneous body (e.g. p-n junction, etc.) in silicon solar cells. Reader may refer to the work of Schick et al (1992) for more details [3].

Depending on the energy sources providing the push of electrons to high energy states (electron excitation), the luminescence radiation can be further categorized into various sub-groups, such as chemiluminescence, electroluminescence, photoluminescence, etc. The chemiluminescence is a radiation resulting from a chemical reaction. Electroluminescence, on the other hand, can be obtained when the semiconductor materials is excited by an electrical current. Photoluminescence is a radiative emission, from any forms of matter, resulting from the absorption of photons. As photons do not interact with each other, their properties are therefore entirely determined by the state of the emitting materials or their interaction with matter. Consequently, many characterization tools have been developed based on luminescence radiation, particularly photoluminescence, for the investigation of material properties.

3.2 Photoluminescence

When light of sufficient energy ($E_{photon} \geq E_g$) is incident on a semiconductor, photons are absorbed and electrons are excited from the valence band to the conduction band. These excited electrons act as free particles and eventually relax back to the ground state. If radiative relaxation (direct jump of excited electrons from conduction band back to valence band) occurs, photons will be emitted along the process. This radiation is called photoluminescence (PL).

The intensity of the emitted PL signal often depends on the density of the photo-generated carriers governed by the excitation intensity as well as the emitting material properties, and its spectrum is defined by the energy gap (E_g) of the materials (see **Figure 3.2**). Furthermore, the whole spectrum of the PL signal can be determined using the generalized Planck's law (Equation 3.4).

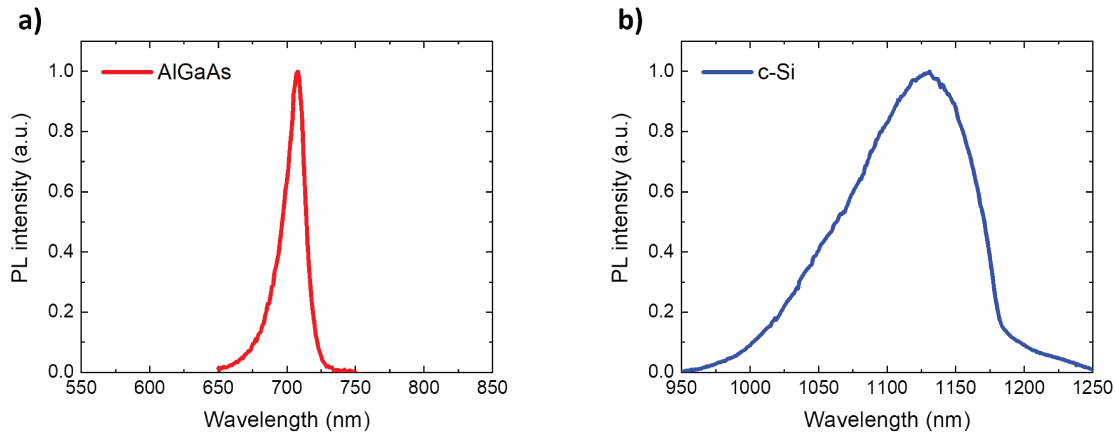


Figure 3.2 – PL spectra emitted from a) AlGaAs ($E_{g,AlGaAs} = 1.75 \text{ eV}$) and b) c-Si ($E_{g,c-Si} = 1.12 \text{ eV}$)

During the last few decades, photoluminescence has gained increasing interest as a characterization technique for semiconductor materials. The choice of the excitation energy and intensity is critical in any PL measurements, as these two parameters have profound effects on the emitted PL signal.

3.2.1 Excitation energy

For most semiconductors, the absorption of incident light depends strongly on the photon energy. As a result, different excitation energies will have different penetration depth and thus allow us to probe different regions of the sample. It is worth mentioning that a penetration depth (the inverse of the absorption coefficient) is a measure of how deep light can penetrate into a material. It is defined as the depth at which the intensity of radiation falls below 37% of its original value at just beneath the surface. In direct-bandgap semiconductors, the above-bandgap excitation has a penetration depth of the order of $1\mu\text{m}$. The diffusion of photo-generated carriers can vary widely but is typically in the range $1 - 10\mu\text{m}$. Hence, the PL with above-bandgap excitation is very sensitive to the surface properties. In contrast, in indirect-bandgap semiconductors, the absorption is weaker and the light can penetrate deeper into the sample. Therefore, the PL is dominated by the bulk properties in this case. For this reason, in more demanding experiments, the laser light which is the source of photo-excitation is carefully chosen to probe a particular depth in the sample. If multiple excitation wavelengths are available, these properties of PL can be used to distinguish surface and bulk contribution.

3.2.2 Excitation intensity

Unlike the excitation energy, which may or may not be important, the excitation intensity will influence the result of any PL experiments. The excitation intensity controls the density of the photo-generated electrons and holes, which governs the behavior of these carriers. One of the main properties that is strongly influenced by the carrier density is the electron-hole recombination mechanism. When the carrier density is low, the recombination is dominated by discrete defects and impurity sites at the surface/interface and the bulk of the material. Therefore, the percentage of the radiative recombination is low compared to the SRH recombination. Under intermediate excitation, the discrete states are filled and radiative recombination plays a greater role. In this regime, the increase of the excitation intensity will linearly increase the intensity of the PL signal. At the highest carrier densities, the three-body Auger recombination dominates the overall carrier recombination process. Consequently, the intensity of the incident beam is commonly adjusted to control the photo-generated carriers, so the electronic properties of the sample can be investigated under different recombination regimes.

In addition to excitation energy and intensity, the excitation profile also plays a very important role in material characterization. By employing different excitation profiles, for example, steady-state or pulse or modulation, various specific properties of materials can be measured. In the following sections, two of the main photoluminescence operation modes, steady-state photoluminescence and modulated photoluminescence, will be presented.

3.3 Steady-state photoluminescence

In steady-state photoluminescence (SSPL), the excitation intensity is maintained at a constant level during the measurements. Generally, in this operation mode, the spectrum and intensity of the emitted PL signal are detected and analyzed to yield the optical and electronic properties of the materials.

3.3.1 Spectral analysis

Peak position

For crystalline materials, the translational symmetry of the crystal lattice leads to the formation of electronic energy bands. However, the presence of defects breaks the periodicity of the lattice and locally perturbs this band structure by introducing discrete energy levels within the forbidden gap. These defect-induced states act as very active traps, capturing the charge carriers in the crystal, particularly when the temperature is sufficiently low. Some of the trapped carriers, mainly those in the shallow traps near the conduction band and valence band edge, are likely to participate in the radiative recombination (see **Figure 3.3**) and thus introduce additional peaks in the PL spectrum. Therefore, by analyzing the peak position of the PL spectrum, the energy levels of defects in the crystal can be determined. It is important to note that the sample temperature must be small enough to discourage the thermal activation of carrier release out of the traps.

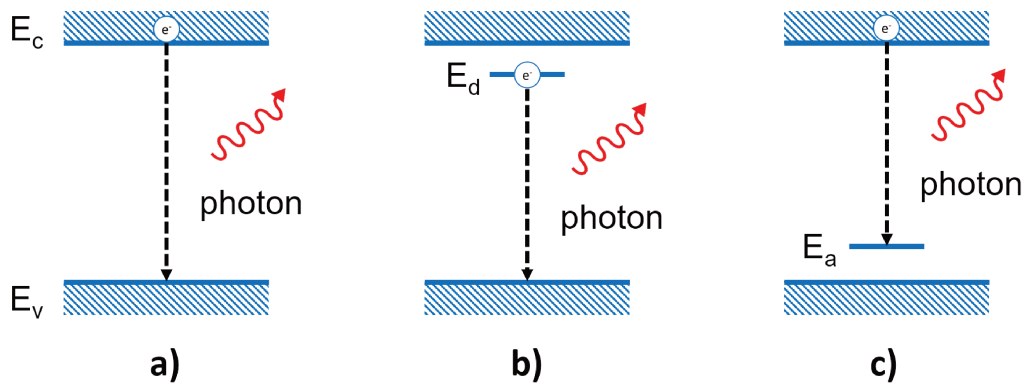


Figure 3.3 – Radiative recombination paths: a) band-to-band; b) donor state to valence band; c) conduction band to acceptor state.

In addition to identifying discrete states, the PL peak positions can be used to evaluate the atomic interdiffusion and interface alloying. In various electronic devices as well as photovoltaic cells, the heterojunction of two semiconductors can be found. For many reasons, e.g. atomic interdiffusion, these heterojunction structures are not abrupt, and unintentional alloy layers can be formed at the interface. These interface alloys can form narrow wells or barriers that have a non-negligible impact on the behavior of carriers. Therefore, a better understanding and control of such layers is important. Depending on the composition, the bandgap of a semiconductor alloy can be larger, smaller, or intermediate between the adjoining materials. So by evaluating the position of the PL peak, the bandgap of the alloy layer can be determined, and so does its composition.

Spectral fitting

Besides the analysis of the peak positions, fitting the PL spectrum will provide a wealth of quantitative information about the emitters. In general, the expression for non-thermal radiation, described by generalized Planck's law, is used for this fitting process. As an example, Katahara et al have developed a model based on sub-gap absorptivity to fit the whole PL spectrum and thus yield the band energy, local lattice temperature, functional form of the sub-bandgap absorption, and the energy broadening parameter (Urbach energy, magnitude of potential fluctuation, etc.) [4]. Furthermore, Nguyen et al have also determined the temperature dependence of the band-to-band absorption coefficient of crystalline silicon by fitting the PL spectra detected at various temperature [5]. Last but not least, the linear fitting at the high energy tail of the PL spectrum provides roughly the emitter temperature as the slope and the quasi-Fermi level splitting as the interception [6, 7].

3.3.2 PL intensity

Of all features, the intensity of emitted PL signal is the most practical parameter for the qualitative analysis of interface properties. Because the density of defects at the interface is high, the carrier recombination in this area is usually non-radiative, suppressing the emission intensity of PL signal. For this reason, although several important mechanisms affect the PL response, the variation of PL intensity generally correlates with the modification of the interface: an increase

of the PL signal indicates a decrease of non-radiative recombination, in other words a decrease of interface defect density. The measurements of PL intensity have been used to evaluate a wide variety of surface treatments, including etching, oxidation, hydrogenation, deposition of coating layers, and hetero-epitaxy.

Furthermore, the measurements of PL intensity have gained increasing interest for monitoring the interface modification (physically or chemically) in real time during the processes. This can be done, because, in addition to its high sensitivity to interface properties, the PL measurement is generally not sensitive to the experimental conditions, e.g. pressure in the sample chamber. Moreover, the technique can be used to investigate contactlessly any surface, as it relies on neither electrical excitation nor detection. Last but not least, the PL measurements are nondestructive or have very little impacts on materials under investigation. It is important to bear in mind that the photo-induced modification and sample heating are possible, but lowering the excitation intensity can minimize these effects.

3.4 Modulated photoluminescence

Modulated Photoluminescence (MPL) is a phase-sensitive characterization technique. Different from steady-state photoluminescence, the MPL technique uses a sinusoidally modulated-intensity light source to excite the sample.

3.4.1 Carrier lifetime measurement

Because the sample is being illuminated by a light source with a modulated intensity, the photogeneration rate of charge carriers in the semiconductor is given by [8, 9]:

$$G = G_0 + G_1 e^{i\omega t} \quad (3.5)$$

where G_0 represents the constant part of photogeneration rate, G_1 is the amplitude of the modulated part, and ω is the modulation frequency of the excitation intensity.

This modulation of the photogeneration rate further leads to a variation of the carrier concentration as a function of time (see **Figure 3.4**), and ultimately a modulation of the emitted photoluminescence. The equation for the variation of the carrier concentration is given by:

$$\Delta n = \Delta n_0 + \Delta n_1 e^{i\omega t} \quad (3.6)$$

Where the Δn_0 and Δn_1 are the amplitude of the constant and the modulated parts of charge carrier concentration. It is worth mentioning that the equation for the modulated photoluminescence take the same form, as the photoluminescence emission rate is strongly related to the carrier concentration in the material, given by the definition of radiative recombination.

From the definition, the variation of charge carrier concentration in a semiconductor allows the determination of the minority carrier lifetime. A general equation for determining the lifetime of charge carriers is given by:

$$\tau = \frac{\Delta n(t)}{G(t) - \frac{d(\Delta n(t))}{dt}} \quad (3.7)$$

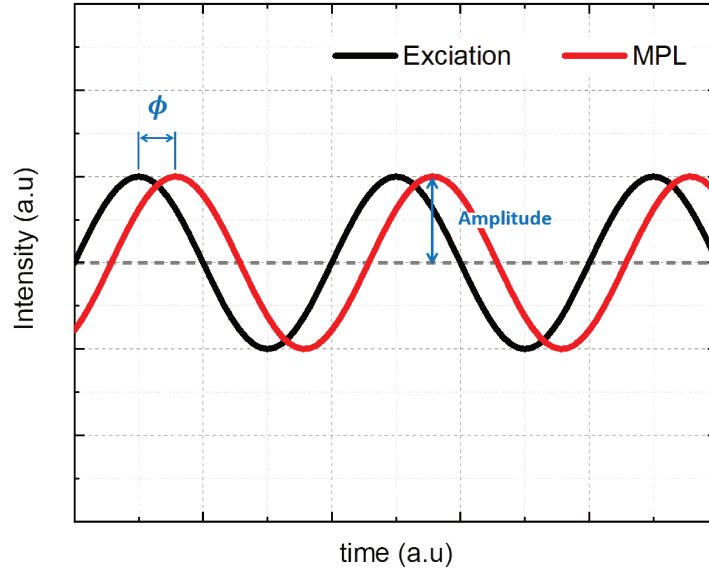


Figure 3.4 – Schematic represents the modulation of excitation intensity and emitted photoluminescence as a function of time during the MPL measurement.

By solving this differential equation, then substituting equation 3.5 and 3.6 into the solution, the relationship between the constant and modulation parts of carrier concentration and generation rate be obtained, and it is given by:

$$\Delta n_0 + \Delta n_1 e^{i\omega t} = \tau G_0 + \frac{\tau G_1}{1 + i\omega\tau} e^{i\omega t} \quad (3.8)$$

So, the modulation amplitude of the carrier concentration as well as the emitted photoluminescence is a complex number with a magnitude of $|\Delta n_1|$ and phase shift (ϕ) compared to the carrier generation rate.

$$|\Delta n_1| = \frac{\tau G_1}{\sqrt{1 + \omega^2 \tau^2}} \quad (3.9)$$

$$\phi = -\arctan(\omega\tau) \quad (3.10)$$

Based on these equations, by measuring the modulation amplitude or the phase shift between the emitted photoluminescence and the carrier generation rate, the lifetime of charge carriers in the semiconductors can be determined.

3.4.2 Differential vs Steady-state lifetime

In the electronics as well as photovoltaics community, the lifetime of charge carriers has been used extensively to represent the quality of semiconductor materials. The interpretation of carrier lifetime is straightforward: the larger the carrier lifetime is the better the quality of materials (both bulk and interface). Various characterization techniques have been developed to measure this minority carrier lifetime. These techniques include quasi-steady-state photoconductance decay, differential photoconductance decay, modulated photoluminescence, etc. Among these, the dynamic measurement techniques feature distinct advantages over steady-state techniques,

due to the fact that they measure carrier lifetime directly from the decay of excess carrier density rather than to implicitly infer lifetime from measured steady-state amplitudes.

However, several artifacts of the dynamic techniques have been addressed in the past. In the 1990s, Brendel, Aberle, and Schmidt identified a difference between the steady-state (actual) injection-dependent lifetime τ_{ss} and the so-called differential injection-dependent lifetime τ_{dif} obtained from light-biased differential photoconductance decay measurement [10–12]. This mismatch between the differential and actual lifetime is, according to Giesecke et al [13], due to the fact that differential lifetime relates a change of generation rate to a change of excess carrier concentration. Generally, in (quasi) steady-state lifetime measurements, the investigated sample has a constant carrier concentration (Δn_0) under a constant carrier generation rate (G_0). The minority carrier lifetime is simply given by:

$$\tau_{ss} = \frac{\Delta n_0}{G_0} \quad (3.11)$$

In a dynamic measurement technique, however, the decay of carrier density $\Delta n(t \rightarrow \infty)$ due to light bias has to be taken into account. Supposing that the measurement is conducted in a very short time frame ($\Delta t \rightarrow 0$). The carrier generation rates at time t and $t + \Delta t$ are G_0 and εG_0 respectively, with a light bias parameter $0 < \varepsilon < 1$. Similarly, the carrier concentrations at t and $t + \Delta t$ are Δn_0 and $\Delta n(t \rightarrow \infty)$. The carrier lifetime is given by:

$$\tau_{dif} = \frac{\Delta n_0 - \Delta n(t \rightarrow \infty)}{(1 - \varepsilon)G_0} \quad (3.12)$$

This form reveals the differential nature of τ_{dif} , which is a change of excess carrier density per change of generation rate. As carrier lifetime varies depending on injection level $d\tau/d\Delta n \neq 0$, the relative change of excess carrier density cannot equal the relative change of generation rate, leading to the difference between differential and actual lifetime.

Due to the nature of differential measurements, it was concluded that integration of measurements throughout the entire injection range was essential in order to obtain actual lifetime from different lifetimes [10]. However, such measurements are time-consuming and additionally complicated by the limitation at $G \rightarrow 0$ due to the sensitivity limit of the instruments. In 2013, Giesecke et al has revealed a relationship between the differential and actual carrier lifetime [13], given by:

$$\tau_{ss,i}(G_i) = \tau_{dif,i}(G_i) \left(1 - G_i \frac{d\tau}{d\Delta n} \right) \quad (3.13)$$

By applying this equation, the actual carrier lifetime can be correctly determined from a combination of at least two measurements of $\tau_{dif}(G)$ to be conducted at adjacent generation rates.

Bibliography

- [1] P. Würfel. The chemical potential of radiation. *Journal of Physics C: Solid State Physics*, 15(18):3967–3985, jun 1982.
- [2] T. Trupke, E. Daub, and P. Würfel. Absorptivity of silicon solar cells obtained from luminescence. *Solar Energy Materials and Solar Cells*, 53(1):103 – 114, 1998.
- [3] K. Schick, E. Daub, S. Finkbeiner, and P. Würfel. Verification of a generalized planck law for luminescence radiation from silicon solar cells. *Applied Physics A*, 54(2):109–114, Feb 1992.
- [4] John K. Katahara and Hugh W. Hillhouse. Quasi-fermi level splitting and sub-bandgap absorptivity from semiconductor photoluminescence. *Journal of Applied Physics*, 116(17):173504, 2014.
- [5] Hieu T. Nguyen, Fiacre E. Rougieux, Bernhard Mitchell, and Daniel Macdonald. Temperature dependence of the band-band absorption coefficient in crystalline silicon from photoluminescence. *Journal of Applied Physics*, 115(4):043710, 2014.
- [6] Y. Rosenwaks, M. C. Hanna, D. H. Levi, D. M. Szmyd, R. K. Ahrenkiel, and A. J. Nozik. Hot-carrier cooling in gaas: Quantum wells versus bulk. *Phys. Rev. B*, 48:14675–14678, Nov 1993.
- [7] G. Lasher and F. Stern. Spontaneous and stimulated recombination radiation in semiconductors. *Phys. Rev.*, 133:A553–A563, Jan 1964.
- [8] R. Brüggemann and S. Reynolds. Modulated photoluminescence studies for lifetime determination in amorphous-silicon passivated crystalline-silicon wafers. *Journal of Non-Crystalline Solids*, 352(9):1888 – 1891, 2006. Amorphous and Nanocrystalline Semiconductors - Science and Technology.
- [9] R. Chouffot, A. Brezard-Oudot, J.-P. Kleider, R. Brüggemann, M. Labrune, P. Roca i Cabarrocas, and P.-J. Ribeyron. Modulated photoluminescence as an effective lifetime measurement method: Application to a-si:h/c-si heterojunction solar cells. *Materials Science and Engineering: B*, 159-160:186 – 189, 2009. EMRS 2008 Spring Conference Symposium K: Advanced Silicon Materials Research for Electronic and Photovoltaic Applications.
- [10] Brendel R. Note on the interpretation of injection-level-dependent surface recombination velocities. *Applied Physics A*, 60:523–524, 1995.
- [11] Armin G. Aberle, Jan Schmidt, and Rolf Brendel. On the data analysis of lightbiased photoconductance decay measurements. *Journal of Applied Physics*, 79(3):1491–1496, 1996.
- [12] J. Schmidt. Measurement of differential and actual recombination parameters on crystalline silicon wafers [solar cells]. *IEEE Transactions on Electron Devices*, 46(10):2018–2025, Oct 1999.
- [13] J. A. Giesecke, S. W. Glunz, and W. Warta. Understanding and resolving the discrepancy between differential and actual minority carrier lifetime. *Journal of Applied Physics*, 113(7):073706, 2013.

Chapter 4

IN-SITU SSPL: A UNIQUE CHARACTERIZATION TOOL

Contents

| | | |
|------------|---|-----------|
| 4.1 | Introduction to in-situ SSPL | 54 |
| 4.1.1 | Tool configuration | 54 |
| 4.1.2 | Operation mode | 56 |
| 4.2 | In-situ study of plasma effects on surface passivation | 57 |
| 4.2.1 | Experiments | 58 |
| 4.2.2 | Results | 59 |
| 4.2.3 | Root cause of plasma effects | 61 |
| 4.2.4 | Mechanisms behind the plasma-induced modifications of surface passivation | 65 |
| 4.2.5 | Effect of passivation layer thickness | 68 |
| 4.2.6 | Effect of RF power & pressure | 69 |
| 4.2.7 | Effect of substrate temperature | 70 |
| 4.2.8 | Recovery of surface passivation | 73 |
| | Summary | 75 |

4.1 Introduction to in-situ SSPL

In-situ SSPL is a unique characterization tool, which was developed based on steady-state photoluminescence technique. The tool is partly integrated into a PECVD reactor (called PLASMAT), allowing us to characterize the properties of samples inside the reactor in real time during the processes (e.g. deposition of passivation/capping layer, thermal treatment, plasma exposure, etc.). During the in-situ measurement, a laser source with a constant laser intensity is employed to excite the sample. Under illumination, charge carriers are generated in the material and eventually recombine through different recombination processes (radiative or non-radiative). In the radiative recombination process, the charge carriers directly recombine, resulting in an emission of photons (PL signal). By detecting and analyzing the emitted PL signal, various properties of materials can be determined (please refer to section 3.3 for further information).

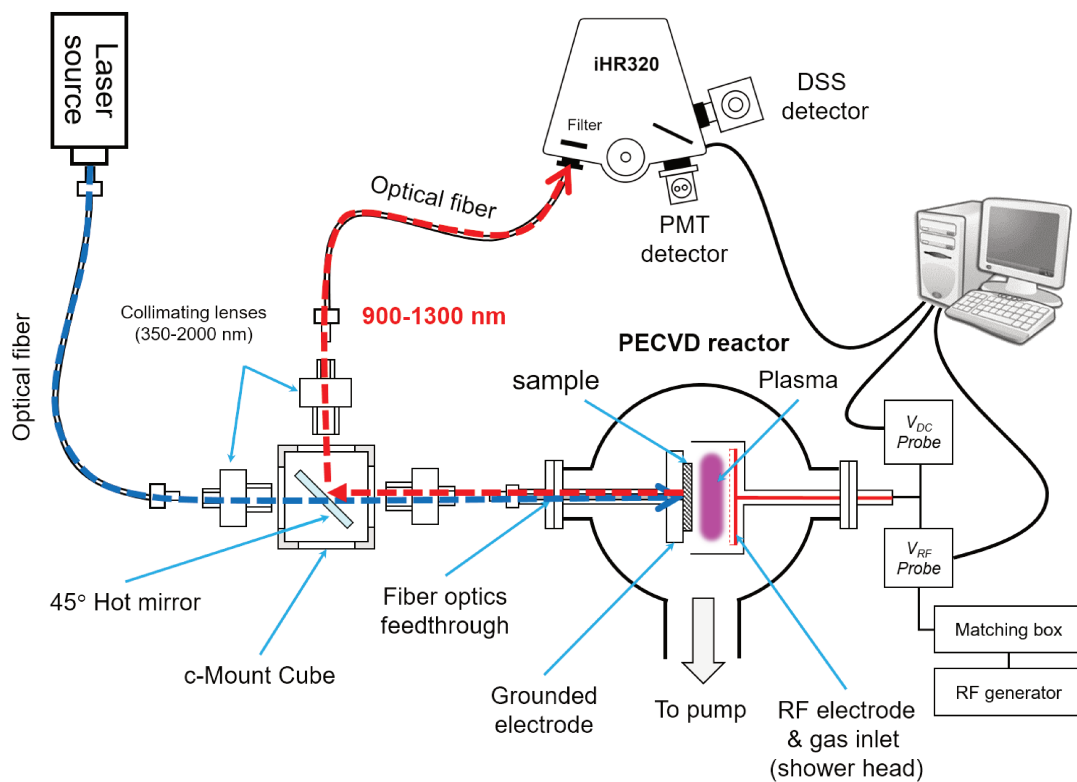


Figure 4.1 – Detail configuration of the in-situ SSPL characterization tool.

4.1.1 Tool configuration

In-situ SSPL consists of three main parts, the excitation system, the optical system, and the detection system, which are interconnected by multi-mode optical fibers with a core diameter of $600\ \mu\text{m}$ (see **Figure 4.1**).

In the excitation system, a fiber-pigtailed laser diode ($785\ \text{nm}$, $100\ \text{mW}$ adjustable) is used as the light source, and it is powered by a programmable current/temperature controller from Thorlabs to ensure optimal operating conditions and precise control of laser optical output.

Leaving the laser diode, the laser light is coupled into an optical fiber and transferred to the optical system.

The optical system of in-situ SSPL is an optical cube, comprised of a dichroic mirror (also known as hot mirror) in the middle of the cube and three collimators on the cube walls (see **Figure 4.2.a**). The dichroic mirror is positioned at a 45° angle with regard to the direction of the laser beam, and its optical properties are shown in **Figure 4.2.b**. The laser light that is transferred from the excitation system enters the cube through collimator (1). As the center wavelength of the laser is in the near-infrared region, the laser light will pass through the mirror to collimator (2), connected with an optical fiber that goes into the PLASMAT reactor until just beneath the sample. As the sample is excited by laser light, the charge carriers are generated

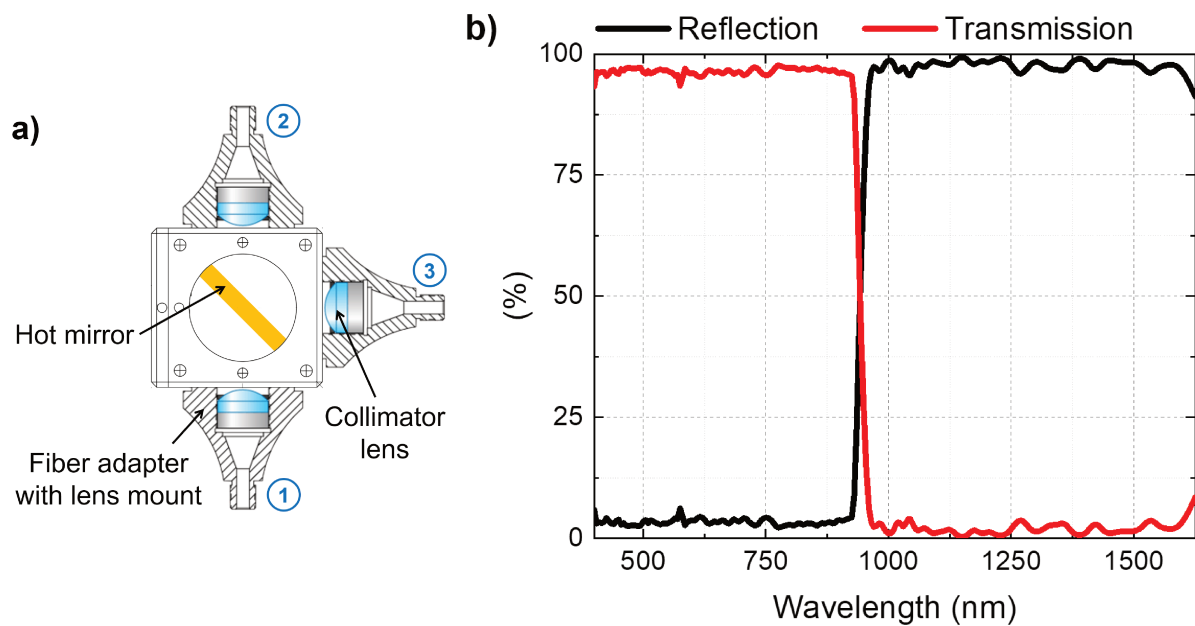


Figure 4.2 – a) Schematic of the optical cube (top view, not to scale); b) the transmission and reflection properties of the dichroic mirror with a cut-off wavelength at 950 nm .

and the photons are simultaneously emitted. These emitted photons are then collected by the same optical fiber and sent back the cube. It is important to mention that the wavelength of the emitted photons depends strongly on the energy gap of the emitting materials. For crystalline silicon, the wavelength of the emitted photon is about 1130 nm , which is in the infrared range. Therefore, these photons are reflected by the dichroic mirror to collimator (3) that is connected to the detection system.

The main component of the detection system of in-situ SSPL is the iHR320 photo-detecting apparatus from HORIBA. It consists of three blazed holographic plane gratings that are dedicated to different wavelength range ($190\text{--}800\text{ nm}$; $400\text{--}1000\text{ nm}$; $600\text{--}1700\text{ nm}$) and two detectors with different sensitivity ranges (photomultiplier tube: $200\text{--}850\text{ nm}$; liquid-nitrogen-cooled DSS: $800\text{--}1550\text{ nm}$) [1]. This apparatus is controlled by SynerJY DATA ACQUISITION, a scientific spectrometer utilities program, which allows a precise control of detection range, position of the blazed grating, and the slit size (both entrance and exit to detector).

4.1.2 Operation mode

Thanks to the versatility of the iHR320 photo-detecting system, the in-situ SSPL can be operated in two different modes: spectra-time and intensity-time.

In the first operation mode, the system is configured to detect the variation of full PL spectra as a function of time (spectra-time). In this case, the blazed grating is set to operate in a range of wavelengths to cover the whole PL spectrum. During the measurement, the grating rotates and thus reflects the photons at each corresponding wavelength to the detector. Once the measurement of a full spectrum is done, the blaze grating return to its initial position, and the cycle repeats. By detecting the whole PL spectra, we are able to access various properties of the emitting materials. However, depending on the integration time chosen, it may require several tens seconds to detect a full PL spectrum. **Figure 4.3** shows a series of full PL spectra emitted from an AlGaAs solar cell during the thermal treatment at 80°C in the hydrogen environment.

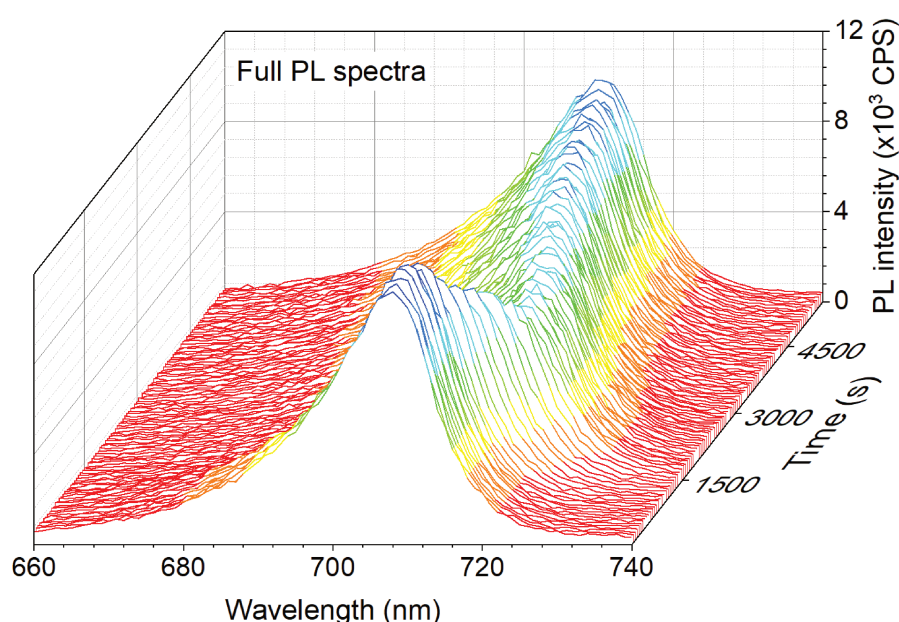


Figure 4.3 – A series of full PL spectra detected by in-situ SSPL in the 1st operation modes. These full PL spectra were measured during a thermal treatment of an AlGaAs solar cell at 80°C in the hydrogen environment.

In the second operation mode, the system is set to measure the PL intensity at one wavelength as a function of time (intensity-time). Here, the blazed grating is fixed at one wavelength, and the intensity of the PL signal at that wavelength is continuously measured. **Figure 4.4** shows the evolution of the PL intensity (@ 1130 nm) emitted from a single-side passivated c-Si wafer during the deposition of an a-Si:H passivation layer at 200°C (passivation layer on the second surface). In this operation mode, the time scale between each measurement can be set to as low as 0.1 second.

It should be mentioned that all the experimental results, presented in the following sections, were measured by in-situ SSPL in the second operation mode.

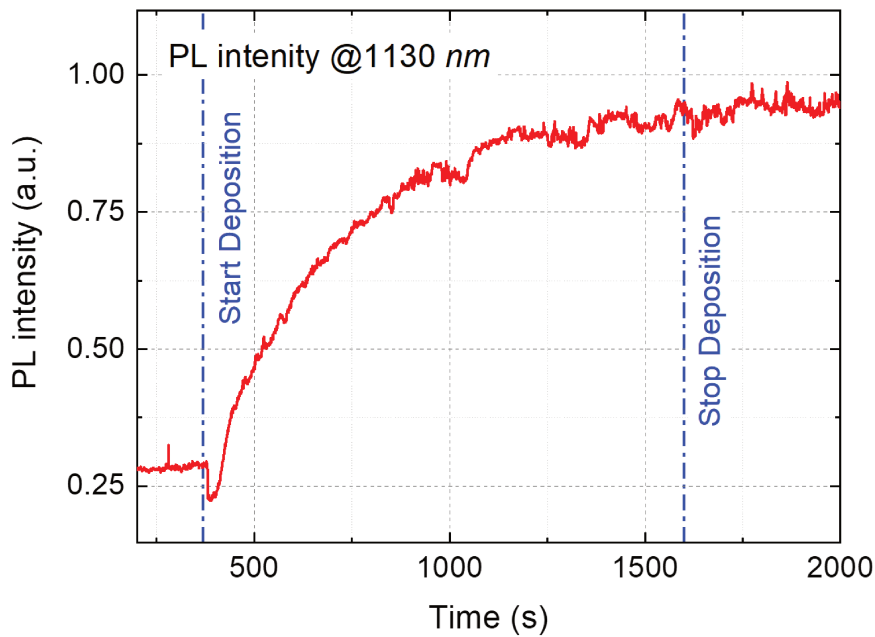


Figure 4.4 – PL intensity detected by in-situ SSPL in the 2nd operation modes. The evolution of the PL intensity (@ 1130 nm) detected during the deposition of an a-Si:H passivation layer on a single-side passivated c-Si wafer.

4.2 In-situ study of plasma effects on surface passivation

Surface properties are extremely crucial for crystalline silicon solar cells, as they are directly linked to the cell conversion efficiency. Naturally, a huge amount of dangling bonds present on surface of c-Si wafer. These dangling bonds act as active traps, capturing the photo-generated carriers and thus inducing the carrier recombination loss. On top of that, the planar c-Si surface also reflects back at least 30% of the incident photons, leading to what is known as the optical reflection loss [2–4].

To tackle these problems, various thin-film semiconductor and dielectric materials are incorporated into the structure of solar cells. For instance, a thin layer of aluminum oxide (Al_2O_3) grown by atomic layer deposition (ALD) [5–12] or hydrogenated amorphous silicon (a-Si:H) grown by plasma-enhanced chemical vapor deposition (PECVD) [13–18] is added directly onto the wafer surface to neutralize the surface dangling bonds and therefore reduce the carrier recombination at the surface. Furthermore, an additional capping layer of hydrogenated amorphous silicon nitride (a-SiN_x:H) or transparent conductive oxide (TCO) is employed to enhance the anti-reflective properties [2, 19–22] and/or to provide a better lateral transport of the generated carriers [23, 24]. Plasma processes such as PECVD and sputtering are commonly used to grow these capping layers, and a degradation of the surface passivation is more often than not observed after these deposition processes [25, 26].

In this section, in-situ SSPL is employed to study in detail the root causes as well as the mechanisms behind the plasma-induced degradation of surface passivation of crystalline silicon wafer coated by Al_2O_3 and a-Si:H. Moreover, the relationship between the dynamics of the passivation degradation and the plasma parameters (e.g. chamber pressure, applied radio frequency power, and substrate temperature) is also discussed.

4.2.1 Experiments

High quality double-side polished 4 inches n-type $\langle 100 \rangle$ FZ c-Si wafers with a resistivity of approximately $3 \Omega \cdot \text{cm}$ and a thickness of about $280 \mu\text{m}$ were used as substrates in the experiments. Prior to deposition of the passivation layers (Al_2O_3 or a-Si:H), all wafers were subjected to a short (≈ 30 seconds) wet chemical cleaning in a 5% hydrofluoric acid (HF) solution in order to remove the native oxide layer. Then the wafers were transferred quickly to different reactors for deposition of the passivation layers with a thickness of about 9 nm on both sides of the substrate to form a symmetrical passivation structure. For one group of samples, a thermal ALD reactor (model R200) from Picosun was used to grow the Al_2O_3 layers. The growth process was performed at 150°C , during which the gas precursors were alternatively introduced to the chamber. Here, trimethylaluminium ($\text{Al}(\text{CH}_3)_3$) was used as the metal precursor, while water vapor was used as the oxidant. For another group of the sample, the a-Si:H layers were grown by the PECVD process in an OCTOPUS reactor from INDEOTEC. This deposition process was conducted at 200°C , and a mixture of silane and hydrogen gases was used as the gas precursor.

After deposition of the passivation layer, the samples were transferred to the PLASMAT reactor, where they were exposed to a 13.56 MHz RF capacitively coupled Ar/ H_2 plasma. It is important to mention that in order to decouple the influences of plasma from the photoluminescence quenching effect and any other interferences induced by the diffusion of atomic hydrogen originating in the passivation layers (Al_2O_3 or a-Si:H), the first set of experiments was performed at room temperature (RT). The baseline plasma conditions are summarized in the table 4.1.

Table 4.1 – Baseline plasma conditions during the plasma exposure experiments.

| Parameters | Value |
|---|------------|
| Pressure | 0.3 Torr |
| RF power | 15 W |
| Ar/ H_2 flow rates | 10/10 sccm |
| Substrate temperature | RT |
| Inter-electrode distance | 25 mm |
| RF voltage (V_{RF}) | 221 V |
| Self-bias voltage (V_{bias}) | - 41 V |
| Plasma potential $V_p = \frac{1}{2}(V_{RF} + V_{bias})$ | 90 V |

During these plasma exposure experiments, the samples are placed on the grounded electrode of the PLASMAT reactor, as indicated in **Figure 4.5**. Its front surface is exposed to the Ar/ H_2 plasma, while the photo-excitation ($\lambda_{laser} = 785 \text{ nm}$ @ 20 mW) and collection of the PL signal ($\lambda_{PL, Si} = 1130 \text{ nm}$) are simultaneously conducted at the rear surface. An ex-situ characterization tool (Sinton WCT-120) is also used to check the minority carrier lifetime of samples before and after the plasma exposure.

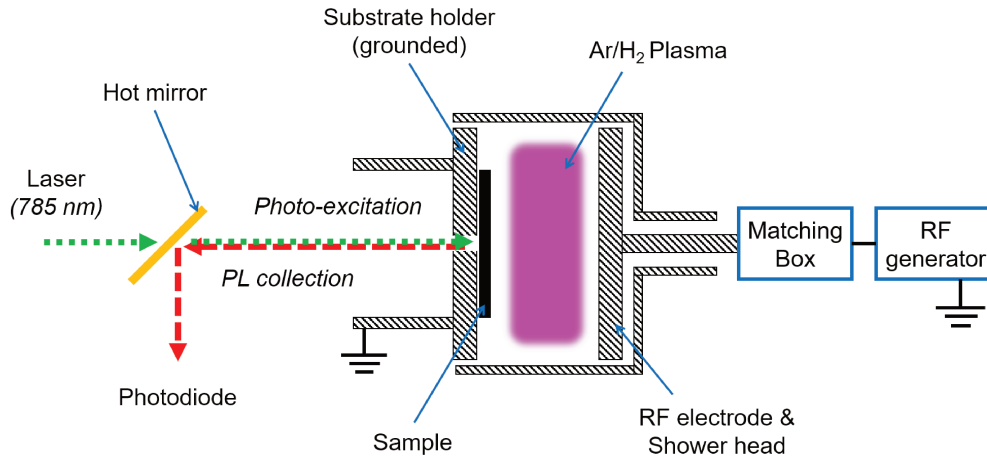


Figure 4.5 – Schematic of the simplified configuration of in-situ SSPL in the PLASMAT reactor during the plasma exposure experiments.

4.2.2 Results

Figures 4.6 shows the evolution of the PL signals, emitted from samples during the exposure. It can be observed that the PL signal of the Al₂O₃-passivated sample abruptly increases just after the plasma ignition. Then it slowly decreases as a function of the plasma exposure time until reaching a steady-state value (see **Figure 4.6**). On the other hand, the PL signal emitted from the a-Si:H-passivated sample exhibits a completely different features (see **Figure 4.6**). The signal plummets as soon as the plasma is ignited, and it remains at that level throughout the experiment.

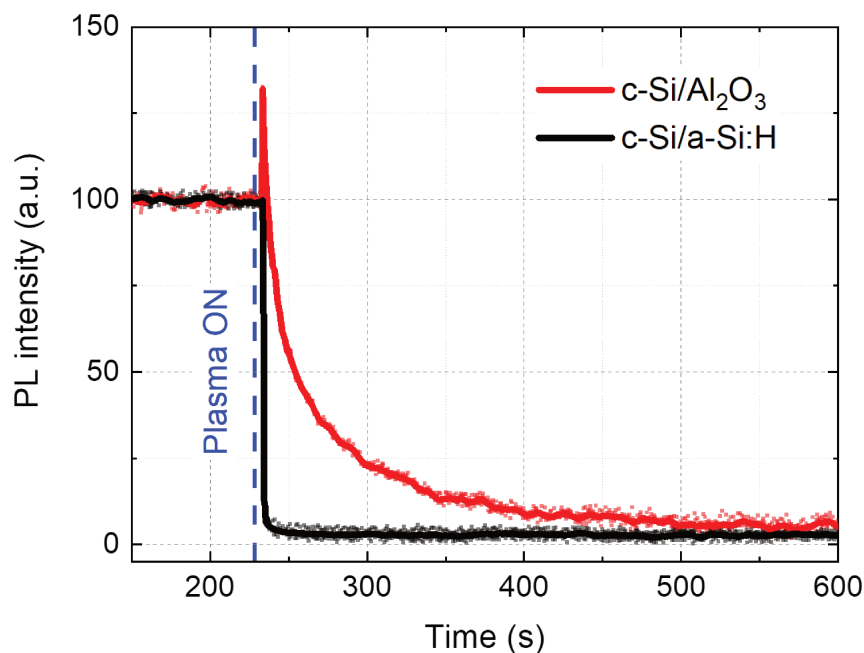


Figure 4.6 – Evolution of the PL signals (normalized) emitted from samples passivated by 9 nm of Al₂O₃ and a-Si:H observed during the Ar/H₂ plasma exposure at room temperature.

In both cases, one can see that the PL signals diminish after being exposed to plasma. This indicates the generation of defects in the samples, particularly at the interface between the c-Si wafer and the passivation layer, in other words the degradation of surface passivation that leads to non-radiative recombination of photo-generated carriers. Regarding the dynamics of the plasma-induced degradation, it is clear that, despite having the same thickness of the passivation layer (9 nm), the a-Si:H-passivated samples degrade faster than the Al₂O₃-passivated samples. It means that the surface passivation provided by a-Si:H is more vulnerable to plasma processes than the passivation provided by Al₂O₃.

It is also important to mention that the abrupt increase of the PL signal, observed during the plasma exposure of the Al₂O₃-passivated sample, is not an artifact, but a very quick activation of the surface passivation properties of the Al₂O₃ layer. The mechanisms behind this rapid activation of surface passivation properties will be discussed later in this section. To check the stability of this feature, a short (approximately 1 s) plasma exposure was conducted on the Al₂O₃-passivated samples. The objective of this experiment is to rapidly activate the passivation properties of this as-deposited Al₂O₃ layer, but to avoid the degradation induced by plasma.

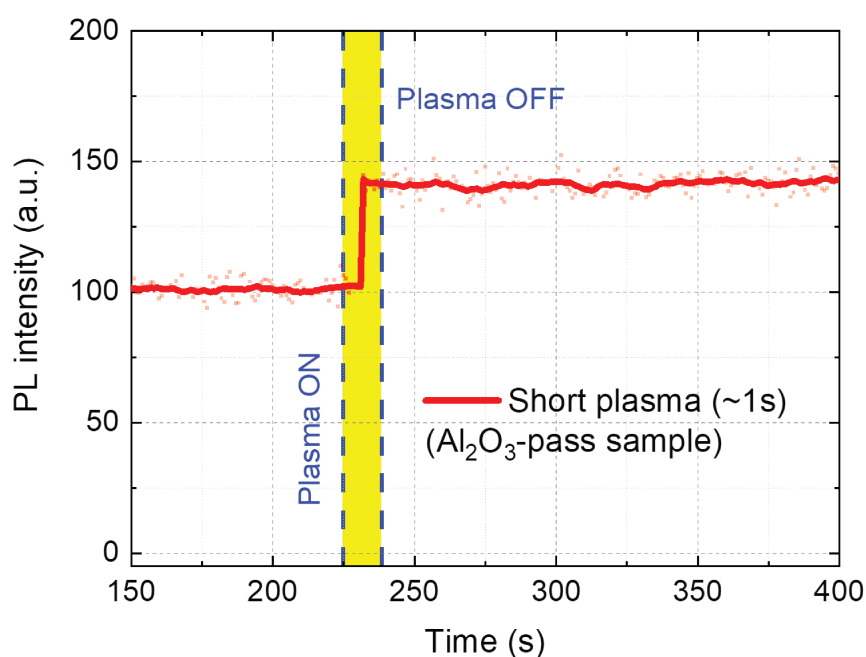


Figure 4.7 – Evolution of the PL signals (normalized) emitted from samples passivated by Al₂O₃ observed during a short (\approx 1s) Ar/H₂ plasma exposure at room temperature.

The obtained PL signal is shown in **Figure 4.7**. One can see that the PL intensity instantly steps up when the plasma was turned on (similar to the feature observed in **Figure 4.6** in the previous experiment), and interestingly it remains stable after the plasma was turned off. The minority carrier lifetime of the samples before and after this experiment were measured by a quasi-steady-state photocurrent decay technique (Sinton WCT-120) and found to increase from around 160 μ s to approximately 270 μ s after this short plasma exposure. It should be emphasized that this improvement of surface passivation properties remained stable even after a few days of storing the samples in ambient air.

4.2.3 Root cause of plasma effects

Hypotheses

As the samples were directly exposed to Ar/H₂ plasma during the experiments, the modification of surface passivation can be induced by the plasma species (e.g. atomic hydrogen, ions, electrons, etc.) and/or plasma emission (e.g. VUV light, UV light, visible light, etc.).

One hypothesis is that the passivation layers were modified by the atomic hydrogen originating from plasma. It has been reported that atomic hydrogen from the plasma is able to penetrate and induce defects in the a-Si:H bulk layer [13, 27]. Therefore, one may expect this to also happen in the passivation layers (not only a-Si:H but also Al₂O₃), which ultimately leads to degradation of surface passivation of the samples.

On the other hand, the bombardment of ions from the plasma upon the sample surfaces may also alter the surface passivation properties. In general, the kinetic energy of ions toward the grounded electrode (sample surface) is proportional to the plasma potential (V_p), which is approximately 90 V in our experiments. With this plasma potential, the bombardment energy of a singly charged ion, e.g. Ar⁺ ions, can reach approximately 90 eV, which is high enough to induce defects in the passivation layer. It is worth mentioning that at 300 mTorr, the plasma sheath is collisional, so the energy of ions impinging the surface can be a bit smaller than the estimated value.

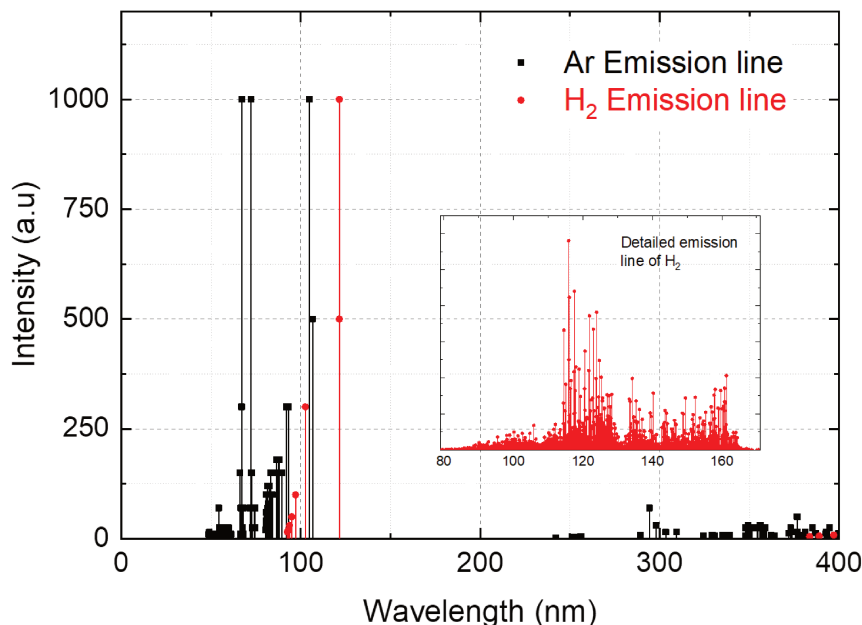


Figure 4.8 – Strong emission line of Argon and Hydrogen glow discharges. Data is obtained from the online publication of the Physical Measurement Laboratory at NIST [28] and Observatoire de Paris [29]

Besides the plasma species, the plasma emission can also affect the passivation layer. According to NIST and Observatoire de Paris [28, 29], both argon and hydrogen glow discharges have strong emission lines in the vacuum UV (VUV) region (see **Figure 4.8**). The energies of

these emitted photons are greater than 10 eV, which is high enough to deteriorate the passivation layers (Al_2O_3 and a-Si:H interfaces) as well as the interface (c-Si/ Al_2O_3 and c-Si/a-Si:H). However, the effect of light-induced degradation (LID) in c-Si bulk materials can be neglected in our experiments, as Niewelt et al. have observed that the LID effect only occurs in boron-doped c-Si wafers [30].

To verify these hypotheses, various plasma exposure experiments were conducted. The results from these experiments are shown as follows:

Exposure to pure-Ar plasma

First of all, in order to check any possible influences of atomic hydrogen (originating in plasma) on the surface passivation properties, a pure-Ar plasma exposure was conducted on an as-deposited Al_2O_3 -passivated sample. It should be mentioned that all other plasma parameters, besides the gas mixture, were kept the same as those in the baseline conditions. As there was no hydrogen in the gas mixture, the presence of atomic hydrogen in the plasma can be eliminated. **Figure 4.9** shows the PL signal emitted from the sample observed during this pure-Ar plasma exposure, compared to the PL signal emitted from identical sample observed during the Ar/ H_2 plasma exposure.

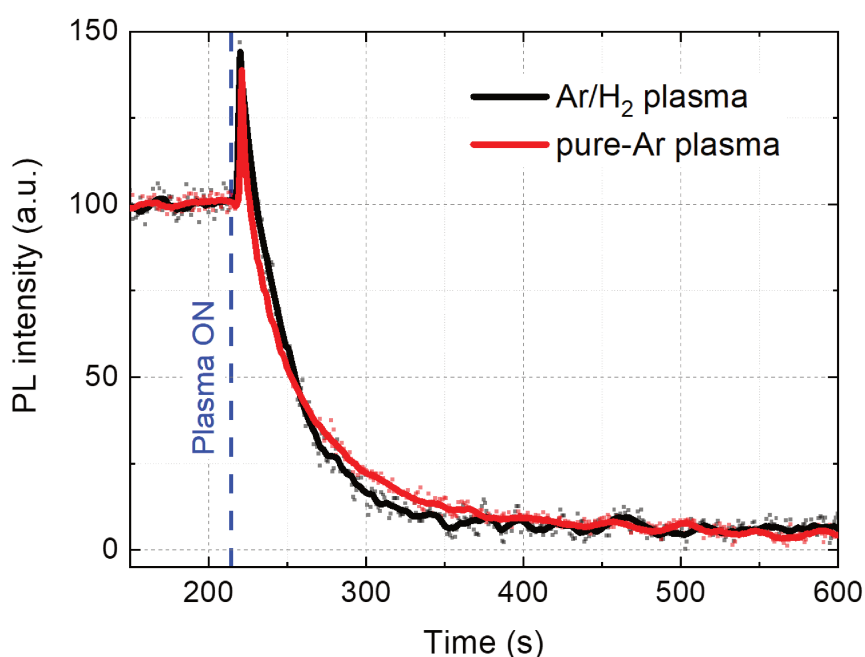


Figure 4.9 – Evolution of the PL signals emitted from sample passivated by Al_2O_3 observed during the pure-Ar plasma exposure at room temperature. It is compared to the PL signal emitted from identical sample observed during the Ar/ H_2 plasma exposure.

It can be observed that both PL signals exhibit the same features: a quick increase, followed by a slow degradation. As mentioned above, there was no presence of atomic hydrogen in the pure-Ar plasma, yet the sample behaved like the one that had been exposure to Ar/ H_2 plasma. Therefore, the hypothesis regarding the possible influences of atomic hydrogen (originating in the plasma) on the passivation layers (Al_2O_3 and a-Si:H) can be excluded.

Ar/H₂ plasma exposure through a MgF₂ window

An effective way to simultaneously verify the two remaining hypotheses is to performed additional experiments on the passivated samples covered by an optical window. Here, a magnesium fluoride (MgF₂) optical window was used. It is important to mention that this material is transparent to the VUV radiation, with a transmission rate more than 50% for photons with wavelengths higher than 120 nm. By covering the passivated samples with this optical window during the plasma exposure, all the plasma species (electrons, ions, radicals, etc.) will be prevented from reaching the sample surface, while the plasma emission (VUV light, UV light, etc.) can pass through to the samples. **Figure 4.10** shows the evolution of the PL signal emitted from the Al₂O₃-passivated sample observed during the Ar/H₂ plasma exposure through the MgF₂ optical window, compared to the PL signal emitted from identical sample under the Ar/H₂ plasma exposure without any optical window. The plasma parameters used in both experiments were identical (the baseline plasma conditions).

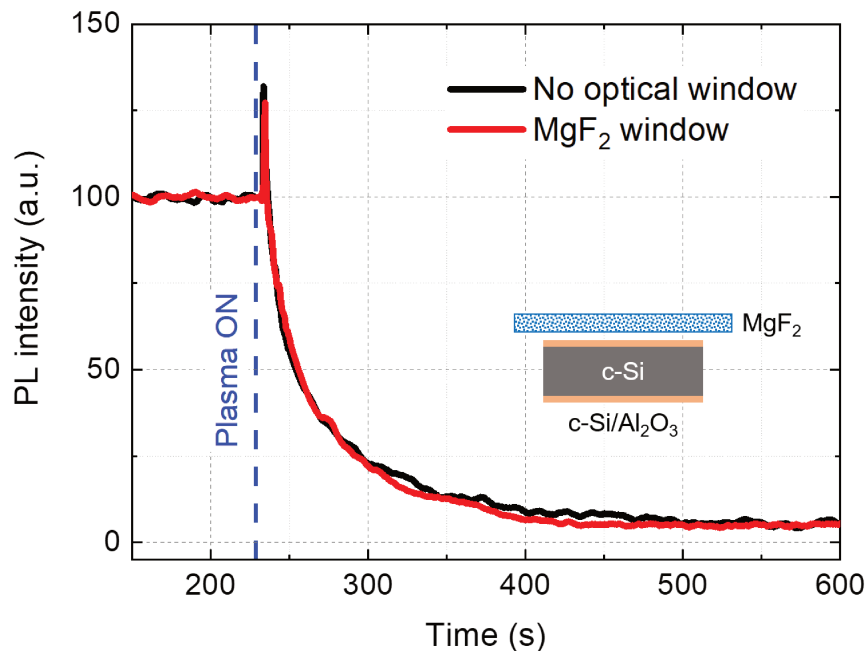


Figure 4.10 – Evolution of the PL signal emitted from an Al₂O₃-passivated sample observed during the plasma exposure through an MgF₂ optical window at room temperature compared to the PL signal obtained during the experiment without an optical window.

One can see that the PL signal obtained during the plasma exposure through MgF₂ optical window exhibits identical features compared to the PL signal observed during the exposure without any optical window. The same holds true for the a-Si:H-passivated samples. Based on these experimental results, it can be concluded that VUV light emitted from plasma is the root cause, leading to modification of the surface passivation.

Ar/H₂ plasma exposure through a Corning glass plate

Similar experiments (plasma exposure through an optical window) were also conducted with a normal Corning glass plate. So instead of using an MgF₂ optical window, an Corning glass

plate is used to cover the samples during the plasma exposure experiments. It is important to mention that the cut-off wavelength ($\lambda_{\text{cut-off}}$) of the Corning glass is approximately 280 nm (measured by the Perkin-Elmer Lambda 950 UV-VIS-NIR Spectrophotometer), which is in the UV-B region. Therefore, by covering the samples with this glass window, we prevent not only the plasma species, but also the high energy photons (VUV and UV-C light) from reaching the sample. Only photons with energy less than 4.42 eV are able to pass through to the sample.

Figure 4.11 shows the PL signals emitted from a sample passivated by Al_2O_3 observed during the plasma exposure through corning glass compared to the PL signal detected during the exposure experiment without any optical window. One can see that, when the Al_2O_3 -passivated sample is covered by a Corning glass plate, the PL signal emitted from the sample does not degrade. Surprisingly, it slightly improves during the plasma exposure. This result suggests that the photons with energy less than 4.42 eV is not strong enough to induce degradation on sample passivated by Al_2O_3 . In addition, the slight increase of PL signal during the experiment is probably due to what is known as light-induced field effect enhancement, which occurs when an Al_2O_3 -passivated sample is exposed to moderately high energy photons [5, 31].

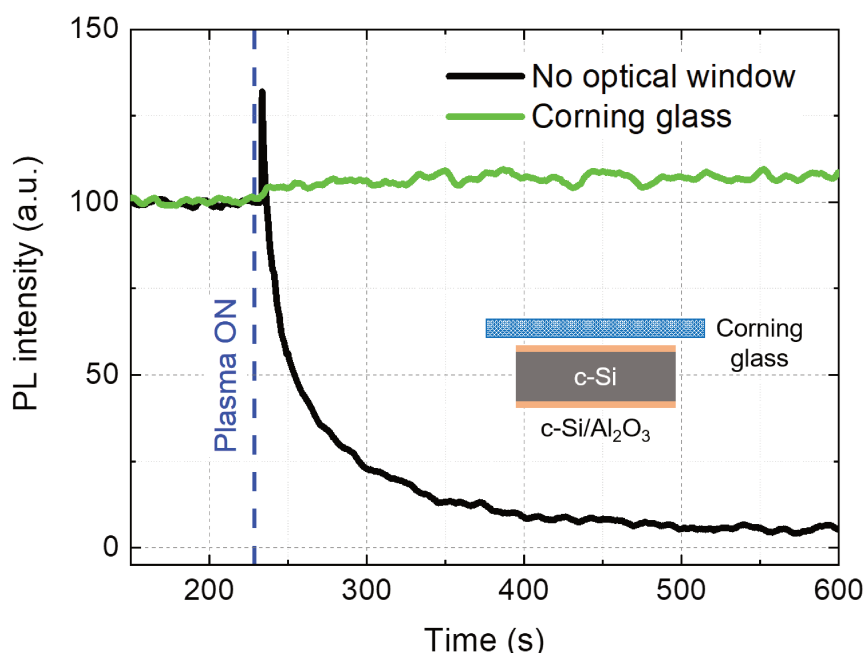


Figure 4.11 – Evolution of the PL signals (normalized) emitted from the Al_2O_3 -passivated sample observed during the plasma exposure through a Corning glass window at room temperature compared to the signal obtained during the experiment without an optical window.

In contrast with the Al_2O_3 -passivated sample, the degradation of surface passivation is still observable on sample passivated by a-Si:H film (see **Figure 4.12**). However, one can see that the degradation rate of the a-Si:H under the plasma exposure through the Corning glass window is a bit slower compared to the degradation rate observed during the direct plasma exposure. This result shows that the c-Si surface passivation provided by a-Si:H can be deteriorated even under the exposure to low energy UV light, the radiation range that causes no damage to surface passivation provided by Al_2O_3 . One may notice that the degradation of surface passivation became a bit slower in this experiment. This is probably due to the fact that VUV light from plasma did not reach the c-Si/a-Si:H interface.

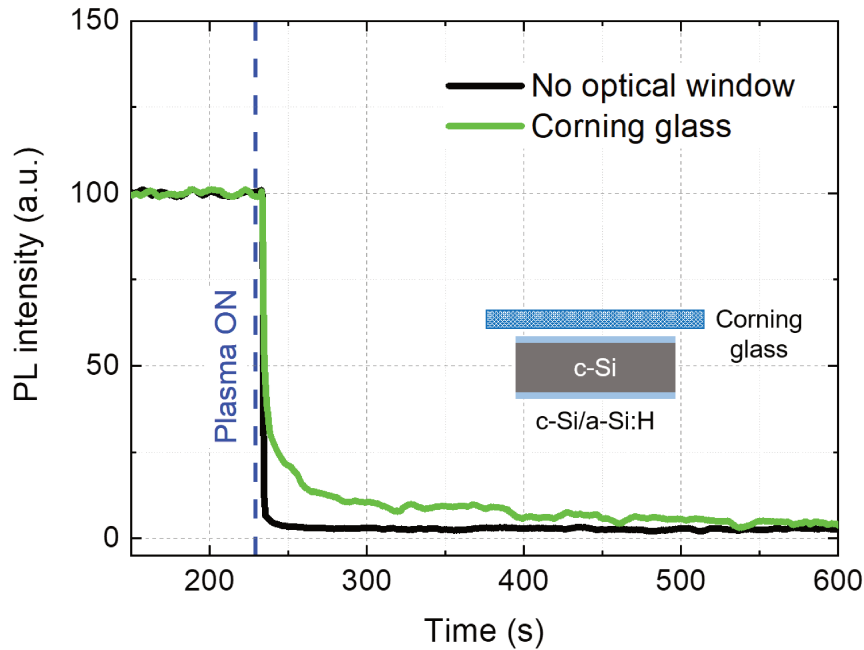


Figure 4.12 – Evolution of the PL signals (normalized) emitted from a c-Si wafer passivated by a 9 nm of a-Si:H observed during the plasma exposure through a Corning glass window at room temperature compared to the signal obtained during the experiment without an optical window.

4.2.4 Mechanisms behind the plasma-induced modifications of surface passivation

Understanding of passivation mechanisms in a-Si:H and Al₂O₃

In order to explain the mechanisms behind the modifications of surface passivation during the plasma exposure, one has to understand the passivation mechanism provided by both a-Si:H and Al₂O₃ as well as the interaction between these layers and the VUV light emitted from plasma. The a-Si:H passivation layer is known to provide excellent chemical passivation for c-Si wafer thanks to the generation of chemical bonds, mainly Si_{wafer}-Si and Si_{wafer}-H, at the interface during the deposition. The film also contains a large amount of hydrogen, which can diffuse throughout the layer to the interface and bond to the remaining silicon dangling bonds.

The Al₂O₃ layer, on the other hand, is also known for providing good chemical passivation thanks to the formation of chemical bonds (e.g. Si_{wafer}-O, Si_{wafer}-H, etc.) at the c-Si/Al₂O₃ interface. This region is commonly known as oxygen-rich layer (O-rich) with a thickness of approximately 1 nm. In addition, the film also contains a high density ($> 10^{12} \text{ cm}^{-2}$) of negative electrostatic charges, leading to a strong field effect passivation and thus enhancing the overall passivation quality. The origin of these electrostatic charges has been attributed to intrinsic and extrinsic defects in the Al₂O₃ structure. In a simulation study using the first principles, Matsunaga et al. have suggested that the Al vacancies and O interstitials can be negatively charged and are stable in their fully ionized states [32]. Furthermore, investigating the InGaAs/Al₂O₃ structure, Shin et al. have found that oxygen dangling bonds can produce an energy level in the Al₂O₃ forbidden gap below the mid-level [33]. These defects behave as traps for electrons from

c-Si and therefore induce the negative fixed charges. One may expect that the fixed charges in c-Si/Al₂O₃ structure have the same origin. The extrinsic point defects (e.g. hydrogen interstitials, etc.) have also been considered as non-negligible sources of negative fixed charges in Al₂O₃ layers. Peacock and Robertson have claimed that the interstitial hydrogen is stable in all three charge states (H⁺, H⁰, and H⁻) depending on the structure of materials they are located [34]. They proposed that in the c-Si/Al₂O₃ structure, a neutral interstitial hydrogen (H⁰) tends to accept an electron from c-Si and changes its charge state to a negative one (H⁻).

Mechanisms behind plasma-induced degradation

For both passivation materials, one can expect that there is a strong relationship between the chemical bonds at the interface and the quality of surface passivation. This brings us to an assumption that the degradation of c-Si surface passivation during the plasma exposure is a result of deterioration of these interfacial chemical bonds. It is possible that the high energy photons (VUV light) emitted from plasma penetrate into the passivation layer and damage the chemical bonds at the interface, which leads to the generation of defects and thus increases the SRH recombination of charge carriers. The difference in terms of degradation rate between samples coated with Al₂O₃ and those coated with a-Si:H is probably related to the type of chemical bonds at the interface. For samples passivated by a-Si:H film, the c-Si/a-Si:H interface is filled with the Si-Si and Si-H bonds. Due to a strong disorder in the a-Si:H network, most of these interfacial bonds are delicate and can be quickly broken by the plasma emission. On the contrary, the c-Si/Al₂O₃ interface contains stronger chemical bonds including the Si-O bonds, making the interface a bit more enduring to the high energy photons from plasma. This assumption also explains the results obtained during the plasma exposure experiment on samples covered by a Corning glass. As the c-Si/a-Si:H interface contains a large amount of weak bonds, the degradation of surface passivation occurs even under the exposure to low energy UV light. The Al₂O₃-passivated samples did not degrade in these experiments due to the fact that its interface contains strong chemical bonds that requires high energy photons to break.

Explanation of the activation of passivation properties of Al₂O₃ under plasma exposure

Looking back into the first set of experiments, one can see that the Al₂O₃-passivated sample behaves differently from the a-Si:H-passivated sample. Its surface passivation abruptly improves just after plasma ignition, then it slowly degrades throughout the rest of the plasma exposure experiment. To understand the mechanism behind this complex surface modification, it is important to remind that our Al₂O₃ passivation layers were grown at 150°C. Therefore, the as-deposited Al₂O₃ layer probably contains a considerable amount of oxygen and hydrogen in form of hydroxyl radicals (Al-OH). It is possible that this Al-OH structure gets broken rapidly by the high energy photons (VUV light) emitted from plasma, providing an oxygen dangling bond and a hydrogen interstitial (or an oxygen and a hydrogen interstitials). As mentioned in the previous section, these intrinsic and extrinsic point defects are the origin of the negative electrostatic charges in the Al₂O₃ film. Therefore, the break of Al-OH structure increases the negative charge density in the as-deposited Al₂O₃ film, leading to an enhancement of the field-effect as well as the overall surface passivation of the sample (increase of the PL signal). It is important to mention that the VUV light from plasma can break not only the hydroxyl radicals in the Al₂O₃ structure but also other chemical bonds (e.g. Si-O, Si-H, etc.) at the

c-Si/Al₂O₃ interface. The damage of these interfacial chemical bonds introduces more defects to the sample and ultimately deteriorate the chemical passivation (slow decrease of PL signal).

The study of the influence of plasma exposure was extended to the annealed Al₂O₃-passivated sample, to check if the enhancement of surface passivation occurs in Al₂O₃ passivation film in general. In this experiment, after the deposition of the Al₂O₃ passivation layer, the samples were annealed for 15 minutes at 300°C (H₂ environment with a chamber pressure of around 300 *mTorr*) before being exposed to the baseline Ar/H₂ plasma. **Figure 4.13** shows the PL signals emitted from the annealed Al₂O₃-passivated sample, compared to the signal from the as-deposited sample, during the plasma exposure at room temperature.

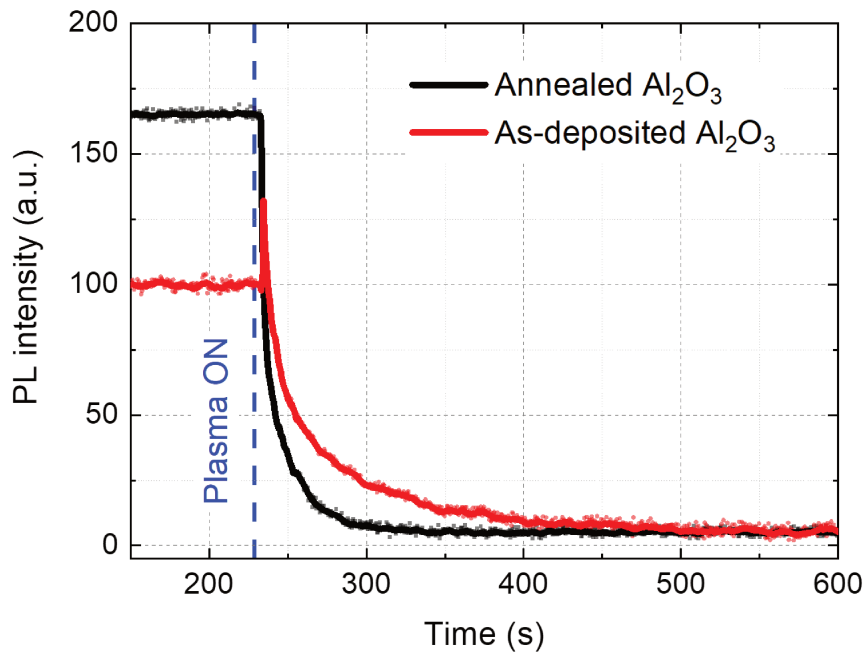


Figure 4.13 – Evolution of the PL signals (normalized) emitted from as-deposited and annealed samples passivated by Al₂O₃ observed during the plasma exposure at room temperature. It is important to mention that the initial PL intensity of the annealed sample is higher than the initial intensity of the as-deposited sample, due to the fact that the surface passivation of annealed sample had been improved by annealing.

One can see that the improvement of surface passivation just after the plasma ignition does not occur on the annealed Al₂O₃-passivated sample. It is very likely that the Al–OH structure in the Al₂O₃ passivation layer had already been modified during the annealing at 300°C. Therefore, as the annealed Al₂O₃ film contains no more hydroxyl radicals, no additional negative fixed charge is induced during the experiment. Moreover, it can be observed that the degradation rate of annealed Al₂O₃-passivated sample is slightly faster than the degradation rate of as-deposited sample. This result slightly contradicts our expectation, as the annealed Al₂O₃-passivated sample was supposed to have strong chemical bonds (e.g. Si–O) at the interface, making it more enduring to the plasma emission. After investigation, we found that the problem lies on the annealing process prior to the plasma exposure. Commonly, the Al₂O₃-passivated sample are annealed at around 400°C for more than 20 minutes to improve the surface passivation, by particularly forming a thin oxide layer at the Al₂O₃ interface. Here, the samples were annealed at 300°C for only 15 minutes. Therefore, it is possible that the interface

was modified, but the thin oxide layer was not perfectly formed yet. Instead, the improvement of minority carrier lifetime ($\tau_{initial} \approx 200 \mu s \rightarrow \tau_{final} > 1000 \mu s$) after annealing at 300°C may result from the dissociation of Al–OH structure and the diffusion of atomic hydrogen to passivate the remaining dangling bonds at the interface. For this reason, the interface of our annealed Al_2O_3 -passivated sample tends to have more Si–H bonds, making it a bit more vulnerable to the plasma exposure.

4.2.5 Effect of passivation layer thickness

In an attempt to reduce the detrimental effect of plasma processes on the crystalline silicon surface passivation, the thickness of the passivation layer has been increased from 9 nm to around 40 nm . In this experiment, the samples were exposed the baseline Ar/ H_2 plasma with the parameters shown in table 4.1. **Figure 4.14** shows the PL signals emitted from samples symmetrically passivated by a-Si:H film of different thicknesses.

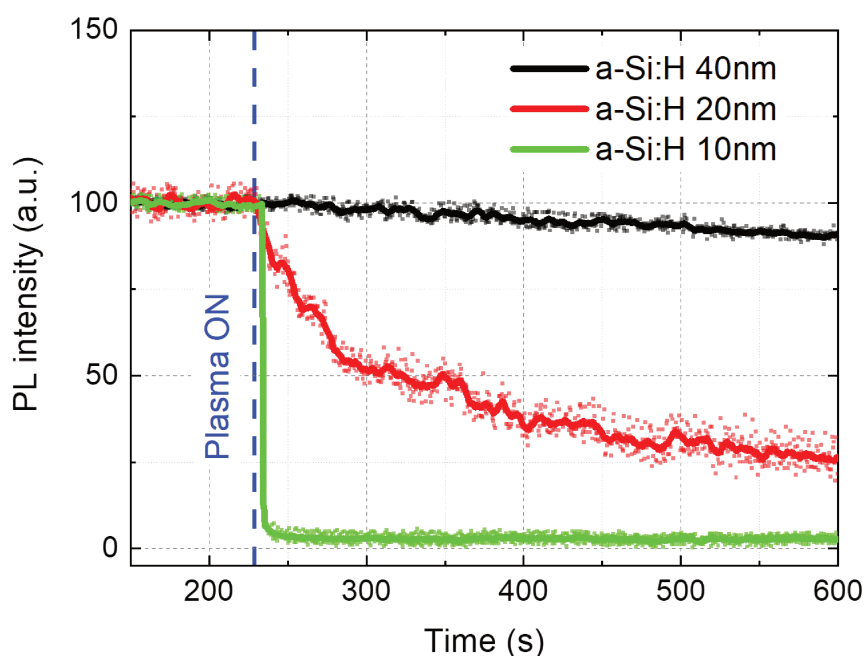


Figure 4.14 – The evolution of the PL signals (normalized) emitted from samples passivated by a-Si:H at different thickness, observed during the plasma exposure at room temperature.

Interestingly, one can see that the degradation of surface passivation is significantly attenuated when the thickness of a-Si:H passivation layer is increased from 9 nm to 20 nm . Moreover, the plasma-induced degradation effect is hardly observed when the a-Si:H passivation layer reaches 40 nm . The reasons behind this thickness dependence of plasma-induced degradation effect lies on the fact that the plasma emission is partly absorbed by the a-Si:H passivation layer, which is a direct bandgap semiconductor with a moderate energy gap of approximately 1.7 eV . Therefore, the thick a-Si:H passivation layer is able to absorb the plasma emission, preventing the VUV light from deteriorating the chemical bonds at the interface. However, it is worth mentioning that this thickness dependent behavior is not found on samples passivated by Al_2O_3 film. This result reflects the fact that Al_2O_3 passivation layer is a material with a large

energy gap of about 7 eV; therefore, its photo-absorption property is less pronounced compared to the absorption properties of a-Si:H layer. It is also important to note that the a-Si:H passivation layer absorbs not only the high energy photons from plasma but also the photon in the visible range. Therefore, an optimal thickness should be determined in order to mitigate the plasma detrimental effect while keeping the parasitic absorption of the a-Si:H layer as low as possible.

4.2.6 Effect of RF power & pressure

Because the plasma-induced degradation of surface passivation is caused by the plasma emission (mainly the VUV light), which is strongly dependent on the density and energy of free electrons in the plasma, the variation of chamber pressure and applied RF power may allow the diminution of the plasma detrimental effects. Here, the samples were exposed at room temperature to Ar/H₂ plasma at various chamber pressure (3 Torr – 0.3 Torr) as well as at different applied RF power (25 W – 2 W). The details parameters of the plasma conditions are shown in table 4.2.

Table 4.2 – Plasma conditions during the study of the influence of chamber pressure and applied RF power on the plasma-induced surface passivation modification.

| Paramaters | Pressure variation | RF power variation |
|------------------------------|--------------------|--------------------|
| Pressure | 0.3 – 3 Torr | 0.3 Torr |
| RF power | 15 W | 2 – 25 W |
| Ar/H ₂ flow rates | 10/10 sccm | |
| Substrate temperature | RT | |
| Inter-electrode distance | 25 mm | |

Figure 4.15.a shows the PL signals emitted from samples passivated by Al₂O₃ (≈ 9 nm) during the plasma exposure at different chamber pressure at room temperature. One can see that the degradation of the PL signals becomes slower when the chamber pressure is decreased. This result suggests that the degradation of surface passivation induced by plasma can be attenuated by lowering the chamber pressure. This pressure dependence behavior is probably related to the variation of plasma emission with the chamber pressure. To find out, the emission of plasma at various pressure were detected, and they are shown in **Figure 4.15.b**. One can see that, in the pressure range between 3 Torr and 0.3 Torr, the plasma emission decreases with the decrease of chamber pressure. That is the reason why the degradation of surface passivation is low under the plasma exposure at low pressure.

The same was observed during the plasma exposure experiment at different applied RF power: the lower the RF power is, the slower the degradation of surface passivation (see **Figure 4.15.c**). Here, one can understand that by reducing the applied RF power, the plasma emission becomes less intense (see **Figure 4.15.d**) due to the fact that free electrons in plasma have less energy. It is worth mentioning that this behavior is hardly observed on samples passivated by 9 nm of a-Si:H because the degradation of such samples is too quick to observe the difference between each condition.

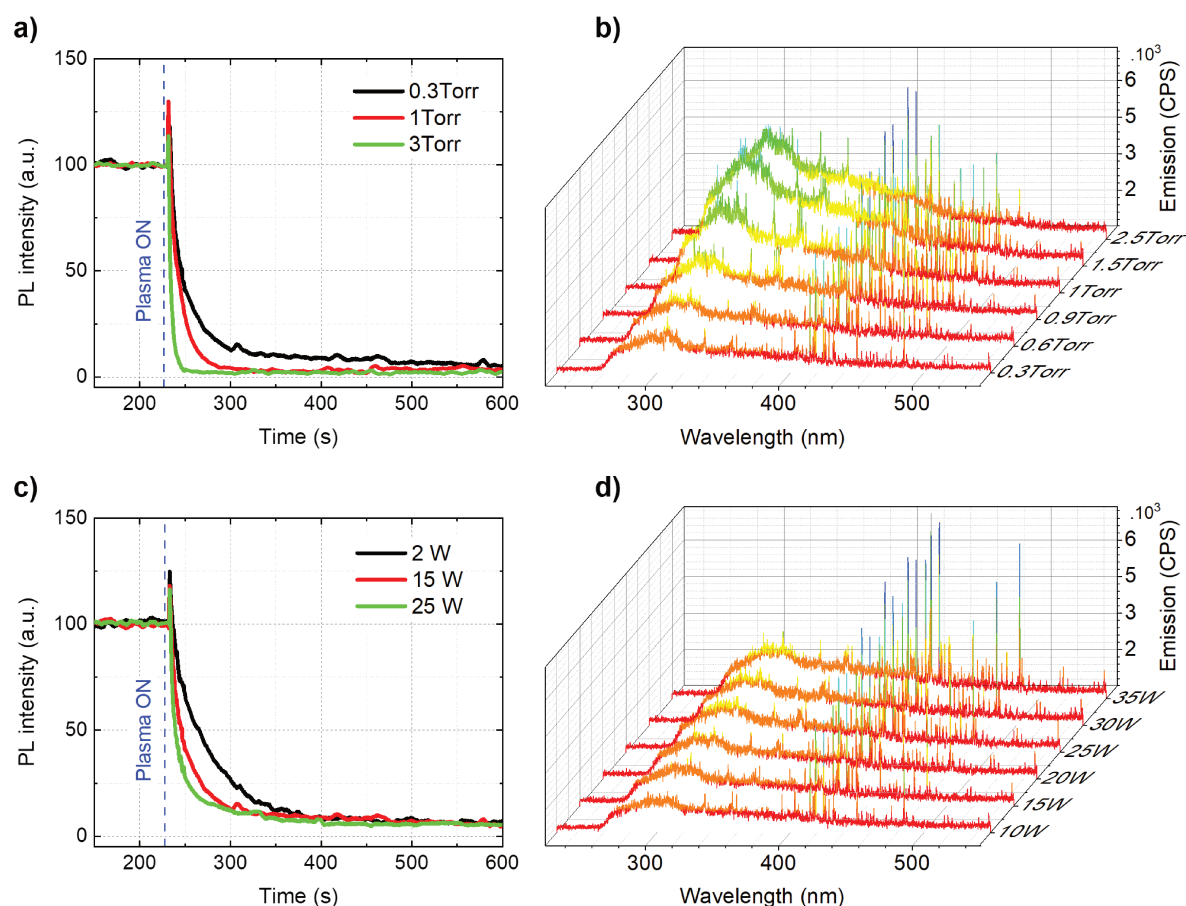


Figure 4.15 – Evolution of the PL signals (normalized) emitted from Al_2O_3 -passivated sample observed during the plasma exposure at a) different chamber pressure; c) different applied RF power. The emission of room-temperature Ar/ H_2 at b) different chamber pressure (constant RF power 15 W); d) different applied RF power (constant pressure 0.3 Torr).

4.2.7 Effect of substrate temperature

Substrate temperature is another important parameter to be investigated for mitigation of the detrimental effect of plasma processes on the surface passivation of crystalline silicon. The variation of substrate temperature may have less influences on the plasma emission; however, it can have a great influence on the properties of the passivation materials, in particular the diffusion of atomic hydrogen that originates in the passivation layers themselves. For further understanding of the influence of substrate temperature on the plasma-induced modification of surface passivation layer, the plasma exposure experiments at 200°C were conducted. In this experiment, the passivated samples (as-deposited) were put into the reactor, filled with argon and hydrogen gases, at room temperature. Then the substrate temperature was increased rapidly to 200°C . As soon as the substrate temperature reached the set-point, the experiment began. It should be mentioned that, besides the substrate temperature, all the plasma parameters were kept the same as the baseline plasma condition.

Figure 4.16 compares the PL signal emitted from samples passivated by Al_2O_3 observed during the Ar/ H_2 plasma exposure at RT and at 200°C . One can see that by increasing the substrate temperature to 200°C , the degradation of surface passivation provided by Al_2O_3 becomes

significantly slower compared to the degradation during the plasma exposure at RT. This result can be explained by two competing mechanisms, simultaneously induced by plasma emission and substrate temperature (200°C) during the exposure. As mentioned in the previous section, the high energy photons induced by plasma are able to induce bond breaking in the passivation layer as well as at the interface, leading to the deterioration of chemical passivation (decrease of PL signal). On the other hand, the increase of substrate temperature can induce the diffusion of atomic hydrogen, originating in the Al_2O_3 passivation layer, to re-passivate the newly-generated defects. Thanks to this influence of substrate temperature, the net degradation rate of surface passivation was decreased, as observed in the experiment.

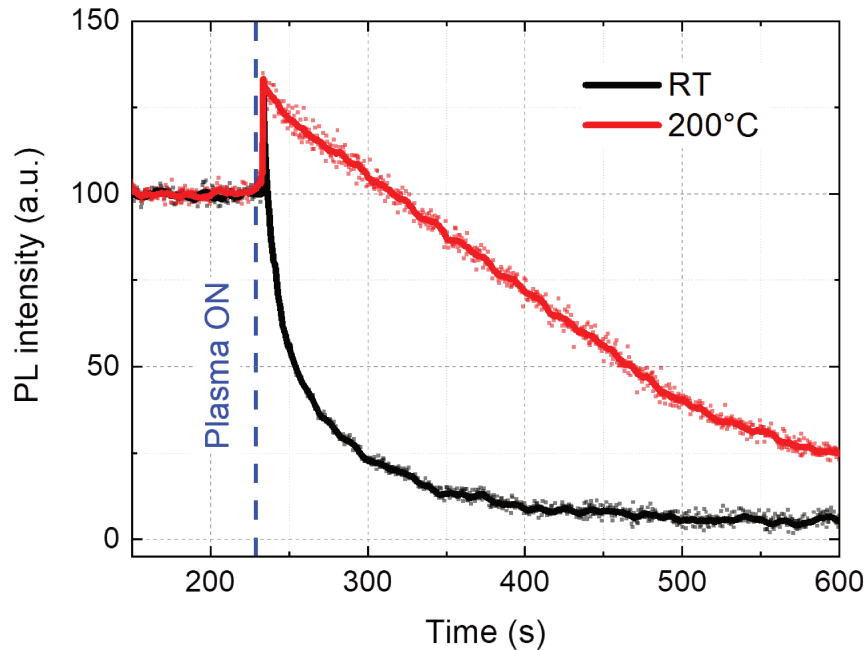


Figure 4.16 – Evolution of the PL signals (normalized) emitted from samples symmetrically passivated by 9 nm Al_2O_3 layers, observed during the Ar/ H_2 plasma exposure at room temperature and at 200°C .

For the a-Si:H-passivated sample, the PL signal detected during the plasma exposure at 200°C is shown in **Figure 4.17** along with the PL signal obtained from the experiment at room temperature. It is important to mention that because the samples passivated by a 9 nm of a-Si:H film degrade too quick under the plasma exposure (making it very difficult to observe the evolution of surface passivation during such experiments), the samples passivated by a 20 nm of a-Si:H layer is used here. In this experiment, a complex behavior of the evolution of surface passivation provided by a-Si:H can be observed.

One can see that, in the exposure experiment at 200°C , the surface passivation of the sample rapidly degrades (more than 50% drop of the emitted PL signal) as soon as the plasma is ignited. It is also obvious that the degradation of surface passivation during the plasma exposure at 200°C is much faster than the one observed during the plasma exposure at room temperature, which is opposite to what has been observed on sample passivated by Al_2O_3 . A possible explanation of this quick drop of PL signal is that the raise of temperature increases the molecular vibration of materials and therefore weakens the chemical bonds in the a-Si:H layer as well as the c-Si/a-Si:H interface. Consequently, the moderate chemical bonds that hardly get broken

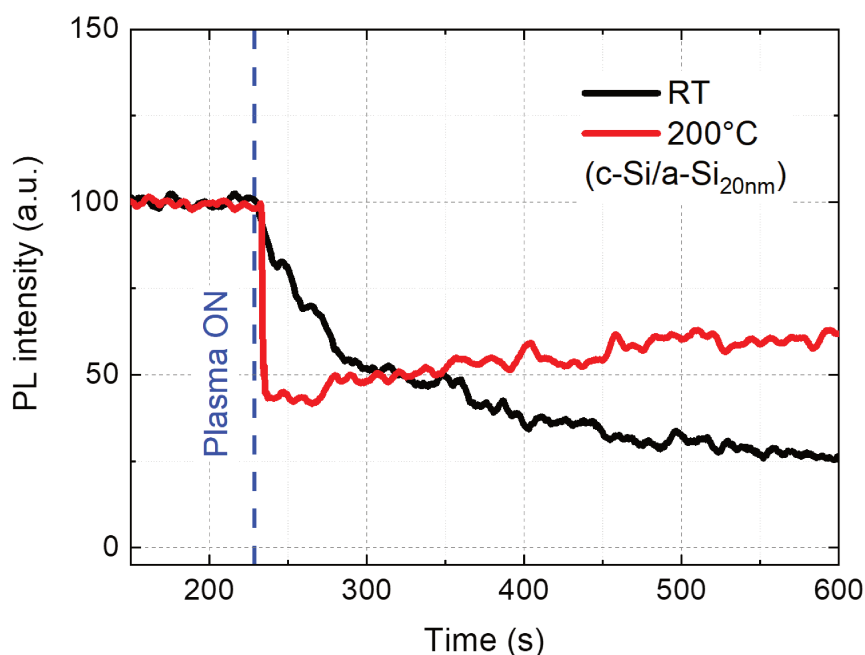


Figure 4.17 – Evolution of the PL signals (normalized) emitted from samples symmetrically passivated by 20 nm a-Si:H layers, observed during the plasma exposure at room temperature and at 200°C.

during the plasma exposure at room temperature can be quickly dissociated during the exposure at 200°C. In addition, the range of high energy photons that are able to break the interfacial bonds also slightly broadens as the interfacial bonds become weaker. For these reasons, the interfacial bond broken rate during the plasma exposure at 200°C is higher than the bond broken rate observed during the plasma exposure at room temperature.

After the abrupt degradation at the beginning, a steady recovery of surface passivation has been observed during the rest of the plasma exposure (@ 200°C). To understand this feature, it is important to notice that only photons with energy equal or less than 3 eV can pass through the 20 nm of a-Si:H layer (measured by the Spectroscopic Ellipsometry). One has seen that, at the beginning of the experiment, most of the weak and moderate chemical bonds at the c-Si/a-Si:H interface get broken, leading to a significant degradation of chemical passivation. In this second stage, similar to what happens during the experiment with Al₂O₃, two competing mechanisms occur simultaneously: the interfacial bond breaking caused by the plasma emission and the neutralization of dangling bonds thanks to the reformation of interfacial chemical bonds. The newly-formed interfacial bonds can be weak, moderate or strong chemical bonds. While the weak and moderate ones may get broken again by the photons that pass through the 20 nm of a-Si:H layer, some newly-generated strong bonds that require photons with energy higher than 3 eV to break may remain. So as the number of strong interfacial bonds gradually increases, the surface passivation also slowly recovers (a slow increase of the PL signal).

It is worth mentioning that these mechanisms could also occur on samples passivated by Al₂O₃. However, as there is nothing to block the high energy photons (VUV light) from reaching the interface, all the newly-generated bonds will get broken again.

4.2.8 Recovery of surface passivation

The PL signal emitted from each sample was also observed after the plasma was turned off. This allows us to have a better understanding of the plasma-generated defects and how they evolve as a function of time.

Figure 4.18 shows the evolution of PL signal emitted from samples passivated by Al_2O_3 and a-Si:H just after the Ar/ H_2 plasma exposure at room temperature. One can see that the PL signal emitted from sample coated with Al_2O_3 remains constant after the plasma was turned off. In contrast, the PL signal emitted from sample coated with a-Si:H layer slightly recovered by itself. These results suggest that the defects induced by plasma on the Al_2O_3 -passivated sample remain stable at room temperature. In contrast, the surface passivation provided by a-Si:H can partially recover by itself even after a significant deterioration induced during the plasma exposure. Further studies are required in order to explain the mechanism behind these results.

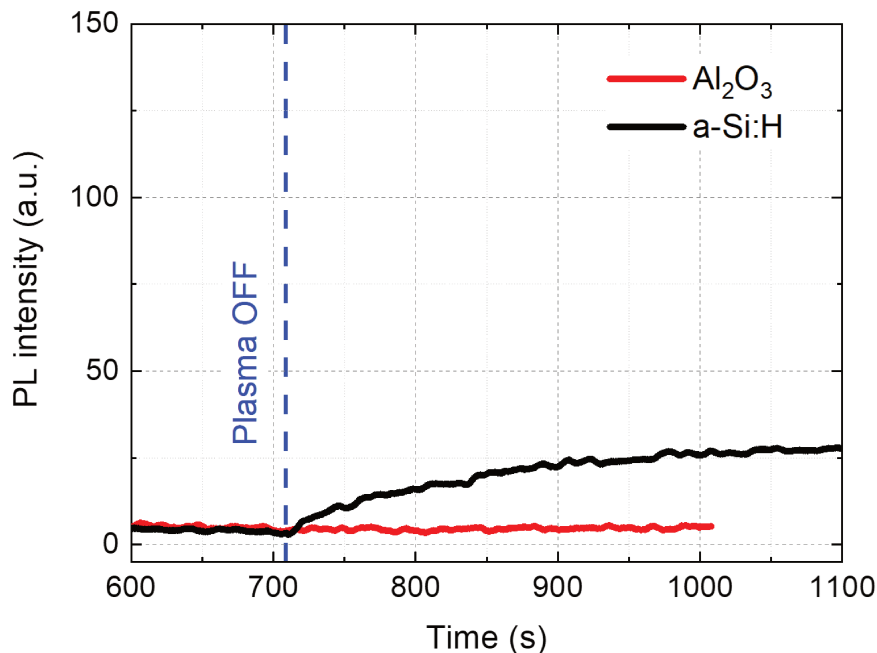


Figure 4.18 – Evolution of the PL signals (normalized) emitted from samples passivated by 9 nm of Al_2O_3 and a-Si:H layers after the plasma exposure at room temperature.

In an attempt to recover the surface passivation, the degraded samples were annealed at 200°C in the hydrogen environment. **Figure 4.19** shows the evolution of the PL signal emitted from the degraded Al_2O_3 -passivated sample during the annealing process, from the beginning at room temperature until reaching the temperature set-point at 200°C and after. The result shows that the surface passivation of the sample starts to recover at around 150°C , and it continues to slowly increase until reaching a steady-state value. The same results could be obtained during the annealing in the vacuum. This recovery of surface passivation is probably due to the diffusion of atomic hydrogen to passivate the plasma-induced defects or due to the reformation of interfacial bonds (from the chemical bonds that had been broken during the plasma exposure).

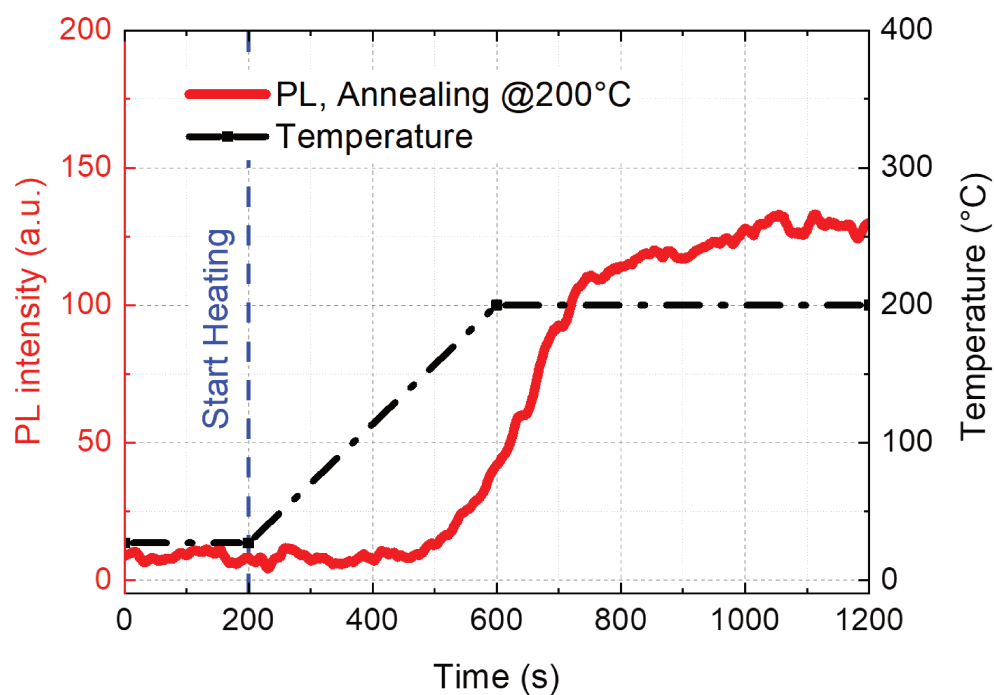


Figure 4.19 – Evolution of the PL signals (normalized) emitted from the plasma-exposed sample passivated by Al_2O_3 during the annealing at 200°C .

It is worth mentioning that, in the plasma exposure experiment at 200°C , the degraded surface quickly recover when the plasma was turned off.

Summary

In this chapter, the configuration and the operation modes of in-situ SSPL have been presented. The tool has been used to characterize the evolution of surface passivation of c-Si wafer under plasma exposure at various conditions. The experimental results show that:

- Despite having the same thickness of passivation layers, the Al_2O_3 -passivated sample and a-Si:H-passivated sample behave differently under the same plasma conditions. The surface passivation of a-Si:H-passivated sample rapidly degraded as the plasma was ignited. In contrast, the surface passivation of Al_2O_3 -passivated sample was enhanced just after the plasma ignition before it slowly degraded as a function of plasma exposure time.
- Among three proposed hypotheses, plasma emission (VUV light) is very likely to be the main root cause of plasma-induced modification of surface passivation during the plasma exposure. This hypothesis was confirmed by a plasma exposure experiment through MgF_2 optical window.
- Under plasma exposure, the improvement of surface passivation provided by Al_2O_3 layer can only be observed on as-deposited sample. Based on the analysis, this improvement can be a result of the dissociation of hydroxyl (Al–OH) radical in Al_2O_3 layer, which leads to an increase of fixed charge density in the layer and ultimately enhancement of field-effect passivation.
- Surface passivation provided by a-Si:H film is more vulnerable to UV light than the passivation provided by Al_2O_3 . It has been observed that, under an exposure to photons with energy less than 4.42 eV, the a-Si:H-passivated sample degraded, while the Al_2O_3 -passivated sample did not.
- The plasma-induced degradation of surface passivation can be altered by modifying the applied RF power and/or the chamber pressure. The lower the applied RF power is the slower the plasma-induced degradation. The same holds true for the chamber pressure.
- Increasing substrate temperature also slowed down the degradation of surface passivation of the sample under plasma exposure. This probably results from diffusion of atomic hydrogen to passivate the dangling bonds, compensating the deterioration of surface passivation caused by plasma emission.
- The deterioration of surface passivation caused by plasma exposure can recover by annealing the sample at temperature higher than 150°C .

Bibliography

- [1] HORIBA Scientific. *iHR fully automated imaging spectrometer operating manual*. 2013.
- [2] Shubham Duttgupta, Fajun Ma, Bram Hoex, Thomas Mueller, and Armin G. Aberle. Optimised antireflection coatings using silicon nitride on textured silicon surfaces based on measurements and multidimensional modelling. *Energy Procedia*, 15:78 – 83, 2012. International Conference on Materials for Advanced Technologies 2011, Symposium O.
- [3] L.A. Dobrzanski, A. Drygaa, K. Goombek, P. Panek, E. Bielaska, and P. Ziba. Laser surface treatment of multicrystalline silicon for enhancing optical properties. *Journal of Materials Processing Technology*, 201(1):291 – 296, 2008. 10th International Conference on Advances in Materials and Processing Technologies.
- [4] A. Najar, A. A. Al-Jabr, A. B. Slimane, M. A. Alsunaidi, T. K. Ng, B. S. Ooi, R. Sougrat, and D. H. Anjum. Effective antireflection properties of porous silicon nanowires for photovoltaic applications. In *2013 Saudi International Electronics, Communications and Photonics Conference*, pages 1–4, April 2013.
- [5] Fabien Lebreton. *Silicon surface passivation properties of aluminum oxide grown by atomic layer deposition for low temperature solar cells processes*. Theses, Université Paris-Saclay, 2017.
- [6] Armin Richter, Jan Benick, Martin Hermle, and Stefan W. Glunz. Excellent silicon surface passivation with 5 Å thin al₂o₃ layers: Influence of different thermal post-deposition treatments. *physica status solidi (RRL) Rapid Research Letters*, 5(56):202–204, 2011.
- [7] Paul Poodt, Adriaan Lankhorst, Fred Roozeboom, Karel Spee, Diederik Maas, and Ad Vermeer. High-speed spatial atomic-layer deposition of aluminum oxide layers for solar cell passivation. *Advanced Materials*, 22(32):3564–3567, 2010.
- [8] G. Dingemans, R. Seguin, P. Engelhart, M. C. M. van de Sanden, and W. M. M. Kessels. Silicon surface passivation by ultrathin al₂o₃ films synthesized by thermal and plasma atomic layer deposition. *physica status solidi (RRL) Rapid Research Letters*, 4(12):10–12, 2010.
- [9] J. Wang, S. Sadegh Mottaghian, and M. Farrokh Baroughi. Passivation properties of atomic-layer-deposited hafnium and aluminum oxides on si surfaces. *IEEE Transactions on Electron Devices*, 59(2):342–348, 2012.
- [10] Chia-Hsun Hsu, Chun-Wei Huang, Yun-Shao Cho, Wan-Yu Wu, Dong-Sing Wu, Xiao-Ying Zhang, Wen-Zhang Zhu, Shui-Yang Lien, and Chang-Sin Ye. Efficiency improvement of perc solar cell using an aluminum oxide passivation layer prepared via spatial atomic layer deposition and post-annealing. *Surface and Coatings Technology*, 358:968 – 975, 2019.
- [11] J. Schmidt, A. Merkle, R. Brendel, B. Hoex, M. C. M. van de Sanden, and W. M. M. Kessels. Surface passivation of high-efficiency silicon solar cells by atomic-layer-deposited al₂o₃. *Progress in Photovoltaics: Research and Applications*, 16(6):461–466, 2008.
- [12] P. Saint-Cast, J. Benick, D. Kania, L. Weiss, M. Hofmann, J. Rentsch, R. Preu, and S. W. Glunz. High-efficiency c-si solar cells passivated with ald and pecvd aluminum oxide. *IEEE Electron Device Letters*, 31(7):695–697, July 2010.
- [13] K. Yoshikawa, H. Kawasaki, W. Yoshida, T. Irie, K. Konishi, K. Nakano, T. Uto, D. Adachi, M. Kanematsu, H. Uzu, and K. Yamamoto. Silicon heterojunction solar cell with interdigitated back contacts for a photoconversion efficiency over 26%. *Nature Energy*, 2(17032), 2017.
- [14] K. Masuko, M. Shigematsu, T. Hashiguchi, D. Fujishima, M. Kai, N. Yoshimura, T. Yamaguchi, Y. Ichihashi, T. Mishima, N. Matsubara, T. Yamanishi, T. Takahama, M. Taguchi, E. Maruyama,

- and S. Okamoto. Achievement of more than 25% conversion efficiency with crystalline silicon heterojunction solar cell. *IEEE Journal of Photovoltaics*, 4(6):1433–1435, 2014.
- [15] M. Taguchi, A. Yano, S. Tohoda, K. Matsuyama, Y. Nakamura, T. Nishiwaki, K. Fujita, and E. Maruyama. 24.7 *IEEE Journal of Photovoltaics*, 4(1):96–99, 2014.
- [16] U. K. Das, M. Z. Burrows, M. Lu, S. Bowden, and R. W. Birkmire. Surface passivation and heterojunction cells on si (100) and (111) wafers using dc and rf plasma deposited si:h thin films. *Applied Physics Letters*, 92(6):063504, 2008.
- [17] Stefaan De Wolf and Guy Beaucarne. Surface passivation properties of boron-doped plasma-enhanced chemical vapor deposited hydrogenated amorphous silicon films on p-type crystalline si substrates. *Applied Physics Letters*, 88(2):022104, 2006.
- [18] S. Dauwe, J. Schmidt, and R. Hezel. Very low surface recombination velocities on p- and n-type silicon wafers passivated with hydrogenated amorphous silicon films. In *Conference Record of the Twenty-Ninth IEEE Photovoltaic Specialists Conference, 2002.*, pages 1246–1249, May 2002.
- [19] Jisoo Ko, Daeyeong Gong, Krishnakumar Pillai, Kong-Soo Lee, Minkyu Ju, Pyungho Choi, Kwang-Ryul Kim, Junsin Yi, and Byoungdeog Choi. Double layer sinx:h films for passivation and anti-reflection coating of c-si solar cells. *Thin Solid Films*, 519(20):6887 – 6891, 2011. 10th Asia-Pacific Conference on Plasma Science and Technology.
- [20] Yimao Wan, Keith R. McIntosh, and Andrew F. Thomson. Characterisation and optimisation of pecvd sinx as an antireflection coating and passivation layer for silicon solar cells. *AIP Advances*, 3(3):032113, 2013.
- [21] B. Hoex, A. J. M. van Erven, R. C. M. Bosch, W. T. M. Stals, M. D. Bijker, P. J. van den Oever, W. M. M. Kessels, and M. C. M. van de Sanden. Industrial high-rate (5nm/s) deposited silicon nitride yielding high-quality bulk and surface passivation under optimum anti-reflection coating conditions. *Progress in Photovoltaics: Research and Applications*, 13(8):705–712, 2005.
- [22] B. Kumar, T. Baskara Pandian, E. Sreekirana, and S. Narayanan. Benefit of dual layer silicon nitride anti-reflection coating. In *Conference Record of the Thirty-first IEEE Photovoltaic Specialists Conference, 2005.*, pages 1205–1208, Jan 2005.
- [23] Martin Bivour, Sebastian Schröer, and Martin Hermle. Numerical analysis of electrical tco / a-si:h(p) contact properties for silicon heterojunction solar cells. *Energy Procedia*, 38:658 – 669, 2013. Proceedings of the 3rd International Conference on Crystalline Silicon Photovoltaics (SiliconPV 2013).
- [24] Martin Bivour, Christian Reichel, Martin Hermle, and Stefan W. Glunz. Improving the a-si:h(p) rear emitter contact of n-type silicon solar cells. *Solar Energy Materials and Solar Cells*, 106:11 – 16, 2012.
- [25] F. Lebreton, S. N. Abolmasov, F. Silva, and P. Roca i Cabarrocas. In situ photoluminescence study of plasma-induced damage at the a-si:h/c-si interface. *Applied Physics Letters*, 108(5):051603, 2016.
- [26] Y.P.B. Mouafi, T Luder, and G. Hahn. Influence of the sinx deposition temperature on the passivation quality of al₂o₃/sinx stacks and the effect of blistering. In *European photovoltaic solar energy conference, EUPVSEC 2013*, pages 1359–1363, 2013.
- [27] U. K. Das, T. Yasuda, and S. Yamasaki. In situ esr study to detect the diffusion of free h and creation of dangling bonds in hydrogenated amorphous silicon. *Phys. Rev. B*, 63:245204, Jun 2001.

- [28] National Institute of Standards and Technology (NIST). Basic atomic spectroscopic data: strong lines. https://physics.nist.gov/PhysRefData/Handbook/element_name_a.htm, June 2019.
- [29] Observatoire de Paris. Vacuum ultraviolet emission spectrum of molecular hydrogen. <https://molat.obspm.fr/index.php?page=pages/Atlas/atlas.php>, June 2019.
- [30] T. Niewelt, M. Selinger, N. E. Grant, W. Kwapil, J. D. Murphy, and M. C. Schubert. Light-induced activation and deactivation of bulk defects in boron-doped float-zone silicon. *Journal of Applied Physics*, 121(18):185702, 2017.
- [31] Baochen Liao, Rolf Stangl, Thomas Mueller, Fen Lin, Charanjit S. Bhatia, and Bram Hoex. The effect of light soaking on crystalline silicon surface passivation by atomic layer deposited Al_2O_3 . *Journal of Applied Physics*, 113(2):024509, 2013.
- [32] Katsuyuki Matsunaga, Tomohito Tanaka, Takahisa Yamamoto, and Yuichi Ikuhara. First-principles calculations of intrinsic defects in Al_2O_3 . *Phys. Rev. B*, 68:085110, Aug 2003.
- [33] Byungha Shin, Justin R. Weber, Rathnait D. Long, Paul K. Hurley, Chris G. Van de Walle, and Paul C. McIntyre. Origin and passivation of fixed charge in atomic layer deposited aluminum oxide gate insulators on chemically treated ingaas substrates. *Applied Physics Letters*, 96(15):152908, 2010.
- [34] P. W. Peacock and J. Robertson. Behavior of hydrogen in high dielectric constant oxide gate insulators. *Applied Physics Letters*, 83(10):2025–2027, 2003.

Chapter 5

IN-SITU MPL: FROM A QUALITATIVE TO A QUANTITATIVE TECHNIQUE

Contents

| | | |
|------------|---|------------|
| 5.1 | System design | 81 |
| 5.1.1 | Excitation system | 81 |
| 5.1.2 | Detection system | 82 |
| 5.1.3 | Optical acquisition system | 82 |
| 5.1.4 | Flexibility of system | 84 |
| 5.2 | Calibration of the system | 86 |
| 5.2.1 | Phase shift calibration | 86 |
| 5.2.2 | Study and optimization of system parameters | 88 |
| 5.3 | Determination of minority carrier lifetime at a specific carrier density | 91 |
| 5.4 | Development of graphic user interface | 93 |
| 5.5 | Carrier lifetime correction | 95 |
| 5.6 | Carrier lifetime vs Temperature | 97 |
| 5.7 | In-situ study of surface passivation during deposition of passivation layers | 100 |
| 5.7.1 | Sample & experimental set-up | 100 |
| 5.7.2 | Results & Discussion | 101 |
| 5.8 | In-situ study of surface passivation during annealing | 103 |
| 5.8.1 | Sample & experimental set-up | 103 |
| 5.8.2 | Results | 104 |
| 5.8.3 | Discussion | 106 |
| 5.9 | In-situ study of surface passivation during deposition of ARC layer | 107 |
| 5.9.1 | Experimental set-up | 107 |
| 5.9.2 | Results | 108 |
| 5.9.3 | Discussion | 110 |
| | Summary | 112 |

As presented in the previous chapter, the in-situ studies of passivated crystalline silicon wafers have provided many interesting insights into the evolution of surface passivation during various processes (e.g. plasma exposure, thermal treatment, etc.). However, one may notice that all those results provide only qualitative information, which tends to describe the surface passivation properties rather than to measure it. This qualitative study of surface passivation can be very useful for evaluation of newly-introduced fabrication processes and materials (e.g. passivation layer, capping layer, etc.). However, when it comes to the optimization of processes (e.g. thermal treatment, deposition of thin-film semiconductors, etc.), a quantitative study is more practical. For this reason, another in-situ characterization tool, so-called in-situ MPL, was developed during the course of my thesis. As the name suggests, the in-situ MPL was developed based on an optical characterization technique, known as modulated photoluminescence. This characterization technique employs an intensity-modulated laser for sample excitation. This leads to an oscillation of the photo-generated carriers in the sample as well as the emitted photoluminescence signal. By measuring the phase shift between the modulated PL signal and the laser excitation intensity, the minority carrier lifetime of the sample can be determined (see section 3.4). Incorporating the modulated photoluminescence technique, the in-situ MPL is able to quantitatively characterize the surface passivation of c-Si wafer in real time during the solar cell fabrication processes. In this chapter, the development of in-situ MPL, from the design to a fully operational tool, will be presented. In addition, several interesting results regarding the in-situ study of surface passivation of c-Si wafers during deposition of passivation layer, thermal treatment, deposition of anti-reflection coating will also be discussed.

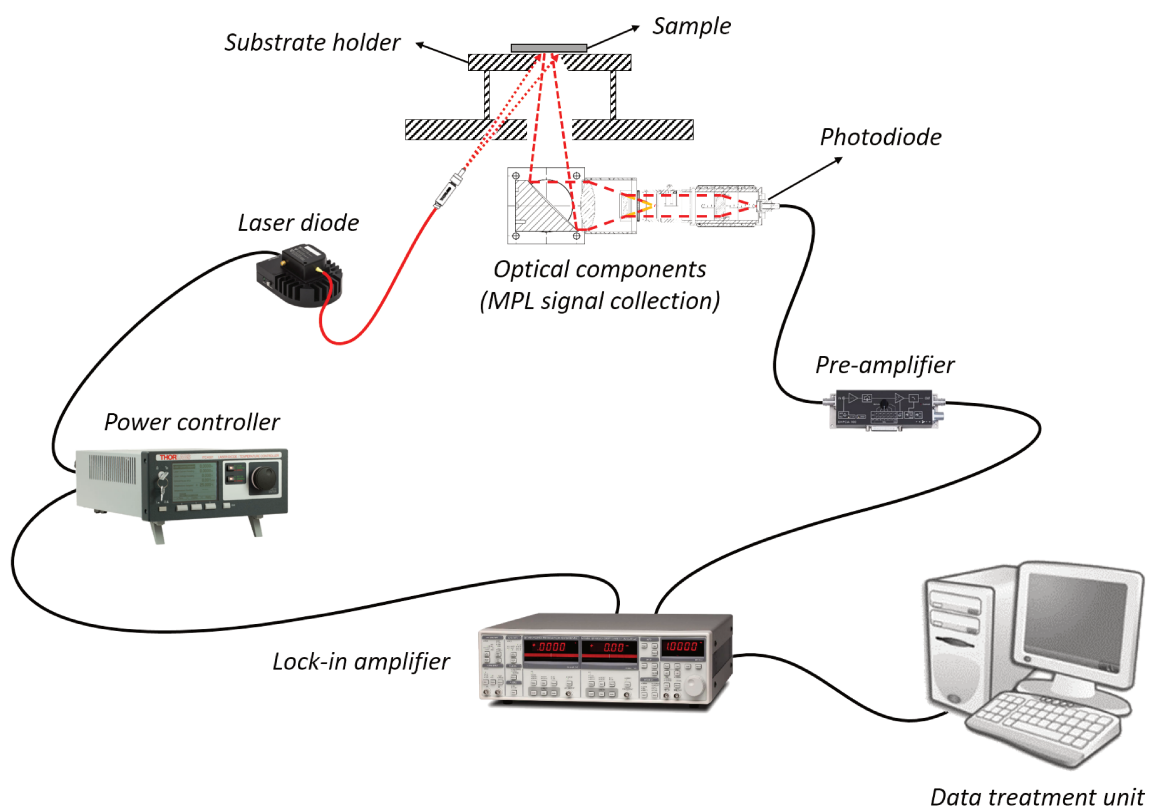


Figure 5.1 – Schematic diagram of in-situ MPL characterization tool. The tool was designed in such a way that can be attached to a PECVD reactor (PLASMAT).

5.1 System design

In order to measure minority carrier lifetimes of a sample during the processes, in-situ MPL must be able to detect the modulated PL signal emitted from the sample inside the reactor. Furthermore, the detection must not cause any disturbances to the processes, and vice versa. Designing such a system is very challenging. As the modulated photoluminescence is an optical characterization technique, similar to the steady-state photoluminescence, various concepts and techniques that have been employed for the development of in-situ PL were adopted and used to facilitate the design of in-situ MPL system. Consequently, the overall configuration of both characterization tools looks quite similar. However, each component of the in-situ MPL system is uniquely designed to adapt with the modulated signals. The entire in-situ MPL is divided into three main parts (see **Figure 5.1**): the excitation system, the detection system, and the optical acquisition system.

5.1.1 Excitation system

As mentioned previously, in-situ MPL requires an intensity-modulated laser light for sample excitation. This can be achieved by using an optical chopper to periodically oscillate the intensity of a constant laser beam [1] or by employing an electronic modulation circuit to continuously regulate the electrical power delivered to the laser diode. Commonly, the second method (electronic modulation) is more favorable, as it provides clean and consistent modulation signals. In addition, it allows a precise control of the laser optical output. Therefore, we decided to employ this modulation method for our excitation system. In our current setup, a combination of a fiber-pigtailed laser diode (see **Figure 5.2.a**) and a programmable current/temperature controller (see **Figure 5.2.b**) are used. It should be mentioned that the LP785-SF100 laser diode emits a continuous wave laser beam with a center wavelength of 785 nm and an adjustable optical output less than 100 mW.

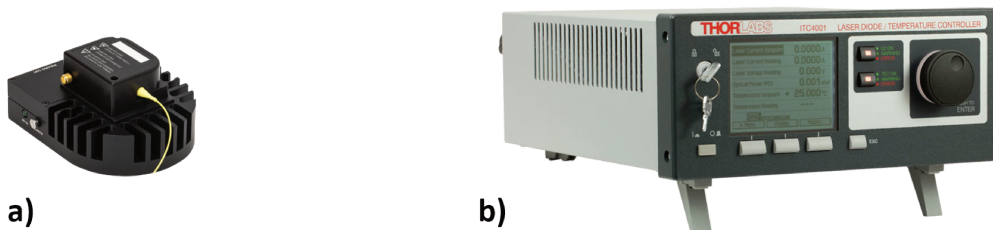


Figure 5.2 – Main components of the excitation system of in-situ MPL: a) the fiber-pigtailed laser diode; b) the programmable current/temperature controller.

It is worth mentioning that only a portion of the total laser intensity is being modulated during the measurement. It means that the laser excitation signal consists of a constant component and a modulated component. These characteristics of laser excitation intensity is determined by three parameters of the controller. The constant component (average laser intensity) is determined by the laser current set-point, while the modulation components are controlled by modulation depth parameter (determine the modulation intensity of laser) and modulation frequency parameter (determine the frequency of the modulation signal).

5.1.2 Detection system

The detection system of in-situ MPL is quite complex, because instead of detecting the intensity of steady-state PL signal as in the previous tool, the system has to measure the phase shift between the laser excitation signal and the modulated PL signal. To do so several key components are required. First of all, a high-sensitivity InGaAs photodiode (see **Figure 5.3.a**) is used to detect the modulated PL signal emitted from the sample. At this point, the optical signal is converted to an electrical one. It is worth mentioning that, in order to optimize the detection of signal, the photodiode is integrated directly into the optical acquisition system (mentioned in section below).

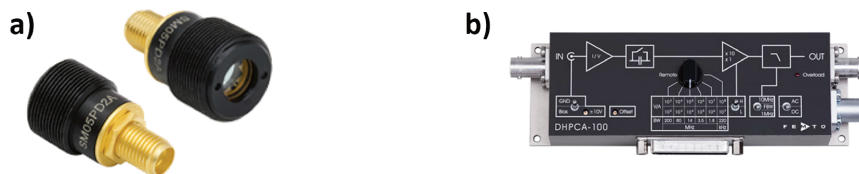


Figure 5.3 – a) High-sensitivity InGaAs photodiode; b) High-speed pre-amplifier.

After being detected, the modulated PL signal is sent to a variable-gain high-speed pre-amplifier (see **Figure 5.3.b**), so as to enhance the signal intensity. The gain of the pre-amplifier is typically set to 10^8 V/A. It is important to mention that, in a same manner as the laser excitation intensity, the modulated PL signal also consists of both a constant component and a modulated component. For this reason, the input coupling of the pre-amplifier is switched to the AC coupling mode in order to filter out the constant component and thus improve the resolution of signal measurement.



Figure 5.4 – Lock-in amplifier model SR830 (phase shift detection)

Finally, the signal is transmitted to a lock-in amplifier (*Model SR830*, see **Figure 5.4**), also known as synchronous detector, where the phase shift of the modulated PL signal is measured in comparison to the laser excitation signal (reference signal). The measured phase shift is then sent to the data treatment unit for data analysis.

5.1.3 Optical acquisition system

As the overall configuration of in-situ MPL is similar to that of in-situ PL, several attempts were conducted to perform MPL measurements with the optical setup of in-situ PL (the optical cube with a dichroic mirror, so-called old setup). It has been observed that, if the sample was excited by a low laser intensity (5.7 mW on a surface area with a diameter about 600 μ m), the phase shift of modulated PL signal could not be measured. This is due to the fact that the modulated

PL signal is not strong enough. Therefore, we increased the laser excitation intensity (24.9 mW on the same surface area). Under high excitation intensity, the phase shift of modulated PL signal can be detected, yet the signal is still quite noisy (see the black curve in **Figure 5.5**). However, the main problem of using high laser intensity for sample excitation is that the sample tends to operate in the Auger regime (high carrier concentration, $> 10^{16} \text{ cm}^{-3}$) rather than in the standard testing condition of the solar cell. That explains why the minority carrier lifetime obtained from the MPL measurements with the old optical setup ($\tau_{MPL, old\ setup} = 122 \mu\text{s}$) is considerably low, compared to the the minority carrier lifetime measured by Sinton WCT-120 ($\tau_{Sinton, @10^{15} \text{ cm}^{-3}} = 1290 \mu\text{s}$).

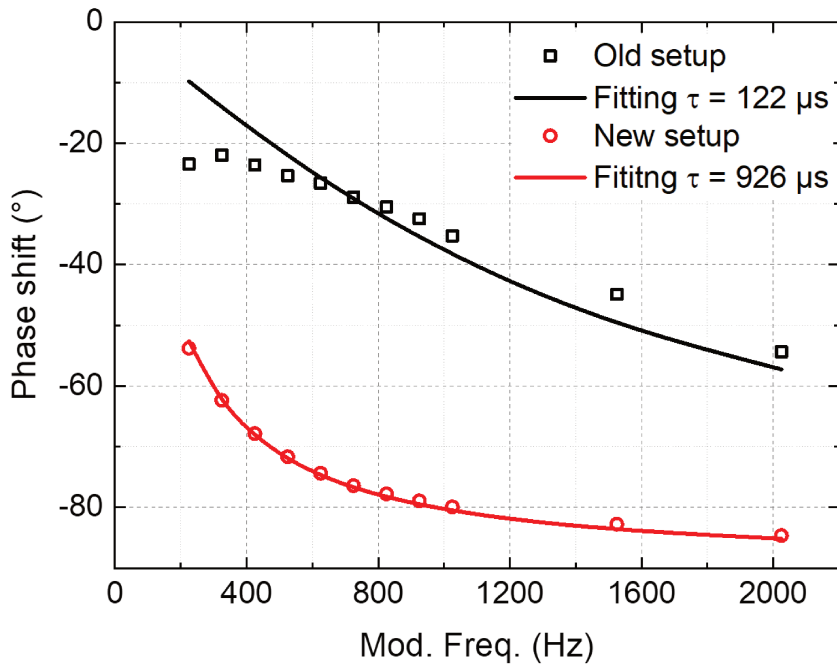


Figure 5.5 – Comparison of phase shift data measured by the in-situ MPL with different optical system: old system (optical cube with a dichroic mirror) and newly-designed system (cube with a parabolic mirror). With the old optical system, a high laser intensity is required, so the collected modulated PL signal was strong enough for the phase shift measurement. In this case, the minority carrier density in the sample is approximately $4.9 \times 10^{16} \text{ cm}^{-3}$. With the newly-designed system, the modulated PL signal could be strongly increased, while keeping the minority carrier density at low injection level ($\approx 3.5 \times 10^{14} \text{ cm}^{-3}$). Note: a c-Si wafer symmetrically passivated by a stack of $\text{Al}_2\text{O}_3/\text{a-SiN}_x\text{:H}$ was used as the sample in this measurements.

Therefore, we need to find a way to increase the detection of modulated PL signal without increasing the carrier concentration in the sample. To do so, a new system (substrate holder + optical system) needs to be particularly designed for in-situ MPL. After analyzing the old optical system, we found that the use of small optical fiber (600 μm of diameter) to collect the modulated PL signal is not efficient. In addition, it limits the excitation zone to only a small surface area (about 1 mm of diameter), leading to a high injection level in the sample during the measurement. So, we decided to fabricate a new substrate holder with an opening in the middle (see **Figure 5.6**). The diameter of the opening is approximately 10 mm, allowing the photo-excitation and collection of modulated PL signal emitted from the sample to be done on

a larger surface area compared to the old system. With this new substrate holder, the amount of modulated PL signal collected by the system can be increased, while the photo-generated carriers inside the sample is maintained at low injection level. Furthermore, the new substrate holder provides separated optical paths for sample excitation and collection of modulation PL signal. This allows the design of optical system to purely focus on signal collection.

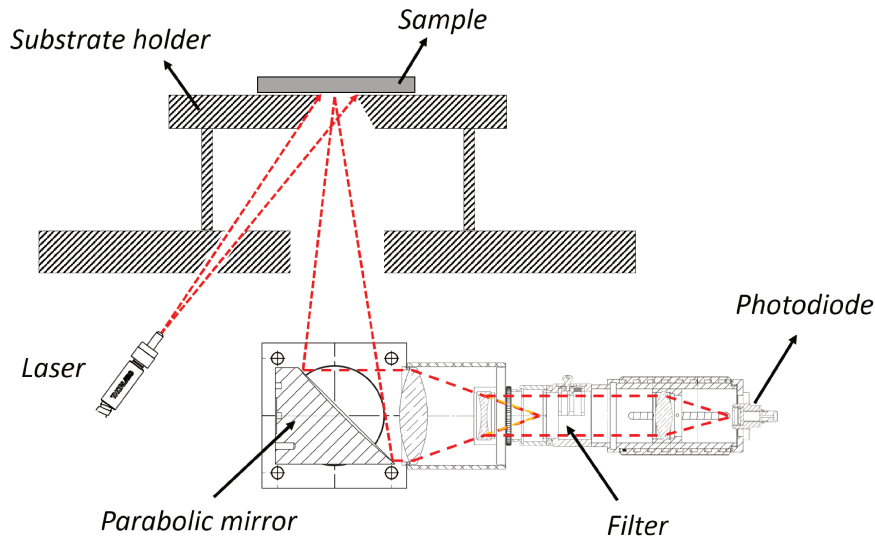


Figure 5.6 – New optical system for in-situ MPL (substrate holder + optical system). The system is particularly designed to increased the amount of modulated PL signal collected, while maintaining the carrier concentration at low injection level.

Regarding the optical system, a 90° off-axis parabolic mirror (*MPD269-M01, Thorlabs*) is used to maximize the collection of the modulated PL signal (see **Figure 5.6**). After being collected, the signal is sent through a system of lenses and focused directly on the photodiode. It is worth mentioning that a longpass filter is added between the parabolic mirror and the photodiode to filter out the laser light, reflected from the sample surface. After finalizing the new system, an MPL measurement test was performed, and the obtained result is shown in **Figure 5.5** (red curve) in comparison to the previous test. One can see that, as the carrier concentration is maintained at low injection level, the new MPL-measured carrier lifetime ($\tau_{MPL, new\ setup} = 926\ \mu s$) is now comparable to the result from Sinton WCT-120. Last but not least, the precision and accuracy of signal detection have also been significantly improved when using the new system.

5.1.4 Flexibility of system

The newly-fabricated optical system is not fixed on the reactor. It was designed in such a way that the parabolic mirror can be re-positioned in X, Y, and Z axis (assuming that XZ plan is in parallel to the sample surface, Z axis points toward the sample). This system flexibility allows user to reconfigure the size and location of surface area under investigation from one spot to another (different points on the sample surface).

For instance, when the distance between the parabolic mirror and the sample is equal to the reflected focal length of the mirror, the detection zone is a spot on the sample surface. By

moving the parabolic mirror in Z axis toward the sample, the detection zone is enlarged to a small circle with a diameter of a few millimeters (see **Figure 5.7.a**). The diameter of the detection zone (D) is given by:

$$D = 0.3092 \times d_{move} \quad (5.1)$$

where d_{move} is the distance that the mirror is moved from its focal distance toward the sample. This allows us to decide whether to characterize a small spot or a large surface area. By moving the mirror closer to the sample, the signal also become stronger (see **Figure 5.7.b**).

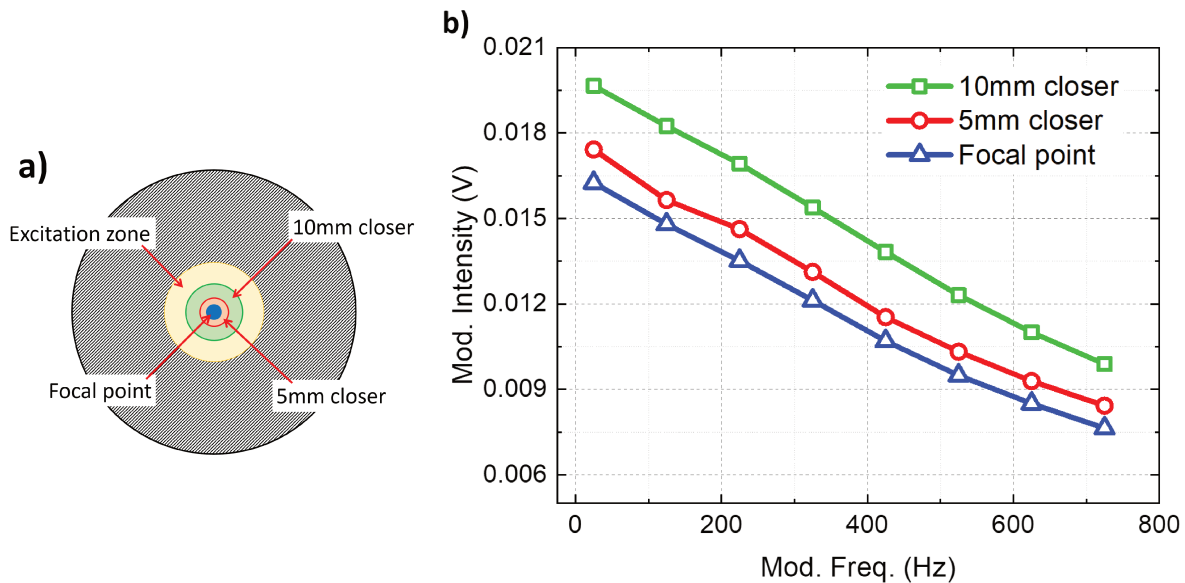


Figure 5.7 – a) Variation of size of detection zone by modifying the distance between the sample and the parabolic mirror (not to scale); b) Intensities of modulation MPL signal detected at different position when the parabolic mirror is move toward the sample.

In addition, by fixing the distance between the sample and the parabolic mirror at the reflected focal length and by moving the mirror in XZ plan (in parallel to the sample surface), the location of surface area under investigation can be changed from one spot to another. To verify the concept, an experiment was conducted to perform MPL measurements on two different samples (different minority carrier lifetime) placed side by side on the substrate holder to replicate a sample with an inhomogeneous surface (see **Figure 5.8.a**). One sample (so-called sample 1) was an as-deposited Al_2O_3 -passivated c-Si wafer, while another sample (so-called sample 2) was a c-Si wafer passivated by a stack of $\text{Al}_2\text{O}_3/\text{a-SiN}_x\text{:H}$ that had been annealed to activate the surface passivation properties. In this experiment, the focal point of the parabolic mirror was first fixed on the as-deposited Al_2O_3 -passivated sample. Then the mirror was moved sideways to have its focal point fixed on the second sample. At each position, an MPL measurement was performed and the obtained results are shown in **Figure 5.8.b**.

One can see that the minority carrier lifetimes obtained from both measurements are different. From the first measurement (sample 1), the minority carrier lifetime is approximately $258 \mu\text{s}$, and from the second measurement (sample 2), the lifetime is about $759 \mu\text{s}$. These results confirm that in-situ MPL with the new system is able to characterize different areas of the same surface. Regarding the minority carrier lifetime of the sample passivated by a stack of $\text{Al}_2\text{O}_3/\text{a-SiN}_x\text{:H}$, one may notice that the lifetime value obtained in this experiment is a bit lower than the result presented in the previous test (**Figure 5.5**, red curve). This is due to the

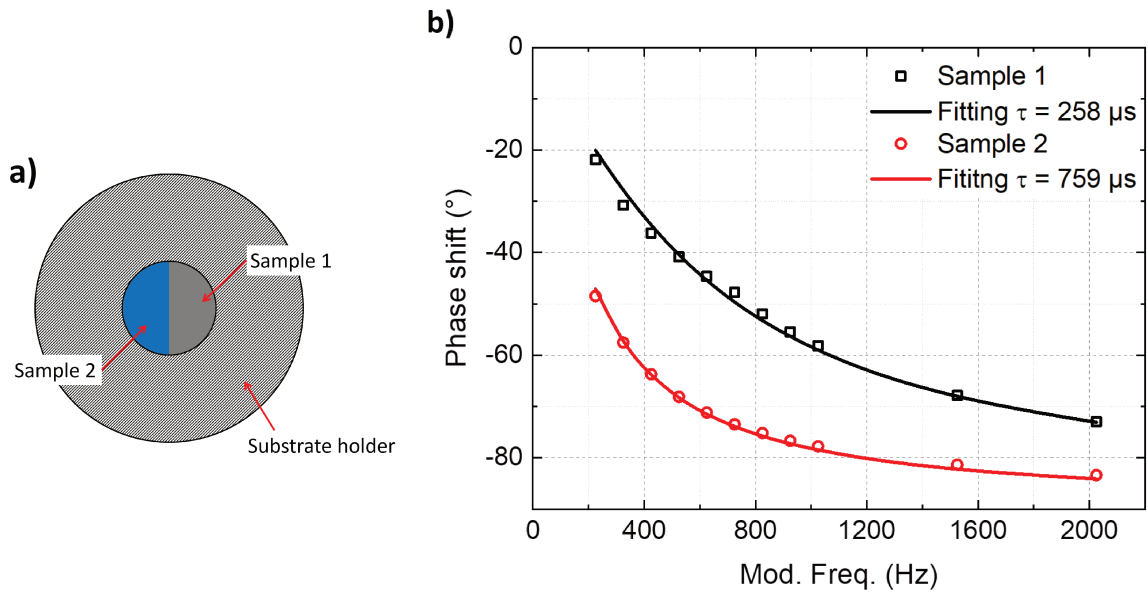


Figure 5.8 – a) Schematic of the sample arrangement (backside view of the substrate holder, not to scale) during the surface scanning test; b) Phase shift data obtained from both surfaces (replicate an inhomogeneous surface) during the test.

fact that both measurements were performed at different spots. In the previous test, the measurement was conducted in the middle of the surface, while in this experiment, the spot under investigation is near to the edge, where the surface passivation is affected by the recombination at the edge of the wafer. It is worth mentioning that only the detection spots were modified in this experiment. The excitation zone remains the same in all cases.

These two features can be very useful for the study of homogeneity of the sample surface, as they allow us to determine the size as well as the location of the surface area under investigation. Combined with an automatic positioning system, the tool will allow us to precisely scan the whole the surface.

5.2 Calibration of the system

5.2.1 Phase shift calibration

The accuracy in measuring the phase shift between the laser excitation signal and the modulated PL signal is important for determination of minority carrier lifetime of the sample. That is the reason why a new optical system was built to improve the acquisition of modulated PL signal. However, despite having a good optical signal, the measured phase shift can be polluted by the phase delay introduced by sensor signal conditioning circuit [2], including electronic filters, amplifier, etc. For this reason, the measured phase shift needs to be calibrated to remove the phase delay induced by the system. To do so, first of all, an experiment was conducted to measure the phase delay of the system. In this experiment, a Corning glass plate was placed into sample position on the substrate holder to diffuse the incident laser beam. There are two main reasons of using Corning glass in this experiment. First, it reflects laser light without inducing additional phase delay. Therefore, only the system characteristic is studied. Second,

its surface reflection is low, less than 10% at 785 nm, preventing the photodiode from overload. It should be mentioned that the longpass filter between the parabolic mirror and the photodiode was removed, so the reflected laser light can reach the detector. In a same manner as the modulated PL signal, after being detected by photodiode, the signal of reflected laser light is sent to the pre-amplifier and finally to the lock-in amplifier for detection of phase delay. This measurement was performed at different modulation frequencies as well as different laser powers, and the obtained results are shown in **Figure 5.9**.

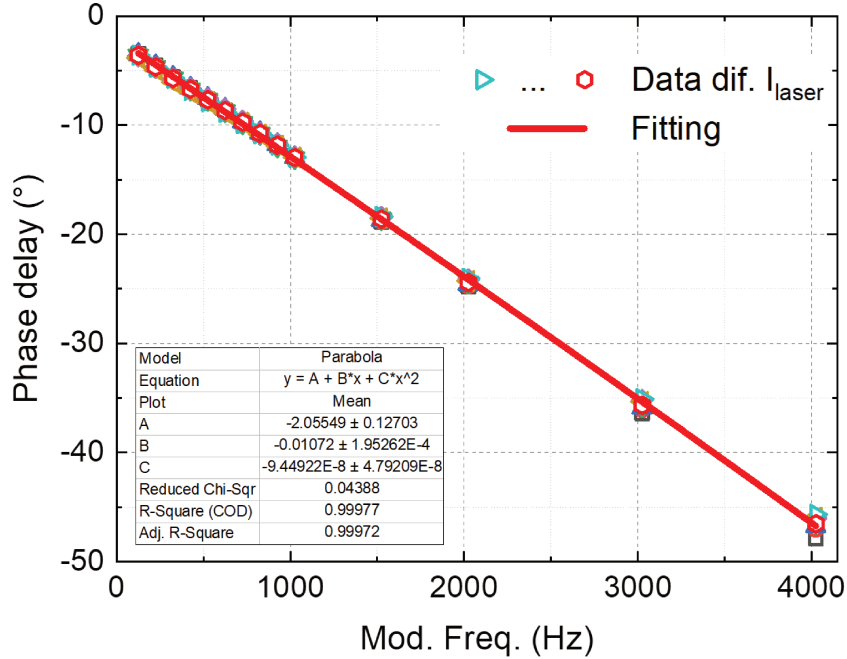


Figure 5.9 – Variation of system-induced phase delay as a function of modulation frequencies. The dots in the figure represent the phase delay measured at different laser intensities. The red line represents the fitting data, using equation ($\phi_{system} = A + B \text{Freq} + C \text{Freq}^2$).

By subtracting these system-induced phase delays from the corresponding raw phase shift data obtained during the MPL measurement, the actual phase shifts of the modulated PL signal can be obtained. This is given by:

$$\phi_{actual, \text{Freq}} = \phi_{raw, \text{Freq}} - \phi_{system, \text{Freq}} \quad (5.2)$$

Furthermore, the experimental results show that the system-induced phase delay varies as a function of modulation frequency. It decreases from -3.5° to around -46.5° when the modulation frequency is increased from 125 Hz to 4025 Hz. However, the phase delays remain roughly constant despite the variation of laser intensity. This allows us to derive an equation 5.3, defining the system-induced phase delay as a function of modulation frequency.

$$\phi_{system} = -2.0555 - 0.0107 \text{Freq} - 9.45 \times 10^{-8} \text{Freq}^2 \quad (5.3)$$

where Freq is the modulation frequency.

It is worth mentioning that different systems may induce different values of phase delay. Therefore, an experiment should be conducted to remeasure the system-induced phase delay when the setup is modified.

5.2.2 Study and optimization of system parameters

For in-situ MPL to work in an effective way, the parameters of the system, both the excitation system and the detection system, have to be set properly. Furthermore, as the tool is built for in-situ characterization of minority carrier lifetime of semiconductor materials, the system parameters are also constrained to minimize the time required for detection of each minority carrier lifetime.

Parameters of the excitation system

Regarding the excitation system, there are two main parameters to be considered: the modulation depth and the average laser intensity. In order to understand the influence of these two parameters, experiments were conducted to measure minority carrier lifetime of a sample under laser excitation at different modulation depths and different average laser intensities.

Figure 5.10 shows, as a function of modulation frequencies, the calibrated phase shifts of modulated PL signals emitted from the sample under laser excitation at different modulation depths (4% to 10%) and a constant average laser intensity (8.8 mW). It is worth mentioning that we also tried to measure the signal at 2% modulation depth, but the lock-in amplifier cannot phase lock to the reference signal. From these experimental results, one can see that the phase shift values remain roughly constant (the maximum variation is less than 2° from the mean value) at each modulation frequency despite the variation of modulation depth.

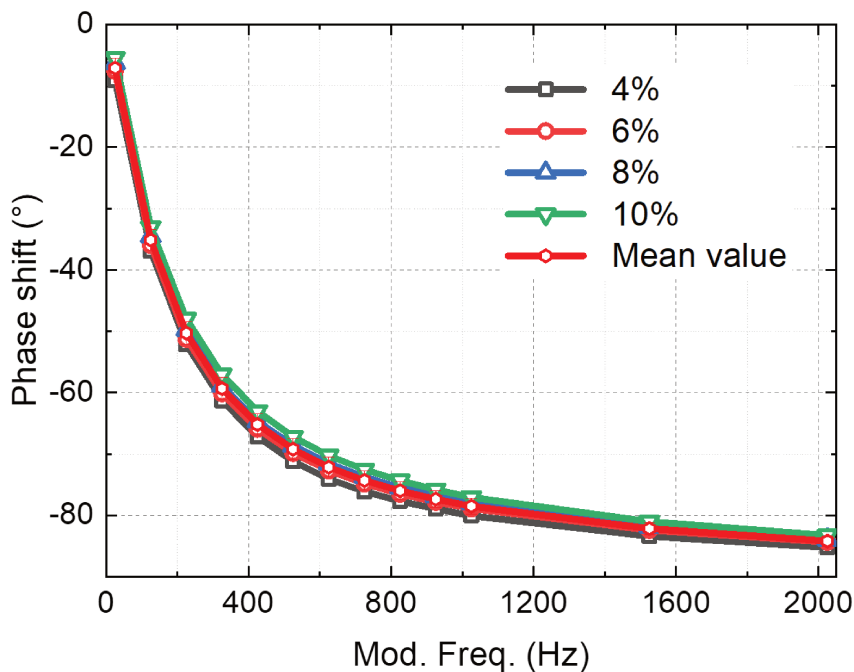


Figure 5.10 – Calibrated phase shifts of modulated PL signals emitted from sample under excitation at different modulation frequencies (constant average laser intensity $I_{laser} = 8.8 \text{ mW}$).

In another experiment, the sample was under laser excitation at a constant modulation depth (6%) and different average laser intensities (1.7, 8.7, 15.4, 22.8, and 36.9 mW). The phase shifts

of modulated PL signals emitted from the sample in each excitation conditions are shown in **Figure 5.11**. One can see that the minority carrier lifetime (calculated from the phase shifts) obtained from each measurement are different: the carrier lifetime decreases as the average excitation intensity increases. This is due to the fact that an increase of the average excitation intensity lead to an increase of carrier generation rate and so does the carrier concentration in the sample. As we already know, for c-Si wafer, the minority carrier lifetime depends strongly on the carrier concentration. Therefore, as the carrier concentration changes, the minority carrier lifetime also changes.

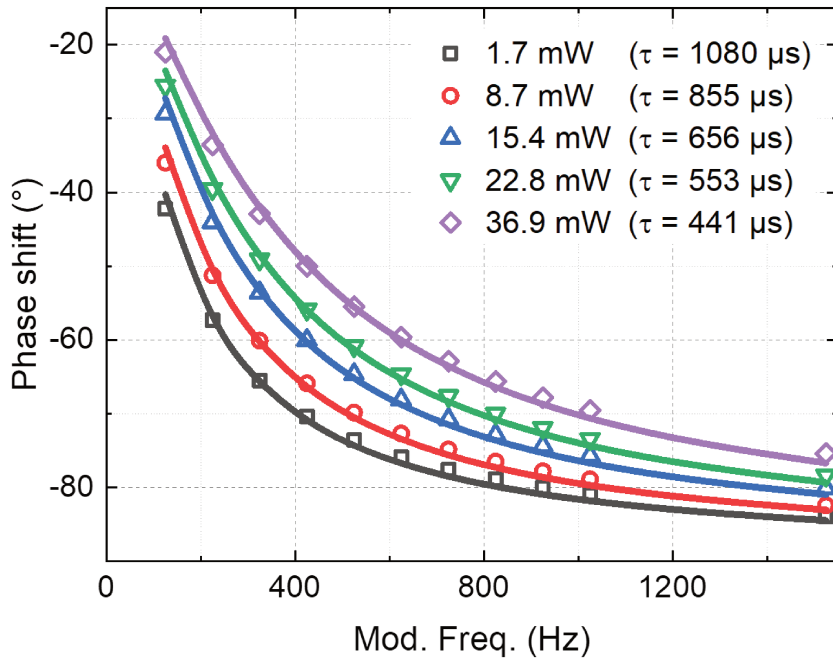


Figure 5.11 – Calibrated phase shifts of modulated PL signals emitted from sample under excitation at different average laser intensities and a constant modulation depth (6%).

Parameters of the detection system

Regarding the detection system, the parameters are set to detect the phase shifts of modulated PL signal as accurate as possible. For instance, the gain of the pre-amplifier is set to 10^8 V/A (max 10^{11} V/A) to amplify the signal (strong enough for the analysis). Furthermore, as we are interested more on the modulation part of the signal, the input coupling of the amplifier is set to AC to remove the constant part and improve the signal resolution. In addition, the time constant (TC) of the internal lowpass filter of the lock-in amplifier is set to 1 second, while the attenuation slopes is set to 24 dB/octave (best possible of our lock-in amplifier) to remove the noise. The integration time factor (ITF), which defines the waiting time ($t_{waiting} = TC \times ITF$) before acquiring a signal, is set to 10. That allows the lock-in amplifier to have enough time to detect the phase shift. Last but not least, the reference input is set to an external source (laser excitation signal).

All these parameters allow the detection system to operate perfectly. However, the time needed to detect one minority carrier lifetime is approximately 31.6 seconds, which should be

minimized if possible. Among many parameters, the time constant and the integration time factor are the two main parameters, determining the characterization time. It should be mentioned that the time constant is the time response of the lowpass filter, and it defines the filter cut-off frequency $f_{cut-off}$ [3], which is given by:

$$f_{cut-off} = \frac{1}{2\pi\tau} \quad (5.4)$$

where τ represents the time constant. So the bigger the time constant is the smaller the cut-off frequency. In other words, the longer the time response of the filter is the better (less noise) the signal. The integration time factor, as mentioned above, defines the waiting time before acquiring a signal.

In order to optimize these two parameters, an experiment was conducted to measure the phase shift of modulated PL signal at different combinations of time constant and integration time factor. Here, the phase shift obtained from the measurement at 1 second of time constant and 10 of integration time factor is considered as the reference. The time constant is varied from 1 s to 10 ms, and the integration time factor is varied from 10 to 2. For each combination, the phase shift of the signal is measured and compared the reference. If the difference between the two phase shift values is less than 1° (at each modulation frequency), the combination is validated. Otherwise, it is rejected (see **Figure 5.12**). A summary of the experimental results is shown in **table 5.1**. The validated combinations are denoted by YES, and the rejected combinations are denoted by NO.

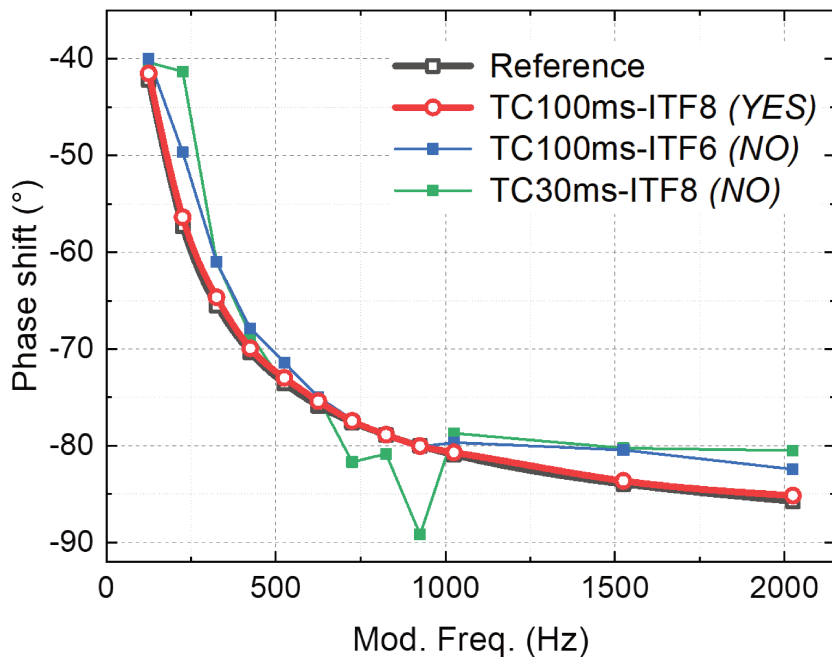


Figure 5.12 – Calibrated phase shifts of modulated PL signals emitted from sample detected with different parameters (TC, ITF) of the lock-in amplifier. The parameters of the excitation system are 1.7 mW and 6% (the experiments were also conducted at other laser excitation intensities).

From these experimental results, one can see that the time constant of the lock-in amplifier can be reduced from 1 s to 100 ms, while the integration time factor can be reduced from 10

Table 5.1 – Summary of experimental results on the optimization of parameters of detection system. YES means that the phase value measured at this combination is the same as the reference signal. NO means otherwise.

| ITF \ TC | 10ms | 30ms | 100ms | 300ms | 1s |
|----------|------|------|-------|-------|-----|
| 2 | NO | NO | NO | NO | NO |
| 4 | NO | NO | NO | NO | NO |
| 6 | NO | NO | NO | NO | YES |
| 8 | NO | NO | YES | YES | YES |
| 10 | NO | NO | YES | YES | YES |

to 8. With these new parameters, the system requires approximately 3.7 seconds to detect one minority carrier lifetime, which is about 8.5 times faster than the time required with previous reference parameters.

5.3 Determination of minority carrier lifetime at a specific carrier density

For crystalline silicon, the minority carrier lifetime varies significantly, depending on the concentration of charge carriers. Therefore, it is very common to find in literature the minority carrier lifetime of a passivated c-Si sample mentioned at a specific minority carrier density (e.g. 10^{15}cm^{-3}) [4–6]. Regarding the MPL characterization technique, to the best of our knowledge, it has been developed and is able to measure minority carrier lifetime of c-Si samples, but not yet the minority carrier lifetime of the sample at a defined minority carrier density. This missing feature strongly limits the application of the MPL technique because the comparison between two different samples or one sample at different points in the fabrication processes can be hardly done (It is very difficult to measure minority carrier lifetimes of the samples at the same specific minority carrier density).

To overcome this hurdle, a characterization method (so-called **LiTe**) was developed to determine the minority carrier lifetime of the sample at a defined minority carrier density from a series of several MPL measurements at different average excitation intensities I_i ($i \in [1, n]$ that $n > 1$). The detailed work flow of this characterization method is illustrated in **Figure 5.13**, and it proceeds as following:

- **Step 1:** illuminate the sample with an average excitation intensity I_i . From this average excitation intensity, the average carrier generation rate in the sample can be estimated by presuming that one photon leads to a generation of one electron-hole pair.
- **Step 2:** measure the phase shift between the laser excitation signal and the modulated PL signal. It is worth mentioning that at each average excitation intensity I_i , the laser is modulated at different modulation frequencies ω_j ($j \in [1, m]$ that $m > 1$). The phase shift corresponding to each modulation frequency is measured in this step.

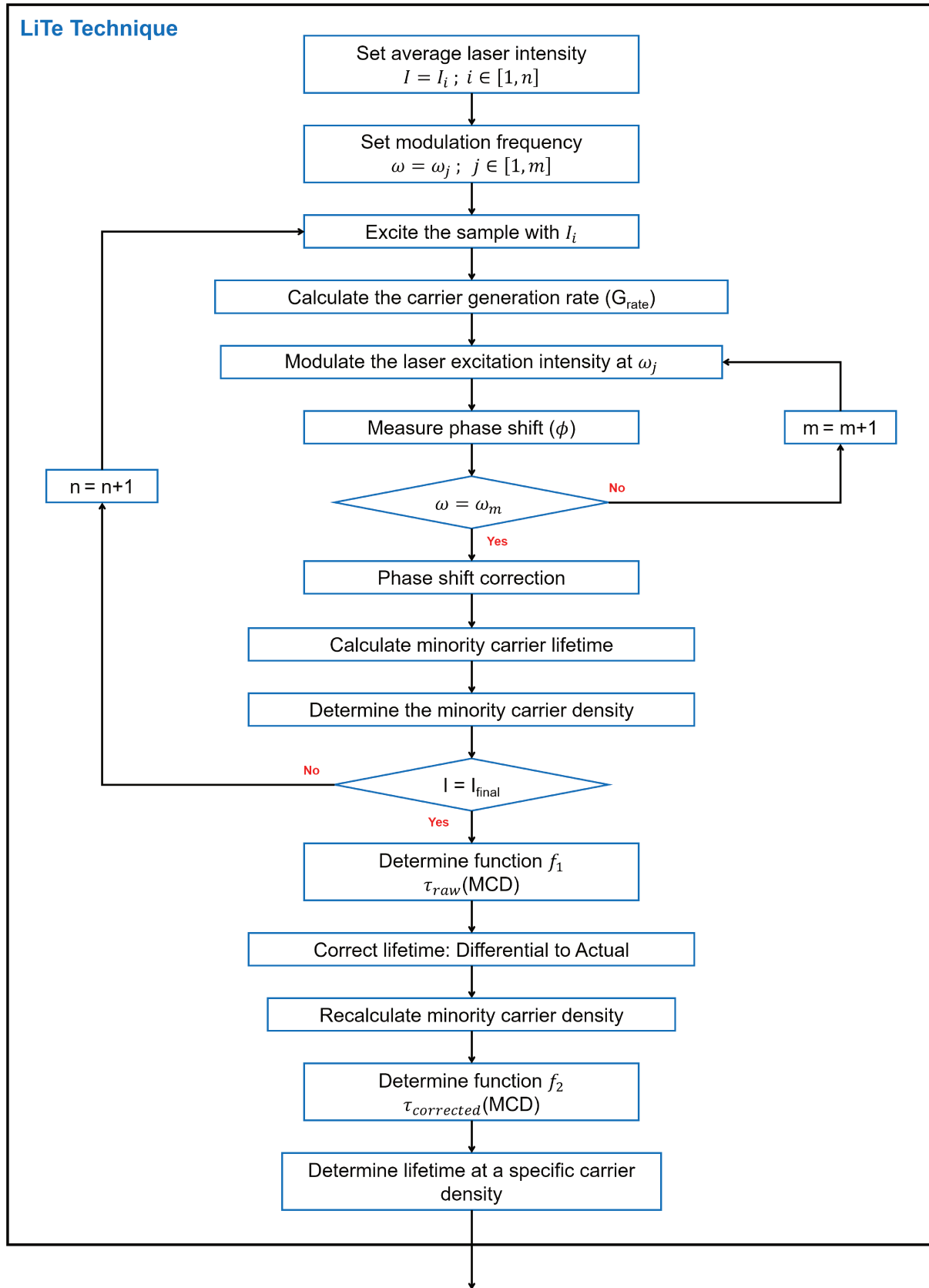


Figure 5.13 – Work flow during the in-situ MPL measurement of minority carrier lifetime of the sample at a specific minority carrier density.

- **Step 3:** calculate the minority carrier lifetime of the sample under illumination I_i . From the modulation frequencies and the corresponding phase shifts measured in step 2, the minority carrier lifetime can be obtained by fitting the equation $\phi = -\arctan(\omega\tau)$. It is important to note that the phase shifts (raw data) obtained in step 2 have to be calibrated prior to the carrier lifetime calculation.
- **Step 4:** determine the minority carrier density under illumination I_i . Thanks to the carrier generation rate from step 1 and the minority carrier lifetime from step 3, the minority carrier density is given by $\Delta n_i = G_i \times \tau_i$.
- **Step 5:** modify the average excitation intensity and repeat step 1 to step 4. As the carrier generation rate is directly proportional to the laser excitation intensity, this will allow the measurement of the minority carrier lifetime of the sample at different minority carrier density value (see **Figure 5.15**, unfilled black squares).
- **Step 6:** determine the actual minority carrier lifetime from the differential carrier lifetime. Knowing that the as-measured carrier lifetimes given by the MPL technique are the differential ones, the lifetime calibration method that will be described in section 5.5 is used to correct the as-measured carrier lifetime data (see **Figure 5.15**, unfilled red circles).
- **Step 7:** re-determine the minority carrier density. From the corrected minority carrier lifetime data in step 6, the minority carrier density in the sample is re-determined $\Delta n_{i, corrected} = G_i \times \tau_{i, corrected}$.
- **Step 8:** determine the minority carrier lifetime of the sample at a defined carrier density. From the corrected minority lifetimes in step 6 and the corresponding carrier densities in step 7, the minority carrier lifetime at a defined carrier density can be determined by interpolation/extrapolation.

By implementing the LiTe technique, a minority carrier lifetime at a specific minority carrier density can be determined. The in-situ measurement of the specific minority carrier lifetime of c-Si samples during various processes can be achieved by repeating over time this characterization method from step 1 to step 8.

5.4 Development of graphic user interface

In the previous section, we have seen that the variation of average excitation intensity I_i and the variation of modulation frequency ω_j are required for characterization of minority carrier lifetime at a specific minority carrier density. In addition, the LiTe technique has to be repeated over time during the in-situ study of materials. This can be cumbersome, if the system has to be operated manually. Therefore, a LabView-based graphic user interface (see **Figure 5.14**) was built to control all the parameters of the system. This allows the measurements to be conducted automatically during the processes. Furthermore, a time delay can be added between each LiTe cycle if required.

This graphic user interface is divided into three main sections, which are used to control all the parameters of the excitation system, the detection system, and the in-situ measurement process. In the first section (blue box), the interface allows the user to control the excitation system. One can configure the average laser intensity, the shape of modulation signal (sinusoid,

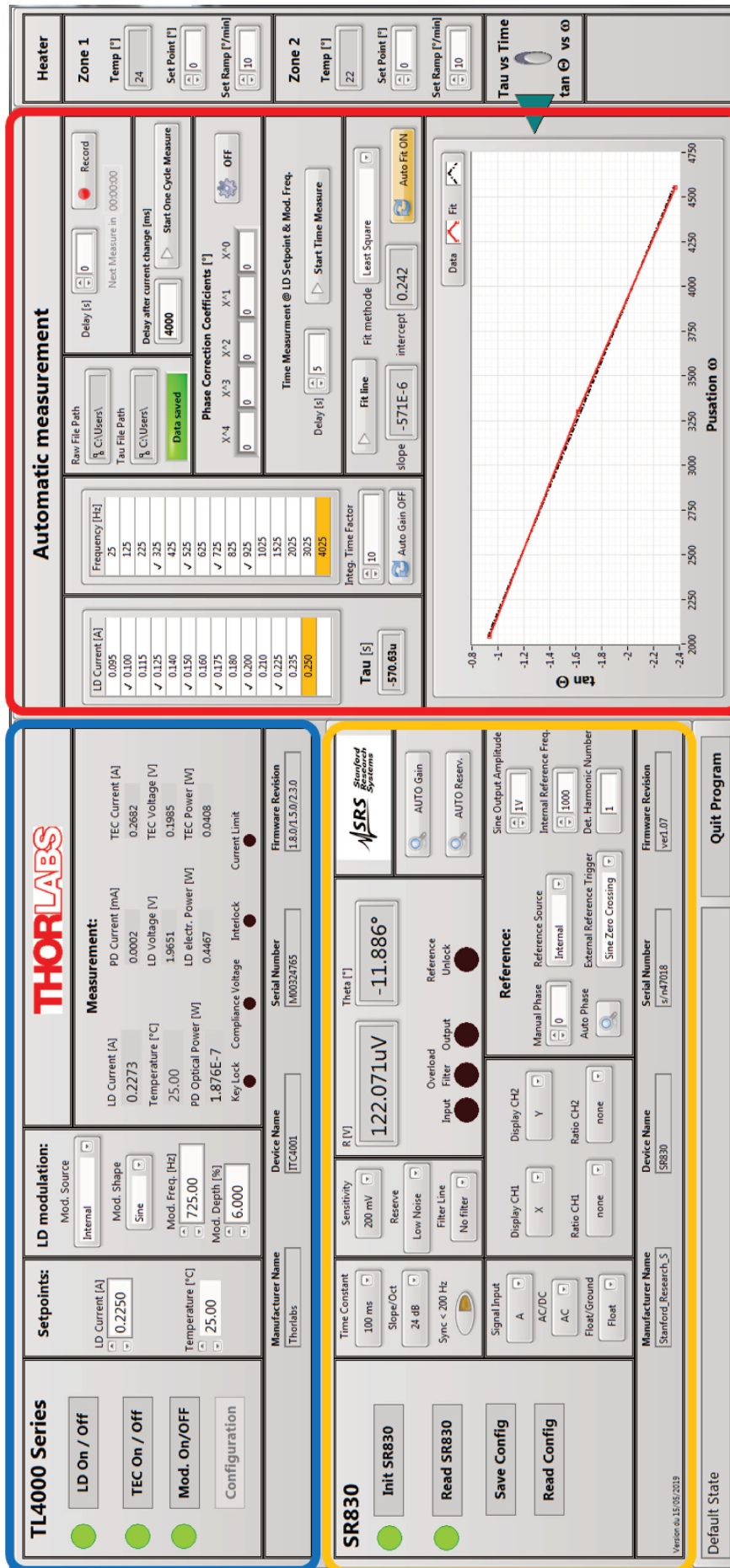


Figure 5.14 – LabView-based graphic user interface, developed for automatic control of the in-situ MPL system. The interface controls all the parameters of the excitation system (blue box), the detection system (yellow box), the in-situ measurement process (red box), and the temperature of substrate holder of PLASMAT reactor.

triangle, or square), the modulation frequency, the modulation depth, etc. The second section (yellow box) allows us to control the parameters of detection system, including the time constant¹, the attenuation slope, the sensitivity range, the input coupling, etc. Furthermore, one can also modify the reference signal for the measurement of phase shift of modulated PL signal. Last but not least, the third section deals with the in-situ measurement process (automation of the system). It allows the user to configure the main parameters of the LiTe technique, a range of modulation frequencies and a range of laser diode currents (average laser intensities) that will be used during the in-situ measurements. Also one can set a time delay, commanding the detection system to pause a few seconds after the modification of laser diode current. This allows the laser optical output to be stable before starting to detect the phase shift of the signal. Last but not least, one can set the coefficients of a polynomial equation, which is corresponding to the system-induced phase delay, for phase shift calibration. It is worth mentioning that another section of this graphic user interface allows the user to control the heating elements of the PLASMAT reactor and record the substrate temperature throughout the measurement.

After the development of this graphic user interface, the system can be controlled in a much efficient way, particularly the in-situ measurement process. In-situ MPL is now fully operational, and it has been used extensively to study the surface passivation of c-Si wafers during various fabrication processes such as deposition of the passivation layer, thermal treatment (annealing), and deposition of the anti-reflection coating.

5.5 Carrier lifetime correction

As mentioned in section 3.4.2, the minority carrier lifetime provided by modulated photoluminescence technique, so-called differential carrier lifetime, has distinct characteristics compared to the actual carrier lifetime provided by steady-state measurement techniques (e.g. steady-state photoluminescence decay, etc.) [7–9]. Therefore, in the interest of comparison with other standard characterization tools (e.g. Sinton WCT-120, etc.), the minority carrier lifetime provided by in-situ MPL should be calibrated.

According to a publication from Giesecke et al. in 2013 [10], the actual carrier lifetime can be correctly determined from a combination of at least two differential carrier lifetimes, measured at adjacent generation rates. The actual carrier lifetime (τ_i) is given by:

$$\tau_i(G_i) = \tau_{m,i}(G_i) \left(1 - G_i \frac{d\tau}{d\Delta n} \Big|_{\Delta n_i} \right) \quad (5.5)$$

Where $\tau_{m,i}$ is the differential carrier lifetime, G_i is the carrier generation rate, and $d\tau/d\Delta n|_{\Delta n_i}$ is the derivative of carrier lifetime with respect to minority carrier density. The value of $\tau_{m,i}$ and G_i are directly measurable, while the value of $d\tau/d\Delta n|_{\Delta n_i}$ is given by the two differential carrier lifetimes that have been measured at adjacent generation rates.

Presuming a local linearity of carrier lifetime at the generation rate of interest (i.e. $d\tau/d\Delta n|_{\Delta n_i}$ is locally constant), the two adjacent differential lifetime can be expressed:

$$\tau_{m_2}(\Delta n) \approx \tau_{m_1} + (\Delta n_2 - \Delta n_1) \frac{d\tau}{d\Delta n} \Big|_{\Delta n_1} \quad (5.6)$$

¹Time constant is directly related to the cut-off frequency of the internal low-pass filter of the lock-in amplifier.

where τ_{m_1} and τ_{m_2} are carrier lifetimes measured at G_1 and G_2 respectively, Δn_1 and Δn_2 are the minority carrier density, given by $\Delta n_i = \tau_{m_i} \times G_i$.

From the equation 5.5 and equation 5.6, the actual carrier lifetime (τ_i) can be determined from two differential carrier lifetimes ($\tau_{m,i}$). To verify this correction method, an experiment was conducted to compare the minority carrier lifetime of a passivated c-Si wafer provided by in-situ MPL (before and after the correction) with the minority carrier lifetime provided by the standard tool "Sinton WCT-120". In this experiment, in-situ MPL employs different laser excitation intensity to measure carrier lifetime at different injection levels. Then the correction method is applied, to determine the actual carrier lifetime. **Figure 5.15** compares the results obtained from both characterization tool. The black square filled is the actual carrier lifetime provided by Sinton WCT-120. The black square unfilled and the red circle unfilled are the minority carrier lifetime provided by in-situ MPL before and after applying the correction respectively.

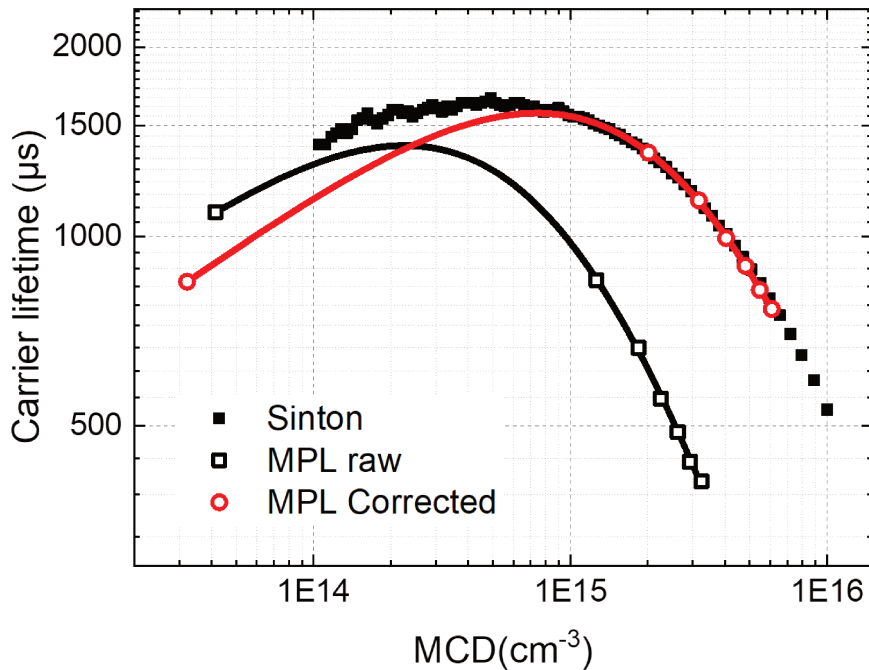


Figure 5.15 – Minority carrier lifetime as a function of minority carrier density (MCD). The black squares (filled) is the carrier lifetime profile provided by Sinton WCT-120. The black squares (unfilled) and the red circles (unfilled) are the carrier lifetime profile obtained from MPL measurement before and after applying the lifetime correction respectively.

From these experimental results, one can see that the as-measured carrier lifetime provided by in-situ MPL is much lower than the actual carrier lifetime provided by Sinton WCT-120. Interestingly, after applying the correction, the obtained carrier lifetime is comparable to the one from Sinton. It can be observed that the corrected lifetime is equal to the actual lifetime at high injection level, but it is slightly lower than the actual lifetime at low injection level. This feature, the difference at low injection level between minority carrier lifetimes provided by photoluminescence techniques and those provided by quasi-steady state photoconductance decay, has also been reported in the Sinton WCT-120PL product note [11] as well as by other researchers [12]. Currently, this deviation is not well understood yet. A possible explanation

of this feature is the effect of trapping and detrapping of generated charge carriers at the defect sites. At low injection level, the trapping and detrapping of charge carriers from defects can strongly influence the photoconductance of the sample and thus the measured minority carrier lifetime. However, the photoluminescence techniques are directly based on the radiative recombination of charge carriers, and therefore the trapping/detrapping of charge carriers from defects have less influence on the measurement results [13].

It is important to note that all minority carrier lifetimes presented in the following sections were corrected from differential lifetime to actual lifetime and determined at a minority carrier density 10^{15} cm^{-3} , except otherwise mentioned.

5.6 Carrier lifetime vs Temperature

In the photovoltaic community, minority carrier lifetime has been used extensively to represent the properties of c-Si wafers, in particular the electrical properties of the wafer surface. For a high quality c-Si wafer, the variation of minority carrier lifetime is commonly interpreted as the improvement or degradation of surface passivation. However, it has been observed that the modification of materials is not the only parameter, affecting minority carrier lifetime. For instance, different minority carrier concentrations also lead to different values of minority carrier lifetime, which is the reason why a specific carrier concentration is chosen as a reference point when two minority carrier lifetimes are compared. Also, it has been reported that minority carrier lifetime in c-Si wafers varies as a function of temperature [14–17]. This has been tentatively explained by the change of thermal velocity of free carriers [18] as well as the variation of capture cross section for electrons and holes [19]. This temperature-dependent feature of minority carrier lifetime imposes a great challenge for interpretation of minority carrier lifetime profile, observed during the processes (in particular the processes that involve modification of temperature in time). For example, the variation of minority carrier lifetime observed during the experiments may result from the evolution of materials (bulk material and surface) or may result from the variation of process temperature.

In order to deal with this complexity, an experiment was conducted to study the variation of minority carrier lifetime of a c-Si sample as a function of temperature. In this experiment, a high quality c-Si wafer (4 inches, n-type, $\langle 100 \rangle$, FZ, resistivity of about $1 \Omega \cdot \text{cm}$) symmetrically passivated by a stack of $\text{SiO}_x/\text{pc-Si}$ was used. Before the experiment, the minority carrier lifetime of the sample was checked by Sinton WCT-120. Of the full wafer sample, the minority carrier lifetime is approximately 3.2 ms. However, after cleaving, the minority carrier lifetime of some samples ($25 \times 25 \text{ mm}$) decreased to approximately 1 ms. It is worth mentioning that, provided by Fraunhofer ISE, the surface passivation properties provided by the $\text{SiO}_x/\text{pc-Si}$ stack had been activated in a tube furnace process with plateau temperatures in the range of $600^\circ\text{C} < T_{\text{anneal}} < 1000^\circ\text{C}$. During the experiment, the sample was placed into the PLAS-MAT reactor, filled with a mixture of argon and hydrogen to improve the thermal conductivity. The substrate temperature was quickly brought up to 300°C and then slowly brought back to room temperature. The minority carrier lifetime of the sample was measured by in-situ MPL throughout the entire process.

Figure 5.16 shows the evolution of minority carrier lifetime and the temperature profile, obtained during the experiment. One can see that, as the substrate temperature increases from room temperature to 300°C , the minority carrier lifetime of the sample increases from approx-

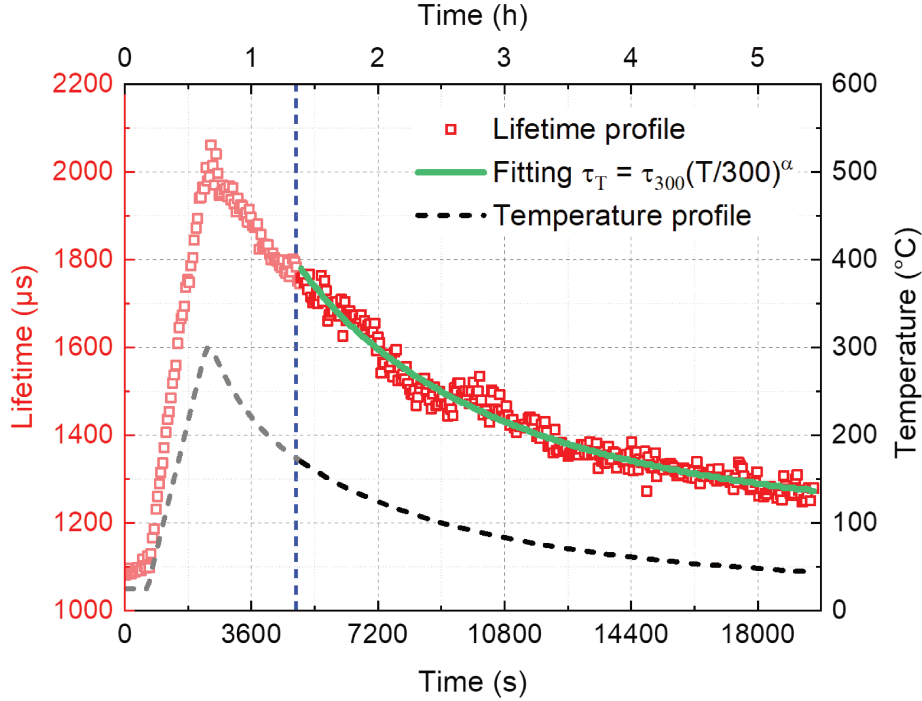


Figure 5.16 – Evolution of minority carrier lifetime, as a function of temperature, of a c-Si wafer passivated by a stack of $\text{SiO}_x/\text{pc-Si}$. Prior to the experiment, the surface passivation properties of the stack had already been activated by annealing ($600^\circ\text{C} < T_{\text{anneal}} < 1000^\circ\text{C}$). It is worth mentioning that these minority carrier lifetimes were corrected and determined at a minority carrier density of 10^{15} cm^{-3} .

imately 1.1 ms to almost 2.1 ms. Then when the substrate was cooled down, the minority carrier lifetime of the sample also decreased. The same behavior has also been reported by other researchers [14, 15]. It should be mentioned that only the cooling section ($T < 170^\circ\text{C}$, after the blue dashed line) is investigated because the variation of temperature in this section was slow, allowing a precise measurement of temperature and carrier lifetime and thus reducing the measurement error.

As mentioned previously, prior to the experiment, the sample had been through an activation process in a tube furnace at high temperature ($600^\circ\text{C} < T_{\text{anneal}} < 1000^\circ\text{C}$). This assures that the sample is stable during our experiment at 300°C . In other words, the variation of minority carrier lifetime observed throughout the experiment is purely caused by the variation of temperature. Based on these experimental data, an empirical equation for the variation of minority carrier lifetime as a function of temperature was derived. It is given by:

$$\tau_T = \tau_{300K} \left(\frac{T}{300} \right)^\alpha \quad (5.7)$$

Where τ_T is the minority carrier lifetime of the sample at temperature $T(K)$, τ_{300K} is the minority carrier lifetime of the sample at $300K$, and α is a constant $\alpha = 1.0026$.

From equation 5.7, the minority carrier lifetimes measured at various temperatures T can be converted to the carrier lifetimes at one temperature ($300K$). This allows the comparison between minority carrier lifetimes measured at different temperatures during the processes to

be done in a more appropriate way. As an example, **Figure 5.17** illustrates a comparison of minority carrier lifetime profiles before and after applying the temperature correction.

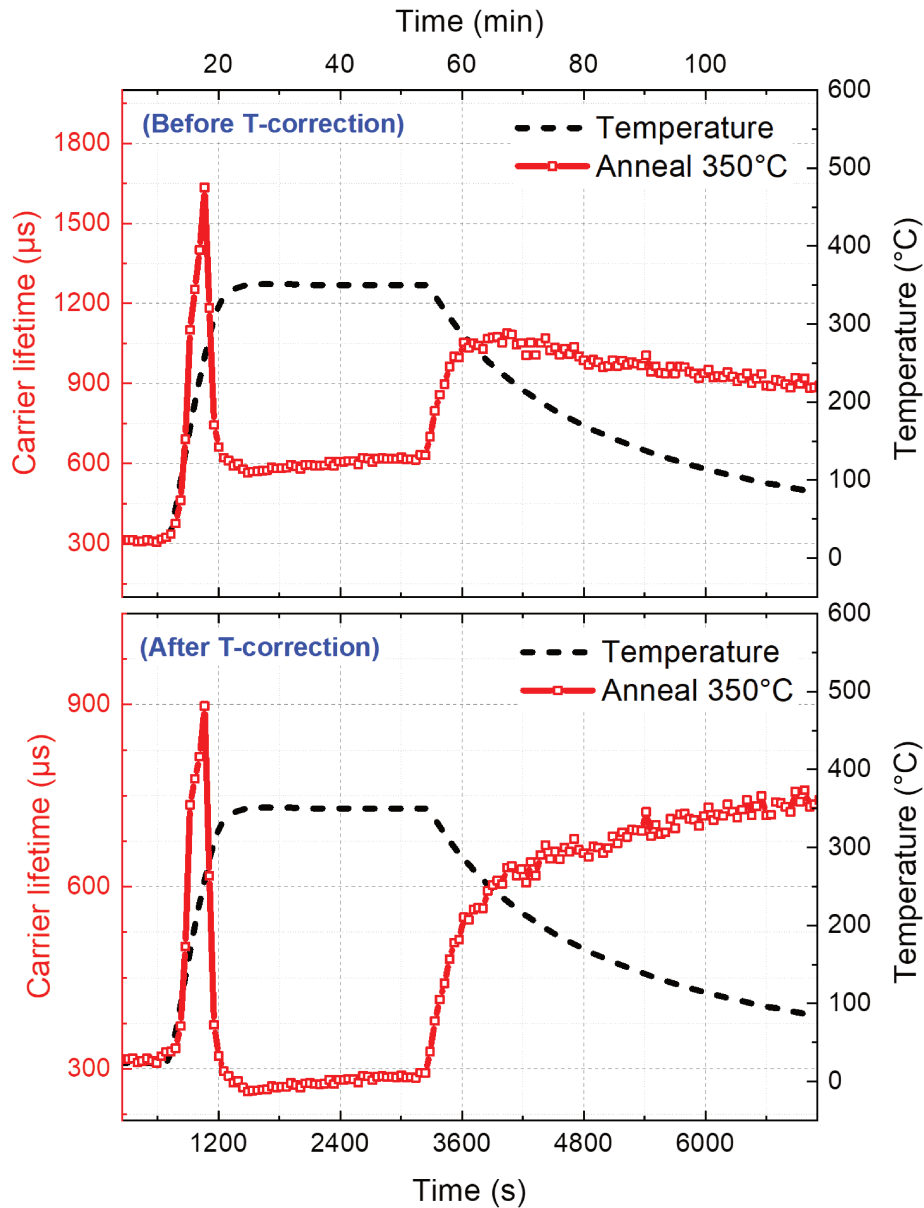


Figure 5.17 – Comparison of minority carrier lifetime profiles before and after applying the temperature correction. The data is obtained during annealing of a c-Si wafer, passivated by Al_2O_3 , at 350°C for 30 minutes.

It should be mentioned that the minority carrier lifetimes presented in the following sections have been converted to the carrier lifetime at room temperature, except otherwise mentioned.

5.7 In-situ study of surface passivation during deposition of passivation layers

In crystalline silicon solar cells, surface passivation layers play a major role in neutralizing the surface dangling bonds, and thus diminishing the surface recombination of photo-generated carriers. The surface passivation properties of each passivation layer are strongly influenced by the process parameters used during deposition of the layer. For the first time after the development, in-situ MPL was used to measure minority carrier lifetime of a c-Si wafer (one-side passivated) during deposition of the second passivation layer.

5.7.1 Sample & experimental set-up

In this experiment, high quality double-side polished 4 inches n-type $\langle 100 \rangle$ FZ c-Si wafers with a resistivity of approximately $3 \Omega \cdot cm$ and a thickness of about $280 \mu m$ were used as substrate. In the preparation of the first passivation layer, the wafers were subjected to a 30-second wet chemical cleaning in a 5% hydrofluoric acid solution in order to remove the native oxide layer. Then they were quickly transferred to a PECVD reactor (ARCAM) for deposition of the first passivation layer, a thin a-Si:H film ($\approx 20 nm$). This film was grown at $200^\circ C$ with a in-house developed standard recipe to ensure good surface passivation properties. After having one surface passivated, the wafers were cleaved into several $25 \times 25 mm$ samples.

After the first passivation layer was prepared, the sample ($25 \times 25 mm$) was ready for deposition of second passivation layer in the PLASMAT reactor. The plasma conditions used for deposition of this second passivation layer are shown in **table 5.2**. It is important to mention that, as the sample had been exposed to air for more than one hour before the second deposition, the sample (one-side passivated) was re-dipped into the 5% hydrofluoric acid solution in order to remove the native oxide layer once again. As soon as the sample was loaded in the reactor, the in-situ characterization of minority carrier lifetime of the sample was initiated. In-situ MPL kept measuring minority carrier lifetime of the sample throughout the process until the plasma was turned off.

Table 5.2 – Plasma conditions used for deposition of a-Si:H film (second passivation layer) in the PLASMAT reactor.

| Process parameters | Value |
|---|-----------|
| Pressure | 1 Torr |
| RF power | 2 W |
| H ₂ /SiH ₄ flow rates | 75/5 sccm |
| Substrate temperature | 200°C |
| Inter-electrode distance | 23.5 mm |
| RF voltage (V_{RF}) | 84 V |
| Self-bias voltage (V_{bias}) | - 19 V |
| Plasma potential $V_p = \frac{1}{2}(V_{RF} + V_{bias})$ | 32.5 V |

5.7.2 Results & Discussion

Experimental Results

Figure 5.18 shows the evolution of minority carrier lifetime of the c-Si sample during deposition of a-Si:H film, the second passivation layer. It should be mentioned that, by using equation 5.7, the minority carrier lifetimes measured at different temperatures during the deposition process were calibrated to minority carrier lifetimes at room temperature. It can be observed that minority carrier lifetime of the sample increases with the rise of substrate temperature, until reaching a peak at around 175°C. As the substrate temperature further increases to 200°C, the minority carrier lifetime of the sample falls back to almost its initial value. Another quick decrease of the minority carrier lifetime can be observed when the plasma was ignited (②). Finally, as the a-Si:H film started to grow, an increase of the minority carrier lifetime occurred, and it continued to rise until the plasma was turned off (③).

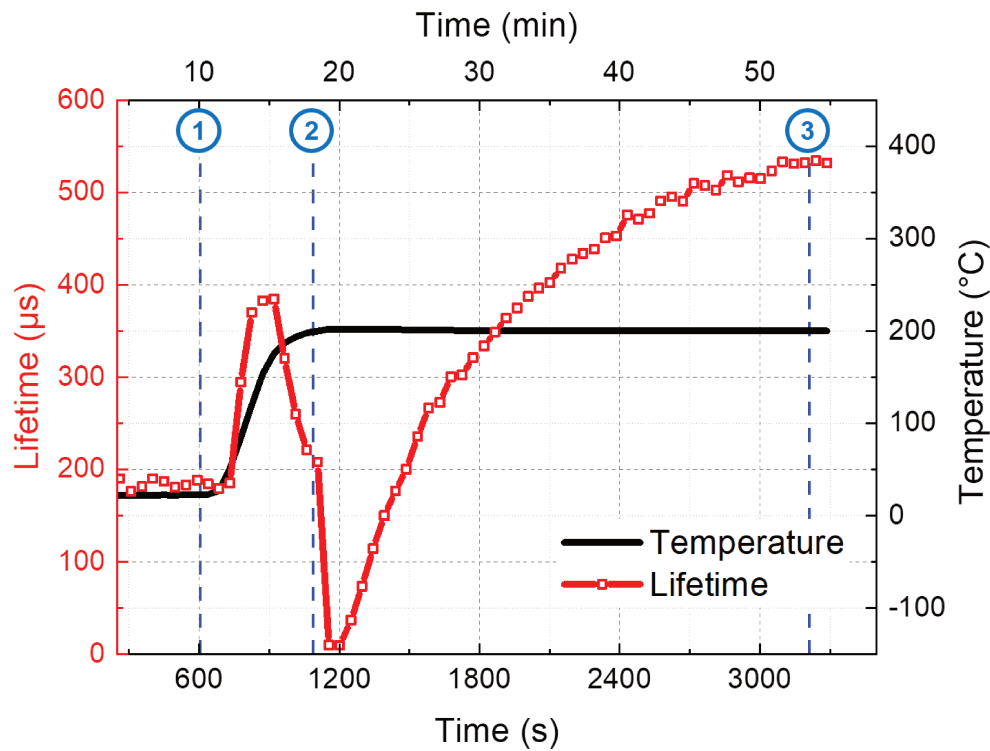


Figure 5.18 – Evolution of minority carrier lifetime of the sample (one surface passivated) during the deposition of an a-Si:H passivation layer (on the second surface) by a PECVD process. Each blue dash line marks the transition from one process step to another: ① the substrate temperature started to increase, ② the PECVD plasma for a-Si:H deposition was ignited, ③ the plasma was turned off. It should be mentioned that the thickness of the newly-deposited a-Si:H passivation layer after is about 85 nm.

Sample properties & influences of processes

Before going into the discussion about the mechanisms behind the evolution of minority carrier lifetime of the sample during the experiment, it is very important to have a good understanding

of the sample properties as well as the possible influences of the processes. The sample used in this experiment is a c-Si wafer, one-side passivated by a-Si:H layer. As the sample was dipped into a 5% HF solution for about 30 seconds, the native oxide layer on the unpassivated surface was probably removed, and the sample was left with a H-terminated surface [20–22]. It is also possible that some surface silicon atoms have one or two unsaturated dangling bonds (see **Figure 5.19**).

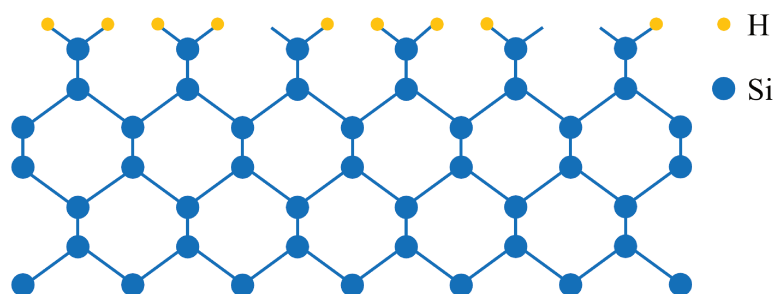


Figure 5.19 – Schematic of the $\langle 100 \rangle$ c-Si surface after wet-chemical cleaning in a HF solution.

Regarding the processes, there are two main factors to be considered: the substrate temperature and the plasma process. In this experiment, the substrate temperature is about 200°C. This temperature is high enough to induce diffusion of atomic hydrogen to passivation the remaining dangling bonds at the interface. Furthermore, in general, the increase of temperature induces the molecular vibration, which may lead to the formation or breaking of chemical bonds depending on the materials. For the plasma process, various things can affect the sample. As mentioned in the previous chapter, plasma emission (VUV light) can induce surface passivation degradation by breaking the chemical bonds in the passivation layer as well as at the interface. The plasma conditions used in this experiment also induce growth of a-Si:H film.

Discussion

Concerning the details of minority carrier lifetime profile shown in **Figure 5.18**, one may notice that the initial minority carrier lifetime of the sample ($\tau_{int} \approx 180 \mu s$) is quite high for a c-Si wafer with only one surface passivated. However, as the sample was dipped for 30 seconds into a 5% HF solution before loading into the reactor, the unpassivated surface was supposed to be a H-terminated surface (as shown in **Figure 5.19**). This can be a reasonable explanation behind the rather high initial minority carrier lifetime.

When the substrate temperature started to increase from room temperature to around 175°C, an increase of minority carrier lifetime can be observed. Here it is possible that the remaining unsaturated dangling bonds, mainly on the unpassivated surface, start to pull toward each other, forming the so-called dimer bonds. However, as the temperature further increases to 200°C, the minority carrier lifetime of the sample declined to almost the initial value. This is probably due to a partial deterioration of the H-terminated surface, the dissociation of Si-H or dimer bonds due to the increase of substrate temperature.

Another quick decrease of minority carrier lifetime can be observed as soon as the plasma was ignited. The minority carrier lifetime of the sample at this point was very low. It is very likely that most of the Si-H and the dimer bonds of the H-terminated surface got broken due to

the plasma emission, leading to an increase of unsaturated silicon atoms on the wafer surface. As the deposition process continued, the formation of chemical bonds between the unsaturated surface silicon atoms and the passivation material occurred. This led to an improvement of chemical passivation of the sample and thus resulted in an increase of minority carrier lifetime.

After about 30 minutes, the improvement of minority carrier lifetime slowed down, and a plateau appeared. This is due to the fact that the number of dangling bonds at the c-Si/a-Si:H interface cannot be further decreased, as the plasma species (e.g. radical, atom, etc.) no longer reached the interface. As soon as this plateau feature was observed, the plasma was turned off to terminate the deposition. This point marked the optimal a-Si:H thickness that provides the highest possible as-deposited surface passivation for c-Si wafer, at least for the deposition recipe used in this experiment.

5.8 In-situ study of surface passivation during annealing

Annealing has been known to activate the surface passivation properties of various passivation materials, such as Al_2O_3 , a-Si:H, etc. However, different materials or even the same material prepared with different processes and/or recipes require different annealing conditions (i.e. chamber environment, temperature, and duration) to activate their passivation properties, so the minority carrier lifetime of the sample can reach its optimal point. In this section, the in-situ MPL study of the evolution of c-Si surface passivation provided by Al_2O_3 during annealing at various conditions will be presented.

5.8.1 Sample & experimental set-up

High quality double-side polished 4 inches n-type (100) FZ c-Si wafers with a resistivity of approximately $3 \Omega \cdot \text{cm}$ and a thickness of about $280 \mu\text{m}$ were used as substrates in this experiment. The wafers were symmetrically passivated by a 6 nm of Al_2O_3 layer, synthesized by a thermal ALD reactor (model R200) from Picosun. It is important to mention that prior to deposition of the Al_2O_3 passivation layers, all wafers were subjected to a short (≈ 30 seconds) wet chemical cleaning in a 5% hydrofluoric acid solution in order to remove the native oxide layer and then transferred quickly to the ALD reactor. The Al_2O_3 growth process was performed at 150°C , during which the gas precursors were alternatively introduced into the chamber. Here, trimethylaluminium ($\text{Al}(\text{CH}_3)_3$) was used as a metal precursor, while water vapor was used as an oxidant. After the passivation layer was deposited, the samples were transferred to the PLASMAT reactor, where they would be annealed at different annealing conditions. For the referencing purpose, the first sample was annealed at 350°C for 30 minutes (baseline annealing condition). Here, the reactor was filled with hydrogen gas (200 sccm of gas flow rate) at a pressure of about 1 Torr. It should be mentioned that this baseline annealing condition was developed by Lebreton [23] and shown to be an optimal annealing condition for Al_2O_3 passivation layers grown at 150°C . The other samples were annealed in the same environment, yet at different temperatures and different time spans. Throughout the annealing processes, from the moment the substrate temperature started to increase until it reached the set-point and then returned back to the room temperature, the in-situ MPL was used to characterize in real time the evolution of minority carrier lifetime of the sample.

5.8.2 Results

Baseline annealing condition

Figure 5.20 shows the evolution of the minority carrier lifetime of an Al_2O_3 -passivated sample during annealing at 350°C for 30 minutes in the hydrogen environment. It should be reminded that the minority carrier lifetimes, measured at different temperatures in this experiment, have been converted to the minority carrier lifetimes at room temperature equivalent by using **Equation 5.7**. One can see that, as the substrate temperature increased, the minority carrier lifetime of the sample rose up until reaching a peak ($\tau_{peak} \approx 900 \mu\text{s}$) at around 250°C . Then, as the temperature further increased to 350°C , the minority carrier lifetime dropped back and only increased slightly throughout the 30 minutes of maintaining the substrate temperature at 350°C . Surprisingly, as soon as the substrate temperature started to decrease, the minority carrier lifetime of the sample quickly jumped up. Then it gradually increased as the temperature gradually declined toward room temperature. These resulted in a final minority carrier lifetime of approximately $900 \mu\text{s}$ when the reactor reached the room temperature.

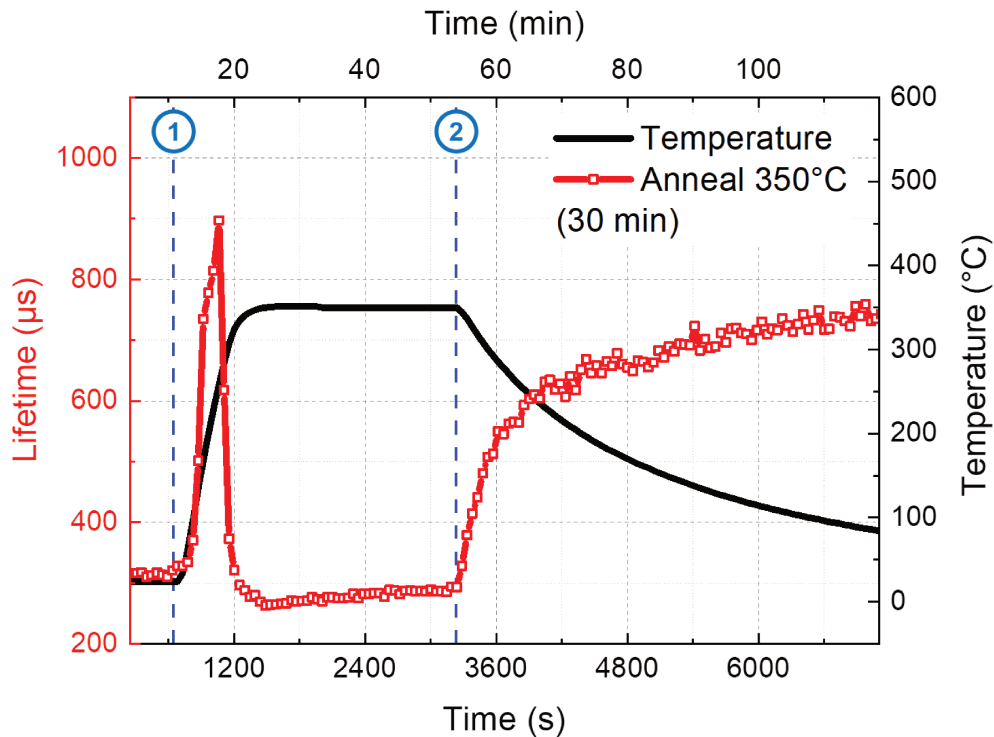


Figure 5.20 – Evolution of minority carrier lifetime of an Al_2O_3 -passivated c-Si wafer during annealing at 350°C for 30 minutes plateau in hydrogen environment. Note: (1) the substrate temperature started to increase, (2) the heating element was turned off and substrate temperature started to cool down.

Modified annealing conditions

Seeing that the minority carrier lifetime of the sample remained almost unchanged while the substrate temperature was maintained at 350°C for 30 minutes, another annealing experiment at

the same temperature was performed. However, instead of waiting for 30 minutes, the waiting time was reduced to less than one minute to see if the same result can be obtained. Furthermore, as there was a sharp peak of carrier lifetime at around 250°C, another additional annealing experiment was conducted at this temperature with a waiting time also less than one minute. The main objective of the latter experiment is to observe whether this carrier lifetime peak can be maintained.

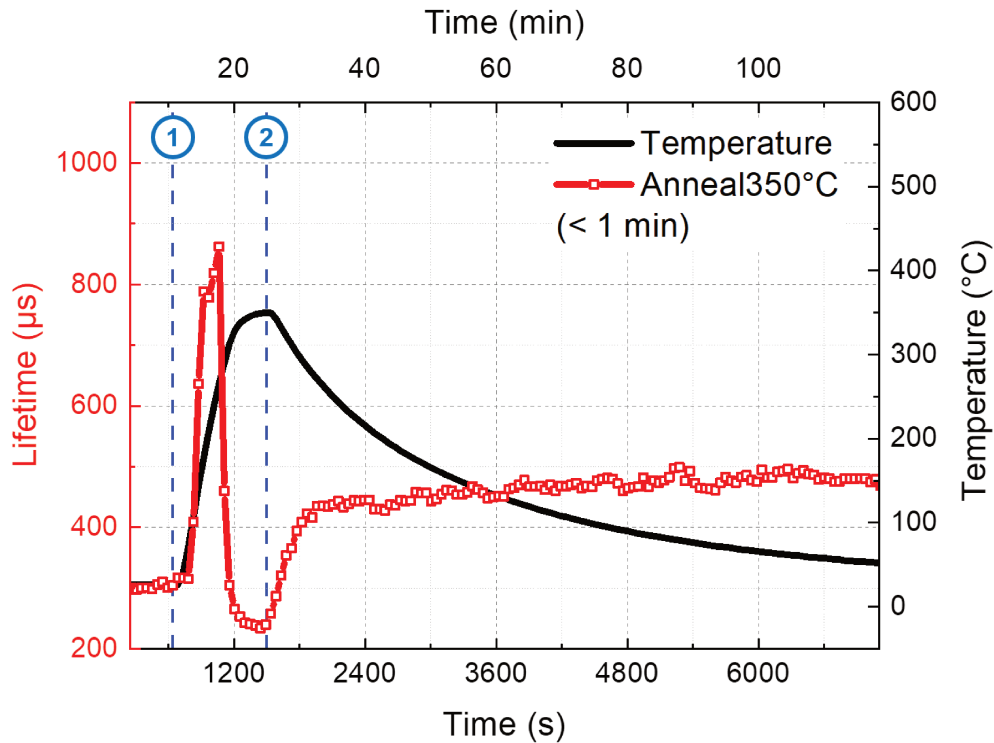


Figure 5.21 – Evolution of minority carrier lifetime of an Al_2O_3 -passivated c-Si wafer during annealing at 350°C for less than 1 minutes plateau in hydrogen environment. Note: ① the substrate temperature started to increase, ② the heating element was turned off and substrate temperature started to cool down.

Figure 5.21 shows the evolution of the minority carrier lifetime of the sample during annealing at 350°C with less than one minute of waiting time. It can be observed that the carrier lifetime profile obtained from this experiment exhibits very similar features compared to the one obtained during the annealing at 350°C for 30 minutes: the lifetime peaks at around 250°C before dropping down when the substrate temperature further increases to 350°C and rising up again when the substrate temperature starts to decrease. However, because of not waiting long enough, the level to which the minority carrier lifetime increases when the reactor starts to cool down is lower than what has been observed in the previous annealing experiment. This leads to a final minority carrier lifetime of only about 500 μs when the reactor reached the room temperature.

The evolution of minority carrier lifetime of the sample during the annealing at 250°C is shown in **Figure 5.22**. The carrier lifetime profile obtained in this experiment is completely different from those observed in the previous cases. It can be observed that the minority carrier lifetime of the sample increased with the increase of temperature until reaching the peak at approximately 250°C ($\tau_{peak} \approx 900 \mu\text{s}$), and then it steadily rose as the substrate temperature

gradually decreased. One may also notice that, as the substrate temperature was prevented from exceeding 250°C, no decrease of minority carrier lifetime was observed during this annealing.

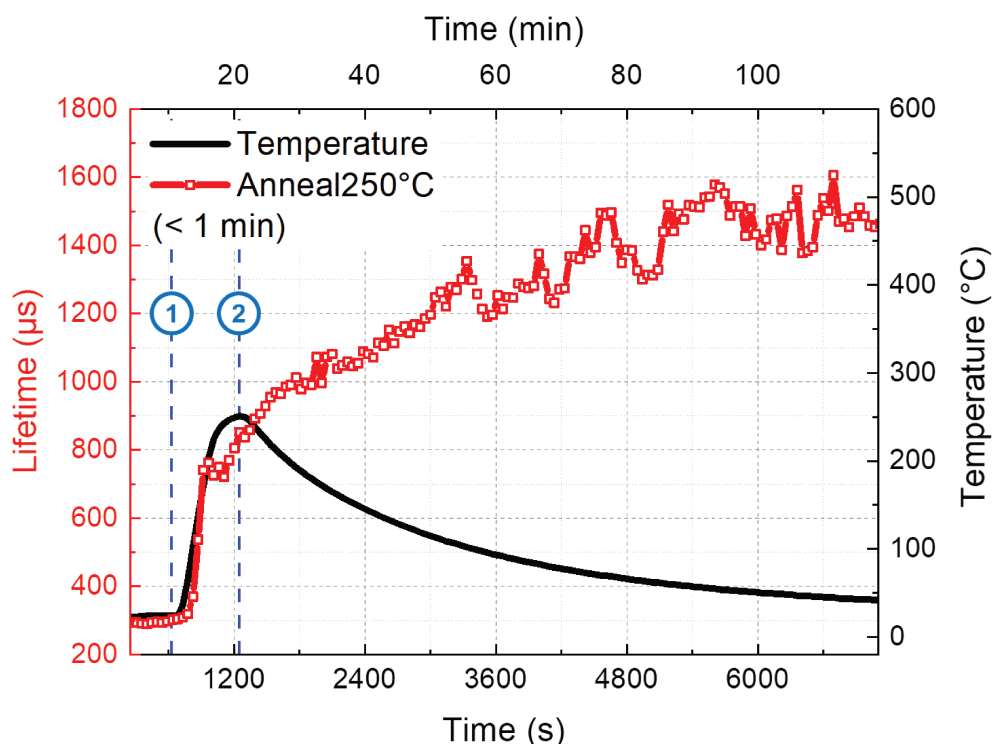


Figure 5.22 – Evolution of minority carrier lifetime of an Al_2O_3 -passivated c-Si wafer during annealing at 250°C for less than 1 minutes plateau in hydrogen environment. Note: ① the substrate temperature started to increase, ② the heating element was turned off and substrate temperature started to cool down.

5.8.3 Discussion

In these annealing experiments, we have seen that the minority carrier lifetime of the sample increased as the substrate temperature started to rise up. This feature could be related to the diffusion of atomic hydrogen, originating in the Al_2O_3 layer, to passivate the dangling bonds at the interface between the c-Si wafer and the Al_2O_3 layer. It is important to remind that the as-deposited Al_2O_3 film grown at 150°C contains a significant amount of hydrogen, approximately 5 atomic percent [24–27], which can make an important contribution to the improvement of surface passivation.

However, as the substrate temperature further increased beyond approximately 250°C, a decrease of minority carrier lifetime occurred. At this point, it is possible that some chemical bonds at the c-Si/ Al_2O_3 interface got broken at high temperature, as the molecular vibration increases with the rise of temperature. On top of that, the atomic hydrogen contained in the Al_2O_3 passivation layer is also very likely to leave the film at this high temperature. This could lead to an increase of the interfacial defect density and therefore reduce the minority carrier lifetime of the sample. When the substrate temperature was maintained at 350°C for 30 minutes, only a very slight increase of minority carrier lifetime could be observed. This

feature could be attributed to the formation of the commonly known thin oxide layer at the interface between the c-Si wafer and the Al_2O_3 layer. Apparently, the formation of this thin interfacial oxide layer is quite slow at 350°C .

Finally, when the reactor started to cool down, an increase of minority carrier lifetime could be observed. This feature appeared in all annealing cases, yet they exhibit different dynamic behaviors. For the sample annealed at 350°C for 30 minutes, a quick increase of minority carrier lifetime occurred. This could be related to the thin oxide layer coupled with the reformation of interfacial bonds that had been broken previously. A quick increase of minority carrier lifetime was also observed in case the sample was annealed at 350°C with less than one minute of plateau. However, the level to which the minority carrier lifetime increases is lower than what had been observed during annealing at 350°C for 30 minutes. This is probably due to the fact that the thin oxide layer had not been fully formed at the interface yet. In case the sample was annealed at 250°C , a steady increase of carrier appeared. Here, as the substrate temperature was kept below 300°C , it is very unlikely that the oxide layer was formed at the interface. Therefore, this steady increase of carrier lifetime is more likely to result from the reformation of interfacial chemical bonds and the diffusion of atomic hydrogen to passivate the remaining dangling bonds.

Based on these experimental results, one can see that the surface passivation properties of the Al_2O_3 grown by thermal ALD at 150°C can be activated by the thermal treatment at 250°C for less than one minute. In this experiment, the obtained result is even more favorable than the one obtained from the baseline annealing condition. It is worth mentioning that the in-situ MPL has also been used to study the evolution of minority carrier lifetime during annealing of the c-Si wafers symmetrically passivated with other passivation materials (e.g. a-Si:H, low temperature $\text{SiO}_x/\text{pc-Si}$, etc.) as well as the c-Si wafers with different types of epitaxy layer (e.g. intrinsic epitaxy layer, boron-doped epitaxy layer, etc.).

5.9 In-situ study of surface passivation during deposition of ARC layer

In order to attain high conversion efficiency, the crystalline silicon solar cell requires not only the surface passivation layers to neutralize the surface dangling bonds but also the anti-reflection coating coupled with the surface texture to minimize the number of photons reflected from the surface. A thin layer of a-SiN_x:H is commonly used as anti-reflection coating for c-Si solar cell, as its reflective index can be varied in a wide range (1.8 – 3.2eV) by modifying the film composition (in particular the nitrogen incorporation). This a-SiN_x:H film also acts as a capping layer, providing a good protection for the passivation layer. However, it has been observed that the minority carrier lifetime of the sample degrades after depositing the a-SiN_x:H layer. In this section, the in-situ study of the evolution of minority carrier lifetime of the Al_2O_3 -passivated samples during deposition of a-SiN_x:H layer was conducted.

5.9.1 Experimental set-up

In this experiment, high quality double-side polished c-Si wafers (n-type, FZ, $\langle 100 \rangle$, resistivity of approximately $3 \Omega.\text{cm}$) symmetrically passivated by a 6 nm of Al_2O_3 grown by thermal

ALD at 150°C were used. It is worth mentioning that the methodologies used to prepare these samples were identical to those described in section 5.8.1.

After finishing the preparation, the sample (as-deposited) was transferred to the PLASMAT reactor for deposition of a-SiN_x:H. First of all, the chamber was filled with precursor gases (e.g. SiH₄, NH₃, and H₂) that would be used for the deposition process. At this point, the in-situ MPL measurement of minority carrier lifetime of the sample began. Then, a few minutes after the chamber pressure stabilized at its set-point, the heating elements of the reactor were powered to bring the substrate temperature up to 350°C. The temperature was maintained at this level for about 30 minutes to pre-anneal the sample (mimic the baseline annealing conditions). After that, without decreasing the substrate temperature, the plasma was ignited and maintained for about 10 minutes to deposit the a-SiN_x:H layer. The detailed plasma condition is shown in **table 5.3**. Finally, the plasma was turned off and the substrate temperature was set back to room temperature. The in-situ MPL measurements were conducted until the substrate temperature was approximately 50°C.

Table 5.3 – Plasma conditions used for deposition of the a-SiN_x:H anti-reflection layer.

| Paramaters | Value |
|---|---------|
| Pressure | 1 Torr |
| RF power | 2 W |
| SiH ₄ flow rate | 5 sccm |
| NH ₃ flow rate | 30 sccm |
| H ₂ flow rate | 75 sccm |
| Substrate temperature | 350°C |
| Inter-electrode distance | 23.5 mm |
| RF voltage (V_{RF}) | 61.94 V |
| Self-bias voltage (V_{bias}) | - 9 V |
| Plasma potential $V_p = \frac{1}{2}(V_{RF} + V_{bias})$ | 26.47 V |

Having seen that minority carrier lifetime of the sample behaved favorably during annealing at 250°C (annealing experiment), an additional deposition experiment was performed at this temperature to see whether better results could be obtained. Besides the temperature, all of the process parameters used in this second experiment are identical to those in the first experiment. However, it is worth mentioning that the pre-annealing duration in the second experiment was reduced from 30 minutes to less than one minute.

5.9.2 Results

Deposition of a-SiN_x:H at 350°C

Figure 5.23 shows the evolution of minority carrier lifetime of the sample during the deposition of a-SiN_x:H layer at 350°C. In the pre-annealing section, one can see that the minority carrier

lifetime peaked at approximately 250°C before dropping back when the substrate temperature further increased to 350°C. A slight increase of minority carrier lifetime was also observed when the substrate temperature was maintained at 350°C for 30 minutes. These features were exactly identical to what had been observed during the annealing of sample in the hydrogen environment at 350°C for 30 minutes (see Figure 5.20).

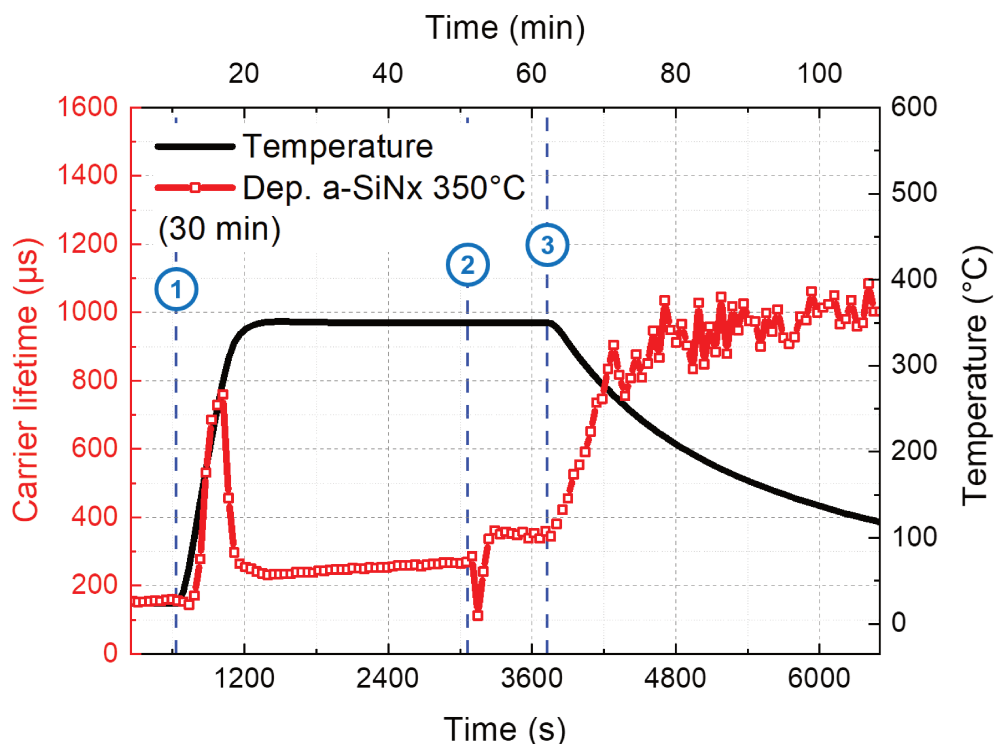


Figure 5.23 – Evolution of minority carrier lifetime of an Al_2O_3 -passivated c-Si wafer during deposition of a-SiN_x:H anti-reflection layer at 350°C. In the same experiment, prior to the deposition, the sample was pre-annealed at 350°C for 30 minutes. Note: (1) the substrate temperature started to increase, (2) the plasma for a-SiN_x:H deposition was ignited, (3) the plasma was turned off and the substrate temperature started to cool down.

In the a-SiN_x:H deposition section, a quick decrease of minority carrier lifetime could be observed as soon as the plasma was ignited. That was followed by a sharp recovery of minority carrier lifetime before it remained roughly constant throughout the deposition process. One may also notice that the plateau observed during the deposition is slightly higher than the minority carrier lifetime of the sample before starting the plasma.

Finally, as soon as the plasma was turned off and the reactor started to cool down, a strong increase of minority carrier lifetime occurred.

Deposition of a-SiN_x:H at 250°C

The evolution of minority carrier lifetime of the sample during deposition of a-SiN_x:H layer at 250°C is shown in **Figure 5.24**. During the pre-annealing at 250°C, it can be observed that the minority carrier lifetime of the sample quickly increased, exhibiting the same features as the carrier lifetime profile obtained during the annealing of sample at 250°C in the pure hydrogen.

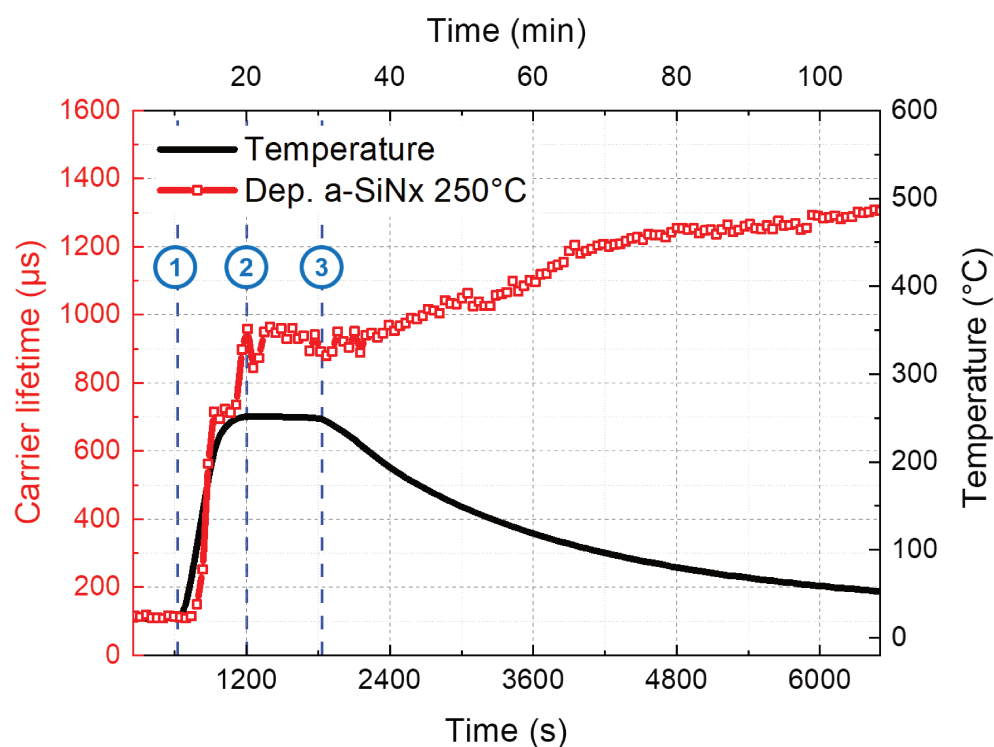


Figure 5.24 – Evolution of minority carrier lifetime of an Al_2O_3 -passivated c-Si wafer during deposition of a-SiN_x:H anti-reflection layer at 250°C. Here, the PECVD plasma for a-SiN_x:H deposition was started as soon as the substrate temperature reached the setpoint. Note: (1) the substrate temperature started to increase, (2) the PECVD plasma for a-SiN_x:H deposition was ignited, (3) the plasma was turned off and the substrate temperature started to cool down.

Then, similar to what had been observed during the deposition at 350°C, a slight decrease of minority carrier lifetime appeared as soon as the plasma was ignited. That was also followed by a steady recovery of minority carrier lifetime until it remained roughly constant during the whole deposition process. Finally, after turning the plasma and the heating element off, a steady increase of carrier lifetime could be observed. This feature is similar to what had been found in the experiment at 350°C, yet with different dynamic behavior.

After the experiment, the optical properties of the a-SiN_x:H films, deposited during the experiments at 250°C and at 350°C, were characterized by Spectroscopic Ellipsometry. The results are shown in **table 5.4**.

5.9.3 Discussion

In these experiments, one can see that the evolution of the minority carrier lifetime during the pre-annealing exhibited similar features as those observed during the annealing experiments in the pure hydrogen. The variation of carrier lifetime during this section is probably caused by the same mechanisms that have been described in the annealing section. Furthermore, these results also suggest that the evolution of minority carrier lifetime in this part depends mainly on the temperature, while the environment (pure hydrogen or a mixture of gases) in which the annealing was performed is less important.

Table 5.4 – Optical properties of the a-SiN_x:H films, deposited during the experiments.

| Film parameters | a-SiN_x:H (250°C) | a-SiN_x:H (350°C) |
|------------------------|--|--|
| Thickness (nm) | 137.42 | 135.09 |
| Bandgap E_g (eV) | 4.77 | 4.74 |
| ϵ^∞ | 0.304 | 0.472 |
| A | 158.74 | 147.70 |
| E_0 | 11.06 | 10.30 |
| C | 10.86 | 7.24 |

When the plasma was ignited, a quick decrease of minority carrier lifetime was observed in both cases. This is probably due to what is known as the plasma-induced degradation of surface passivation (see section 4.2): the deterioration of interfacial chemical bonds caused by the plasma emission, which led to an increase of interfacial defect density (SRH recombination of charge carriers) and ultimately a decrease of minority carrier lifetime. Soon after the quick decrease of carrier lifetime, a steady recovery of carrier lifetime appeared. This feature could be related to the newly-deposited a-SiN_x:H layer. During the deposition process, several mechanisms could occur, affecting the surface passivation of the sample. Firstly, the degradation of interfacial chemical bonds caused by plasma (mentioned above). Secondly, the simultaneous annealing effect as the process was conducted at high temperature (> 200 °C). At the beginning of deposition process, the sample had only a thin Al_xO₃ layer, which make it vulnerable to the plasma. However, as the deposition process continued, the newly-deposited a-SiN_x:H became thicker and somehow partly blocked the plasma VUV light from reaching the interface. At this point, the annealing effect became dominant, leading to a steady recovery of minority carrier lifetime. After the thickness of a-SiN_x:H film reached a certain level, the plasma VUV photons no longer reached the interface (no more degradation). In other words, only the simultaneous annealing process affected the interface. This brought the minority carrier lifetime to roughly its initial value and remained constant (plateau).

Finally, soon after the plasma was turned off and the reactor started to cool down, the minority carrier lifetime increased. It is probably due to the reformation of interfacial bonds (e.g. Si–H, etc.) that led to a decrease of interfacial defect density. However, it can be observed that the dynamic of increase of minority carrier lifetime in both cases (deposition at 350°C and at 250°C) is quite different. This may be related to the temperature of the process as well as the number of dangling bonds remaining at the interfacial. Further study is required for a better understanding of this feature.

Summary

This chapter presents the development of in-situ MPL, from the design to a fully operational characterization tool, as well as some interesting results obtained during the in-situ studies of surface passivation of c-Si wafers during various processes. It has shown that:

- In-situ MPL was developed based on modulated photoluminescence technique, allowing the characterization of minority carrier lifetime of the samples in real time during the processes. Although in-situ MPL and in-situ PL have similar configuration, the substrate holder and the optical system were redesigned to mitigate the problem of high carrier concentration during the measurement and to improve the detection of modulated PL signal. This new system also allows user to reconfigure the size and location of surface area under investigation that can be useful for the study of homogeneity of the sample surface.
- The parameters of the system have been studied and optimized. Regarding the excitation laser, we found that the modification of modulation depth (more than 4%) has no influence on measurement results. However, the modification of average excitation intensity varies the carrier concentration in the sample, leading to different minority carrier lifetime. Regarding the detection system, the time constant and the integration time factor of lock-in amplifier have been optimized. With the new parameters, the system is now able to measure one carrier lifetime in approximately 3.7 seconds.
- A characterization method, so-called LiTe, was developed to determine minority carrier lifetime of the sample at a specific minority carrier density from a series of several MPL measurements at different average excitation intensities.
- A LabView-based graphic user interface was also built. It allows user to effectively control the in-situ MPL system, in particular the in-situ measurement process.
- The minority carrier lifetime provided by MPL technique (so-called differential lifetime) has distinct characteristic compared to the minority carrier lifetime provided by the standard measurement technique (so-called actual lifetime). Therefore, an analytical model is used to correct the carrier lifetime profile provided by in-situ MPL from differential to actual lifetime.
- The minority carrier lifetime of c-Si wafer also varies with temperature, which imposed a great challenge for in-situ study of materials. To deal with the problem, an empirical model was also developed to convert the minority carrier lifetime measured at different temperature to the minority carrier lifetime at one temperature (300K).
- In-situ MPL has been used to characterize the evolution of surface passivation of c-Si wafer in real time during various processes, include deposition of passivation layers, thermal treatment, and deposition of anti-reflection coating.
- The surface passivation properties provided by Al₂O₃ grown by thermal ALD at 150°C can be activated at approximately 250°C. If the temperature further increases, a decline of minority carrier lifetime occurs.
- Evolution of minority carrier lifetime could be related to the diffusion of atomic hydrogen originating from the passivation layer. At 250°C, the atomic hydrogen in the as-deposited Al₂O₃ layer diffuses throughout the film and could possibly passivate the defects at the

c-Si/Al₂O₃ interface. However, as the temperature further increases, atomic hydrogen is more likely to leave the film, leaving the dangling bonds unpassivated.

- Despite the fact that atomic hydrogen could leave the Al₂O₃ film, conducting the experiment at 350°C could lead to a formation of thin oxide layer (SiO_x) at the c-Si/Al₂O₃ interface, which could possibly be the reason behind an increase of carrier lifetime when the reactor started to cool down.

Bibliography

- [1] D. Vincent. Amplitude modulation with a mechanical chopper. *Appl. Opt.*, 25(7):1035–1036, Apr 1986.
- [2] H. Zumbahlen. Phase response in active filters. <https://www.analog.com/en/analog-dialogue/articles/phase-relations-in-active-filters.html>, July 2019.
- [3] Stanford Research System. *Model SR830, DSP lock-in amplifier*. SRS, Inc, 2011.
- [4] Jan Deckers, Emanuele Cornagliotti, Maarten Debucquoy, Ivan Gordon, Robert Mertens, and Jef Poortmans. Aluminum oxide-aluminum stacks for contact passivation in silicon solar cells. *Energy Procedia*, 55:656 – 664, 2014. Proceedings of the 4th International Conference on Crystalline Silicon Photovoltaics (SiliconPV 2014).
- [5] M. Labrune. *Silicon surface passivation and epitaxial growth on c-Si by low temperature plasma processes for high efficiency solar cell*. PhD thesis, Ecole Polytechnique, 2011.
- [6] Nicholas E. Grant, Vladimir P. Markevich, Jack Mullins, Anthony R. Peaker, Fiacre Rougieux, and Daniel Macdonald. Thermal activation and deactivation of grown-in defects limiting the lifetime of float-zone silicon. *physica status solidi (RRL) Rapid Research Letters*, 10(6):443–447, 2016.
- [7] Brendel R. Note on the interpretation of injection-level-dependent surface recombination velocities. *Applied Physics A*, 60:523–524, 1995.
- [8] Armin G. Aberle, Jan Schmidt, and Rolf Brendel. On the data analysis of lightbiased photoconductance decay measurements. *Journal of Applied Physics*, 79(3):1491–1496, 1996.
- [9] J. Schmidt. Measurement of differential and actual recombination parameters on crystalline silicon wafers [solar cells]. *IEEE Transactions on Electron Devices*, 46(10):2018–2025, Oct 1999.
- [10] J. A. Giesecke, S. W. Glunz, and W. Warta. Understanding and resolving the discrepancy between differential and actual minority carrier lifetime. *Journal of Applied Physics*, 113(7):073706, 2013.
- [11] Sinton Instruments. WCT-120PL, wafer lifetime measurement with photoluminescence detector. <https://www.sintoninstruments.com/products/wct-120pl/>, July 2019.
- [12] D. Chung, B. Mitchell, M. Goodarzi, C. Sun, D. Macdonald, and T. Trupke. Bulk lifetimes up to 20 ms measured on unpassivated silicon discs using photoluminescence imaging. *IEEE Journal of Photovoltaics*, 7(2):444–449, March 2017.
- [13] T. Trupke and R. A. Bardos. Photoluminescence: a surprisingly sensitive lifetime technique. In *Conference Record of the Thirty-first IEEE Photovoltaic Specialists Conference, 2005.*, pages 903–906, Jan 2005.
- [14] P. C. Mathur, R. P. Sharma, P. Saxena, and J. D. Arora. Temperature dependence of minority carrier lifetime in singlecrystal and polycrystalline si solar cells. *Journal of Applied Physics*, 52(5):3651–3654, 1981.
- [15] Simone Bernardini, Tine U. Nærland, Adrienne L. Blum, Gianluca Coletti, and Mariana I. Bertoni. Unraveling bulk defects in high-quality c-si material via tidls. *Progress in Photovoltaics: Research and Applications*, 25(3):209–217, 2017.
- [16] J. P. Seif, G. Krishnamani, B. Demareux, C. Ballif, and S. D. Wolf. Amorphous/crystalline silicon interface passivation: Ambient-temperature dependence and implications for solar cell performance. *IEEE Journal of Photovoltaics*, 5(3):718–724, May 2015.

- [17] Masahiro Inaba, Soichiro Todoroki, Kazuyoshi Nakada, and Shinsuke Miyajima. Temperature-dependent minority carrier lifetime of crystalline silicon wafers passivated by high quality amorphous silicon oxide. *Japanese Journal of Applied Physics*, 55(4S):04ES04, 2016.
- [18] Martin A. Green. Intrinsic concentration, effective densities of states, and effective mass in silicon. *Journal of Applied Physics*, 67(6):2944–2954, 1990.
- [19] David M. Goldie. Hole dangling bond capture cross-sections in a-Si:H. *American Journal of Materials Science*, 3(4):70–76, 2013.
- [20] M. Hirose, M. Hiroshima, T. Yasaka, M. Takakura, and S. Miyazaki. Ultra-thin gate oxide growth on hydrogen-terminated silicon surfaces. *Microelectronic Engineering*, 22(1):3 – 9, 1993.
- [21] D. B. Fenner, D. K. Biegelsen, and R. D. Bringans. Silicon surface passivation by hydrogen termination: A comparative study of preparation methods. *Journal of Applied Physics*, 66(1):419–424, 1989.
- [22] P. J. Grunthaner, M. H. Hecht, F. J. Grunthaner, and N. M. Johnson. The localization and crystallographic dependence of si suboxide species at the SiO_2/Si interface. *Journal of Applied Physics*, 61(2):629–638, 1987.
- [23] Fabien Lebreton. *Silicon surface passivation properties of aluminum oxide grown by atomic layer deposition for low temperature solar cells processes*. Theses, Université Paris-Saclay, 2017.
- [24] Carlos Guerra-Nuñez, Max Döbeli, Johann Michler, and Ivo Utke. Reaction and growth mechanisms in Al_2O_3 deposited via atomic layer deposition: Elucidating the hydrogen source. *Chemistry of Materials*, 29(20):8690–8703, 2017.
- [25] G. Dingemans, F. Einsele, W. Beyer, M. C. M. van de Sanden, and W. M. M. Kessels. Influence of annealing and Al_2O_3 properties on the hydrogen-induced passivation of the Si/SiO_2 interface. *Journal of Applied Physics*, 111(9):093713, 2012.
- [26] J. L. van Hemmen, S. B. S. Heil, J. H. Klootwijk, F. Roozeboom, C. J. Hodson, M. C. M. van de Sanden, and W. M. M. Kessels. Plasma and thermal ald of Al_2O_3 in a commercial 200 mm ald reactor. *Journal of The Electrochemical Society*, 154(7):G165–G169, 2007.
- [27] M. D. Groner, F. H. Fabreguette, J. W. Elam, and S. M. George. Low-temperature Al_2O_3 atomic layer deposition. *Chemistry of Materials*, 16(4):639–645, 2004.

CONCLUSION & PERSPECTIVES

In response to the need for a better understanding of the evolution of material properties during the fabrication processes, my three-year doctoral studies have been focused mainly on the development of in-situ characterization tools. In this thesis, three photoluminescence-based in-situ characterization tool are presented.

In-situ SSPL, a unique characterization tool

In-situ SSPL is a unique characterization tool, which allows the study of semiconductor materials in real time during the processes. The tool employs a laser diode with a constant laser intensity to excite the sample and simultaneously detects the steady-state PL intensity/spectra emitted from the sample, which are directly connected to the properties of materials, e.g. surface properties, etc.

The in-situ SSPL has been used to study the evolution of surface properties of crystalline silicon, passivated by Al_2O_3 as well as a-Si:H, under the Ar/ H_2 plasma exposure at various conditions. It has been shown that despite having the same thickness of passivation layers, the Al_2O_3 -passivated sample and a-Si:H-passivated sample behave differently under the same plasma conditions. The surface passivation of a-Si:H-passivated sample rapidly degraded as the plasma was ignited. In contrast, the surface passivation of Al_2O_3 -passivated sample was enhanced just after the plasma ignition before it slowly degraded as a function of plasma exposure time. This difference lies on the fact that the strength of chemical bonds at the c-Si/a-Si:H and c-Si/ Al_2O_3 interfaces is different (the chemical bonds at the c-Si/a-Si:H interface are more vulnerable). Based on the results obtained during the plasma exposure experiment through MgF_2 optical window, the main root cause of plasma-induced modification of surface passivation during the plasma exposure has been pinpointed to plasma emission (in particular the VUV light), which is able to break chemical bonds at the interface between the crystalline wafer and the passivation layer. It has also been observed that the improvement of surface passivation provided by Al_2O_3 layer can only be found on as-deposited sample. Based on the analysis, this improvement can be a result of the dissociation of hydroxyl (Al-OH) radical in Al_2O_3 layer, which leads to an increase of fixed charge density in the layer and ultimately enhancement of field-effect passivation. We have also learned that the plasma-induced degradation of surface passivation can be altered by modifying the applied RF power and/or the chamber pressure. The lower the applied RF power is the slower the plasma-induced degradation. The same holds true for the chamber pressure. Moreover, the increase of substrate temperature also slowed down the degradation of surface passivation of the sample under plasma exposure. This probably results from diffusion of atomic hydrogen to passivated the dangling bonds, compensating

the deterioration of surface passivation caused by plasma emission. Last but not least, experiment also showed that the deterioration of surface passivation caused by plasma exposure can recover by annealing the sample at temperature higher than 150°C.

The in-situ SSPL can be very useful for the study of material behaviors during the processes. Also, it could be used to evaluate the properties of newly-introduced materials as well as the new fabrication processes.

In-situ MPL, from a qualitative to a quantitative characterization tool

In-situ MPL has brought the real-time study of materials for photovoltaic application one step further, as it allows the quantitative measurements of the minority carrier lifetime during the processes. The tool uses an intensity-modulated laser for sample excitation, leading to a modulation of photoluminescence signal with certain phase shift, from which the minority carrier lifetime can be determined.

In the development of in-situ MPL, it was observed that the modulated PL signal can hardly be detected by the old system due to the use of a small optical fiber for collection of emitted photons. On top of that, the samples were found to operate at high injection level (Auger regime) rather than in the standard testing conditions for the solar cell during the measurement due to a small (≈ 1 mm of diameter) excitation zone. These problems were tackled by designing a new substrate holder and a new optical system. The new substrate holder incorporates a large opening (≈ 10 mm of diameter) in the middle of the substrate, allowing to increase the amount of modulated PL signal that can be detected by the system, while maintaining the carrier concentration in the sample at low injection level (standard testing conditions). The new optical system incorporates an off-axis parabolic mirror to maximize the collection of the modulated PL signal. This new system also provides a flexibility for the user to reconfigure the size and location (in the excitation zone) of the surface area under investigation. After the system was built an experiment was conducted to measure the phase delay introduced by the system, which is used for the phase shift calibration. The parameters of the in-situ MPL system were also studied and optimized. Regarding the excitation system, it has been observed that the modification of modulation depth (more than 4%) has no influence on measurement results. However, the modification of average excitation intensity varies the carrier concentration in the sample, leading to different minority carrier lifetimes. Regarding the detection system, the time constant and the integration time factor of the lock-in amplifier have been optimized. With the new parameters, the system is now able to measure one carrier lifetime in approximately 3.7 seconds. In addition, a characterization method, so-called LiTe, was developed to determine minority carrier lifetime of the sample at a specific minority carrier density from a series of several MPL measurements at different average excitation intensities. A LabView-based graphic user interface was also built. It allows the user to effectively control the in-situ MPL system, in particular the in-situ measurement process. Furthermore, as the minority carrier lifetime provided by MPL technique (so-called differential carrier lifetime) has distinct characteristic compared to the minority carrier lifetime provided by the standard measurement technique (so-called actual carrier lifetime), an analytical model is used to correct the carrier lifetime profile provided by in-situ MPL from differential to actual lifetime. Last but not least, the minority carrier lifetime of c-Si wafer also varies with temperature, which imposed a great

challenge for the in-situ study of materials. To deal with the problem, an empirical model was also developed to convert the minority carrier lifetime measured at different temperature to the minority carrier lifetime at one temperature (300K). This allows the comparison between minority carrier lifetimes measured at different temperatures during the processes to be done in a more appropriate way.

After the development of in-situ MPL was finished, the tool has been used to characterize the evolution of minority carrier lifetime of passivated crystalline silicon wafers during various processes. In the thermal treatment processes, it has been observed that the surface passivation properties provided by Al_2O_3 grown by thermal ALD at 150°C can be activated at approximately 250°C . If the temperature further increases, a decline of minority carrier lifetime occurs. This evolution of minority carrier lifetime could be related to the diffusion of atomic hydrogen originating from the passivation layer. At 250°C , the atomic hydrogen in the as-deposited Al_2O_3 layer diffuses throughout the film and could possibly passivate the defects at the c-Si/ Al_2O_3 interface. However, as the temperature further increases, atomic hydrogen is more likely to leave the film, leaving the dangling bonds unpassivated. Despite the fact that atomic hydrogen could leave the Al_2O_3 film, the annealing at 350°C (standard temperature) could lead to a formation of thin oxide layer (SiO_x) at the c-Si/ Al_2O_3 interface, which could possibly be the reason behind an increase of carrier lifetime when the reactor started to cool down. Also, we have observed that maintaining the substrate temperature at around 250°C during the deposition of the anti-reflection coating also provides a higher minority carrier lifetime compared to the deposition process at 350°C .

The ability to measure minority carrier lifetimes of samples during the processes makes the in-situ MPL an efficient characterization tool for not only the study of material behavior but also the optimization of process conditions. After in-situ MPL was successfully developed on an in-house made PECVD reactor (PLASMAT), the tool was transferred to a commercial multi-chamber MVS cluster. This allows the in-situ study of c-Si wafer during deposition of various thin-film semiconductors. It also serves as a model for the integration of in-situ MPL into commercial process tools.

In-situ PLt, beyond the single-junction solar cell

As the tendency toward tandem solar cell is progressively growing, another in-situ characterization tool was built. In-situ PLt (in-situ photoluminescence for tandem solar cell) combines the steady-state photoluminescence and the modulated photoluminescence, allowing the tool to cover a wide variety of material properties. The optical acquisition system was particularly designed with a longpass dichroic mirror to separate the photoluminescence signals from each sub-cell. This allows the in-situ PLt to study in real time the properties of both sub-cells independently yet simultaneously. This concept has been validated by a measurement test with a real tandem solar cell. As the measurement conducted by in-situ PLt requires no electrical contact, the study of the properties of tandem solar cells can be done from the very first stage. This can provide a better understanding on how the processes (e.g. deposition process, thermal treatment, etc.) affect the properties of each sub-cell. Also, it allows the study of interaction of both materials during certain fabrication processes.

Perspectives & future work

Based on the experimental results presented so far, it can be seen that the in-situ photoluminescence tools can provide plenty of interesting information regarding the electrical properties of materials and how they evolve during the processes. In addition, due to its contactless nature, the tool can be used to study the properties of solar cells from the very first step. These in-situ photoluminescence tools can be coupled with other characterization techniques, such as spectroscopic ellipsometry (SE) or Fourier transform infrared spectroscopy (FTIR) to further access other properties of materials.

The spectroscopic ellipsometry is an optical technique, which can be used to access the thickness and the optical properties (including the refractive index and extinction coefficient) of thin-film materials. Therefore, the combination with in-situ photoluminescence tools can be very practical for the study and optimization of materials for surface passivation and anti-reflection coating.

The FTIR is another optical technique, which can be used to study the film compositions (particularly the chemical bonds in the film) by analyzing the absorption of infrared radiation passing through the sample. The wavelength of light absorbed by a particular molecule is a function of the energy difference between the ground state and excited vibrational states. Thus the wavelengths that are absorbed by the sample are characteristic of its molecular structure. The combination between in-situ photoluminescence tools and FTIR will allow a profound study of the influence of structural modification of for example passivation layer on the electrical properties of the solar cells.

It should be mentioned that the coupling of in-situ photoluminescence tools with other optical techniques will broaden the range of material properties the tool can cover, while maintaining the contactless property that allows the study of solar cell precursors from the very first step.

Appendix A

IN-SITU PLt: BEYOND THE MONOJUNCTION SOLAR CELL

Over the last few decades, thanks to the development of new technologies and the improvement of material quality, the conversion efficiency of single-junction solar cell has been greatly enhanced, almost reaching the Shockley-Queisser limit (29.8% for c-Si and 33.4% for GaAs). To go beyond this theoretical limit, many studies have been conducted on the development of multi-junction solar cells. Among many different cell structures, the tandem (two-junction) solar cell between a high band-gap material (e.g. perovskite, III-V material, etc.) and a c-Si wafer is the most studied structure. As there is a strong tendency in the photovoltaic community toward the tandem solar cell, another in-situ characterization tool, so-called in-situ PLt (in-situ photoluminescence for tandem solar cell), was developed.

A.1 Introduction to tandem solar cells

As mentioned previously, the tandem solar cell comprises a stack of two semiconductor materials with different absorption characteristics (different band gap values) to harvest a broader spectrum of solar radiation. In such a structure, the top cell is always the high band-gap material, while the bottom cell has a smaller energy gap compared to that of the top cell. By arranging the cells in this way, the high energy photons of the solar spectrum get absorbed in the top cell, whereas the low energy photons pass through the top cell and get absorbed in the bottom cell.

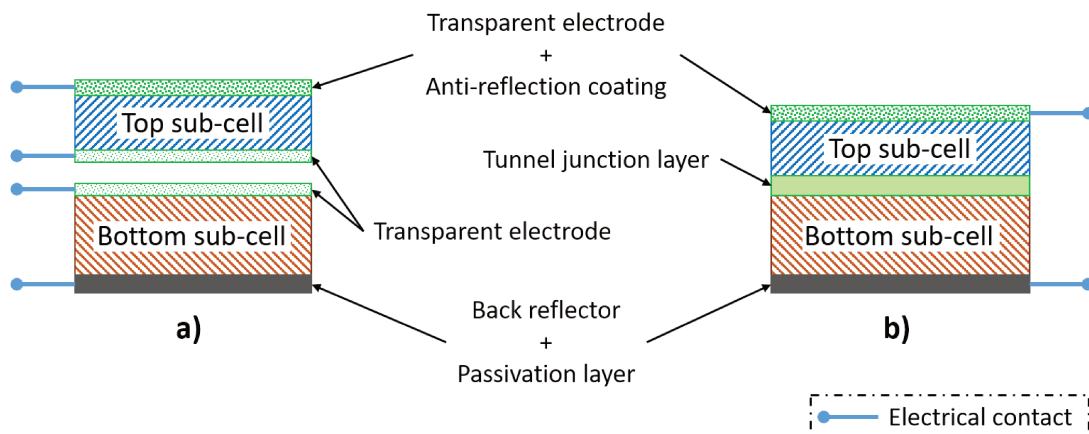


Figure A.1 – Schematic of the structure of tandem solar cells: a) tandem solar cells in 4-terminal configuration; b) tandem solar cell in 2-terminal configuration.

The configuration of the tandem solar cell can be divided into two main groups: four-terminal (4T) configuration and two-terminal (2T) configuration. In 4T configuration, the sub-cells are electrically decoupled, so their operating point are independently controlled (see **Figure A.1**). The great majority of tandem cells employ the 2T configuration, in which the sub-cells are electrically connected in series. This configuration is simpler to fabricate, as it results naturally from the monolithic deposition process (individual cells are connected by tunnel junctions). Yet this series connection imposes an important boundary condition - that the current in both sub-cells must be equal to achieve optimal power output. This condition constrains the band gaps that can be used as well as the thickness of the absorber layers.

Of various material combinations, the tandem solar cells on c-Si are the most studied structure, as the technologies for c-Si solar cells have been extensively well developed. Nowadays,

the highest record efficiencies of tandem solar cell on c-Si are 28% for perovskite/c-Si tandem solar cell [1] (OxfordPVTM) and 33.3% for III-V/c-Si tandem cell [2] (Fraunhofer Institute for Solar Energy Systems-ISE). This proves the right direction toward high efficiency solar cell, yet it is far beyond the theoretical limit ($> 40\%$) of tandem solar cell on c-Si [3]. Therefore, a better understanding of the material properties as well as the influence of each fabrication process of both sub-cells is required for the cell optimization toward the highest possible conversion efficiency.

A.2 Development of in-situ PLt

A.2.1 Introduction to in-situ PLt

In-situ PLt (in-situ photoluminescence for tandem cell) is a characterization tool, which allows the measurement of electrical properties of tandem solar cells in real time during the process. The tool combines two optical characterization techniques, the steady-state photoluminescence (SSPL) and the modulated photoluminescence (MPL), allowing us to cover a wide variety of material properties. As mentioned in chapter 3, the SSPL can be used to access the band energy of materials, the defect-induced energy levels, the defect density (qualitatively), etc. On the other hand, the MPL can be employed to measure the minority carrier lifetime of semiconductor.

Depending on the sample as well as the properties to be investigated, the in-situ PLt can be arranged in three different configurations: in-situ PL/PL, in-situ MPL/MPL, and in-situ MPL/PL. In this chapter, we will focus mainly on the in-situ MPL/PL configuration, which is particularly designed for the in-situ study of tandem solar cells with c-Si wafer: measure the minority carrier lifetime of the c-Si bottom cell and detect the PL intensity/spectrum of the top cell.

It is worth mentioning that, thanks to a specifically designed optical system, the characterization of both sub-cells can be performed simultaneously yet independently during the processes.

A.2.2 Tool configuration

Figure A.2 shows the schematic diagram of the in-situ PLt. The system incorporates two laser sources (L_1 and L_2) with different wavelengths (λ_1 and λ_2), which are dedicated to excitation of the top sub-cell (SC_1) and the bottom sub-cell (SC_2) of the tandem solar cell. Each laser source was carefully chosen in such a way that its photon energy¹ is larger than the band gap of the corresponding sub-cell ($E_{photon,1} > E_{g,SC_1}$ and $E_{photon,2} > E_{g,SC_2}$), so the charge carriers can be generated in the material. In addition, the photon energy of the second laser source is chosen be smaller than the energy gap of the first sub-cell ($E_{photon,2} < E_{g,SC_1}$), so it can pass through the first sub-cell without getting absorbed. It is important to mention that the intensity of the first laser is maintained constant throughout the measurement process, while the intensity of the second laser is modulated at different frequencies.

¹photon energy $E_{photon} = hc/\lambda$

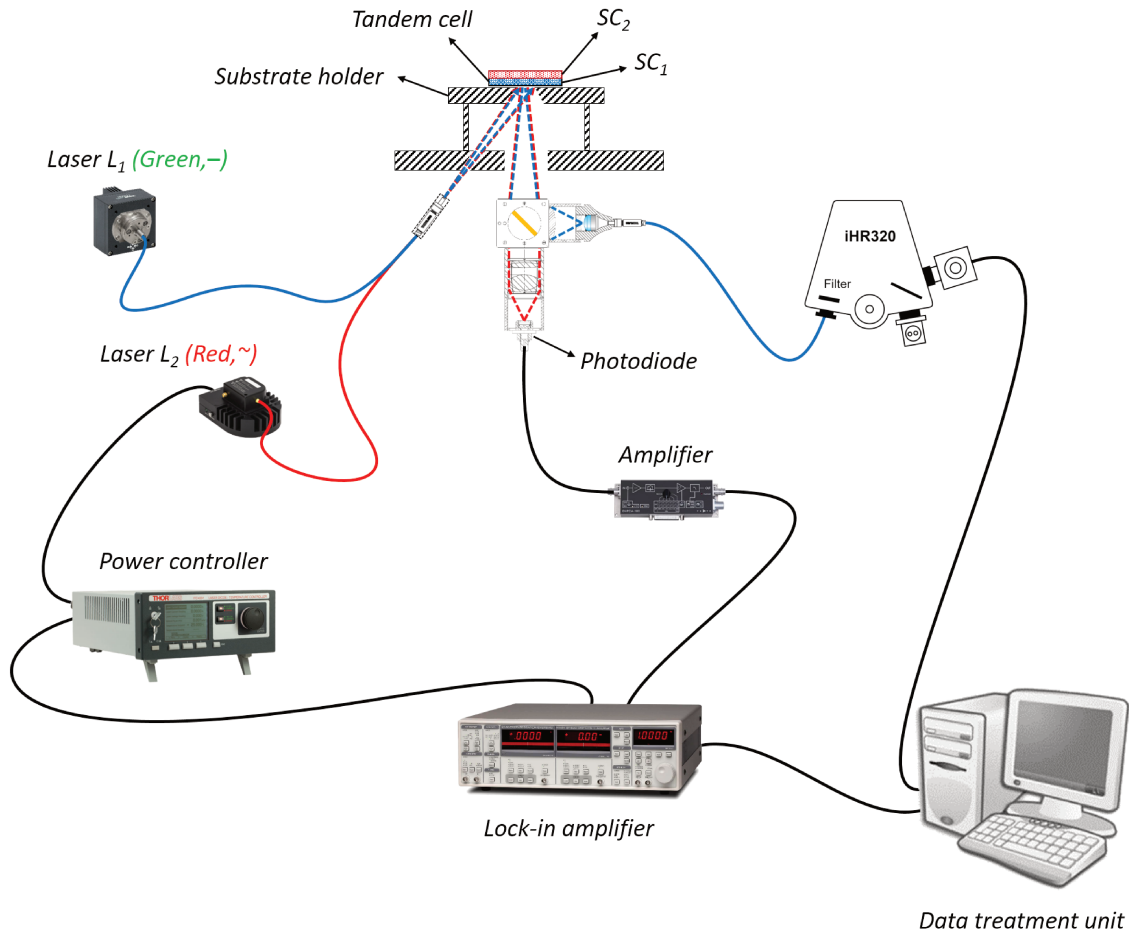


Figure A.2 – Schematic diagram of the in-situ PLt characterization tool. The line colors represent the laser light and the photoluminescence signals in each system, steady-state PL system (blue) and modulated PL system (red).

The photoluminescence signals, simultaneously emitted from both sub-cells, are collected and separated by an optical system, mainly comprised of an optical beamsplitter and two sets of optical lens. The optical beamsplitter is a longpass dichroic mirror (positioned at a 45° angle with respect to the incident photoluminescence beams), which is used to spatially separate the steady-state PL signal of the top sub-cell from the modulated PL signal of the bottom sub-cell. It is worth mentioning that the photoluminescence signal emitted from both sub-cells can be separated due to the fact that they are electromagnetic radiations with different wavelengths λ_{SC1} and λ_{SC2} ($\lambda_{SC2} > \lambda_{SC1}$). Therefore, by choosing the cut-on wavelength (λ_{cut-on}) of the longpass dichroic mirror between λ_{SC1} and λ_{SC2} ($\lambda_{SC1} < \lambda_{cut-on} < \lambda_{SC2}$), the modulated PL signal will pass through the mirror, while the steady-state PL signal will be 45-degree reflected to the side.

After being separated, the modulated PL signal of the bottom cell is sent straight to a lens system, a doublet achromatic pair and a long pass filter, where the signal is collimated and focused directly on an InGaAs photodiode (*SM05PD4A, Thorlabs*). The signal is then sent to the pre-amplifier (*DHPCA-100, Femto*) and finally the lock-in amplifier to measure the phase shift. On the other hand, the steady-state PL signal of the top cell is reflected to another lens system, where the signal is coupled into an optical fiber (diameter of $600 \mu m$). This signal is then sent to the iHR320 photo-detecting apparatus (monochromator + liquid N₂-cooled pho-

todiode) from HORIBA to measure its intensity/spectrum. Finally, these signals (phase shift of modulated PL signal and intensity/spectrum of steady-state PL signal) are transferred to the signal treatment unit for data analysis.

The in-situ characterization can be achieved by continuously exciting the sample with both lasers and repeatedly detecting the photoluminescence signals (steady-state PL and modulated PL) throughout the processes.

A.2.3 Improvement of optical lens system

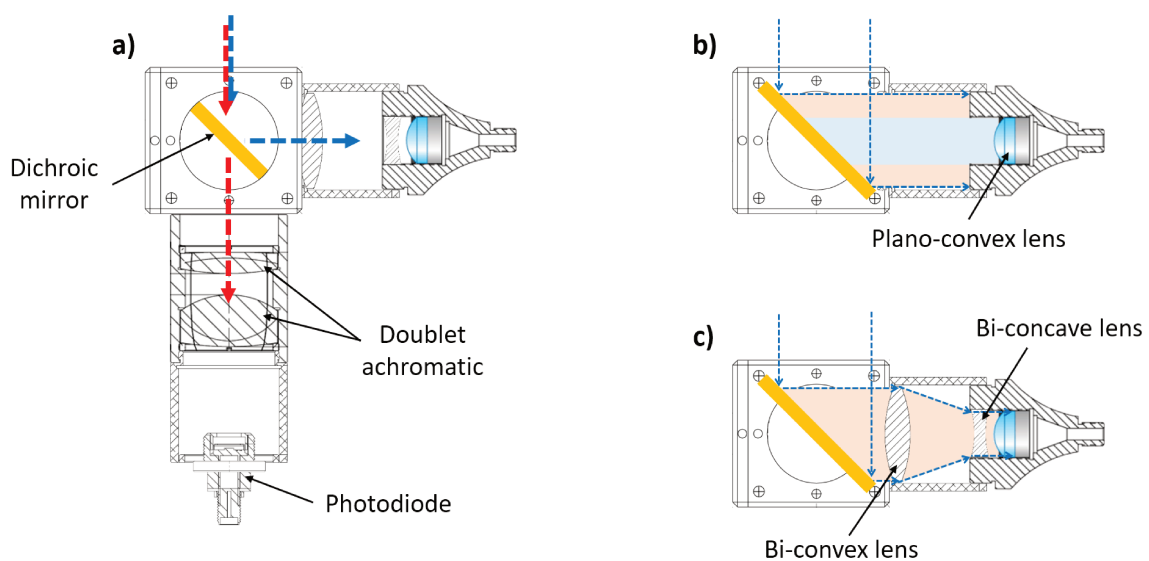


Figure A.3 – Schematic diagram of the optical lens system of the in-situ PLt characterization tool. a) the complete optical system; b) the optical part used for collection of steady-state PL signal (before the modification); c) the optical part used for collection of steady-state PL signal (after the modification).

The optical lens systems play a major role in collecting the photoluminescence signals (See **Figure A.3**). For the modulated PL signal, a doublet achromatic pair is used to maximize the collection of signal passing through the mirror. However, only a small plano-convex lens with a diameter of 12.7 mm (a standard collimator lens for 30 mm cage cube from *Thorlabs*) is used to collect and couple the steady-state PL signal into the optical fiber. With this collimator, the collection of steady-state PL signal suffered a great loss as only a small portion of the signal was collected. To deal with this problem, a new optical lens system was designed. In this new system, three optical lenses are used. First, a 25.4 mm bi-convex lens is used to focus the steady-state PL signal, reflected from the mirror, into a spot. Then a 12.7 mm bi-concave lens is used to re-collimate the signal but in a smaller diameter. Finally, a 12.7 mm plano-convex lens is used to couple the signal into an optical fiber. With this new optical lens system, the collection of signal has been significantly improved - the intensity of signal collected by the new system is increased 4 times higher than the one collected with the old system (see **Figure A.4**).

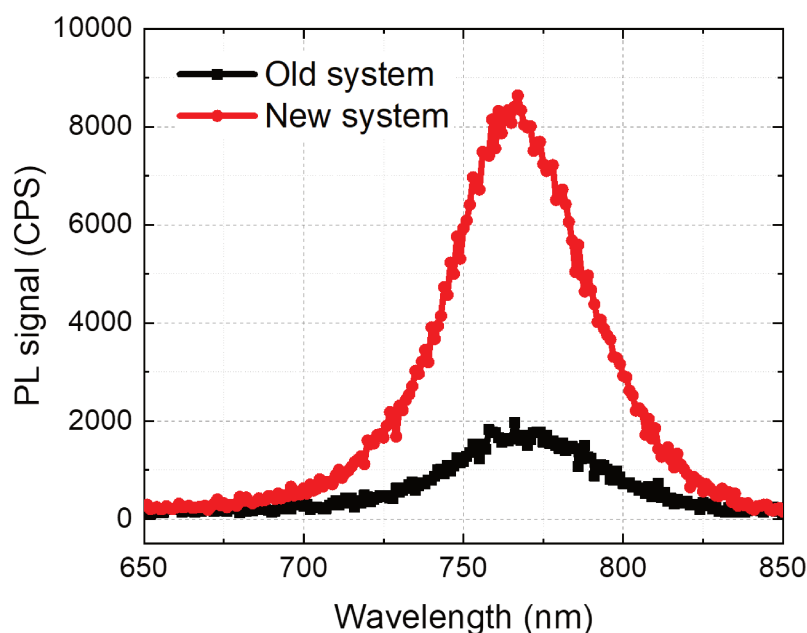


Figure A.4 – Comparison of PL spectra of a perovskite cell measured by the in-situ PLt with the old and new optical systems.

A.3 Measurement test with in-situ PLt

After the development of in-situ PLt was finished, a small test was conducted to measure the properties of tandem solar cells. Here, an as-fabricated monolithic two-terminal tandem solar cell was used. The cell comprises a $525\ \mu\text{m}$ c-Si bottom sub-cell and a $3\ \mu\text{m}$ aluminum gallium arsenide (AlGaAs) top sub-cell, which were bonded together by surface-activated direct wafer bonding technique. The detailed description of cell fabrication is reported elsewhere [4].

During the test, the sample was placed into the reactor filled with hydrogen gas with the chamber pressure of approximately 1 Torr. The in-situ PLt was then used to characterize simultaneously the properties of both sub-cells. It should be mentioned that the measurements were conducted at room temperature. **Figure** A.5a and A.5b show respectively the steady-state PL spectra of top sub-cell and the minority carrier lifetime of bottom sub-cell, obtained from the in-situ PLt measurements of the sample.

Despite the fact that this test was not conducted during the processes (e.g. thermal treatment, deposition of capping layer, etc.), these experimental results confirm that the in-situ PLt is fully functional and the simultaneous measurement of both sub-cells can be conducted without any problems.

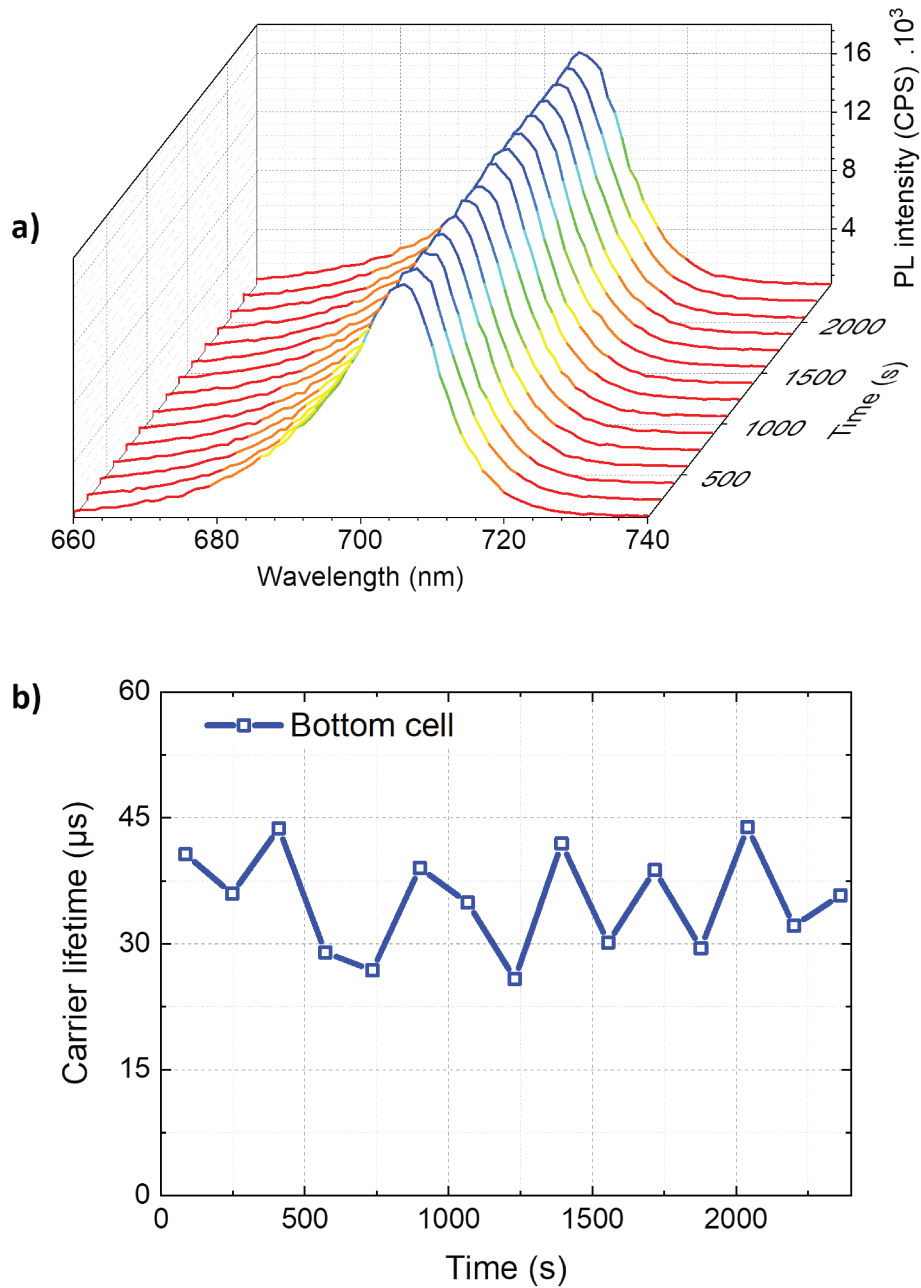


Figure A.5 – Results obtained from the in-situ PLT measurement of an AlGaAs/c-Si tandem solar cell. a) steady-state PL spectra of the top sub-cell (AlGaAs); b) minority carrier lifetime of the c-Si bottom sub-cell. It is important to mention that, in this test, the PL spectral measurements were configured to re-start the cycle at the same time the MPL cycle started.

Bibliography

- [1] OxfordPV-The perovskite company. Oxford pv perovskite solar cell achieves 28 <https://www.oxfordpv.com/news/oxford-pv-perovskite-solar-cell-achieves-28-efficiency>, 2019.
- [2] R. Cariou, J. Benick, F. Feldmann, O. Höhn, H. Hauser, P. Beutel, N. Razek, M. Wimplinger, B. Bläsi, D. Lackner, M. Hermle, G. Siefer, S. W. Glunz, A. W. Bett, and F. Dimroth. III-V-on-silicon solar cells reaching 33% photoconversion efficiency in two-terminal configuration. *Nature Energy*, 3:326, April 2018.
- [3] T. Leijtens, K. A. Bush, R. Prasanna, and M. D. McDehee. Opportunities and challenges for tandem solar cells using metal halide perovskite semiconductors. *Nature energy*, 3(10):828–838, 2018.
- [4] Elias Veinberg-Vidal, Laura Vauche, Karim Medjoubi, Clément Weick, Claire Besançon, Pablo Garcia-Linares, Alejandro Datas, Anne Kaminski-Cachopo, Philippe Voarino, Pierre Mur, Jean Decobert, and Cécilia Dupré. Characterization of dual-junction iii-v on si tandem solar cells with 23.7% efficiency under low concentration. *Progress in Photovoltaics: Research and Applications*, 27(7):652–661, 2019.

Appendix B

IN-SITU MPL IN MVS CLUSTER

After in-situ MPL was successfully developed on an in-house made PECVD reactor (PLAS-MAT), the tool was transferred to a commercial multi-chamber MVS cluster. This transfer allows the in-situ study of the properties of c-Si wafer during deposition of various thin-film semiconductors, which are potential for c-Si photovoltaic application. It also serves as a model for the integration of in-situ MPL into commercial process tools.

B.1 MVS cluster

B.1.1 Introduction

MVS cluster (see **Figure B.1a**) is a commercial reactor from MVSystems. It comprises an ITZ (isolation and transfer zone with a robot arm) and 10 separated chambers. Each chamber can be a load-lock, a characterization unit, or a chamber that is dedicated for deposition of thin-film semiconductors. The use of multiple deposition chambers eliminates the cross-contamination in multi-layer thin film structure and allows the production of high quality devices (electronics or solar cells). It is worth mentioning that the MVS cluster incorporates various techniques (e.g. PECVD, ALD, HWCVD¹, sputtering, etc.) for deposition of materials [1].

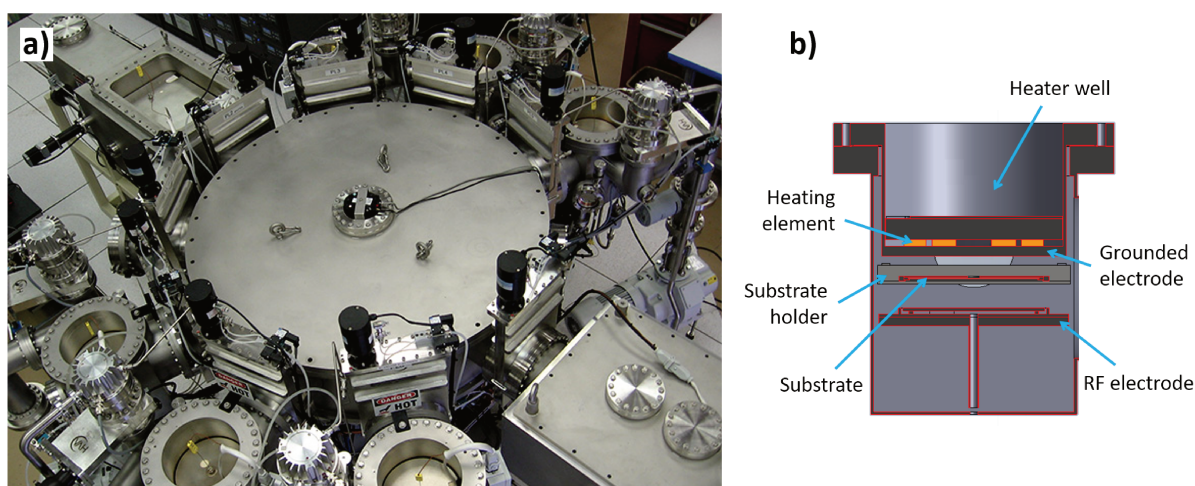


Figure B.1 – a) MVS cluster view from the top. The large cylinder in the middle is the ITZ zone, surrounded by deposition chambers and characterization units. b) Schematic of a PECVD chamber of the MVS cluster.

Each deposition chamber of the MVS cluster can be considered as a small reactor by itself. For instance, a PECVD chamber has its own gas lines, a RF power source, a matching box, and an independent control system. Inside each chamber (see **Figure B.1b**), there are two horizontal electrodes (one is grounded, and another is connected to the RF power source) that are equipped with two independent heating elements. It should be mentioned that the ground electrode is positioned above the RF electrode with an adjustable distance. It is where the substrate holder are attached to during the processes. Regarding the substrate holder, it has no embedded heating element. So the heating of substrate relies on the heat transfer from the grounded electrode.

¹HWCVD: Hot-wire chemical vapor deposition

B.1.2 Feasibility study

The integration of in-situ MPL into MVS cluster (a deposition chamber of MVS cluster to be more precise) requires optical windows, which allow the access to sample during the processes. On a standard PECVD chamber of MVS cluster, there are two optical windows on the chamber wall, which are commonly used to check the plasma. However, non of these can be used for sample excitation nor collection of modulated MPL signal. Therefore, a detail study of the chamber was conducted. We found that the sample can be optically accessed by drilling open the grounded electrode and the backside of the substrate holder. However, due to a complex heating element embedded inside the electrode, the only space available is at its center with a diameter of about 20 mm, large enough for one optical window. A larger opening may damage the heating element. The opening on the backside of substrate holder is not limited, but it has to be aligned with the opening in the grounded electrode. After the studied were done, a decision was taken to make a 20 mm optical window in the middle of the grounded electrode and a 10 mm opening in the middle of the substrate holder.

B.2 Modification of in-situ MPL

During the transfer, a few modification of in-situ MPL were made to adapt with the new chamber as well as to improve the system. However, one should note that the overall configuration of the tool remains the same (see **Figure B.2**), not to mention the user control interface.

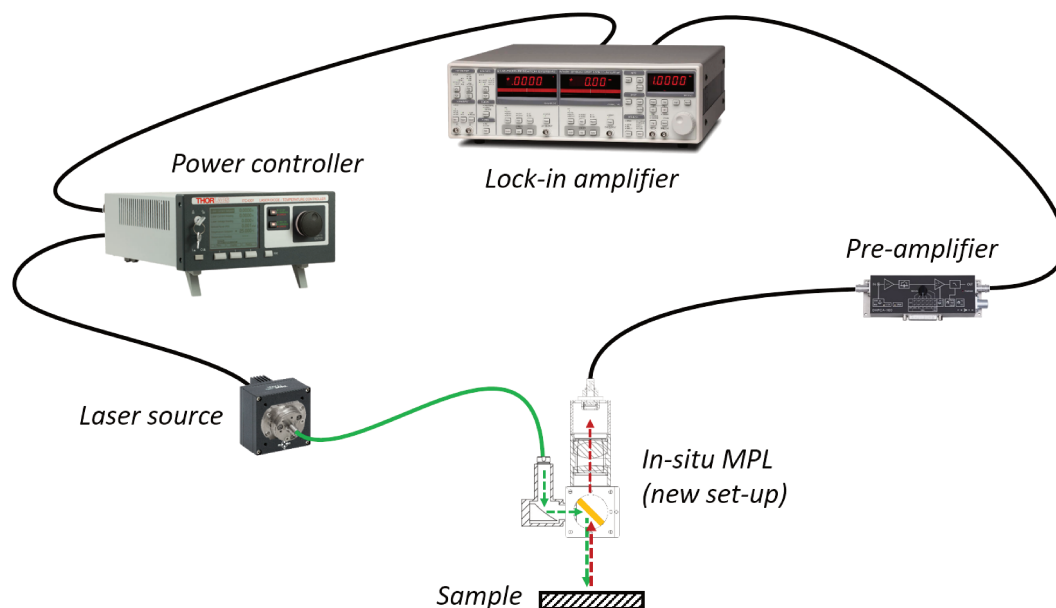


Figure B.2 – Schematic of in-situ MPL on MVS cluster.

B.2.1 Redesign the optical system

As only one optical window can be made, the optical system of in-situ MPL has to be re-designed in a way that the excitation laser and the modulated PL signal can go through the

same path. To do so, an optical system (see **Figure B.3**) with a longpass dichroic mirror [2, 3] is used. The mirror is placed 45° angle with respect to the vertical line, so the laser beam is reflected into the reactor for sample excitation, while the modulated PL signal emitted from sample can pass through. Also, a doublet achromatic pair is used to collect the signal that pass through the mirror and focus it onto an InGaAs photodiode. It should be mention that, between the doublet achromatic pair and the photodiode, a longpass filter is used to block the reflected laser from reaching the photodiode.

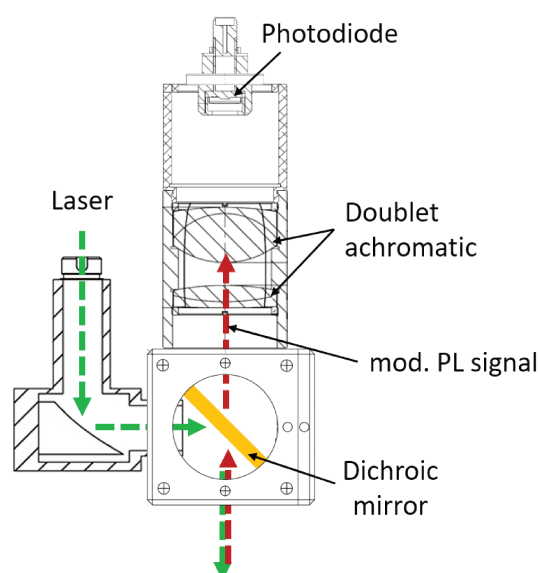


Figure B.3 – Optical system designed for integration of in-situ MPL into MVS cluster.

To collect the modulated PL signal, the newly designed optical system was supposed to be right above the grounded electrode in the heater well. However, during the processes, this electrode may reach the temperature up to 400°C, which may affect the optical system, mainly the InGaAs photodiode. To deal with the problem, the distance between the grounded electrode and the optical system is extended to reduce the heat transfer. A metal tube is used to connect between the electrode and the optical system in order to seal out the ambient light.

B.2.2 A new laser source

Regarding the laser for sample excitation, instead of using the fiber-pigtailed laser diode (785 nm), a TO-package² laser diode setup is used (see **Figure B.4**). This new setup allows us to switch the laser diode from one wavelength to another with much ease compared to the previous setup. This ability to switch the laser excitation from one wavelength to another is expected to bring more interesting result, as laser with different wavelengths excite different area (depth) of the sample. It is important to mention that the laser power controller is kept the same.

²TO-package: transistor outline package

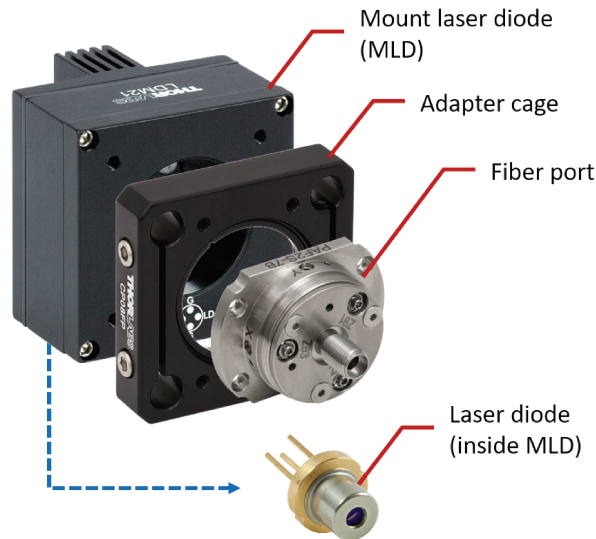


Figure B.4 – TO-package laser diode setup used in the new in-situ MPL.

B.3 Calibration of the tool

After the system was rebuilt, an experiment was conducted to measure the phase shifts introduced by the system (see **Figure B.5**). It should be mentioned that different system has different phase shift, so the calibration should be conducted when the system is modified. A Corning glass is used in this calibration process, as its surface reflection is less than 10%, so the saturation of the photodiode can be avoided. Furthermore, different from a passivated crystalline silicon wafer, Corning glass does not induce additional phase shift to the signal. After the calibration, the new in-situ MPL is now ready for the in-situ study of c-Si wafer during the process in MVS cluster.

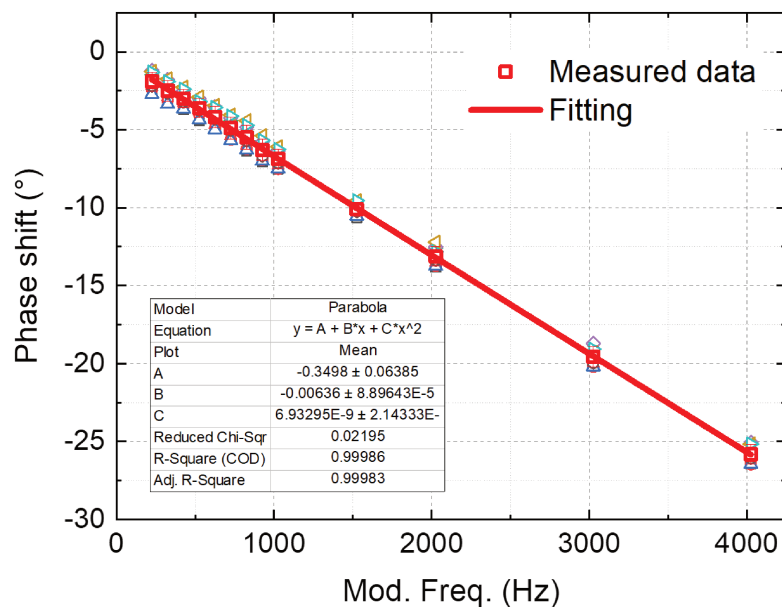


Figure B.5 – Phase shifts introduced by the in-situ MPL system (on MVS cluster).

B.4 Test: in-situ MPL study of c-Si during the position of passivation layer

After the tool was calibrated, an experiment was conducted to test the system. The newly-built in-situ MPL was used to measure the minority carrier lifetime of the sample during the deposition of the passivation layer. In this experiment, a high quality c-Si wafer (n-type, $\langle 100 \rangle$, FZ, $3 \Omega \cdot cm$ of resistivity, $280 \mu m$ of thickness) was used. This sample had been passivated on one side by a $20 nm$ of a-Si:H, grown in a PECVD reactor (so-called ARCAM) at $200^\circ C$.

Before loaded into the MVS reactor, the sample was subjected to a 30 seconds wet chemical cleaning in a 5% hydrofluoric acid solution to remove the native oxide on the unpassivated surface. After that, it was transferred quickly to the MVS cluster to avoid the reformation of the oxide layer.

As soon as the sample was in the chamber, the in-situ measurement of minority carrier lifetime was initiated. However, the deposition process (the plasma condition is shown in **table B.1**) was started about 10 minutes after the sample was in its place to ensure a good thermal stability in the chamber.

Table B.1 – Plasma conditions used for deposition of the a-Si:H passivation layer in the MVS cluster tool.

| Parameters | Value |
|---|------------|
| Pressure | 750 mTorr |
| RF power | 5 W |
| H ₂ /SiH ₄ flow rates | 60/15 sccm |
| Substrate temperature | 200°C |
| Inter-electrode distance | 20 mm |

The obtained results, the evolution of minority carrier lifetime of the sample during the deposition, is shown in **Figure B.6**. It is important to mention that these minority carrier lifetimes is determined at one specific minority carrier density ($\Delta n = 10^{15} cm^{-3}$).

One can see that the minority carrier lifetime of the sample started to increase slightly since the beginning. This is probably due to the fact that the substrate temperature starts to increase, which may cause the formation of dimer bonds. Then a drop of minority carrier lifetime can be observed when the plasma was ignited. This decrease of minority carrier lifetime is probably caused by the plasma-induced degradation of surface passivation (For more details on plasma-induced degradation of surface passivation, please refer to section 4.2 in chapter 4). Finally, as the a-Si:H passivation layer started to grow, a progressive increase of minority carrier lifetime of the sample can be observed.

Although this experiment is a small one, it shows that the new in-situ MPL on the MVS cluster is now fully operational. This system allow us to study the properties of c-Si sample during the processes in MVS reactor, and from this, more interesting results are expected. In addition, this is a solid proof that the in-situ MPL can be transferred to commercial reactor or other process tool.

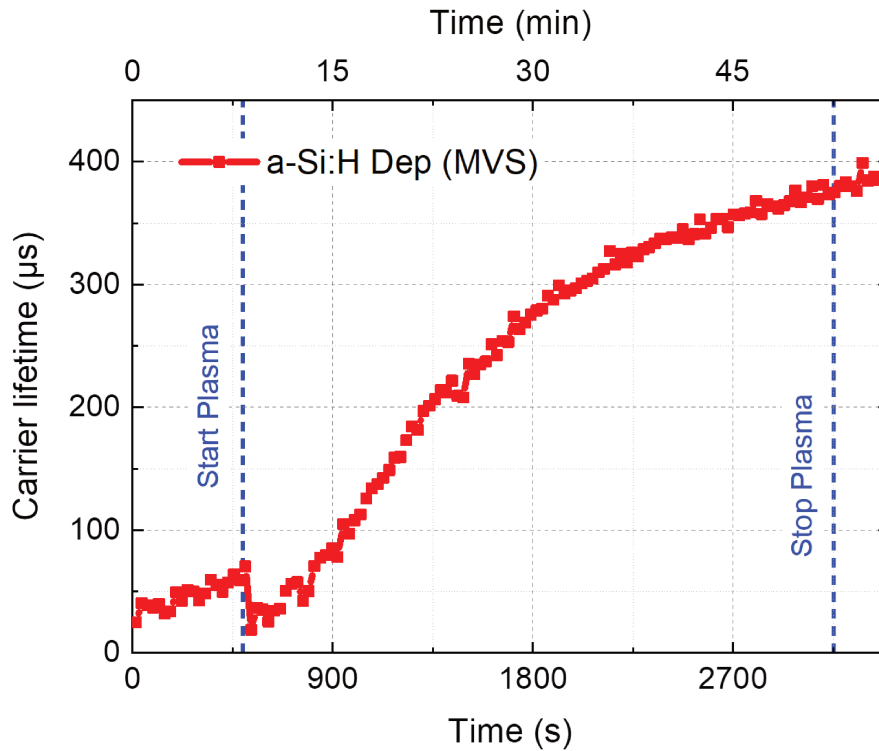


Figure B.6 – Evolution of minority carrier lifetime of a c-Si wafer during the deposition of a-Si:H in the MVS cluster.

Bibliography

- [1] MVSystems LLC. Cluster tool for R&D. <http://www.mvsystemsinc.com/products/cluster-tool-for-rd/>, July 2019.
- [2] Thorlabs Inc. Longpass dichroic mirrors and beamsplitters. https://www.thorlabs.com/newgrouppage9.cfm?objectgroup_id=3313, July 2019.
- [3] E. Mathews (BMG LABTECH USA). What is a dichroic mirror? <https://www.bmglabtech.com/what-is-a-dichroic-mirror/>, July 2019.

RÉSUMÉ

Au cours des dernières décennies, le rendement des cellules photovoltaïques a été considérablement amélioré, atteignant presque la limite théorique de Shockley-Queisser. À ce stade, une compréhension profonde des propriétés des matériaux et de leur évolution au cours des processus de fabrication des cellules solaires devient de plus en plus cruciale pour améliorer encore l'efficacité de conversion des cellules. Pour cette raison, ma thèse a été axée sur le développement des outils de caractérisation *in situ*, qui permettent d'étudier les propriétés des matériaux en temps réel pendant les processus de fabrication et de traitement. Les outils qui ont été développés font appel à une technique appelée photoluminescence (PL). Il s'agit d'un processus en deux étapes qui implique une photo-excitation pour générer des paires électron-trou dans l'échantillon (matériaux semi-conducteurs), suivi d'une photoémission résultant de la recombinaison radiative des porteurs générés. Dans ce manuscrit, trois outils de caractérisation *in situ* seront présentés.

Tout d'abord, la "in-situ SSPL" est un outil de caractérisation qui nous permet d'étudier les propriétés des matériaux semi-conducteurs au cours des processus en mesurant directement l'intensité du signal de photoluminescence émis par l'échantillon. Cet outil a été développé sur la base de la technique de photoluminescence en régime stationnaire, dans laquelle l'échantillon est excité par un laser à puissance constante. Après l'optimisation du système de collection optique, l'outil a été largement utilisé pour étudier l'évolution de la passivation de surface du silicium cristallin, revêtu d'une fine couche d'oxyde d'aluminium (Al_2O_3) déposée par ALD, et d'une couche de silicium amorphe hydrogéné (a-Si:H) déposée par PECVD, sous exposition au plasma Ar/ H_2 dans différentes conditions de décharge. À partir de ces expériences, les différences de comportement entre l'échantillon passivé par Al_2O_3 et l'échantillon passivé par a-Si:H, ont été observées et discutées. De plus, grâce aux expériences d'exposition au plasma effectuées au travers de fenêtres optiques, telles que le fluorure de magnésium (MgF_2) et le verre Corning (CG), la cause première de la dégradation de la passivation de surface induite par le plasma a été déterminée. Enfin, la relation entre la dynamique de la dégradation induite par le plasma et les paramètres de la décharge (notamment puissance RF injectée et pression de travail) a également été étudiée.

Pour aller encore plus loin, l'outil "in-situ MPL" a été construit pour mener une étude quantitative *in-situ* des propriétés des matériaux semi-conducteurs. Cet outil de caractérisation a été développé sur la base d'une technique, appelée photoluminescence modulée (MPL), dans laquelle un laser à intensité modulée est utilisé pour exciter l'échantillon, ce qui nous permet de mesurer la durée de vie des porteurs minoritaires. Après la conceptualisation et la fabrication d'un nouveau système de collection optique, l'étalonnage du système et l'optimisation des paramètres MPL ont été réalisés. En outre, une méthode de caractérisation a été développée, de sorte que l'in-situ MPL est capable de déterminer la durée de vie des porteurs minoritaires à une densité de porteurs souhaitée (par exemple, 10^{15} cm^{-3} pour une cellule solaire

de silicium cristallin à mono-jonction, éclairée sous un soleil). Après de nombreux travaux, l'outil est maintenant pleinement opérationnel et a été utilisé pour mesurer la durée de vie des porteurs minoritaires de silicium cristallin au cours du dépôt de la couche de passivation a-Si:H, du traitement thermique et du dépôt du revêtement antireflet en nitrure de silicium amorphe hydrogéné (a-SiN_x:H). Il a été observé que la durée de vie des porteurs minoritaires de l'échantillon variait fortement au cours des différents processus et diverses hypothèses ont été proposées pour expliquer ces variations. Les résultats expérimentaux montrent également que la température à laquelle les processus ont été conduits joue un rôle majeur dans l'activation et la modification des propriétés de passivation de surface apportée par la couche d'Al₂O₃.

Enfin, comme la tendance aux cellules solaires tandem ne cesse de croître, un autre outil de caractérisation in situ, appelé in-situ PLt (photoluminescence in situ pour cellule solaire tandem) a été créé. Cet outil de caractérisation résulte d'une combinaison de techniques de photoluminescence en régime stationnaire et de photoluminescence modulée. Le système optique du dispositif nous permet d'étudier en temps réel les propriétés des deux sous-cellules de la structure tandem, de manière indépendante et simultanée. L'in-situ PLt constitue un outil de caractérisation potentiel pour la recherche sur les cellules solaires tandem à haut rendement.

Titre : Développement des outils de caractérisation de photoluminescence in-situ pour l'étude de semi-conducteurs pour l'applications photovoltaïques

Mots clés : Photoluminescence in-situ, Durée de vie des porteur, Passivation de surface, cellule mono-jonction, celle tandem

Résumé : Au cours des dernières décennies, le rendement des cellules solaires a été considérablement amélioré, atteignant presque la limite théorique de Shockley-Queisser. À ce stade, une compréhension profonde des propriétés des matériaux et de leur évolution au cours des processus devient de plus en plus cruciale pour améliorer encore l'efficacité de conversion de la cellule. Pour cette raison, ma thèse a été axée sur le développement des outils de caractérisation in-situ, qui permettent d'étudier les propriétés des matériaux en temps réel pendant les processus d'élaboration et de traitement.

Dans ce manuscrit de thèse, trois outils de caractérisation in-situ sont présentés. Premièrement, la « In-situ SSPL », basée sur la technique de photoluminescence en régime stationnaire, est développée pour étudier les propriétés des matériaux semi-conducteurs au cours des processus en mesurant directement l'intensité du signal photoluminescence emis par l'échantillon. Deuxièmement, l'outil « In-situ MPL », basé sur la technique de photoluminescence modulée, est conçu

pour mener des études quantitative in-situ des propriétés de silicium cristallin. Cet outil utilise un laser à intensité modulée pour exciter l'échantillon, de sorte que la durée de vie des porteurs minoritaires puisse être mesurée. En outre, une méthode de caractérisation a été développée, permettant de mesurer la durée de vie des porteurs minoritaires à une densité de porteurs spécifique désirée. Enfin, la « In-situ PLt », résultant d'une combinaison de photoluminescence en régime stationnaire et de photoluminescence modulée, a été construite pour étudier en temps réel les propriétés des deux sous-cellules de la structure tandem de manière indépendante et simultanée au cours du processus.

Grâce à ces outils de caractérisation in-situ, les études sur l'évolution de la passivation de surface du silicium cristallin au cours de différents processus ont été menées, et diverses caractéristiques intéressantes qui n'avaient jamais été rapportées auparavant ont été observées.

Title : Development of in-situ photoluminescence characterization tools for the study of semiconductors for photovoltaics application

Keywords : In-situ photoluminescence, Minority carrier lifetime, Surface passivation, Mono-junction solar cell, Tandem solar cell

Abstract : During the last few decades, the conversion efficiency of solar cell has been significantly improved, almost reaching the Shockley-Queisser theoretical limit. At this point, a profound understanding of material properties and its evolution during the processes become increasingly crucial to further improve the conversion efficiency of the solar cells. For this reason, my doctoral studies have been focused on the development of in-situ characterization tools, which allow the studies of material properties in real time during the processes.

In this thesis, three in-situ characterization tools are presented. Firstly, In-situ SSPL, based on steady-state photoluminescence technique, is developed to study the properties of semiconductor materials during the processes by directly measuring the intensity of photoluminescence emitted from the sample. Secondly, in-situ MPL, based on modulated photolu-

minescence technique, is built to conduct quantitative in-situ study of the properties of crystalline silicon wafer. This tool employs an intensity-modulated laser to excite the sample, so the minority carrier lifetime can be measured. Furthermore, a characterization method was developed, allowing the measurement of minority carrier lifetime at a specific minority carrier density. Lastly, in-situ PLt, resulting from a combination of steady-state photoluminescence and modulated photoluminescence, was built to study in real time the properties of both sub-cells of the tandem structure independently yet simultaneously during the processes. Thanks to these in-situ characterization tools, the studies of the evolution of crystalline silicon surface passivation during different processes were conducted, and various interesting features that have never been reported before were observed.